The Pennsylvania State University

The Graduate School

Department of Materials Science and Engineering

CRYSTALLIZATION AND MICROSTRUCTURE DEVELOPMENT IN SOL-GEL LEAD ZIRCONATE TITANATE THIN FILMS

A Thesis in

Materials Science and Engineering

by

Pavadee Aungkavattana

Submitted in Partial Fulfillment
of the Requirements
for the Degree of
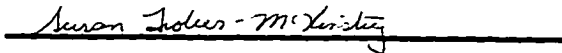
Doctor of Philosophy

December 1996

UMI Number: 9716186

UMI Microform 9716186
Copyright 1997, by UMI Company. All rights reserved.

This microform edition is protected against unauthorized
copying under Title 17, United States Code.

UMI

300 North Zeeb Road
Ann Arbor, MI 48103
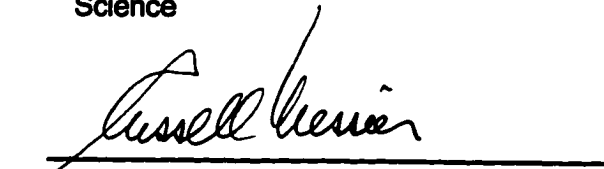
We approve the thesis of Pavadee Aungkavattana.

Date of Signature

Susan Trolier-McKinstry

Susan Trolier-McKinstry
Assistant Professor of Ceramic
  Science and Engineering
Thesis Advisor
Chair of Committee

Nov 22, 1996

Robert E. Newnham

Robert E. Newnham
Alcoa Professor of Solid State
  Science

Nov. 21, 1996

Russell Messier

Russell Messier
Professor of Engineering Science and
  Mechanics

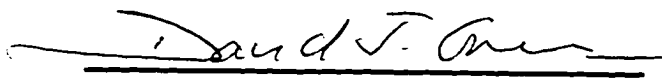Nov. 21, 1996

Clive A. Randall

Clive A. Randall
Associate Professor of Materials
  Science and Engineering

Nov 21 1996

Clayton O. Ruud

Clayton O. Ruud
Professor of Industrial Engineering

Nov. 21 1996

David J. Green

David J. Green
Professor of Ceramic Science and
  Engineering
In Charge of Ceramic Science Option

Nov 27, 1996

ABSTRACT

Lead zirconate titanate (PZT) thin films with a Zr/Ti ratio of 52/48 were prepared by a sol-gel method and spin-coated onto various substrates, including Pt-coated Si, (0001) sapphire, and (100) MgO. The evolution in crystallinity was studied real-time during annealing with *in-situ* spectroscopic ellipsometry (SE) and X-ray diffraction. SE was used in this study to examine the microstructure evolution and the optical properties of PZT films during annealing. Changes in the optical properties, i.e. the refractive index, as a function of temperature were determined. Because the refractive index depends on the crystal phase, SE can serve as an indirect means of following the crystallization. From the SE modeling, PZT films showed quite a homogeneous microstructure with a thin layer of the roughness at the surface after 600°C anneals. As the PZT films crystallized to the perovskite phase, the film refractive indices increased and became comparable with reference data for lanthanum-doped PZT bulk ceramics. This result indicates that the PZT films prepared in this study could be prepared with high densities.

Various annealing rates from 5 to 100°C/minute were utilized in high temperature X-ray diffraction experiments to study the crystallization kinetics and the phase development of the intermediate and the perovskite PZT phases. The fastest ramp rate used in this study (100°C/min) did not allow the bypass of the intermediate phase formation in PZT thin films.

The sol-gel derived PZT films prepared in this study showed good electrical properties with the dielectric constant range between 820 and 1140. A remanent polarization of 23-32 $\mu C/cm^2$ was achieved for film rapid thermally

annealed at 700°C for 30s. The film microstructure was also investigated using a field emission scanning electron microscope (FESEM) and atomic force microscopy (AFM). PZT films show a dense, uniform, fine-grained, and a smooth surface. A cluster structure was also found with a cluster size of about 150 nm to 10 μm. The primary grain size found was 10-15 nm. Excellent agreement between AFM and SE measurements of surface roughness was observed.

TABLE OF CONTENTS

LIST OF FIGURES

LIST OF TABLES

ACKNOWLEDGMENTS

As a child, I always dreamed about growing up to be someone who can do something for my country. I wanted to be a doctor who would work in a small hospital, far from big cities- like the place I grew up. I used to feel very disappointed in myself when I missed a chance to get in the medical school. I used to think that my whole dream was gone and I will never be happy with my life again.

For four years in college, I studied science and I chose to focus on Materials. I spent time getting to know ceramics, mostly conventional ones. I learned about pottery, porcelain, all kinds of glazes, and how sanitary wares and floor tiles could be made. I finally found myself enjoying very much in what I was doing and also deep down in my mind, I kept asking myself what about the 'advanced ceramics'? Here comes the second of my lifetime dreams- I wanted to go to a graduate school, definitely a school of ceramics somewhere in world.

I got my M.S. degree in Ceramic Science here at Penn State after spending my first 2 years working on Y_2O_3-stabilized ZrO_2 and $YFeO_3$ materials for solid oxide fuel cells with Prof. Vladimir S. Stubican. I graduated at the same time as Dr. Stubican's retirement in Fall 1992 and came to join Dr. Susan Trolier-McKinstry's thin film group at the Materials Research Lab at the end of Fall 1992. Ferroelectric thin films and spectroscopic ellipsometry are completely new things for me. I have learned slowly to operate the 'complicated' optical instrument (in my opinion) such as an ellipsometer. Thinking back to my first day with the ellipsometer, I would not have thought it could work friendly with me. Once again, I finally found myself enjoying very much in what I have been working.

For making me whom I am today, I would like to express my sincere gratitude and appreciation to my advisor, Dr. Susan Trolier-McKinstry for her patience, invaluable

guidance throughout the entire study, and for all that I have learned from her. Most of all, I appreciate her understanding, being a good friend and always being there for me during my difficult times.

I wish to thank each of my committee members, Dr. Robert Newhnam, Dr. Clive Randall, Dr. Russell Messier, and Dr. Clayton Ruud for their valuable contributions and suggestions. I also wish to specially thank Dr. Newnham, who always warms the 'far-from-home' students' hearts including mine- thanks for those Thanksgiving and Christmas dinners for all these years.

My appreciation also goes to Sonny Gross at the MRL machine shop and Jon-Paul Maria, my colleague, for their expertise in helping with designing and constructing the conductive block heater for the *in-situ* high temperature measurement. I also wish to thank Herb McKinstry for his technical skill with the spectroscopic ellipsometer, the computer interface used in the heater control, and the electronic systems for the entire study. Thanks also go to Mark Angelone and Mark Erwin for their time helping with the FESEM at the MRI, Penn State.

My student life at the MRL would not be so joyful and memorable without these people: Brady J. Gibbons, Jon-Paul Maria, Johanna Lacey, Joe Shepard, Fei Xu, Tao Su, Heather T. Hawkins, Ed Alberta, Chris Bowen, Francis Toal and Maureen Mulvihill. I have had many precious moments working around them- thanks for their friendship.

I also wish to express my love to my father and mother and our family back in Thailand. For their love and encouragement, I am grateful beyond expression. Finally, I would like to thank my best friend and all-time roommate during my years at Penn State, Wannee Chinsirikul, for her 11-years of invaluable friendship.

Chapter 1

INTRODUCTION

In recent years, interest in ferroelectric thin films has grown rapidly with on-going studies exploring several ferroelectric compositions and deposition techniques. Ferroelectric thin films have unique properties which render them useful in applications including optical devices (Araujo et al. 1990, and Dimos et al. 1995), non-volatile Random Access Memories (RAMs) (Bondurant 1990, Scott and Araujo 1989, and Naik et al. 1992), Dynamic Random Access Memories (DRAMs) (Melnick et al. 1991), integrated capacitors on Si (Lee et al. 1993, Sayer et al. 1992a, and Hsu and Kalish 1992), non-linear optical elements, pyroelectric detectors (Takayama et al. 1987, Shorrocks et al. 1995), microelectromechanical systems (MEMS) (Polla and Schiller 1995 and Polla 1995), and micromotors and actuators (Muralt et al. 1995a, Muralt et al. 1995b, and Robbins 1995). Among ferroelectrics, lead zirconate titanate (PZT) is one of the best candidate materials for these applications because of its remarkable ferroelectric and dielectric properties. However, previous investigations reviewed by Kwok and Desu (1992, 1994), and Griswold et al. (1995) demonstrated that it has been difficult to prepare phase-pure perovskite PZT thin films because evolution of an intermediate phase (identified as either a fluorite-structured compound or a pyrochlore phase) at temperatures as low as 350°C has been difficult to avoid.

Since the intermediate phase is non-ferroelectric, it does not possess the advantageous properties needed for the above applications. Therefore, understanding the evolution of microstructure in thin films and the

transformation of the intermediate phase to the perovskite phase is important for the synthesis of superior ferroelectric thin films. Several studies have reported that the intermediate phase can be bypassed by rapid thermal annealing (RTA) through the first crystallization temperature (Huang et al. 1992 and Chen et al. 1992a). There is, however, little data available on the minimum heating rate required to circumvent the intermediate phase and whether its nucleation can be eliminated when an RTA is used for crystallization. To determine this type of information, *in-situ* structure-sensitive techniques are required.

It is proposed in this study that spectroscopic ellipsometry (SE) be used to examine real time microstructure evolution in ferroelectric PZT thin films during *in-situ* annealing. SE is one of the most powerful techniques for optical nondestructive and non-invasive characterization of surfaces and thin films. Since SE independently measures two parameters (the relative phase and amplitude change of the p and s polarization states of the light due to reflection from the materials under study) at many wavelengths, it can be used to determine the depth profile of the complex dielectric function of the films with resolution approaching the angstrom (Å) level (Chindaudom 1991 and McKinstry 1992). These results allow for the determination of the optical properties (i.e. the refractive index, and the complex reflection coefficients) of thin films as a function of annealing temperature. By making either *in-situ* or *ex-situ* measurements on films, SE data should be useful in calculating the volume fraction transformed into one of the crystalline phases, and thus allow direct application of Avrami kinetics (Avrami 1941).

In order to examine the pyrochlore-perovskite phase transformation using an *in-situ* structure-sensitive technique, a new X-ray diffraction system

(the Ruud-Barrett Position Sensitive Scintillation Detector (R-B PSSD) X-ray diffraction system) developed at the Materials Research Laboratory of The Pennsylvania State University, and the high temperature X-ray diffractometer (HTXRD) of the Oak Ridge National Laboratory, Oak Ridge, TN, were used to study the real time crystallization and growth kinetics of the intermediate phase and the perovskite phases. It was hoped that these results would provide direct evidence on structure evolution in ferroelectric PZT thin films during thermal processing.

By comparing these different techniques, this thesis intends to demonstrate that spectroscopic ellipsometry can be used as a fast quantitative probe of crystallization and microstructure in PZT thin films.

In summary, the objectives of this thesis are:

- to prepare high quality PZT ferroelectric thin films at the morphotropic phase boundary composition (52/48) by sol-gel processing and measure their optical and electrical properties;

- to study microstructure development in PZT thin films during annealing using spectroscopic ellipsometry;

- to examine the phase transformation kinetics for the amorphous to the intermediate and intermediate to perovskite phase changes in PZT thin films during annealing by *in-situ* X-ray diffraction methods.

Chapter 2

LITERATURE REVIEW

2.1. Basic of Ferroelectrics

A ferroelectric material is one in which a spontaneous polarization, P_s can be reoriented between equilibrium domain states by an applied electric field. The spontaneous polarization arises from a non-centrosymmetric arrangement of ions in the unit cell which produces an electric dipole moment. In ferroelectrics, neighboring unit cells tend to deform in the same direction and form a region called a domain. Domains in ferroelectrics differ in the direction of the spontaneous polarization and can be switched by an electric field. In polycrystalline ferroelectric materials, a multiple domain configuration is typically found in single grains.

Many common ferroelectrics have the ABO_3 perovskite structure as shown in Figure 2.1 (Jaffe et al. 1971). For materials like $BaTiO_3$ or $PbTiO_3$, the material undergoes a structural phase transition from the cubic phase shown, to a new low temperature ferroelectric phase. Above the transition temperature or Curie temperature (T_c), the material possesses a centrosymmetric structure and does not show a spontaneous polarization. This phase is called the paraelectric phase. On the other hand, the material enters its ferroelectric phase as the temperature is lowered through the Curie temperature. In Figure 2.1, the B ion is displaced from its body-centered position so that the cubic unit cell deforms into a non-centrosymmetric tetragonal, rhombohedral, or monoclinic phase (Lines and Glass 1977). A spontaneous polarization
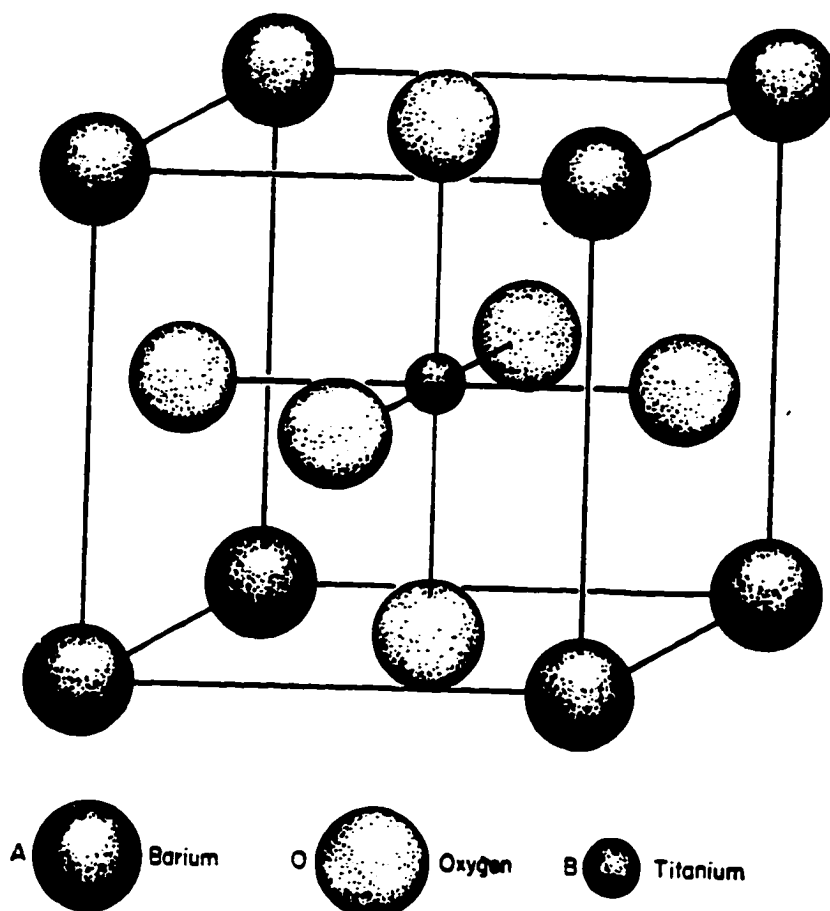
Figure 2.1. The perovskite unit cell of BaTiO₃ (after Jaffe et al. 1971)

develops and these phases are said to be ferroelectric. At the transition, the material shows a maximum in the dielectric permittivity, ε. Data for $BaTiO_3$ is shown in Figure 2.2 (Burfoot and Taylor 1979).

The most recognizable feature of a ferroelectric material is its polarization response to an applied electric field. This feature is represented by the hysteresis loop shown in Figure 2.3 (Jaffe et al. 1971). When an electric field with increasing field strength is applied to the ferroelectric, domains oriented favorably with respect to the field direction grow in size at the expense of the other domains. Also, some of the domains reorient along the direction of the applied field. This will continue until all of the domain growth and reorientation possible have occurred. At this point, the material has reached its saturation polarization (P_{sat}). If the electric field is then removed, many of the domains remain aligned. The polarization at this stage is called the remanent polarization (P_r). When the electric field is switched into the opposite direction, a coercive field (E_c) is required to reduce the net polarization to zero. Again, this occurs by re-orienting domains in the direction of the applied field. Further field increases in this direction will finally produce a saturation polarization in the opposite direction. The ability to produce more than one remanent polarization state makes ferroelectrics interesting for device applications such as nonvolatile memories.

2.2 Ferroelectric Applications

Valasek (1921) discovered the phenomenon of ferroelectricity in Rochelle Salt (sodium potassium tartrate tetrahydrate, $NaKC_4H_4O_6 \cdot 4H_2O$).
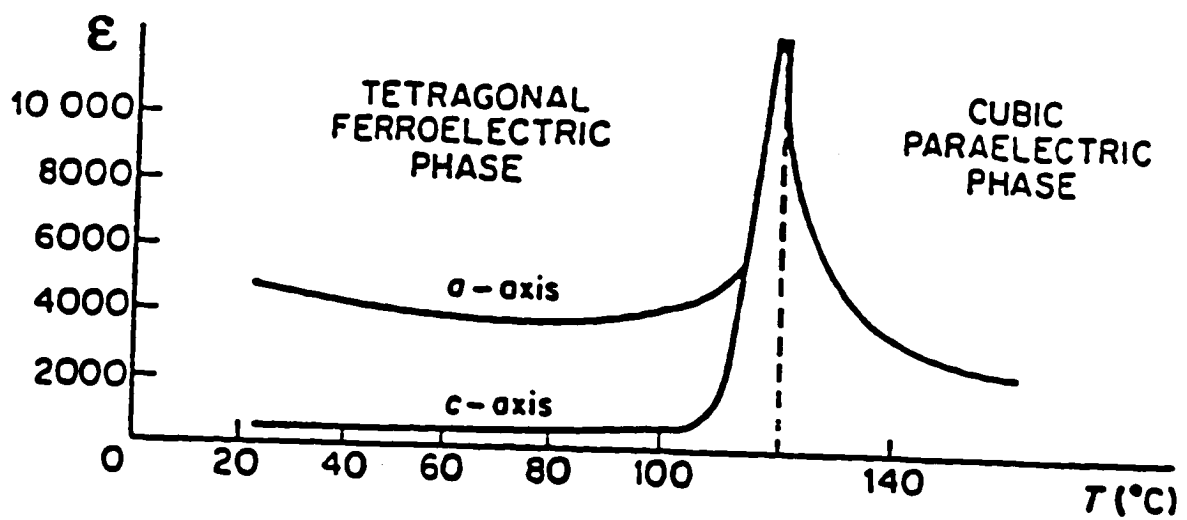
Figure 2.2. The ferroelectric-paraelectric phase transition in a BaTiO$_3$ single crystal. The sharp increase of ε near the transition temperature is shown for measurements along the a and c-axes of BaTiO$_3$ (after Burfoot and Taylor 1979).
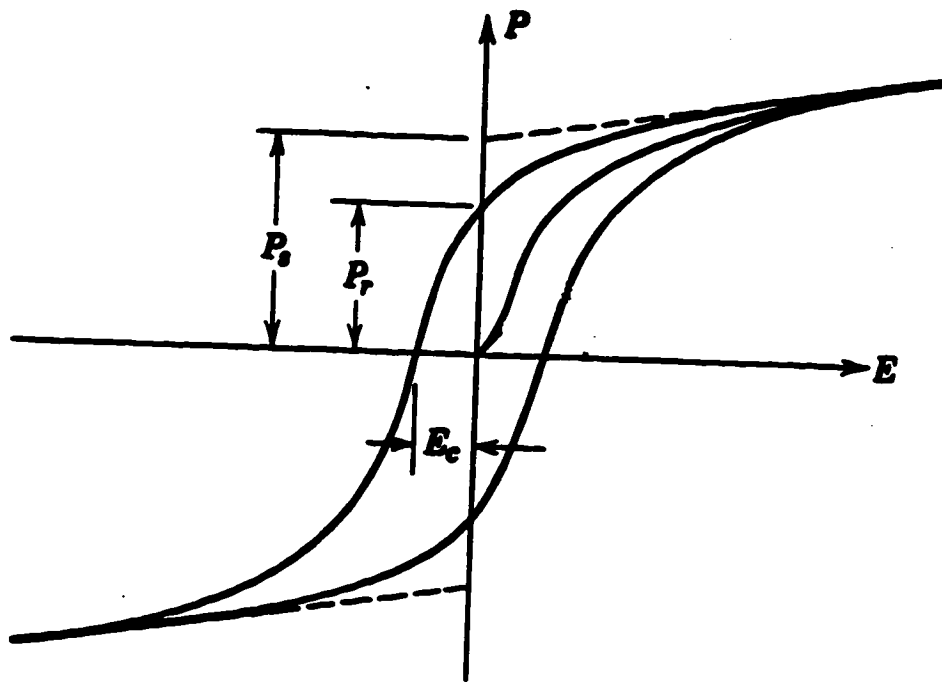
Figure 2.3. A typical hysteresis loop of a ferroelectric material. The features E_c, P_r and P_s are the coercive field, the remanent polarization, and the saturation polarization, respectively (from Kingery, Bowen and Uhlmann 1976).

However, there was only little interest in the development of ferroelectric materials until twenty years later. During the early 1940s, ferroelectricity and the resulting high dielectric constant in $BaTiO_3$ was discovered for the first time. After that, the development of important practical applications of ferroelectrics was focused and by the 1950s many other compounds in different structural families were found to have ferroelectric phases (Othmer 1980).

Ferroelectric materials were initially developed as bulk ceramic compounds for industrial applications including ultrasonic cleaners, sonar transducers and capacitors (Jona and Shirane 1962). In addition to $BaTiO_3$, other compounds included $CdTiO_3$, $PbTiO_3$, $KNbO_3$, $BiFeO_3$, and $NaTaO_3$ and their solid solutions as well as tungsten-bronze compounds such as $(Sr,Ba)Nb_2O_6$ (Zheludev 1971 and Jaffe et al. 1955). All of the early memory devices used bulk ferroelectric material with a thin film of semiconductor on top. This geometry required unacceptably high switching voltages and was plagued with significant cross-talk problems (Zuleeg and Wieder 1966 and Atkin 1972).

Recently, there has been a resurgent interest in ferroelectric thin films for many applications. An extensive array of compounds, including barium titanate $(BaTiO_3)$, barium strontium titanate (BST), lead zirconate titanate $(Pb(Zr,Ti)O_3$ or PZT), $SrBi_2Ta_2O_9$, $Bi_4Ti_3O_{12}$, $PbTiO_3$, and many others have been fabricated in thin film form (Scott et al. 1989, 1991 and Scott and Araujo 1989). Of these, the largest effort has been directed at PZT. The phase diagram of the $Pb(Zr_xTi_{1-x})O_3$ system is shown in Figure 2.4 (Jaffe et al. 1971). PZT of the morphotropic phase boundary (MPB) composition, where the ratio of $PbZrO_3:PbTiO_3$ is close to 1:1, exhibits superior dielectric, ferroelectric and piezoelectric properties. The proximity to such a phase boundary is believed to favor the enhancement of the
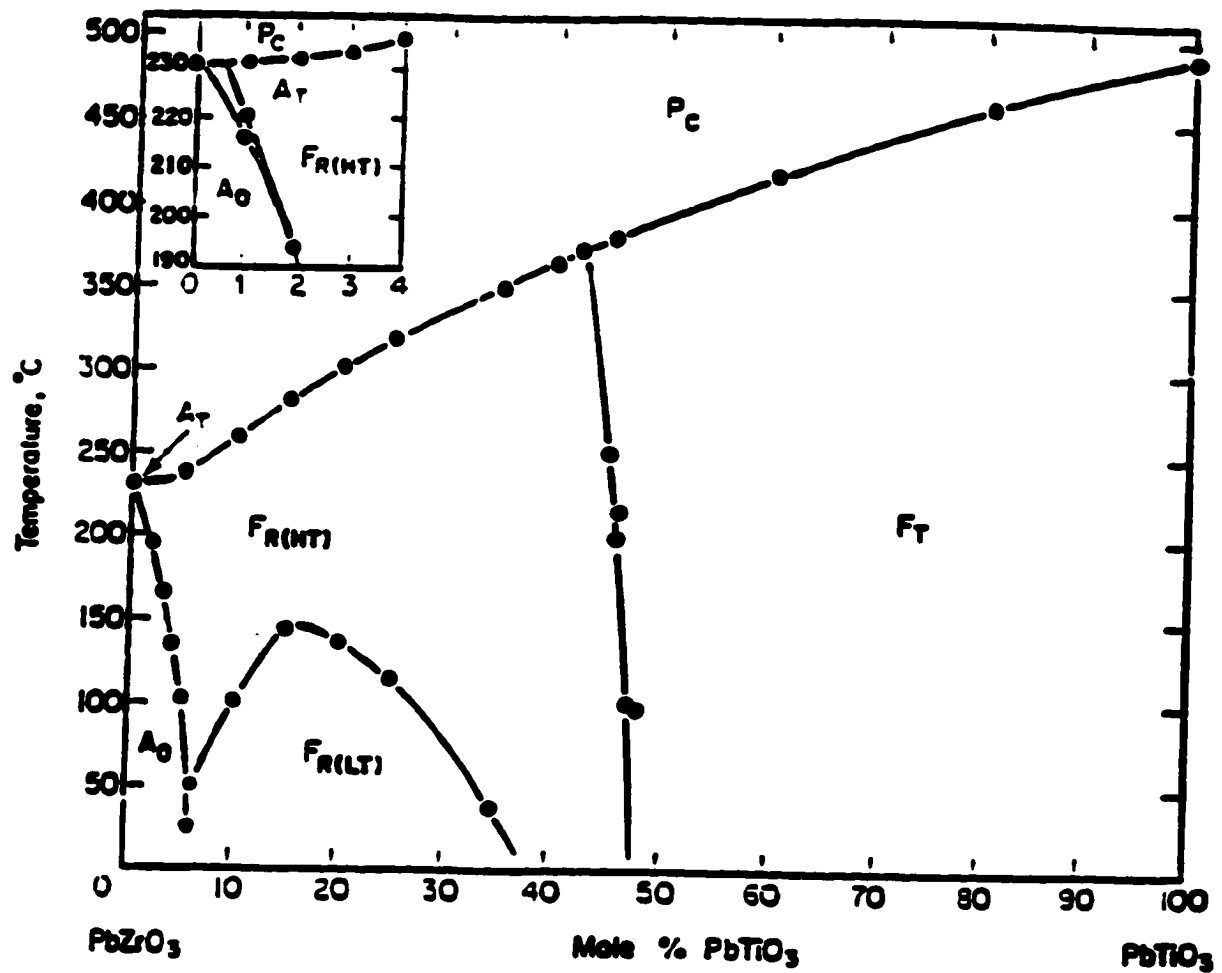
Figure 2.4. The phase diagram for the Pb(Zr$_x$Ti$_{1-x}$)O$_3$ system (after Jaffe et al. 1971).

orientation during poling: with 6 orientation states for the tetragonal phase, and 8 for the rhombohedral phase, the MPB composition has a maximum number of 14 possible orientation states (Jaffe et al. 1971).

The remarkable ferroelectric and dielectric properties, including the high dielectric constant, polarization switching, pyroelectricity, piezoelectricity, and high charge storage capacities of ferroelectric films make them attractive for ultra large scale integration (ULSI) capacitors (Larsen et al. 1992 and Xiao et al. 1994), dynamic random access memories (DRAM's) (Vest 1990 and Scott and Araujo 1989), ferroelectric random access memories (FRAM's) (Bondurant and Gnadinger 1989), microactuators (Fan et al. 1989), infrared sensors (Takayama et al. 1987, and Sayer et al. 1992a, 1992b) and other integrated capacitors (Dey and Zuleeg 1990 and Scott et al. 1991).

Much of the recent research effort for PZT thin films is directed towards development of non-volatile memory devices (e.g., FRAMs) (Tuttle 1987, Tuttle et al. 1993, 1994, Chen et al. 1992b, and Bennett et al. 1992). Because no external electric field is required for a ferroelectric to retain its remanent polarization, no applied field or voltage is required to maintain the memory, which is why the device is termed "nonvolatile".

Wu (1974) reported the fabrication of the first thin film ferroelectric memory device at Westinghouse Research Laboratories. The structure used was a metal-ferroelectric-semiconductor transistor (MFST), which is shown in Figure 2.5 (after Wu 1974). It was identical to the standard silicon metal-insulator-semiconductor field effect transistor (MISFET), except that the insulator in the MISFET was replaced by a thin layer (3 to 4 μm) of sputter deposited,
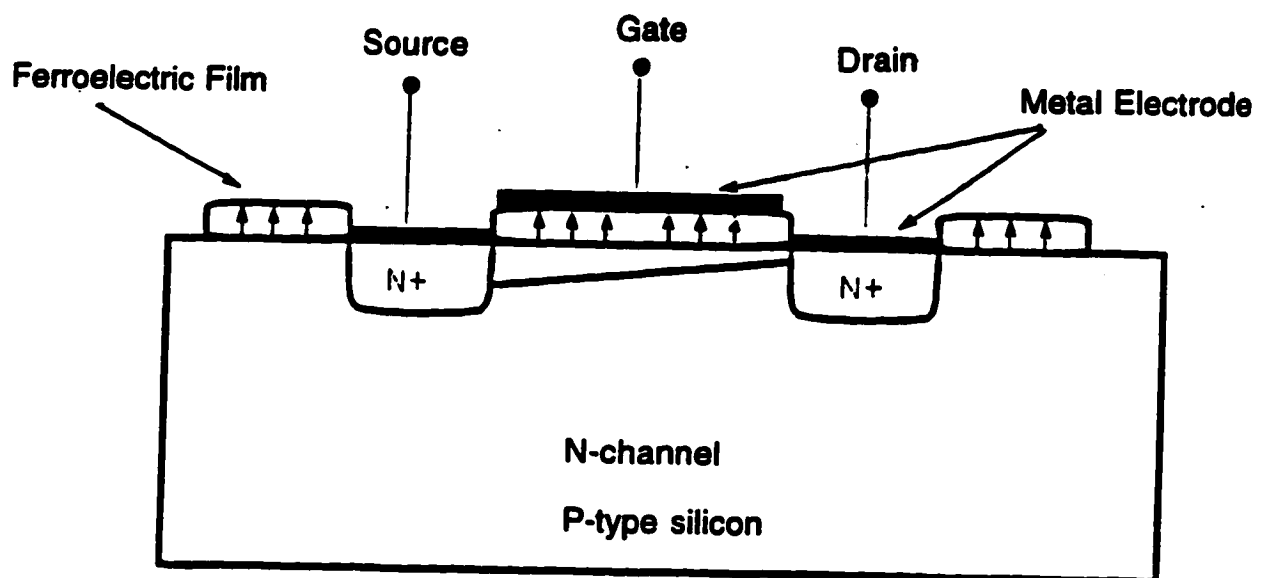
Figure 2.5. The metal-ferroelectric-semiconductor field effect transistor (MFSFET) (after Wu 1974).

ferroelectric bismuth titanate. Although the device was stable and functional, it required a very large switching voltage, thus make it incompatible with silicon integrated circuits (Sinharoy et al. 1992). Despite this high voltage, it was rather slow to erase and rewrite (microseconds). For these reasons, Westinghouse suspended the development of these devices from 1976 to 1988 (Scott and Araujo 1989).

Another possibility for using lead-based compound ferroelectrics is in pyroelectric detectors (Clarke et al. 1976, Shorrocks et al. 1995, and Kohli et al. 1996) and infrared sensors (Takayama et al. 1987, Muralt et al. 1996). Pyroelectric materials in point-detectors or arrays have many applications in temperature sensing systems like fire-detection, intruder alarms, air conditioning controls, and thermal imaging (Whatmore 1991). A number of research groups have concentrated their efforts on preparation of highly c-axis oriented ferroelectric thin films including lead titanate (PT) (Iijima et al. 1986), lead lanthanum titanate (PLT), lead lanthanum zirconate titanate (PLZT) (Adachi et al. 1985) and PZT (Muralt et al. 1996). For pyroelectric applications, it is advantageous to have a textured film with the ferroelectric polarization perpendicular to the substrate plane.

Recently, ferroelectric thin films have shown a great potential application in microelectromechanical systems, or MEMS (Howe 1985, Robbins 1995, and Polla 1995). Several thin films of the PZT family have been used in the formation of both microsensors (Muralt et al. 1995a, 1995b) and microactuators (Robbins 1995) using processing compatible with 2 μm analog CMOS technology. Ferroelectric MEMS offer significant advantages of high signal-to-noise ratio, low power dissipation, and high force generation in comparison to

other MEMS technologies such as those based on piezoresistive sensing or electrostatic actuation (Polla 1995).

Muralt et al. (1995a) have reported the fabrication of piezoelectric membranes consisting of PZT thin films on silicon diaphragms for use in micromotors. To achieve this, PZT films were deposited by sputtering and sol-gel techniques. Resonance amplitudes of up to 1000 nm/V have been measured for 16 μm thick, 2 mm diameter membranes with 0.6 μm thick PZT. The motor could be operated with voltages as low as 1.0 V_{rms}, which is much less than the one has been obtained from ZnO micromotors. Moreover, the PZT micromotors are sufficiently low voltage for standard battery and IC supply voltages (Muralt et al. 1995b).

In order to incorporate ferroelectric thin films, in particular, PZT into these applications, there are several requirements on the microstructural, optical, and electrical properties of the films which have to be optimized. Therefore, it is of technological importance to understand the microstructure evolution, and crystallization and growth kinetics of PZT films for the synthesis of high quality and uniform films.

2.3 Deposition Methods

2.3.1 Introduction

PZT thin films have been fabricated by a number of techniques, including electron-beam evaporation (Oikawa and Toda 1976 and Castellano and Feinstein 1979), sputtering (Krupanidhi et al. 1983 and Okada 1978), sol-gel (Fukushima et al. 1984, Budd et al. 1985 and Udayakumar 1992), metallo-

organic decomposition (Kojima et al. 1983 and Okada et al. 1989a, 1989b) chemical vapor deposition (Nakagawa et al. 1982), rf magnetron sputtering (Krupanidhi et al. 1983) multi-ion beam reactive sputtering (Hu et al. 1992), and laser ablation (Ramkumar et al. 1991, Chiang et al. 1992, and Ogawa et al. 1994). These techniques are classified as physical and chemical methods as described in Table 2.1 (Xu and Mackenzie 1992). The choice of an appropriate preparation technique depends on the final application of these ferroelectric films. The primary requirements for an acceptable process are the following:

1) strict control of stoichiometry;

2) uniform deposition over a large area;

3) high deposition rate.

The advantages and disadvantages of the above mentioned deposition methods are briefly described as follows. For vacuum and electron-beam evaporation (Oikawa and Toda 1976 and Castellano and Feinstein 1979), it is possible to achieve high deposition rates and relatively uniform films. However, control of the stoichiometry of multi-component films is difficult due to the different vapor pressures from the different source materials (Roy et al. 1990). Sputtering methods, including magnetron, rf- and ion-beam sputtering are capable of producing high quality ferroelectric thin films and are compatible with large scale processing for industrial applications (Krupanidhi 1992). Depending on the details of the deposition method, either metallic or oxide targets can be used. Nevertheless, for rf systems, it is difficult to prepare large and dense ceramic targets, which are necessary for getting uniform layers over a large substrate area (Sreenivas and Sayer 1988). Moreover, there are some other technical problems associated with the sputtering techniques, such as

Table 2.1

Various deposition techniques employed for the preparation of ferroelectric thin films, showing several of the compositions which have been investigated. (after Xu and Mackenzie 1992).

```
                        ┌─────────────────────┐
                        │   FERROELECTRIC     │
                        │    THIN FILMS       │
                        └─────────────────────┘
```

Physical techniques   **Chemical techniques**

Evaporation (thermal, electron beam, Laser, MBE, MOMBE, etc.)	Sputtering (dc or rf-, magnetron, ion beam, etc.)	Liquid phase epitaxy	Chemical vapour deposition (CVD, MOCVD pyrolysis, etc.)	Metallo-organic deposition (MOD)	Sol-Gel
$BaTiO_3$	$BaTiO_3$	$LiNbO_3$	$PbTiO_3$	$PbTiO_3$	PZT
$PbTiO_3$	$PbTiO_3$	$LiTaO_3$	PZT	PZT	$KNbO_3$
PZT	PZT	KTN	$Pb(Sc_{0.5}Ta_{0.5})O_3$	$Pb(Zr,Sn,Ti)O_3$	$BaTiO_3$
$Bi_4Ti_3O_{12}$	PLZT	etc.	etc.	PLZT	$LiNbO_3$
$Pb_5Ge_3O_{11}$	$Pb(Bi,La,Fe,Zr)O_3$			etc.	SBN
SbSI	$KNbO_3$				PBN
$BaMgF_4$	$LiNbO_3$				PLZT
etc.	$LiTaO_3$				PMN
	etc.				KTN
					etc.

1)   a limited control over the composition of the films, due to the large differences in the sputter yields and as a result, the preferential deficiency of volatile elements in the films. Often, in the case of Pb-based perovskites, the starting targets have to be made Pb-rich to compensate for any subsequent losses during the deposition;

2)   a gradually changing target composition over a period of time due to preferential sputtering;

3)   the presence of negative ions during sputtering of oxide targets has been shown to bombard the growing film uncontrollably and damage the bulk stoichiometry and the growth morphology and the crystalline perfection (Sreenivas and Sayer 1988);

4)   relatively low deposition rates with oxide targets.

Chemical vapor deposition (CVD) (Ohring 1992) is a deposition process whereby gaseous precursors are reacted and a solid phase is precipitated on a heated substrate.   CVD processes have been widely utilized in thin film applications for electronic devices (Blocher 1982), ball bearing manufacture and for cutting tool coatings (Schuegraf 1988).   Among the reasons for the preferential adoption of the CVD method for large-scale integration is the ability to produce a large variety of high-purity films of metals, semiconductors, and compounds in either a crystalline or vitreous form.   Furthermore, CVD also allows good conformal coverage over non-planar substrates with a good uniformity over a large area, stoichiometry control, and the possibility of easily accommodating dopant atoms (Okada et al. 1989a, 1989b, and Sakashita et al. 1991).

Nonetheless, CVD for multi-component oxides is a very complicated process. The criteria for precursor selection is very critical. Not only should each precursor decompose and form good quality films of its oxide component, but each must also react and form the final complex oxide at the same deposition temperature and same total pressure (Peng and Desu 1994). Processing parameters such as the source delivery rate, the total pressure, and the deposition temperature have to be optimized to obtain good quality films with the desired composition and uniformity.

Pulsed laser ablation (Ramkumar et al. 1991, Chiang et al. 1992, and Ogawa et al. 1994) is a recently developed thin film deposition technique in which a plume of ionized and ejected material is produced by high intensity laser irradiation of a solid target. Most commonly, UV excimer lasers are being employed for this purpose and the wavelength of the radiation is tuned by the lasing gas composition (Krupanidhi 1992). This technique has been popularly employed for the successful deposition of high T_c superconductors and is currently being exploited for the growth of device quality *in-situ* stoichiometric ferroelectric thin films, such as $Bi_4Ti_3O_{12}$ and PZT. The major drawbacks of this technique are the occurrence of particulates on the surface of the film, non-uniformity of the deposited films and the limited ability to scale up the process for industrial applications (Chiang et al. 1992).

2.3.2 Sol-Gel Processing

The sol-gel process (Fukushima et al. 1984, Budd et al. 1985 and Udayakumar et al. 1991) is a method of preparing inorganic materials via chemical routes. In general, this process involves the following steps: 1)

precursor (sol) formation, 2) hydrolysis, 3) polycondensation, 4) film or gel formation, 5) low temperature heat treatment for organic pyrolysis, and 6) annealing for film densification and crystallization.

The first stage in the sol-gel process involves the preparation of a solution of the oxide materials of interest. A variety of materials can be used to prepare the precursor solution. Metal alkoxides, $M(OR)_n$, where R is an alkyl group, are appropriate components for sol-gel preparation and have been used extensively in SiO_2 and Si-containing glass compositions (Jones 1989). By hydrolysis and gelation among precursors, a three dimensional network forms according to the reactions (Yi and Sayer 1991):

$$M(OR)_n + H_2O \longrightarrow M(OR)_{n-1}(OH) + ROH \qquad \text{(hydrolysis)} \quad (2.1)$$

$$M(OR)_n + M(OR)_{n-1}(OH) \longrightarrow M_2O(OR)_{2n-2} + ROH \qquad \text{(condensation)} \quad (2.2)$$

$$M(OR)_{n-1}(OH) + M(OR)_{n-1} \longrightarrow M_2O(OR)_{2n-2} + H_2O \qquad \text{(condensation)} \quad (2.3)$$
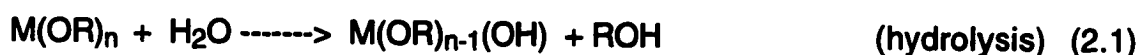
Polycondensation reactions (2.2) and (2.3) produce the M-O-M network and also produce alcohol and water by-products. The sol is ready for film deposition at this stage. The common method of depositions are dipping, spraying, and spin-coating (Dey et al. 1988 and Budd et al. 1985). The film thickness and uniformity are determined by the solute concentration, viscosity, and surface tension of the solution and the technique of application.

Upon deposition, films may undergo a pyrolysis step which involves the thermal decomposition of organometallic compounds on hot substrates. Finally, some films need to be annealed to promote crystallization and densification. This can be achieved by conventional furnace annealing or by utilizing a rapid

thermal annealing (RTA) technique. Typically, conventional annealing conditions for PZT films are at temperatures around 650° to 700°C for 15 to 60 minutes. For RTA, crystallization is often performed using a heating rate of 100°C/s and a 10-60 second hold (Chen et al. 1992a and Huang et al. 1992).

In sol-gel processing, chemicals for preparing films are dissolved in a liquid to form a solution. Since all the starting materials are mixed at the molecular level in the solution, a high degree of homogeneity in the film can be expected. The pores in properly dried gels are often extremely small and the components of the homogeneous gels are intimately mixed. This allows lower processing temperatures to be used for sol-gel derived thin films than is characteristic of powder processing routes for the same composition.

In summary, the advantages of the sol-gel process are the following:

1) molecular homogeneity;

2) high deposition rate;

3) excellent composition control;

4) easy introduction of dopants;

5) deposition can be done at ambient conditions, no vacuum processing is needed,

6) low capital cost;

7) materials can be produced in a variety of forms such as fine powders, thin films, monoliths and fibers.

Some of the disadvantages of sol-gel process are as follows:

1) excessive shrinkage during film formation may lead to cracking;

2) limited selection of some of the precursor materials.

2.3.3. Sol-Gel Processing of PZT Thin Films

Sol-gel PZT films were first reported by Fukushima et al. (1984). Many other groups of researchers including Budd et al. (1985), Yi et al. (1988), Chapin and Myers 1990, Tohge et al. (1991) have investigated sol-gel PZT films from a variety of precursor chemistries. The details on processing and film properties are summarized and shown in Table 2.2. It is worth noting that the sol-gel route by Budd et al. (1985) has been extensively followed by a number of researchers including Udayakumar (1992), Chen et al. (1992a), Gibbons (1995) and this study.

Sol-gel PZT is deposited as an amorphous film. During crystallization, PZT films typically transform to the required ferroelectric perovskite phase via an intermediate phase. Diffraction patterns obtained from the intermediate phase have generally been attributed to a pyrochlore structure (Kwok and Desu 1992). However, there has recently been some speculation that the structure is fluorite rather than pyrochlore (Wilkinson et al. 1994). In either case, the coexistence of secondary phases in the films leads to a deterioration in the values of measured properties compared with those of phase-pure materials.

Many of the studies on sol-gel PZT thin films (Chen et al. 1986, Chapin and Myers 1990, Lee et al. 1993, Sayer et al. 1992b, Kwok and Desu 1994, and Griswold 1995) have reported formation of the intermediate phase at temperatures as low as 350-450°C. The perovskite phase was then formed when the film was heat-treated conventionally at 600-750°C for 30 minutes to 2 hours. High temperature, long-term anneals will certainly lead to diffusion either between the PZT thin films and the Si layers or within the underlying

Table 2.2

A summary of sol-gel processing of PZT thin films

Compositions by	Precursors	Annealing Temperature (°C)/ Time	Film Properties
PZT (50/50) Fukushima et al. (1984)	Lead (II) 2-ethylhexanoate Zirconium acetylacetonate Titanium tetrabutoxide Butanol	500-700°C 30 mins	Dielectric constant = 300, $P_r = 30.6\ \mu C/cm^2$, $E_C = 45\ kV/cm$
PZT (53/47) Budd et al. (1985)	Lead acetate trihydrate Zr-alkoxide, Ti-alkoxide Methoxyethanol	500-700°C 30 mins	$P_r = 32.5\ \mu C/cm^2$, $E_C = 30\ kV/cm$
PZT (50/50) Yi et al. (1988)	Lead acetate trihydrate Ti-isopropoxide Zr-n-propoxide Acetic acid	700°C 30 mins	$P_r = 1\text{-}7\ \mu C/cm^2$, $E_C = 26\text{-}80\ kV/cm$
PZT (50/50) Tohge et al. (1991)	Lead ethoxide (Pb(OEt)2 Titanium n-butoxide Zirconium n-butoxide Ethanol Acetyl acetone	700°C 30 mins	$P_r = 25\ \mu C/cm^2$, $E_C = 107\ kV/cm$

semiconductor electronics (Wu et al. 1984). This presents a problem when incorporating PZT thin films into Si-based semiconductor devices (Dey and Zuleeg 1990, and Larsen et al. 1992).

Thus, efforts have been made to reduce the processing temperature or the holding times by using rapid thermal annealing (RTA), where process times are measured in seconds rather than hours (Pasual et al. 1991, Chen et al. 1992a, and Vasant Kumar et al. 1992). Details on RTA will be further reviewed in section 2.4.

One of the primary factors in synthesis and crystallization of PZT films is the proper control of the lead content of the films. Both stoichiometric and lead deficient (Vasant Kumar et al. 1992) films develop the intermediate phase for low temperature heat treatments. Many researchers (Ameen et al. 1990, Roy et al. 1990, and Polli and Lange 1995) have reported that the intermediate phase can be converted to the perovskite phase by increasing the Pb content, or increasing the post-deposition annealing temperature and times (Kwok et al. 1990, and Krupanidhi et al. 1992). The upper bound on the temperature is given by the point at which enough lead evaporates from the films to stabilize a lead-deficient pyrochlore. Excess lead thus seems to have two roles; it favors nucleation of the perovskite phase and helps prevent formation of a pyrochlore surface layer.

The reaction sequences in the formation of PZT bulk solid solutions have been reported by many workers (Hankey and Biggers 1981, and Hiremath et al. 1983). It is generally agreed that PbO and TiO_2 react to form $PbTiO_3$ first, and then $PbTiO_3$ will react with the residual PbO and ZrO_2 to form perovskite PZT. In thin films, however, there have been no clear reports on the reaction sequences

and the intermediate products that form, although the nature of such products is a key factor influencing the film crystallization, and the identification of the mechanism involved would lead to a better control over reproducibility (Vasant Kumar et al. 1992).

Based on the XRD studies by Vasant Kumar et al. (1992), the full reaction sequences of PZT (52/48) thin film deposited at low substrate temperatures by the sputtering technique was evaluated and is shown as the steps below:

as grown: αPbO_2 + PT3 + a-TiO_2 + a-ZrO_2,

1st step: PbO(ss) + PT3 + PZ + PT,

2nd step: PT + PZ,

3rd step: PZT

where the αPbO_2 is the orthorhombic structure, PT3 is the monoclinic type of lead titanate ($PbTi_3O_7$) according to JCPDS files no. 21-949 and 21-949A (McClune 1986), and a-TiO_2 and a-ZrO_2 are the bulk of titania and zirconia, which are present in an amorphous form as a homogeneous mixture with lead oxide. PT and PZ are $PbTiO_3$ and $PbZrO_3$.

As films are annealed, Vasant Kumar et al. (1992) reported that an increasing amount of PT3, PbO(ss), and PZ are formed due to the reaction of lead oxide with titania and zirconia. The formation of PT3 and PZ is completed and stabilized between 500 and 550°C. The intermediate phases present at this stage are PT3, PZ, and PbO (ss). The final reaction occurs between 550 and 600°C, where PT3 reacts with PbO(ss) and PZ to form PZT. During the final stage of annealing, the formation of $PbTiO_3$ is observed for films annealed at 580°C for 5 seconds. As discussed by Vasant Kumar et al. (1992), the

formation of PT may be due to a reaction between PT3 and lead oxide, PbO(ss). This PT reacts immediately with PZ to form PZT at around 600°C.

Vasant Kumar et al. (1992) finally concluded that the crystallization of PZT took place either through formation of a pyrochlore phase or through intermediate products of lead titanate and lead zirconate, depending on the lead stoichiometry. They reported that the perovskite phase formed via the pyrochlore phase has a defect structure due to an excess of lead vacancies. The formation of intermediate products is suppressed by the presence of excess lead oxide in as-grown films.

As previously mentioned, high temperature crystallization of PZT films is required in order to obtain the perovskite phase and PZT films are to be integrated into devices with semiconductors in many of their prospective applications. Such devices cannot stand intensive heat treatment (e.g. 650°C for 1 hour) as they tend to undergo interface reactions or show degradation (Vasant Kumar et al. 1991 and Hu et al. 1992). Therefore, attempts have been made to reduce the processing temperature or holding time of the films. In this practice, rapid thermal annealing (RTA) has been shown to be a suitable technique to crystallize PZT films.

Previous investigations (Chen et al. 1992a, Dana et al. 1991, and Xu and Mackenzie 1992) have demonstrated that RTA with heating times in the range of 1 to 300 seconds, can not only reduce the thermal budget in the semiconductor industry, but also can suppress the intermediate fluorite-type or pyrochlore-like phase evolution in PZT films. In addition, these rapid heat treatments can reduce the difficulties associated with interlayer diffusion. Some

of the previous investigations of rapid thermal annealing for PZT thin films will be briefly summarized in the next section.

2.4. Rapid Thermal Annealing of Ferroelectric Thin Films

Recently, rapid thermal annealing (RTA) has been applied to PZT thin films. As stated previously, RTA can reduce the thermal budget (temperature/time product) significantly in semiconductor processing (Singh 1988, O'Brien et al. 1990, and Pasual et al. 1991). Commercial instruments are now available which are capable of producing rapid and linear heating rates from $10^\circ C/s$ to $200^\circ C/s$ with accurate hold conditions (Singh 1988).

A study by Udayakumar et al. (1990) was one of the first reports on employing RTA in the area of ferroelectric thin films. It took advantage of the short processing time to suppress the pyrochlore phase that degrades the electrical properties of materials in the lead magnesium niobate-lead titanate (PMN-PT) system. A relative permittivity of 2900 and a remanent polarization of 11 $\mu C/cm^2$ were reported for the PMN-PT films.

Chen et al. (1992b) prepared PZT films with the morphotropic phase boundary composition (Zr/Ti = 52/48) by a sol-gel spin-on technique. The films were RTAd at $700^\circ C$ for times between 1 and 10s or at temperatures between 500 and $850^\circ C$ for hold times of 10s. The remanent polarization was reported to approach 25 $\mu C/cm^2$ at $600^\circ C$, for a constant dwell time of 10s. The films annealed at less than $600^\circ C$ showed the pyrochlore-like phase; full crystallization to the perovskite phase was observed as the temperature approached $700^\circ C$ for 1 to 5 s. For the constant temperature regime of $700^\circ C$,

a dwell time of 10 s appeared optimal, as it leads to high polarization values ($\sim$35 $\mu C/cm^2$) and low coercive fields (30-40 kV/cm). Finally, they concluded that RTA is a very promising technique to improve the quality of PZT films, as it reduces surface layer effects.

A study by Lakeman et al. (1994) also reported using RTA to crystallize sol-gel derived PZT (53/47). Films were prepared by a method similar to Budd et al. (1985) and were deposited onto Pt-coated Si substrates by spin coating. Each layer was pyrolyzed at 300°C on the hot-plate. The films were then RTAd at 50°, 500°, and 5000°C/min to temperatures between 350°C and 700°C in 50°C intervals. It was determined that medium-range order developed during low temperature (300°C) heat treatment, and also that some compositional heterogeneity existed. After higher temperature heat treatment, structural rearrangement occurred, and the composition became more uniform. An intermediate pyrochlore-like phase crystallized before the perovskite phase, at temperatures between 500°C and 550°C. The perovskite phase was observed to nucleate from the intermediate phase as the temperature approached 700°C (Lakeman et al. 1994).

Reaney et al. (1994) studied the microstructure and preferred orientations of RTAd PZT (53/47) films deposited on Pt/Ti/SiO_2/Si/substrates by sol-gel spinning. The films were pyrolyzed after each coating at 350° or 420°C for 15 s and annealed at 700°C for 1 min. They showed that the addition of Pb up to 10% can control the A-site stoichiometry in PZT thin films without the retention of PbO as a second phase. In addition, it was also demonstrated that significant microstructural and orientation control could be achieved in sol-gel derived PZT thin films by using RTA. The pyrolysis temperature can alter the

degree of preferred orientation and the grain size in the film; a 350°C pyrolysis temperature gives a (111) columnar microstructure with a lateral grain size of 0.1-0.2 μm, whereas a 420°C pyrolysis temperature gives a grain size of greater than 0.5 μm and a (100) preferred orientation.

In another systematic investigation from the same group, Brooks et al. (1994) suggested that for a pyrolysis temperature of 350°C, the amorphous PZT films first fully transformed into a metastable pyrochlore phase $(Pb_2(Zr_{0.53}Ti_{0.47})_2O_6)$, when the O_2 concentrations in the post-pyrolysis treatment was low, and then rapidly transformed to a perovskite phase at higher annealing temperatures (600°C). They further reported that when the films were pyrolyzed at 420°C at higher O_2 concentration, the x-ray amorphous PZT films first transformed into a stable pyrochlore phase $(Pb_2(Zr_{0.53}Ti_{0.47})_2O_{7-x})$, which slowed down the transformation of this phase into the perovskite phase.

Based on these results, a question of what factors control the kinetics of the intermediate to perovskite phase transformation arises. Thus, the use of *in-situ* X-ray diffraction techniques and SE in this thesis is proposed to study crystallization kinetics for both the intermediate and perovskite phases in PZT films.

2.5. Crystallization Kinetics of PZT Thin Films

An understanding of the crystallization kinetics of the intermediate fluorite-type or pyrochlore phase as well as the intermediate to perovskite phase transformation kinetics is crucial for the development of high quality ferroelectric materials. The information gathered from the kinetics study can be

used in modifying the process to produce PZT films with desirable microstructures and properties. Recently, there have been a few kinetics studies on PZT thin films (Kwok and Desu 1992, 1993 Dang and Gooding 1995, Griswold et al. 1995), and all of them will be briefly summarized in the following section. In addition, the Avrami model and transformation theory will also be reviewed.

2.5.1. Avrami Kinetics

2.5.1.1. Isothermal Crystallization Kinetics

Many PZT as-deposited films are amorphous, and post-deposition annealing is needed to transform the film from the amorphous structure to the desirable ferroelectric-perovskite phase (Budd et al. 1985 and Chen et al. 1990). The amorphous structure will first transform into an intermediate fluorite-type or pyrochlore phase at temperatures between 350° and 450°C and then this intermediate phase will transform into the perovskite phase at temperatures higher than 500°C (Kwok and Desu 1994). The formation of the perovskite phase from the intermediate phase is treated as one solid phase nucleated within another and the intermediate phase is considered to be less stable than the perovskite phase at the transformation temperature (Hu et al. 1993 and Griswold et al. 1995). Although the presence of an intermediate fluorite-type or pyrochlore phase is commonly observed, not much effort has been made to study the intermediate to perovskite transformation of PZT thin films.

Generally, crystallization occurs via crystal nucleation at a number of sites, followed by crystal growth. The crystals that are nucleated grow until they

impinge on one another, forming grain boundaries. There are two general nucleation conditions; homogeneous and heterogeneous (Porter and Easterling 1992). The expressions for nucleation and growth rates are similar for both homogeneous and heterogeneous cases. For the homogeneous nucleation condition, sites are randomly located. This yields a constant nucleation rate per unit area of untransformed material which is known as the Johnson-Mehl approximation. (Johnson and Mehl 1939). In the case of heterogeneous nucleation, it is assumed that a limited number of sites are present and nucleation occurs at defect locations. In either case, growth begins following nucleation and gradually decreases upon impingement with other grains. The activation energies for the nucleation rate, N, and growth rate, G, are expressed by

$$N = N_0 \exp\left[-\frac{\Delta G_n}{k_B T}\right]; \quad G = G_0 \exp\left[-\frac{\Delta G_g}{k_B T}\right] \tag{2.4}$$

where ΔG_n and ΔG_g are the activation energies for nucleation and growth respectively, k_B is the Boltzmann constant and T is the temperature (Porter and Easterling 1992).

The Johnson-Mehl-Avrami (JMA) model is used to explain the crystallization kinetics which occur by nucleation and growth under isothermal annealing. In this model, Johnson and Mehl (1939) suggested that a spontaneous rate of nucleation is constant throughout the transformation. Avrami (1939, 1940, 1941) studied the kinetics of phase changes and pointed out that "germ nuclei" exist at the onset of the transformation and that the nucleation rate could be altered by the temperature and duration of superheating. Transformations that take place by nucleation and growth

processes can be described by using the concept of an extended volume (Conde et al. 1989). The extended volume X_{ex} is the volume fraction that would be transformed if the impingement of growing regions did not occur. The total volume fraction transformed at a time t is f(t):

$$f(t) = 1 - \exp(-x_{ex})$$ (2.5)

If we consider a fixed number of nuclei N_0 per unit volume, for a crystal where the nuclei are growing at a constant rate G:

$$x_{ex} = (\frac{4\pi}{3})N_0 G^3 t^3$$ (2.6)

For a constant growth rate G, where the nucleation rate, N, per unit volume is constant:

$$x_{ex} = (\frac{\pi}{3})NG^3 t^4$$ (2.7)

The general form for the transformed volume fraction can be described by the Avrami equation (Avrami 1941):

$$f(t) = 1 - \exp(-Kt^n)$$ (2.8)

where f(t) is the volume fraction transformed, t is the time, and n is referred to as the Avrami coefficient, which reflects the nucleation and growth morphology. K is the rate constant for the transformation, and since, it includes the nucleation and growth terms, it is temperature dependent (Griswold et al. 1995). This K value is used to extract the activation energy for the entire transformation process; therefore the value represents some average of the activation energies for nucleation and growth. The isothermal transformation rate is determined by

taking the first derivative with respect to time and is referred to as the Johnson-Mehl-Avrami (JMA) rate equation (Henderson 1979):

$$\frac{df(t)}{dt} = Knt^{n-1}\exp(-Kt^n) \tag{2.9}$$

The JMA model was developed for isothermal transformations, and it requires the following conditions: the transformation conditions must be isothermal, nucleation must be spatially random, and the growth rate of the new phase must be dependent only on temperature and not on time (i.e. linear growth kinetics).

A plot of the volume fraction transformed, f(t) against time (t) will have an S-shape or sigmoidal curvature which is shown in Figure 2.6 (after Griswold 1995). Sigmoidal transformation curves are generated for isothermal transformations and have been exhibited by diffusion-controlled transformations. The lower part of the curve corresponds to the nucleation regime and the gradient increases as growth begins. Growth typically begins slowly as nuclei of critical size are generated. Growth increases and then slows again as the grains begin to impinge. Ideally, at some point the material becomes 100% transformed and in Eqn. 2.8, f(t) = 1, corresponds to the limit where $t \rightarrow \infty$.

Avrami (1939) showed that for all transformations involving nucleation and growth, there are distinct similarities in the kinetics curves. These similarities occur even for variations in composition, concentration of nucleation sites and diffusion parameters. In Figure 2.7, Avrami illustrated the dependence of the Avrami coefficient (n) on the shape of the curve. Since n is directly associated with nucleation and growth, it follows that the shape of the Avrami plots reflects the nature of the transformation process. The
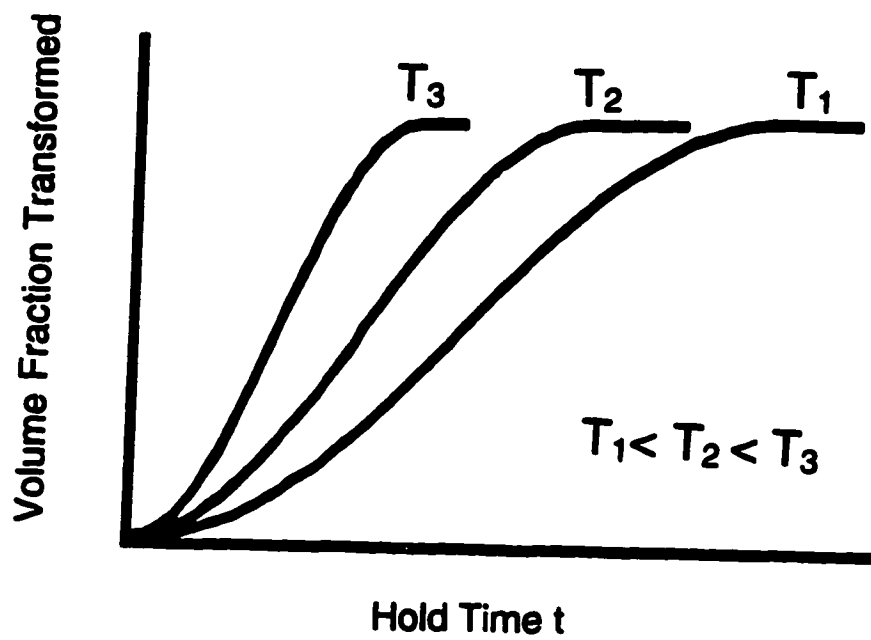
Figure 2.6. Volume fraction transformed versus time (isothermal curves) (after Griswold 1995).
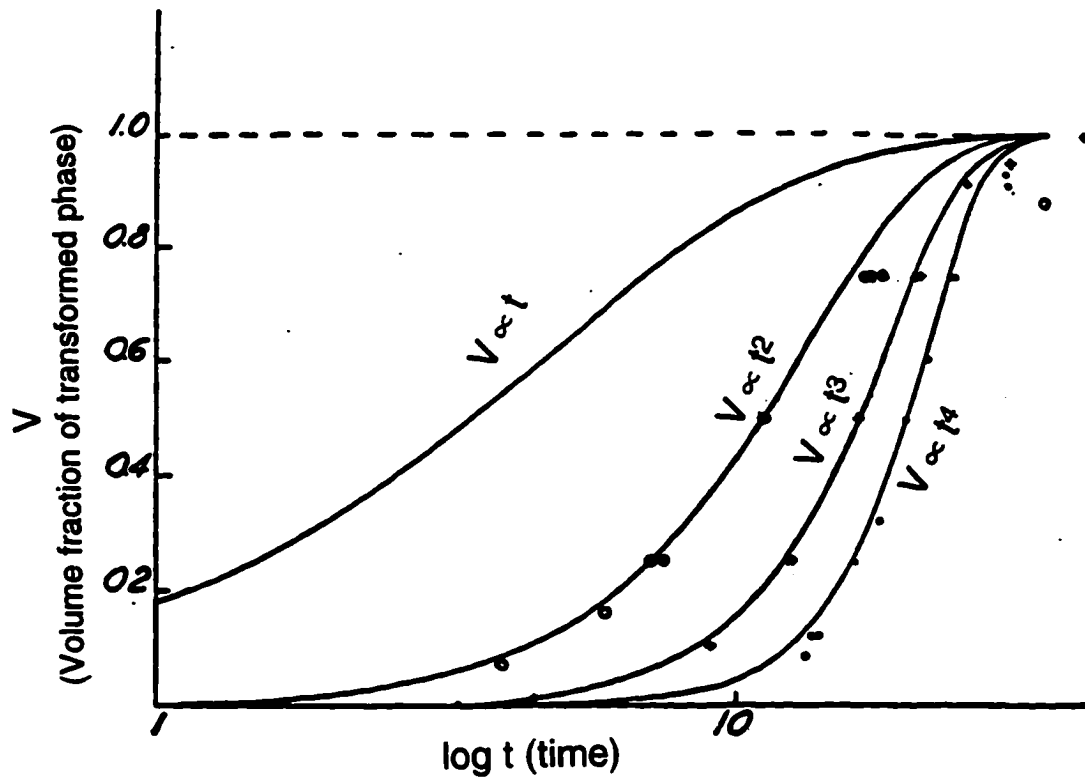
Figure 2.7. Avrami transformation curves: the shape depends upon n (after Avrami 1941).

Avrami coefficient n is extracted from isothermal plots of ln(-ln(1-f)) versus ln (t) as shown in Figure 2.8 (after Griswold 1995). The plots are straight lines with a slope of n and an intercept of lnK. The rate constant for the transformation K varies in an Arrhenius relationship with T:

$$K = K_0 \exp(-\frac{E_a}{k_B T})$$ (2.10)

The activation energy for the transformation E_a is determined by plotting values of lnK against 1000/T (°K) and extracting E_a from the slope.

The Avrami coefficient n is associated with different nucleation and growth processes. Here n = 2 implies a zero nucleation rate (i.e. all nucleation sites are available at the onset) and n = 3 implies a constant nucleation rate and a two-dimensional polymorphic growth (which means changes from one single phase structure to another). Ranganathan and Von Heimendahl (1981) reported the possibilities for isothermal transformations including linear growth and parabolic growth with zero, constant or varying nucleation rates. The generalized morphology index for the evaluation of the Avrami coefficient n is as follows:

For linear growth: n = a+b
For parabolic growth: n = a+ b/2

Growth index:

b = 3 for three-dimensionally growing particles

b = 2 for two-dimensionally growing particles

b = 1 for one-dimensionally growing particles
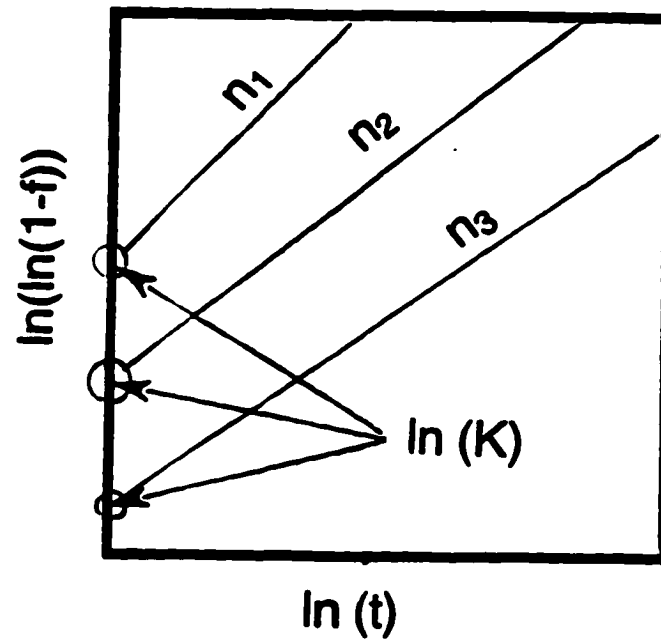
Figure 2.8. Isothermal curves to determine n and ln K (after Griswold 1995).

Nucleation index:

a = 0 for zero nucleation rate

a = 1 for constant nucleation rate

a > 1 for increasing nucleation rate

2.5.1.2. Non-Isothermal Crystallization Kinetics

Generally, isothermal measurements have been used to study the phase transformation and the crystallization of solids and thin films since they are more definitive and easier to interpret (Henderson 1979, Kwok and Desu 1992, Kwok et al. 1992, and Griswold et al. 1995). However, the non-isothermal measurements using a constant heating rate are commonly used in the study of the crystallization of amorphous solids such as glasses (Macfarlane et al. 1984, Matusita et al. 1984, Mahadevan et al. 1986, and Komatsu et al. 1993) since the non-isothermal measurements can access a broader range of temperatures and can detect phase transformations that occurs too rapidly to be seen in isothermal measurements.

As discussed by Henderson (1979), the nucleation rate and the growth rate in crystallizations are no longer constant during phase transformations under non-isothermal conditions. In general, the nucleation and growth rates vary rapidly with temperature, and their functional dependence on temperature is quite different. To correctly apply the JMA equation to transformations in which nucleation and growth occurs non-isothermally, the following conditions are required: (1) the growth rate depends only on instantaneous temperature and is independent of time, (2) nucleation is random (either homogeneous or

heterogeneous at randomly dispersed second phase), (3) all nucleation occurs early in the process (Graydon et al. 1994).

Matusita and Sakka (1980) have proposed a method for analyzing non-isothermal crystallization kinetics involving nucleation and growth process. Both bulk and surface crystallization are accounted for in order to be able to obtain a meaningful activation energy. Their equation is

$$\ln\left[-\ln\left(1-x\right)\right] \;=\; -n\ln\alpha \;-\; 1.052\frac{mE_a}{RT} \;+const. \tag{2.11}$$

where x is the volume fraction of the phase transformed, α is the constant heating rate, E_a is the activation energy, R is the gas constant, T is the temperature at which the crystal volume fraction reaches a specific value, and n and m are numerical factors which depends on the crystallization mechanism, i.e., the morphology of the growth. The values of n and m are summarized in Table 2.3 (after Matusita and Sakka 1980). Further theoretical details on non-isothermal kinetics are given by Ozawa (1970), Augis and Bennett (1978), and Yinnon and Uhlmann (1983).

The morphology index, m, can be determined from the slope of the plot of ln[-ln(1-x)] versus 1000/T, (Augis and Bennett 1978 and Afify et al. 1991) where T is the temperature in Kevin. This plot is expected to be linear over most of the temperature range. For different heating rates (α), it is possible to evaluate ln[-ln(1-x)] as a function of ln (α) at a fixed temperature (Afify et al. 1991). The morphology index n, i.e., the Avrami exponent can be obtained from the slope of the plot of ln[-ln(1-x)] versus ln (α) (Afify 1991).

<u>Table 2.3</u>

Values of n and m for various crystallization mechanisms

(after Matusita and Sakka 1980)

Crystallization Mechanism	n	m
Bulk crystallization with a constant number of nuclei (i.e. the number of nuclei is independent of the heating rate)		
three-dimensional growth of crystals	3	3
two-dimensional growth of crystals	2	2
one-dimensional growth of crystals	1	1
Bulk Crystallization with an increasing number of nuclei (i.e. the number of nuclei is inversely proportional to the heating rate)		
three-dimensional growth of crystals	4	3
two-dimensional growth of crystals	3	2
one-dimensional growth of crystals	2	1
Surface Crystallization	1	1

To date, there are no reports on attempts to apply non-isothermal kinetics to study crystallization and growth in PZT thin films during annealing. Since, however, these boundary conditions are more appropriate to the *in-situ* SE and X-ray diffraction measurements conducted, they will be used in this study. This information will be compared to the previous isothermal studies (Kwok and Desu 1992, Kwok et al. 1992, and Griswold et al. 1995).

2.6. Considerations for PZT Crystallization Kinetics

The Avrami model has been applied extensively in phase transformations of bulk materials such as metallic glasses (Greer 1982, Wei and Hallaran 1988), glass ceramics (Subbanna et al. 1989, Walck and Pantano 1990) steels, and precipitate hardened alloys (Porter and Easterling, 1992). In thin films, computer simulations of nucleation and growth kinetics in two-dimensional systems have been performed by a number of authors (Frost and Thompson 1987, Mahin et al. 1987, and Saetre et al. 1986).

A study by Wilkinson et al. (1994) was the first report using *in-situ* X-ray powder diffractometry to study crystallization kinetics in $PbZr_{1-x}Ti_xO_3$ (x = 0.0, 0.55, 1.0) alkoxide gels. They observed that $PbTiO_3$ gel crystallized without the formation of any intermediate phase, while both $PbZrO_3$ and PZT gels formed an intermediate non-perovskite crystalline phase, which was concluded to be a fluorite-structured solid solution rather than a well ordered pyrochlore. Since it is known that zirconia solid solutions adopt the fluorite structure, while solutions with titania do not, it was expected that an intermediate phase in $PbTiO_3$ would not be observed. Finally, they were able to fit the Avrami model to the

transformation data and determine the value of n in the Avrami equation (eqn. 2.8) in the range of 1-2, which reflected the dimensionality of the transformation.

It was demonstrated by Shur et al. (1995) that the elastic light scattering method with its very rapid data collection rate can yield the information about kinetics of crystallization using the appropriate mathematical treatment. They assumed that the relative change of the total intensity of scattered light is directly proportional to the fraction of non-crystallized volume and the data were fitted by the Kolmogorov-Avrami (K-A) formula (Kolmogorov 1937 and Avrami 1939). This approach is based on the idea of independent nucleation and growth of individual crystallites. They considered two processes corresponding to limiting cases of nucleation: the β process, characterized by appearance of all crystallites at the very beginning, and the α process which allowed for nucleation to occur continuously. They finally derived the time dependence of crystallization rate at a linearly increasing temperature as in Eqn. 2.12:

$$f_c(t) = 1-\exp\{-(t-t_{st})^4 t_o^{-4} [1 + (t-t_{st})^2 t_m^{-2}]\} \qquad (2.12)$$

where f_c is the rate of the fraction transformed, $t_o = (1/4c\beta u^2 Z^2)^{-1/4}$, c - the shape constant, β -nuclei density per area, $Z = dT/dt$, $t_m = (1/6 \, a \, Z/b)^{-1/2}$, $t_{st} = (T_{th} - T_o)/Z$, T_{th} = threshold temperature, a and u = temperature independent constants. This equation (2.12) was used for mathematical treatment of experimental data and allowed the time dependence of the density of crystallites per area to be extracted from experimental data. It was concluded that elastic light scattering can be used to investigate the phase transformation kinetics. However, this method suffers from complex and indirect mathematical treatment of experimental data. In addition, the inherent assumption in the method is that changes in light scattering (which is probably associated largely

with roughening of the film surface) is a direct measure of the crystallization. This is not necessarily a valid assumption for all material systems.

A recent study by Griswold et al. (1995) suggested that glancing angle X-ray diffraction (XRD) in combination with Transmission Electron Microscopy (TEM) could be used to identify the location of phases and to determine their relative volume fractions after transformation. The transformation from the intermediate to perovskite phase was completed after a 15 second anneal at 650°C, and the Avrami coefficient (n) was found to range from 2.10 to 2.65. Griswold et al. (1995) analyzed the n values following the work by Ranganathan and von Heimendahl (1981) by assuming the crystallization followed linear growth, so that n equal to two could be predicted for two-dimensional growth with either constant or linear nucleation rate with time. However, no further explanations about their assumptions were given.

Kwok and Desu (1992) characterized the transformation kinetics in PZT (55/45) films on Pt electrodes which were sputtered deposited at a relatively low temperature (200°C) and conventional furnace annealed. The pyrochlore to perovskite phase transformation was studied by X-ray diffraction (XRD) and transmission-electron microscopy (TEM). The kinetics of the perovskite formation were studied isothermally between 525°C and 575°C for various annealing times. They found that the perovskite nucleation was random, the nucleation rate for perovskite formation was at a maximum in the early stages of transformation, and the growth rate of the perovskite phase was constant. The growth rate was found to increase with temperature. The Avrami coefficients obtained were 2<n<2.6, which for two-dimensional transformations implied

linear growth with zero or constant nucleation. The JMA was also applied, and an activation energy of 494 kJ/mol was determined.

Kwok et al. (1992) also stated that there was no preferred growth orientation for the perovskite phase in their films. That is the growth was isotropic and occurred primarily in two dimensions parallel to the plane of substrate. However, they did not give any information regarding the transformation through the film thickness. Finally, the volume fraction of the transformed material, f(t), was determined from light and dark areas in an SEM plan view specimen, in the range 525°C to 575°C. Only 60% or less of the transformed volume was determined, and no explanation was given why higher amounts of transformed material were not considered.

Voight et al. (1993) also investigated the transformation kinetics of sol-gel PZT using SEM plan view. This group of researchers determined f(t) and again only f(t) up to 0.6 was reported. The authors also used RTA to anneal their films and stated that the transformation above 525°C was too rapid to be analyzed. The activation energy they obtained for PZT (20/80) was 575 kJ/mol. Finally, Voight et al. reported the Avrami coefficient n to be 2.23 which implied a constant nucleation rate with linear growth. The PZT films in this study were highly oriented.

It is worth noting that the influence of substrate materials and the annealing method on the transformation was not addressed in either of these studies. In Kwok and Desu (1992) and Voight et al. (1993), the transformation was observed in two dimensions by SEM plan view, therefore, the possibility of variation through the film thickness as a result of substrate influence was not considered in these studies. In addition, as has been shown elsewhere, the

surface microstructure in thin films is not necessarily indicative of the whole film (McKinstry et al. 1993, 1995 and Tani et al. 1994).

In summary, the properties of PZT films are greatly dependent upon the microstructure evolution and the perovskite phase development during the film crystallization. Therefore, it would be helpful to employ an *in-situ* structure-sensitive method to obtain this type of information. It is proposed in this study that spectroscopic ellipsometry (SE) be used to examine the real-time microstructure evolution (including the inhomogeneities throughout the film thickness and surface roughness) which are generated during annealing. Unlike other reflection methods, SE can be used to depth-profile the dielectric functions of PZT films with a resolution approaching the angstrom level (Chindaudom 1991, McKinstry et al. 1993, 1995). Thus, SE can be used to follow the crystallization kinetics of PZT films during annealing. Moreover, optical reference dielectric function data for both the intermediate and perovskite phases can also be determined by SE in this study.

As stated throughout this chapter, it has been difficult to prepare phase-pure perovskite PZT films because evolution of the fluorite-structure or pyrochlore phase at temperatures as low as 350°C has been difficult to avoid. Hence, understanding the transformation between the intermediate phase and the perovskite during annealing is crucial for the synthesis of high quality ferroelectric thin films. To examine the phase transformation and crystallization kinetics of these films, high temperature X-ray diffraction has been utilized in this study. In addition, since there is little data available on the minimum heating rate required to circumvent the intermediate phase, and since nucleation can, in fact, be eliminated, then a series of constant heating rates

including 5°, 10°, 20°, 50°, and 100°C/minute can be used to crystallize PZT films during annealing *in-situ* in the high-temperature X-ray diffractometer. This is the first report of a complete set of X-ray diffraction data for the formation of the intermediate and perovskite PZT phases for a series of heating rates.

Chapter 3

EXPERIMENTAL PROCEDURE

This chapter will be divided into three sections. The first section is a detailed description of the sol-gel process for PZT thin films, including the preparation of the stock solutions and the fabrication of thin films. Section 3.2 discusses the optical characterization utilized; here spectroscopic ellipsometry (SE) and its operations are introduced. Following this, the structural characterization techniques used, including room temperature X-ray diffraction (XRD), high-temperature *in-situ* x-ray diffraction, and the Field Emission Scanning Electron Microscope (FESEM) are described in section 3.3. The chapter closes with a description of the thin film electrical characterization, using standard measurements for the polarization hysteresis and dielectric constant.

3.1. Sol-Gel Process and Thin Film Preparation

3.1.1. Preparation of Stock Solution

In this study, a modification of the sol-gel process reported by Budd et al. (1985) and Udayakumar (1992) was used. Thin films of lead zirconate titanate, $Pb(Zr_{0.52}Ti_{0.48})O_3$, were prepared by the sol-gel processing method using metal alkoxides. The precursors used for the synthesis of the complex alkoxides were lead acetate trihydrate, $Pb(CH_3COO)_2.3H_2O$, titanium (IV) isopropoxide, $Ti(OCH(CH_3)_2)_4$, and zirconium (IV) n-propoxide,

$Zr(OCH(CH_3)_2)_4$ with 2-methoxyethanol, $CH_3CH_2CH_2OH$, as a solvent. These chemicals were purchased from Aldrich Chemical Company, Inc., Milwaukee, WI. A schematic of the solution preparation and film coating process is shown in Figure 3.1. Lead acetate trihydrate was dissolved in 2-methoxyethanol and dehydrated at 125°C under flowing Ar. The solution was cooled to room temperature and then mixed with zirconium (IV) n-propoxide and titanium (IV) isopropoxide in a glove box to prevent adsorption of moisture from the ambient air. The resulting solution was subsequently refluxed at 90°C for 4-5 hours to promote complexation. Then 1.5 moles of H_2O to 1 mole of PZT and 4 vol% of formamide were added to the sol in order to provide partial hydrolysis. This ratio was found to optimize the quality of the films (Gibbons 1995).

3.1.2. Thin Film Fabrication

The substrates used in this study were (0001) one-side polished sapphire (Union Carbide Corporation Crystal Products, Washougal, WA), (100) MgO (Marketech International, Pittsburgh, PA), and Pt-coated Si substrates (Nova Electronic Materials, Inc., Richardson, TX). The Pt-coated Si substrates were 3- inch Si wafers coated with 1 μm of thermally grown SiO_2 and a 200 Å Ti interlayer to promote bonding of the top 1000-1500 Å layer of sputtered platinum. Thin films were deposited onto the substrates using a spin coater (model P-6204, Integrated Technologies, Inc., Acushnet, MA), operated at 3000 rpm for 20 seconds. The films were pyrolyzed on a hot plate for 1 minute in air at temperatures ranging from 200° to 350°C following each layer of film deposition. This process was repeated until the desired film thickness was obtained. In this study, 7 to 9 layers of solution were deposited onto the

Lead (II) acetate trihydrate
+
2-methoxyethanol

↓

Distillation at 125°C
under Ar

↓

Add Zr (IV) n-propoxide
Ti (IV) isopropoxide

↓

Reflux at 90-100°C

↓

PZT Solution ← add water
+ formamide
4 vol%

↓

Spin Coat at 3000 rpm on
Pt-coated Si, MgO and
sapphire substrates

↓

Pyrolyze at 200°, 300°,
and 350°C

Repeat until
desired
numbers of
layers is
achieved

↓

In-situ annealing in high
temperature XRD system
from 25°C to 650°C

In-situ annealing in SE
system from 25°C to
600°C and 700°C

Figure 3.1. Schematic of sol-gel processing and preparation method for PZT films.

substrates in order to achieved films approximately 3500-5000 Å in thickness. Films were in-situ annealed in both the spectroscopic ellipsometer (SE) and in high temperature X-ray diffraction systems in order to examine the phase transformations and the optical properties of the PZT films. Films were also rapid thermally annealed in an AG Associates Heatpulse 210T-02 at 500°C to 700°C for 0 to 75 seconds.

3.1.3. Annealing Parameters and RTA Conditions

The annealing conditions used in this study for the different characterization methods are summarized in Table 3.1. For RTA films, the AG Associates Heatpulse 210 was employed. This instrument is capable of achieving rapid and linear heating and cooling rates. The effect of RTA on the crystallization was determined using hold temperatures between 500°C to 700°C with holding times of 0 to 75 seconds. The effect of annealing rates on the film microstructure and crystallization were examined by heat treatment with different ramp rates in the range of 5 to 100°C/minute by SE and high temperature X-ray diffraction. All samples were annealed in ambient air.

3.2. Optical Characterization

3.2.1. Introduction to Spectroscopic Ellipsometry (SE)

Spectroscopic ellipsometry (SE) is a very sensitive and versatile optical method for analysis of reflecting surfaces or films deposited on them. Ellipsometry is fundamentally concerned with the changes in polarization state of light upon reflection from a surface. This phenomenon was recognized by

Table 3.1

Annealing Parameters and RTA Conditions for PZT Films used in this study.

Annealing	Temperature (°C)	Hold Time	Annealing Rate
In-situ in SE	25°C to 600°C or 650°C	30 mins at a hold temperature	5°C/min to the desired temperature and SE data were taken from 250 to 750 nm
In-situ in XRD (R-B PSSD)	25°C to 600°C and 650°C	5 to 30 mins at a hold temperature	50°C/min 100°C/min
In-situ in XRD (HTXRD)	25°C to 700°C	-	5°C/min 10°C/min 20°C/min 50°C/min 100°C/min
RTA	500°C to 700°C	0 to 75 seconds	100°C/second
RTA	700°C	30 seconds	100°C/second

Drude (1890) more than 100 years ago. SE is a technique in which polarized light of a known wavelength is reflected from a sample surface and the relative changes in phase and amplitude of the parallel (p) and perpendicular (s) components of the light are measured. Since these changes are characteristic of the depth profile of the dielectric function of the films, the optical properties of the materials under study can be determined. The "null ellipsometer" was an early instrument which could only be operated manually and was limited to a small number of wavelengths. Therefore, it was time consuming in practice and tedious in its data acquisition. Cahan and Spanier (1969) first introduced the automatic rotating-analyzer ellipsometer which acquired data without the direct involvement of the operators. Also with the development of the laboratory computer, the limitations of the null ellipsometer including the time-consuming data aquisition and the wavelength range limitation have been eliminated. Using a continuous monochromator and a broad band source, spectroscopic ellipsometry (SE) can measure optical spectra as a continuous function of wavelength at high resolution from the IR to the near UV.

The basic principle of ellipsometry can be described in terms of equation (3.1), in which a monochromatic plane electromagnetic wave propagating in free space can be represented in a local coordinate system as

$$E(r,t) = (E_x X + E_y Y) \exp(ikZ - i\omega t) \tag{3.1}$$

where Z is the direction of propagation, X and Y are unit vectors perpendicular to Z, and E_x, E_y are the complex amplitude of the electric field. When the electromagnetic wave is reflected off a smooth surface, the reflected wave can be expressed in another coordinate system as

$$E(r,t) \quad = \quad (r_p E_x \, X + r_s E_y \, Y) \exp (ik'z - i\omega t) \tag{3.2}$$

where, for both local coordinate systems, the X axes are in the plane of incidence, and the Y axes are perpendicular to the plane of incidence, and r_p and r_s are complex Fresnel reflectance coefficients for light polarized parallel and perpendicular to the plane of incidence, respectively. The ellipsometric measurements give the phase angle difference (Δ) and the amplitude ratio angle (Ψ) between the parallel polarized (p) and perpendicularly polarized (s) light. Spectroscopic ellipsometry also permits measurements of the complex reflection coefficients at many wavelengths. The basic equation for modeling (Δ, Ψ) is given by

$$\rho \quad = \quad r_p/r_s \quad = \quad \tan\Psi \, e^{\,i\Delta} \tag{3.3}$$

where ρ is the complex reflectance ratio between the Fresnel reflection coefficients r_p and r_s.

In order to analyze the light after reflection from the sample surface, a rotating analyzer ellipsometer (RAE) is employed. The spectroscopic rotating analyzer ellipsometer (RAE) was developed by Aspnes (Aspnes 1975). By rotating the analyzer, the intensity of light can be sampled at many analyzer angles during a 360° rotation. Thus, the ellipsometric parameters can be obtained by analyzing the intensity of light as a function of the azimuth of the rotating analyzer. Microcomputer-controlled automated ellipsometers are capable of collecting data at speeds much faster than the null ellipsometer, so that spectroscopic and *in situ* studies are now possible. A full description of the basic principles of the RAE was given by Chindaudom (Chindaudom 1991).

To understand the basic theory of RAE, it is important to introduce a significant mathematical method called the Jones matrix, which is a useful tool in dealing with polarized light (Jones 1941). Polarized light is represented as a 1x2 matrix with each matrix element representing the component of the electric field. The phase information of the two polarizations is contained in the complex nature of the matrix element, and the time factor $e^{i\omega t}$ is omitted in the expression. Any optical component in the path of the light beam can be represented by a 2x2 matrix (McMarr 1985). The ideal polarizer is represented by:

$$T_p = \begin{bmatrix} 1 & 0 \\ 0 & 0 \end{bmatrix}$$

$$(3.4)$$

The change in the electric vector of polarized light propagating through a polarizer may be expressed by

$$\begin{bmatrix} E'_x \\ E'_y \end{bmatrix} = \begin{bmatrix} 1 & 0 \\ 0 & 0 \end{bmatrix} \begin{bmatrix} E_x \\ E_y \end{bmatrix} = \begin{bmatrix} E_x \\ 0 \end{bmatrix} \qquad (3.5)$$

If there are N optical devices in the system, the relation between the emerging light **E'** and the incident light **E** may be written as

$$\mathbf{E'} = T_N T_{N-1} \ldots\ldots\ldots T_2 T_1 \mathbf{E} \qquad (3.6)$$

where T_i is the Jones matrix of the ith device (Azzam and Bashara 1977).

The light reflected from the sample is usually elliptically polarized, and it can be characterized by 2 parameters: the ratio of minor to major axis, a, and

the azimuth angle, Q (see Figure 3.2). The components of the electric field vector can be described as follows:

$$\begin{bmatrix} E_x \\ E_y \end{bmatrix} = \begin{bmatrix} \cos Q & -\sin Q \\ \sin Q & \cos Q \end{bmatrix} \begin{bmatrix} 1 \\ ia \end{bmatrix} E_0 \tag{3.7}$$

where $|a| \le 1$, $|Q| \le \pi/2$, the x axis is in the plane of incidence and y is perpendicular to x. In the frame of the rotating analyzer, the projection in the electric vector on the local coordinate system is given by (Chindaudom 1991),

$$\begin{bmatrix} E_u \\ E_v \end{bmatrix} = \begin{bmatrix} 1 & 0 \\ 0 & 0 \end{bmatrix} \begin{bmatrix} \cos(A-Q) & \sin(A-Q) \\ -\sin(A-Q) & \cos(A-Q) \end{bmatrix} = \begin{bmatrix} 1 \\ ia \end{bmatrix} E_0 \tag{3.8}$$

where A is the azimuth angle of the analyzer. The total flux I which is incident on the detector is proportional to the square of the E field, i.e.

$$I \quad \propto \quad 1 + [(1-a^2)/ a^2] [\cos 2Q \cos 2A + \sin 2Q \sin 2A]$$

$$= \quad I_0 [1 + \alpha \cos 2A + \beta \sin 2A] \tag{3.9}$$

where α and β are the normalized Fourier coefficients determined experimentally either by direct computation (Aspnes 1973) or from phase and amplitude measurements (Cahan and Spanier 1969). The mode parameters a and Q therefore, are given in terms of experimental variables by (Chindaudom 1991)

$$Q \quad = \quad 1/2 \tan^{-1} (\beta/\alpha) + \pi/2 u (-\alpha) \, \text{sgn} \, (\beta) \tag{3.10}$$

$$a \quad = \quad \frac{\pm\sqrt{1-\zeta^2}}{1+\zeta} \tag{3.11}$$

where $u(x) = 0$ for $x<0$ and 1 for $x\ge0$, sgn $(x) = -1$ for $x<0$ and $+1$ for $x\ge0$, and

a = B/A
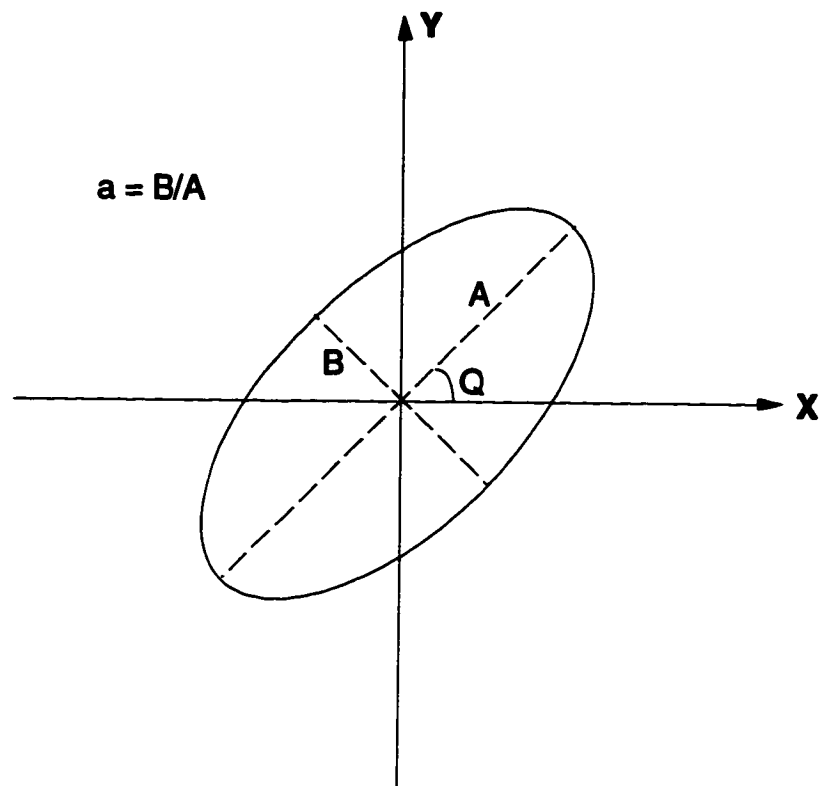
Figure 3.2. The ellipse representing the polarization state of light (after Yang 1988).

$$\zeta \quad = \quad [\alpha^2 + \beta^2]^{1/2} \geq 0 \qquad (3.12)$$

It should be noted that the $\pm$ sign in Eqn. (3.11) cannot be resolved in a rotating analyzer ellipsometer but it must be determined by comparing the results to a null ellipsometric measurement (Aspnes 1974 and Chindaudom 1991).

In order to determine the complex reflectance ratio, we should consider the polarization state in Eqn. (3.7) as a resultant polarization generated by the polarizer and the reflecting sample. If we assume the plane of incidence to be the same as the x-plane of the laboratory reference frame, the polarization state (E_x, E_y) of light reflected from a sample surface is given by (Chindaudom 1991)

$$\begin{bmatrix} E_x \\ E_y \end{bmatrix} \quad = \quad \begin{bmatrix} r_p & 0 \\ 0 & r_s \end{bmatrix} \begin{bmatrix} \cos P & -\sin P \\ \sin P & \cos P \end{bmatrix} \begin{bmatrix} 1 \\ 0 \end{bmatrix} E_0 \qquad (3.13)$$

where P is the azimuth angle of the polarizer fast axis. By equating Eqn. (3.7) and (3.13), we can solve for the complex reflection coefficients (Chindaudom 1991)

$$r_p \quad = \quad \frac{\cos Q - ia \sin Q}{\cos P} \qquad (3.14)$$

$$r_s \quad = \quad \frac{\sin Q + ia \cos Q}{\sin P} \qquad (3.15)$$

Therefore, the complex reflectance ratio ρ in terms of the mode parameters is

$$\rho \quad = \quad \frac{r_p}{r_s} \quad = \quad \tan \Psi \, e^{i\Delta}$$

$$= \quad \frac{(\cot Q - ia)}{(1 + ia \cot Q)} \tan P \qquad (3.16)$$

From this, Δ and Ψ are calculated by Eqn. 3.3. Further general equations were given by Aspnes (1974) and Chindaudom (1991), including the effects of component optical activity of the polarizer and analyzer and the calibration for the actual azimuth angles of the polarizer and analyzer, measured with respect to the sample plane of incidence.

3.2.2. Operation of Spectroscopic Ellipsometer

In 1961, the automatic ellipsometer was first used in determining the optical dielectric functions of metals and semiconductors (Takasaki 1961) and its progress continued on through 1975 by a number of researchers (Ord and Willis 1967, Jerrard 1969, Hauge and Dill 1973, and Stobie et al. 1975). A rotating analyzer ellipsometer (RAE) was first developed by Aspnes (1975). As discussed by Collins (1990), there are five fundamental steps in ellipsometry measurements: (1) an incident light wave is generated in a given polarization state, (2) the wave interacts with a sample, producing an emergent wave in a new polarization state, (3) the emergent polarization state is characterized, (4) the parameters that characterize the ratio of the complex amplitude reflection coefficients for p- and s- polarized waves, $\rho \equiv r_p/r_s$, from the information available on the two polarization states are determined, and (5) the physical parameters of the sample (e.g., the complex dielectric function, ε or film thickness) are deducted from the interaction parameters.

The spectroscopic rotating analyzer ellipsometer used in this study was originally constructed by Prof. K. Vedam and his students at the Materials Research Laboratory in 1979 (Mariner 1985). Since then, the system has been

modified in order to improve both the accuracy and the efficiency (McMarr 1985). In 1988, a control computer (IBM PS/2 model 30) was installed to the system in order to provide faster speed and on line measurement capabilities. With this installation, it was found that some experimental errors were caused by the low intensity of the light reflected from transparent samples (Chindaudom 1991). At this low signal level, the effect of the nonlinearity of the detector and the background level of the measured signal becomes significant, especially in the case of a transparent sample where any small error can be magnified. The signal corrections which were necessary for transparent samples are detailed elsewhere (Chindaudom 1991).

In 1995, the spectroscopic rotating analyzer ellipsometer used in this study was modified again by Dr. Susan Trolier-McKinstry and her students. The system is now interfaced with a Gateway 2000 486 DX2 computer which controls the data acquisition. A diagram of the rotating analyzer spectroscopic ellipsometer used in this study is shown in Figure 3.3. The basic optical devices used in the ellipsometer are as follows: a high pressure 75W short arc Xe lamp in its housing (from Hamamatsu, NJ) as the light source, a SPEX Doublemate double grating monochromator with gratings blazed at 330 nm, two Rochon prism type polarizers, and the photomultiplier tube (PMT) as a detector.

From Fig. 3.3, the light beam from the lamp is focused and directed to the entrance slit of the monochromator. The exiting beam is collected by another concave mirror adjusted to focus the slit image on the sample. The beam reflected from the sample is passed through the analyzer to the PMT where the intensity is detected as a function of analyzer position. Sample alignment is
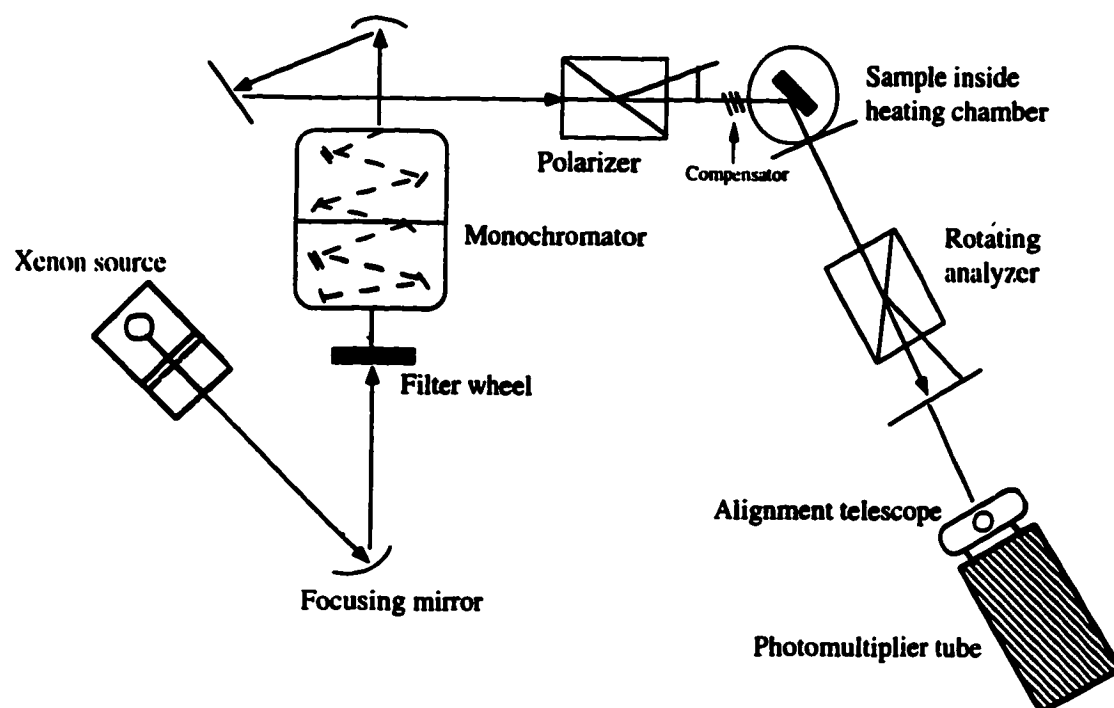
Figure 3.3. Diagram of the rotating analyzer SE used in this study.

made with the sample holder position and tilt control screws on the sample mount. For alignment, a cross-section of the beam can be viewed through the alignment telescope which is in front of the PMT. Both polarizer and analyzer are Rochon prisms which are housed in holders and can be rotated about the beam axis by synchronous motors. A compensator mounted on a precision positioner is placed on the ellipsometer table between the first polarizer and the sample. This unit can be removed easily when it is not needed. For a transparent sample the compensator is needed. Since the operating wavelength range spans from the ultra-violet region to the near infrared region (250-800 nm), all the optical components through which light is transmitted, the polarizer, the analyzer, and the compensator, are made of α-quartz which has low absorption coefficient in the UV (Chindaudom 1991).

There are four procedures used to align and calibrate the ellipsometer. They are 1) the system alignment, 2) system calibration, 3) the eta calibration, and 4) the dark current calibration.

The system alignment is required after a large system disruption (e.g. the light source replacement). It is important in ellipsometric measurements that the beam position not deviate substantially over the spectral region of interest (Aspnes and Studna 1975). Thus, the system alignment was achieved via tracing and centering the light beam path throughout the ellipsometer optical components using a reference laser beam. A reference laser beam was established by positioning a He-Ne laser at the PMT position and adjusting the laser beam position to the target mounted on the ellipsometer rails in the straight-through position. After this is done, the laser was replaced by the PMT detector and the final alignment was made by viewing the beam cross-section

through the alignment telescope. Once satisfactory system alignment was achieved, the ellipsometer arm was rotated to the desired angle of incidence. Then, the sample was mounted and aligned through the alignment telescope. The requirements for the sample alignment have been described elsewhere (Chindaudom 1991).

The system calibration essentially provides the information necessary to calculate the complex reflectance ratio of the reflecting surface from the measured coefficients a_2 and b_2. Aspnes (1974) described the residual calibration, R(P), as

$$R(P) = 1 - (a_2{}^2 + b_2{}^2) \tag{3.17}$$

It is shown by Collins (1990) that R(P) is approximately parabolic near the maximum modulation as in the equation:

$$R_p = 1 - \frac{1}{\eta^2} - \frac{(2\sin\Delta\cot\psi)^2(P-P_s)^2}{\eta^2}, \quad |P - P_s| \leq 1 \tag{3.18}$$

If the effects of component optical activity are ignored, P_s can be determined by fitting the experimental data set of R(P), where $P \cong P_s$, to a parabola. Therefore, $R(P_s)$ can be found at the minimum value of the best-fit function, where P is equal to P_s and $R(P_s)$ can be used to evaluate η.

Collins (1990) defined the phase function as $\theta(P) = (1/2) \tan^{-1} (b_2/a_2)$, therefore, $\theta(P)$ is linearly dependent on P where $P \cong P_s$

$$\Theta(P) \cong A_s + \cot\Psi \cos\Delta \, (P\text{-}P_s), \quad |P\text{-}P_s| \leq 1 \tag{3.19}$$

A_S can be calculated by $\theta(P)$ and the known value $P \cong P_S$, if the experimental curve of the phase function is fitted to a linear relationship.

Aspnes and Studna (1975) first derived the equations for the calibration angles P_S and A_S with first order corrections for the optical activity. Following their derivation, the function

$$R(P) = c_0 + c_1 P + c_2 P^2 \tag{3.20}$$

is used to describe the best fit parabola curve of the experimental data set of $R(P)$ by a least-squares method, where $P \cong P_S$. Likewise, the phase function, $\Theta(P)$ can be fitted to a linear function

$$\Theta(P) = c_3 + c_4 P \tag{3.21}$$

where $P \cong P_S$. Also, η, P_1 and A_1 can be determined at P_1 as

$$\eta = (1 - c_0 + c_1^2 / 4c_2)^{-1/2}, \tag{3.22}$$

$$P_1 = -c_1 / (2c_2), \tag{3.23}$$

$$A1 = c_3 + c_4 P_1 \tag{3.24}$$

where $R(P)$ reaches a minimum value at $P = P_1$. Then, P_S and A_S, which are the azimuth of the plane of incidence in the polarizer and analyzer frame, respectively, are given by (Aspnes 1974):

$$P_s = P_1 - \frac{\gamma_A \tan \Psi + \gamma_P \cos \Delta}{\sin \Delta}, \quad P \cong P_s \tag{3.25}$$

$$A_s = A_1 - \frac{\gamma_P \cot \Psi + \gamma_A \cos \Delta}{\sin \Delta}, \quad P \cong P_s \tag{3.26}$$

where Δ and Ψ are determined as zero-order approximations without any optical activity corrections. γ_A and γ_P are the optical activity coefficients of the analyzer and polarizer, respectively. In this study, the system calibrations were performed once there was a change in the position of any of the optical instruments, e.g. a focusing mirror was moved in order to align the light beam.

The eta calibration accounts for the change in the gain ratio of the ac to dc components of the incident light as the voltage on the PMT is increased. The parameter η describes the difference between the PMT voltage signal and the light intensity incident on the PMT. Chindaudom (1991) found that η can vary significantly when the average intensity is low, so that the large errors can occur at both ends of the spectral range, where the source intensity is low. The errors are magnified when transparent samples are measured. Thus, a procedure for calibrating η throughout the spectral range was needed. The method of using a neutral density filter in the SE system, when the angle of incidence was set at a 90° (straight-through) was used. Finally, η can be determined by the equation:

$$ \eta = \frac{1}{\sqrt{\alpha^2 + \beta^2}} \tag{3.27} $$

The average intensity of light at the PMT can be varied by rotating the variable neutral density filter. The η values calculated from Eqn. (3.27) can then be plotted as a linear function of PMT voltage. These η values are used to correct the experimental values, Δ and Ψ, in all measurements of the data in this study. Typically, the eta calibration was done once there was a system calibration.

The dark current calibration imparts the amount of current detected from the PMT when the light beam is blocked. This calibration was done for PMT voltages from 500V to 1100V. The results were fitted to a fifth order polynomial in terms of the voltage. This process is essential, particularly when taking data on low reflectivity samples, since dark current contributions can show a major effect on the measured intensity and in turn, the measured ellipticities. In addition, dark current correction became especially significant during high temperature measurements, where glow from the furnace contributed to the ambient light level (McKinstry 1992). In order to minimize this error, the dark current intensity is subsequently subtracted from the measured intensity after the data collection (McKinstry 1992). In this study, the dark current correction was performed before taking each set of high temperature measurements.

3.2.3. Spectroscopic Ellipsometric Data and Interpretation

After all the calibrations were completed, ellipsometric data could be taken. For room temperature measurement, the sample was placed on a vacuum mount in the path of the beam. The high temperature *in-situ* annealing in the ellipsometer will be detailed in the next section. The angle of incidence was set at 70° and 80° for Pt-Si substrates and transparent substrates, respectively. It was found that at these two incidence angles, accurate measurements of the ellipsometric parameters, Δ and Ψ could be obtained (Azzam and Bashara 1977).

The sample was then aligned by adjusting the sample holder position and the tilt control screws on the sample mount. Once the sample alignment was completed, the monochromator was set to 250 nm and the computer was

programmed to take data at 5 nm increments to 750 nm. The reflected light intensity was measured at 90 points for each analyzer rotation and 50 mechanical cycles were averaged for each wavelength. The computer then converted the measured intensity data to the ellipsometric parameters, Δ and Ψ, as a function of wavelength. The process of taking data takes about 18 minutes for the IBM PS/2 microcomputer, but it takes only 5 minutes for the Gateway 2000 486 DX2.

Once the ellipsometric data were obtained, they must be analyzed in order to depth profile the dielectric function of the sample. This can be done by constructing a model and fitting the calculated Δ and Ψ spectra of the model to the experimental data. The optical properties and the microstructure of the films (e.g., film thickness, volume fraction of air) are obtained from the fitting parameters. A model was generally constructed based on the quantitative information of the sample such as the refractive index, the film structure, film thickness, and composition. The values of Δ and Ψ are then calculated as a function of wavelength by using the optical properties of each component, and a reasonable starting value assigned to each unknown parameter.

The computer software for the modeling process was developed by Prof. K. Vedam and his research group at the Materials Research Laboratory (Chindaudom 1991). First the program searches for a set of the parameter values that yields the lowest value of σ by an iteration method. The σ value or the unbiased estimator is defined by the following equation (Chindaudom 1991):

$$\sigma = (\frac{1}{N-P-1}) [\sum_{i=1}^{N} (\cos\Delta^i_{exp} - \cos\Delta^i_{cal})^2 + (\tan\Psi^i_{exp} - \tan\Psi^i_{cal})^2]^{\frac{1}{2}} \qquad (3.28)$$

where N is the number of the data points taken and P is the number of unknown variables in the model. Δ^i_{exp} and Ψ^i_{exp} are the measured ellipsometric parameters, and Δ^i_{cal} and Ψ^i_{cal} are the calculated values obtained by model parameters. The model parameters which minimized the σ value could be found by a regression analysis. For transparent samples, a different form of σ in Eqn. (3.29) can be used (Chindaudom 1991):

$$\sigma = (\frac{1}{N-P-1}) [\sum_{i=1}^{N}(\Delta^i_{exp} - \Delta^i_{cal})^2 + (\Psi^i_{exp} - \Psi^i_{cal})^2]^{\frac{1}{2}} \tag{3.29}$$

The final model was selected based on these following criteria: 1) a physically realistic model; 2) the lowest value of σ; 3) reasonably low values of the confidence limits; 4) both the calculated Δ and Ψ spectra must fit well throughout the spectrum range; and 5) acceptably low values of the cross-correlation coefficients (McKinstry 1992).

In order to determine the optical properties of the thin film sample, reference optical data for all substrates used in this study are required. The reference data for Pt-coated Si substrates was obtained from SE measurement (McKinstry 1992 and Gibbons 1995). For transparent substrates such as sapphire and MgO, the optical reference data given by Malitson (1962) was used to describe the ordinary index. Reference data on the extraordinary index reported by Jeppesen (1958) was used (McKinstry 1992). For PZT films which are transparent in the UV to near IR region, the dispersion in the refractive index can be expressed by a Sellmeier oscillator dispersion equation:

$$n^2 = A_1 + \frac{A_2\lambda^2}{(-A_3^2 + \lambda^2 - i2A_4\lambda)}$$ (3.30)

where A_1, A_2, A_3, and A_4 are constants determined from the model, n is the complex index of refraction, and λ is the wavelength in nm. For modeling, the data set was truncated to 400-750 or 450-750 nm to avoid the onset of the absorption edge in PZT (McKinstry 1992). After the computer program modeled the film as a number of discrete layers, with a specific thickness, volume fraction of air, and refractive index, the film geometry was determined. For each sample, several different geometries were postulated. The best fit was finally chosen based on the criteria stated previously.

For modeling in systems that have a mixture of two or more phases, the effective dielectric constants can be approximated by Bruggeman's effective medium theory (Aspnes 1982 and Bruggeman 1935):

$$\sum_{i=1}^{n} f_i \frac{\varepsilon_i - \varepsilon}{\varepsilon_i + 2\varepsilon} = 0$$ (3.31)

where ε = the complex effective dielectric function of the composite,

ε_i = the complex dielectric functions for the ith phase,

f_i = the volume fraction of the ith phase,

n = the number of phases in the composite.

3.2.4. *In-Situ* Annealing Studies by SE

In order to examine the microstructure development and the crystallization kinetics of the PZT thin films, a windowless electrical resistance furnace was used to anneal the films *in-situ* on the ellipsometer. This furnace was originally built by McKinstry (1992) at the Materials Research Laboratory. It is a kanthal-wire wrapped alumina tube furnace which is powered by TTL logic-triggered, on-off signal from a solid state relay (Omega Inc. 25 amp dc solid state relay). An Apple computer was used to control the ramp rates and the constant temperature soaks. A variac controlled the total power dissipated through the furnace. Temperatures range from 25°C to 600°C were achieved without any difficulty. However, a practical upper limit for *in-situ* ellipsometric measurement was ~500°C, where the glow from the furnace significantly decreased the signal-to-noise ratio (McKinstry 1992).

From previous results of the *in-situ* XRD studies in PZT thin films during annealing (Aungkavattana et al. 1995), the intermediate fluorite-type or pyrochlore phase was still found accompanying the perovskite PZT phase at temperatures higher than 600°C. In order to follow the complete crystallization of the intermediate fluorite-type material or pyrochlore-like phase to the fully crystallized perovskite phase, a higher temperature furnace, which can reach 700°C was required.

A new high temperature conductive block heater was built to allow this. The block heater was made of the stainless steel (Hanes Alloy #804) and was drilled with three 0.25" holes for the cartridge heaters. Drawings of the heater block, and the insulating base plates, including the sample holder are given in

Figures 3.4 and 3.5. Since this heater block is used to *in-situ* anneal the sample on the ellipsometer, a cooling system is crucial in order to protect all the optical instruments. To achieve this, a water cooling coil wrapped around a stainless steel tube was used. A drawing of the cooling coil is shown in Figure 3.6. Light entrance and exit spaces were left unwrapped. The same variac was used to control the total power of the heater. Ramp rates of $5°$ to $100°C/min$ from $25°C$ to $700°C$ were achieved easily.

3.3. Structural Characterization

3.3.1. *In-Situ* R-B PSSD X-Ray Diffraction System

The Ruud-Barrett Position Sensitive Scintillation Detector (R-B PSSD) X-Ray Diffraction system used in this study was designed at Advanced Technology Materials, Inc. (ATMI, Danbury, CT) with assistance from the Materials Research Laboratory at Penn State University. The system utilizes a fiber-optic based position sensitive scintillation detector (PSSD), which was originally developed for portable X-ray stress analysis (Ruud 1983). By modifying the focusing geometry and making improvements to several detector components, the PSSD system has been successfully used as an *in-situ* CVD thin film growth monitor (Kozazeck et al. 1993).

The PSSD provides improved speed and accuracy and expanded versatility over existing X-ray diffraction techniques. The detector is based on the conversion of the diffracted X-ray pattern into an optical signal, i.e., light. The light is then conducted via a fiber-optic bundle over several centimeters and is amplified by electro-optical image intensification. After electronic
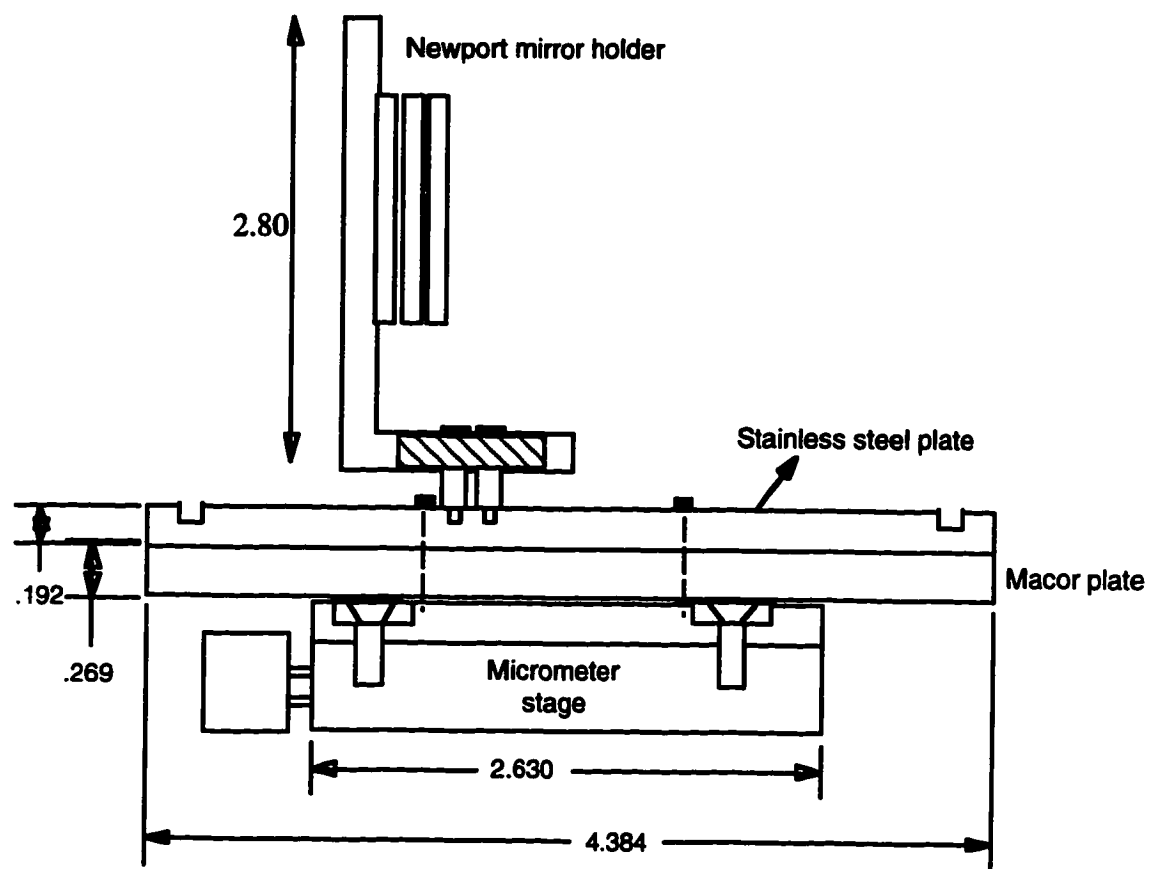
Figure 3.4. The side view of the bottom-plate insulators and the sample holder used in the *in-situ* SE annealing studies. The size units are in inches.

a)

.250   .250   Top view

.125   Stainless steel plate 1.5"x1.5"x 0.25"
              (mounted on the Newport holder)

1.500   .375

              Tapped hole 4-40

Thru hole

|← 1.500 →|

b)   Top view

.250   .125   .250

                        Stainless steel heater block
1.000   .125   Thickness = 0.5"

                Thru hole
                4-40

|← 1.500 →|

                        Side view

c) |← 1.000 →|

              Hole diameter = 1/4"
.500   Distance between holes = 1/16"
.250

|← 1.500 →| .125
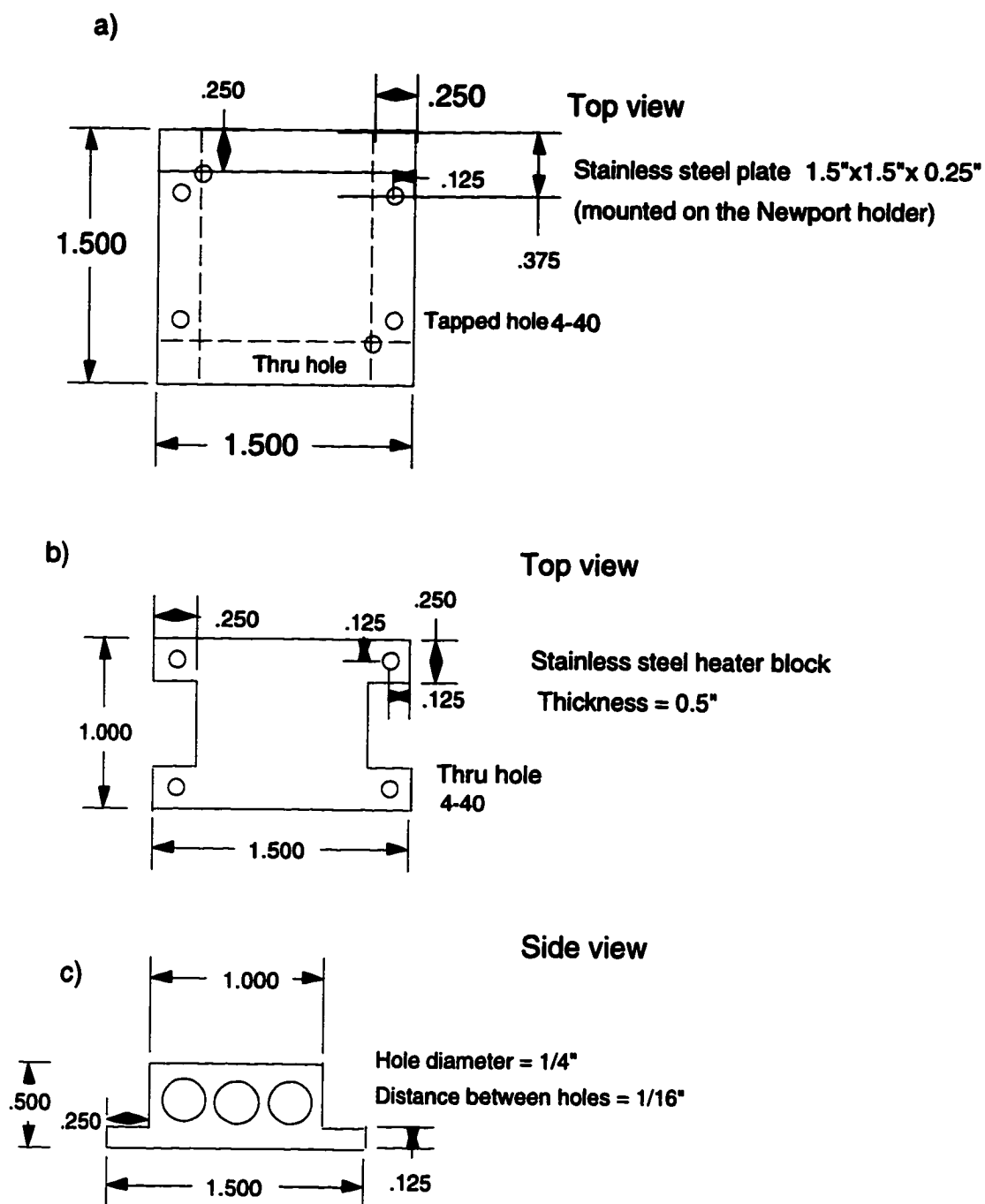
Figure 3.5. The drawings show (a) the real size of the stainless steel adapter for the sample holder, (b) the top view of the heater block, and (c) the side view of the heater block. The material used to make this heater block was Hanes Alloy #804.
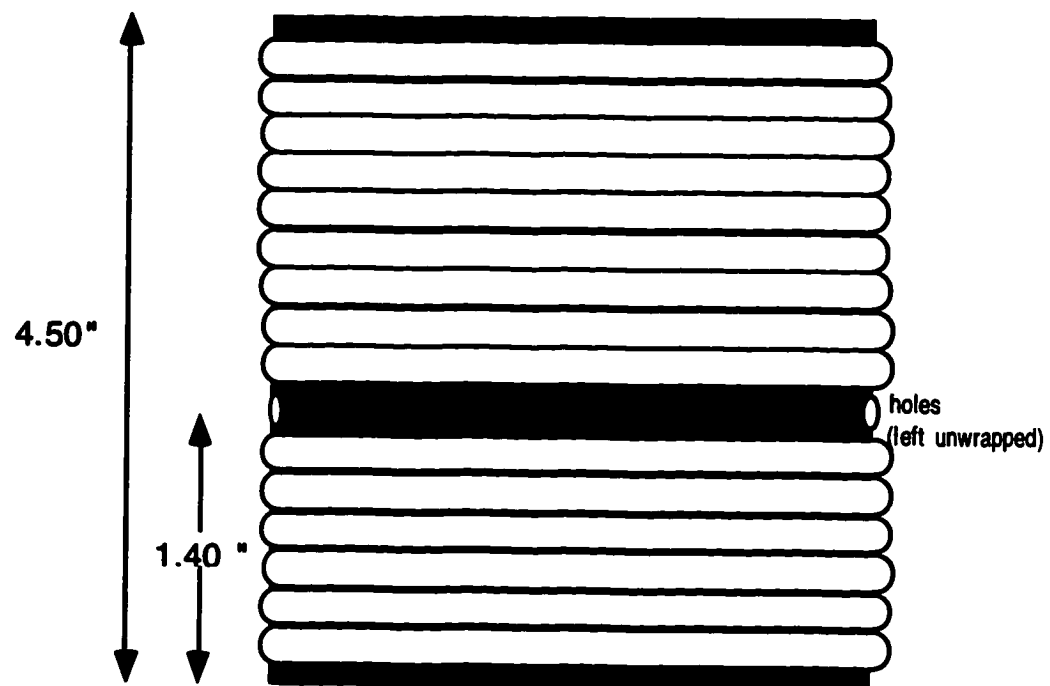
Figure 3.6. The stainless steel tube with the outside diameter (OD) 5" wrapped with the stainless steel cooling coil (OD 0.25"). The coil was spot-welded to the tube. The diameter of each hole is 0.25"

conversion, the signal is then transferred to a computer for refinement and interpretation (Ruud 1993).

The present version of the PSSD has a linear resolution of approximately 50 μm over its entire length along with a photon conversion efficiency of about 15% (Kozazeck et al. 1993). Linear resolution is defined as the detector's ability to accurately identify the point along its x-ray detection length at which an x-ray photon is incident. The linear resolution of 50 μm is comparable to the best resolution of about 60 μm at the center of the detector for a few position-sensitive proportional detectors (PSPD) and 100 to 200 μm for most of the PSPDs used in X-ray diffraction (Ruud 1983). In addition, PSPDs usually show poorer resolution away from the center of their x-ray-sensitive area.

The advantage of the scintillation-coated glass bundle detector is that it makes up the X-ray-sensitive surface of the PSSD and does not limit the surface shape to a long, thin plane. It can be ground and polished to other configurations; e.g., a circle in order to conform to the radius of the focusing circle in a special X-ray diffraction application. Also, since the X-ray-sensitive surface is a simple fiber end, it is possible to adapt the PSSD to a number of X-ray focusing geometries.

In addition, the PSSD has no dead-time period. The proportional detectors usually are inherently capable of processing only one x-ray photon at a time with a time delay, or dead time, during which no other photon can be processed (Ruud 1983). The dead time is usually a few microseconds, and the maximum x-ray flux in which a detector is functional is a few ten-thousand counts. This means that under application conditions where rapid data

accumulation requires very high X-ray fluxes continuously, a PSSD is more effective than the PSPD over a very broad range of x-ray flux intensities.

A schematic giving the configuration of the PSSD system for the *in-situ* PZT thin film heat treatment analysis is shown in Figure 3.7. X-rays from a fixed source located exterior to the process environment enter through a small opening of the alumina tube furnace, and are diffracted off the sample surface. After exiting the furnace on the other side, the diffracted beam impinges upon the scintillating surface of a one dimensional rigid fiber-optic array, generating visible light, which is coherently transported along the flexible portion of the array. After being amplified by an image intensifier, the light is converted to an analog electrical signal with a linear diode array, digitized via an A-D board and immediately stored on computer disk. The same computer is used to control the detector operation, including automated data acquisition and data analysis.

The resolution of the PSSD system, as measured by peak half width, is typically within 10% of a commercial scanning system (Kozazeck et al. 1993). It should be noted that the diffracted peaks from both the pyrochlore and perovskite phases formed during heat treatment of PZT thin films are weak but clearly distinguishable when measured using a traditional $\Theta/2\Theta$ Bragg-Brentano scanning X-ray diffractometer. The low signal-to-noise ratio is due to several factors, including low film thickness (< 0.5 μm) and small grain size (<1.0 μm).

For the *in-situ* annealing studies, the sample was placed inside an alumina tube furnace situated on the R-B PSSD X-ray diffraction system. The annealing rates used in this study were 50°C and 100°C/min to 600°C and 650°C. The X-ray diffraction patterns were collected over a 2Θ range of

X-ray
Source

Incident
beam

Diffracted
beam

Fiber-optic
detector

sample in
furnace

Computer

Computer-controlled
alumina tube
furnace

Detector/source
mounting frame

Image intensifier/
diode array
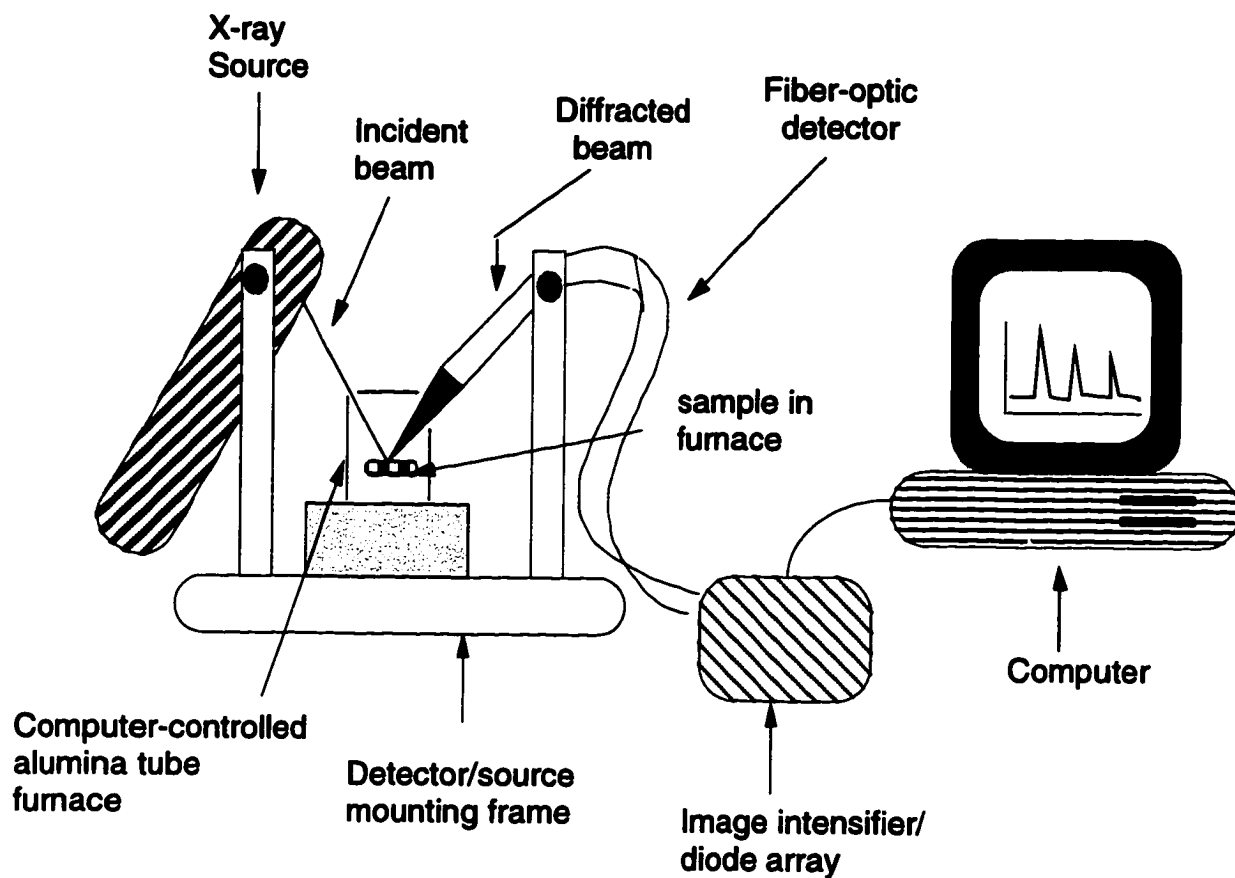
Figure 3.7. *In-situ* PSSD X-ray diffraction system configurated for PZT thin film heating experiments.

approximately 6° under parafocusing conditions, observing both the pyrochlore-like peak at $2\Theta = 29°$ and the perovskite peak at $2\Theta = 30.9°$. The ramp rates of 50°C/min were generally achieved, however, for a 100°C/min ramp rate, a temperature gradient of 15-20°C between the setpoint and the real temperature was observed.

X-ray diffraction patterns were collected every 30 seconds during the heating. At soaking temperatures of 600°C and 650°C, X-ray patterns were collected once a minute. A 15 second exposure time was used for isothermal patterns during soaking at a given temperature. The thermocouple used to control the temperature was placed underneath the sample. The X-ray source-to-sample and the sample-to-detector distances were both 20 cm, this value being dictated by the size of the alumina heating furnace. The angle of incidence between the X-ray source and the sample was 14°.

To compensate for weak diffraction signals, longer data acquisition times were used. Data-collection times were increased from the typical 0.1-6 seconds range to 30 seconds, with longer times giving improved signal-to-noise ratios. This acquisition time is still much less than that required from a scanning system, which typically required 6 minutes to cover 6° at a similar signal-to-noise ratio. Even with a hot-stage attachment, a standard scanning diffractometer would have been unsuitably slow based on the observed phase-change rates during heating. With the R-B PSSD system, some run-to-run shift in the detector channel position for both pyrochlore-like and perovskite peaks was observed due to small differences in the flexible detector position. Within a heating run, however, the measured diffraction angle for a given X-ray peak was stable. In all cases, peak identification was unambiguous.

3.3.2. Room Temperature X-Ray Diffraction

The room temperature structural characterization of PZT thin films was also conducted using a Scintag thin film diffractometer using CuKα radiation (λ = 1.5418 Å). In order to obtain a better resolution of thin film x-ray peaks without interference from the high intensity substrate peaks, a grazing angle method was used in this study. The X-ray patterns were recorded at a scan rate of 2° min⁻¹ for phase and structure analysis. The 2-theta range scanned was from 18° to 75° and the grazing angle was set to 7.5° to 9° depending on the thickness of the sample.

3.3.3. High Temperature X-Ray Diffraction

A set of PZT thin films deposited onto Pt-coated Si and MgO substrates were *in-situ* annealed in the high temperature X-ray diffractometer (HTXRD) at the High Temperature Materials Laboratory of the Oak Ridge National Laboratory, Oak Ridge, TN. The high temperature X-ray diffraction patterns were collected using a Scintag Θ–Θ "PAD X" diffractometer equipped with an Edmund Buhler Model HDX-2 hot stage (Cavin and Wolf 1993). The photographs of the HTXRD and the radiation heater setup are shown in Figures 3.8 and 3.9. The sample was placed on a piece of fused silica, which was located between the Pt-strip heaters. The thermocouple was 1 mm away from the sample, as shown in Fig. 3.9.

The X-ray source used was from a copper target tube with a λKα1 = 1.540598 Å which operated at 45 kV and 40 mA. An automated scanning position-sensitive detector (PSD) was also installed on the instrument.
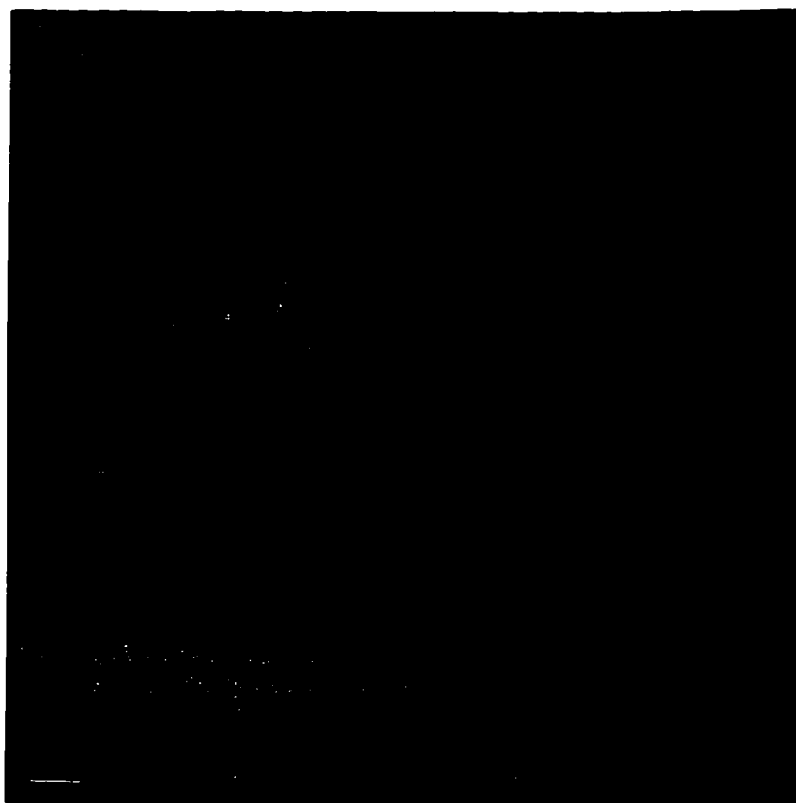
Figure 3.8. A high temperature X-ray diffractometer (HTXRD) system

(High Temperature Materials Laboratory, Oak Ridge National Laboratory, TN).
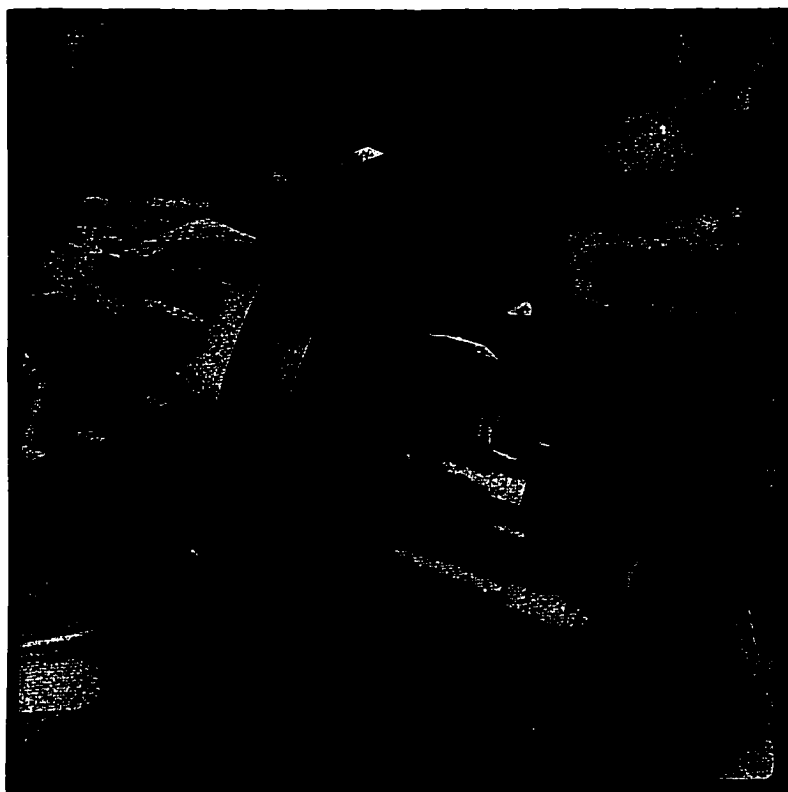
Figure 3.9. A Pt-strip heater setup used in the HTXRD. The fused silica sample holder, the heater shield, and the thermocouple are shown.

Constant ramp rates of 5, 10, 20, 50 and 100°C/minute were used to study PZT films on both Pt-coated Si and MgO substrates. For slower heating rates including 5, 10 and 20°C/minute, a scan rate of 20°/minute was used. In the case of faster heating rates (50 and 100°C/minute), a 50°/minute scan rate was chosen to keep up with the fast ramp rates.

3.3.4. Field Emission Scanning Electron Microscopy (FESEM)

The microstructure and the surface morphology of the PZT films were studied using a scanning electron microscope (SEM). A *JEOL JSM-6300F* which is equipped with a cold cathode field emission electron gun (FEG) was used to obtain a high resolution scanning electron microscopy image. This source is up to five orders of magnitude greater in brightness than conventional thermionic tungsten or lanthanum boride guns (JSM-6300F Instruction Scanning Microscope, No. ISM 63F-2). The result is enhanced signal-to-noiseratios for a smaller probe size, giving an ultimate spatial resolution of 1.5 nm at an operating potential of 30 KeV and magnification of 10 to 500,000X (JSM-6300F Instruction Scanning Microscope, No. ISM 63F-2). The high signal-to-noise ratio also allows the use of low accelerating potentials, which facilitates high resolution studies of the surface details and minimizes charging problems in poorly conducting specimens.

3.4. Electrical Characterization

Hysteresis measurements were made using a Radiant Technology RT66A Ferroelectric Tester on PZT films ranging in thickness from 2000 Å to 5000 Å. The bottom electrode was the platinum surface of the substrate and the top electrode was gold sputtered on the film for 40 seconds. The area of the top electrode used in this study was 7.065×10^{-4} cm^2.

Chapter 4

RESULTS AND DISCUSSION

This chapter will be divided into three main sections. In the first section, results from the optical characterization experiments, including the SE data for PZT films on various substrates, and the crystallization kinetics studies via SE are given. Following this, results from the structural and microstructural characterization, including phase identification by x-ray diffraction, the *in-situ* x-ray diffraction studies, the non-isothermal crystallization kinetics by high-temperature X-ray diffraction, and the microstructural investigation are detailed in section 4.2. The last section covers the electrical characterization.

4.1. Optical Characterization

4.1.1. *In-situ* Annealing Studies by Spectroscopic Ellipsometry

In order to study the development of film microstructure, as well as to follow the evolution of the optical properties, PZT films on Pt-coated Si, sapphire, and MgO substrates were *in-situ* annealed in the ellipsometer using a windowless electrical-resistance alumina tube furnace. Temperatures between 25°C and 650°C could be achieved without any difficulty. However, a practical upper limit for *in-situ* ellipsometric measurements was at around 390°C, where the furnace glows and significantly decreases the signal to noise ratio of the ellipsometer.

4.1.1.1. SE Data for PZT Films on MgO Substrates

For films on MgO substrates, SE data were collected as a function of temperature at an incidence angle of 80°. The compensator was also used. The sample was annealed from 25°C to 600°C at 50°C intervals between 100°C and 300°C and 30°C intervals from 300°C to 600°C to follow the crystallization of the film. The data were collected at annealing temperatures between room temperature and 390°C. Above 390°C, the sample was heated to the desired temperature, soaked for 30 minutes, and then cooled down to 350°C for measurement.

The experimental data were modeled with a single term oscillator in order to get the best fit for both of the ellipsometric parameters, Δ and Ψ. Figure 4.1 shows the best fit models for room temperature, 300°C, 420°C, and 600°C anneals of a PZT film on an MgO substrate. The fit of Δ and Ψ curves for the 300°C anneal is also illustrated in Figure 4.2. A low refractive index interfacial layer between the MgO substrate and the film, modeled here as a mixture of the substrate and film was required in the model to obtain the best fit, for all temperatures. The reason for this may be due to the surface of the MgO substrate itself. To prove this, SE data was also taken on one of the plain MgO substrates. The model for the MgO substrate is illustrated in Figure 4.3, it does show a thin surface layer approximately 217 Å thick on the surface. This layer could be due to polishing damage produced during the process of cleaning a previous film off the surface of the MgO for reuse. This accounts for the interfacial layer found by SE measurements in most of the films on MgO substrates used in this study.
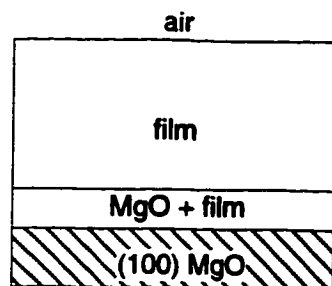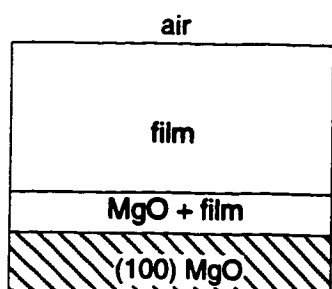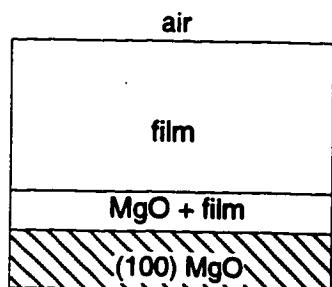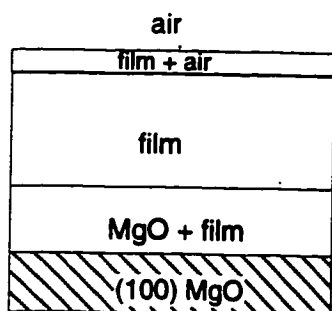
Figure 4.1. Best fit models for a sol-gel PZT film on an MgO substrate at various annealing temperatures. The film was pyrolyzed at 200°C.
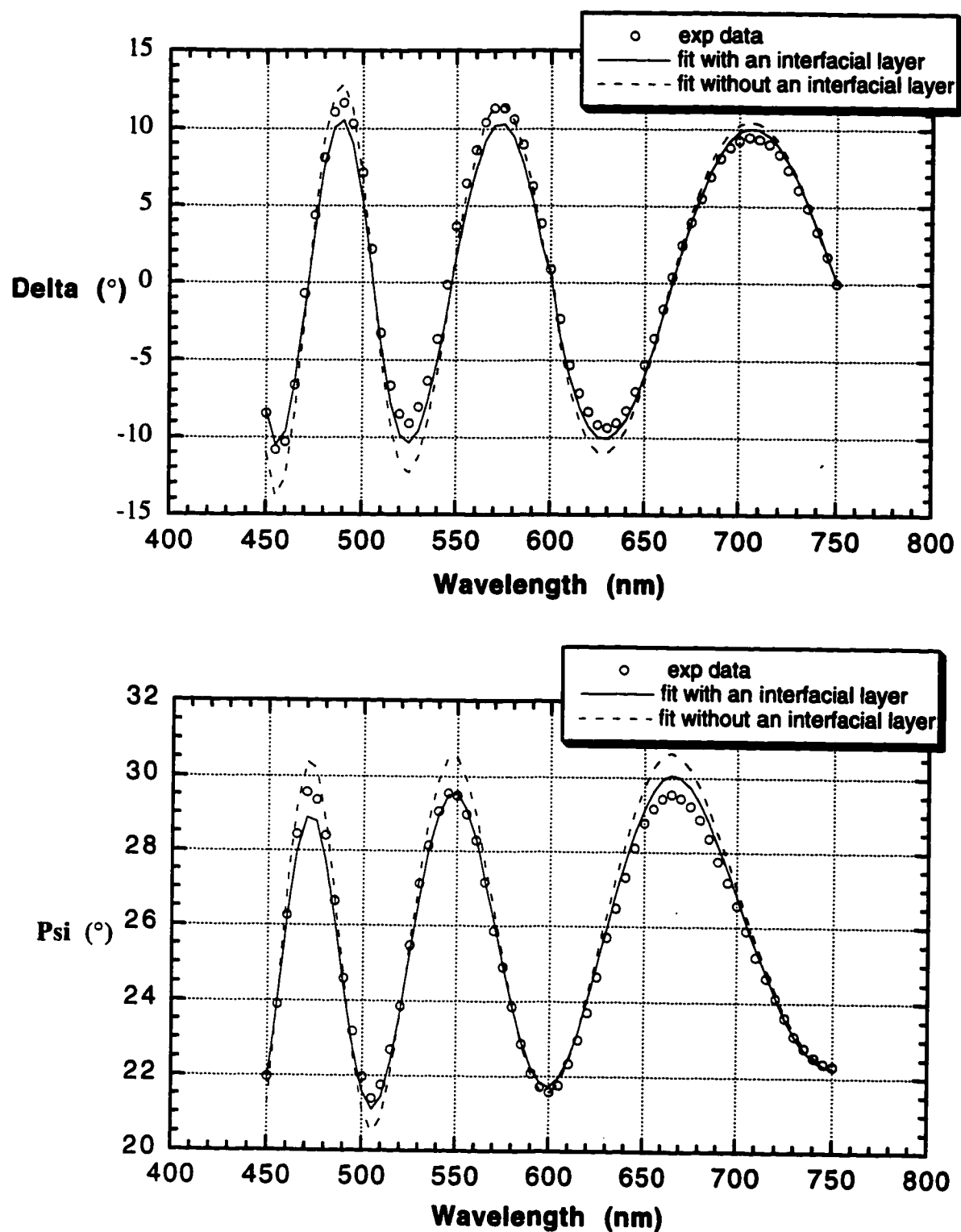
Figure 4.2. The Δ and Ψ fits for a sol-gel PZT film on MgO following the 300°C anneal.

air

MgO + air

(100) MgO substrate

t = 217±44 Å   Vol.% of air = 50%

σ = 0.01
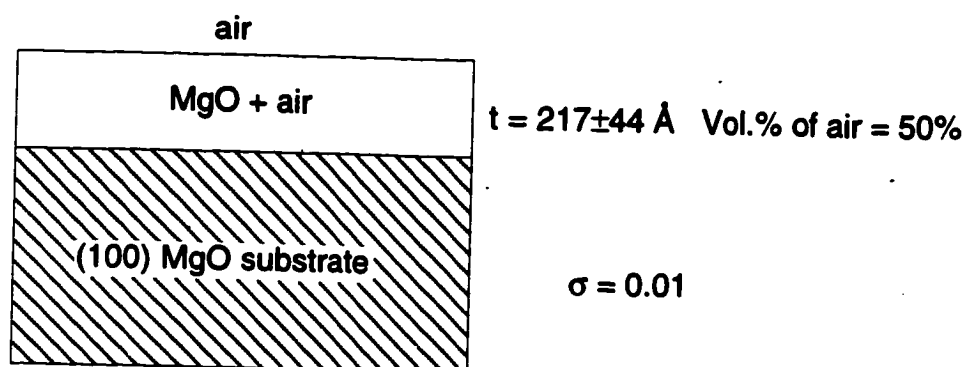
Figure 4.3.   Model for a re-used MgO substrate after polishing film off the surface.

The summary of the models for the microstructure evolution in PZT films on MgO substrates during annealing from 25°C to 600°C *in-situ* in the ellipsometer is shown in Table 4.1. The film shows quite a smooth surface with a homogeneous microstructure with only a thin bottom layer which is due to the substrate itself. The bottom layer, which was modeled as a mixture of MgO and film, shows only modest change in thickness for all annealing temperatures. A surface roughness layer of a 26±9 Å thick was found between 550° and 600°C anneals.

Discounting the interfacial layer, the thickness of the as-deposited film was approximately 6700 Å and showed no significant change between room temperature and 390°C. Since the pyrolysis temperature for this film was at 200°C, the reason that the film thickness started to drop at 420°C may be due to the removal of organic materials which remained after the pyrolysis step. As the film crystallized at higher temperatures, the film thickness continued to drop, and the final thickness of film after crystallization at 600°C was 5000 Å. Figure 4.4 shows a plot of the total thickness of the film on an MgO substrate over a range of annealing temperatures.

The refractive index of the film over a range of annealing temperatures can be determined using a single term oscillator equation (Eqn. 3.30), where the constants A_2 and A_3 in Table 4.1 were obtained from the modeling. A_1 was assigned to a value of one and A_4 to zero. The dispersion curves which show the refractive index (n) changes over wavelength as a function of annealing temperature are shown in Figure 4.5. From this plot, the film refractive index increased markedly with the annealing temperature, particularly at the 525°C and 600°C anneals. This is most likely due to the crystallization of the

Table 4.1

Models of microstructure for a PZT film on an MgO substrate.

Data were taken during *in-situ* annealing on a spectroscopic ellipsometer from 25°C to 600°C

Temp (°C)	Bottom Layer Thickness (Å)	% of air in Bottom Layer	Dense Layer Thicknesss (Å)	Surface Roughness Thickness (Å)	% of air in Surface Roughness layer	σ	A2	A3
25	366±18	50%	6691±31	-	-	0.008	3.33±0.04	210.1±3.7
100	297±23	50%	6748±36	-	-	0.008	3.32±0.04	212.7±3.4
150	286±24	50%	6795±35	-	-	0.008	3.28±0.03	213.0±3.0
200	302±22	50%	6796±35	-	-	0.008	3.27±0.04	214.7±3.3
250	312±21	50%	6755±34	-	-	0.007	3.30±0.04	217.6±3.0
300	316±20	50%	6752±32	-	-	0.007	3.33±0.03	217.8±2.8
330	307±19	50%	6735±31	-	-	0.007	3.33±0.03	217.8±2.8
360	310±19	50%	6728±31	-	-	0.007	3.32±0.01	219.3±2.8
390	307±15	50%	6597±25	-	-	0.006	3.41±0.03	219.4±2.3
420	276±13	50%	6314±22	-	-	0.008	3.66±0.03	212.4±2.1
450	270±10	50%	6140±18	-	-	0.005	3.83±0.02	222.9±1.4
500	266±13	50%	5994±24	-	-	0.007	3.97±0.03	238.8±1.6
525	329±11	50%	5768±27	-	-	0.008	4.20±0.04	239.8±2.1
550	423±11	50%	5180±33	26±9	50%	0.011	4.84±0.06	221.5±4.1
575	429±10	50%	5118±31	29±8	50%	0.009	4.87±0.05	205.1±4.1
600	437±10	50%	5114±32	27±9	50%	0.010	4.92±0.05	213.4±4.3

(A1 = 1 and A4 = 0)
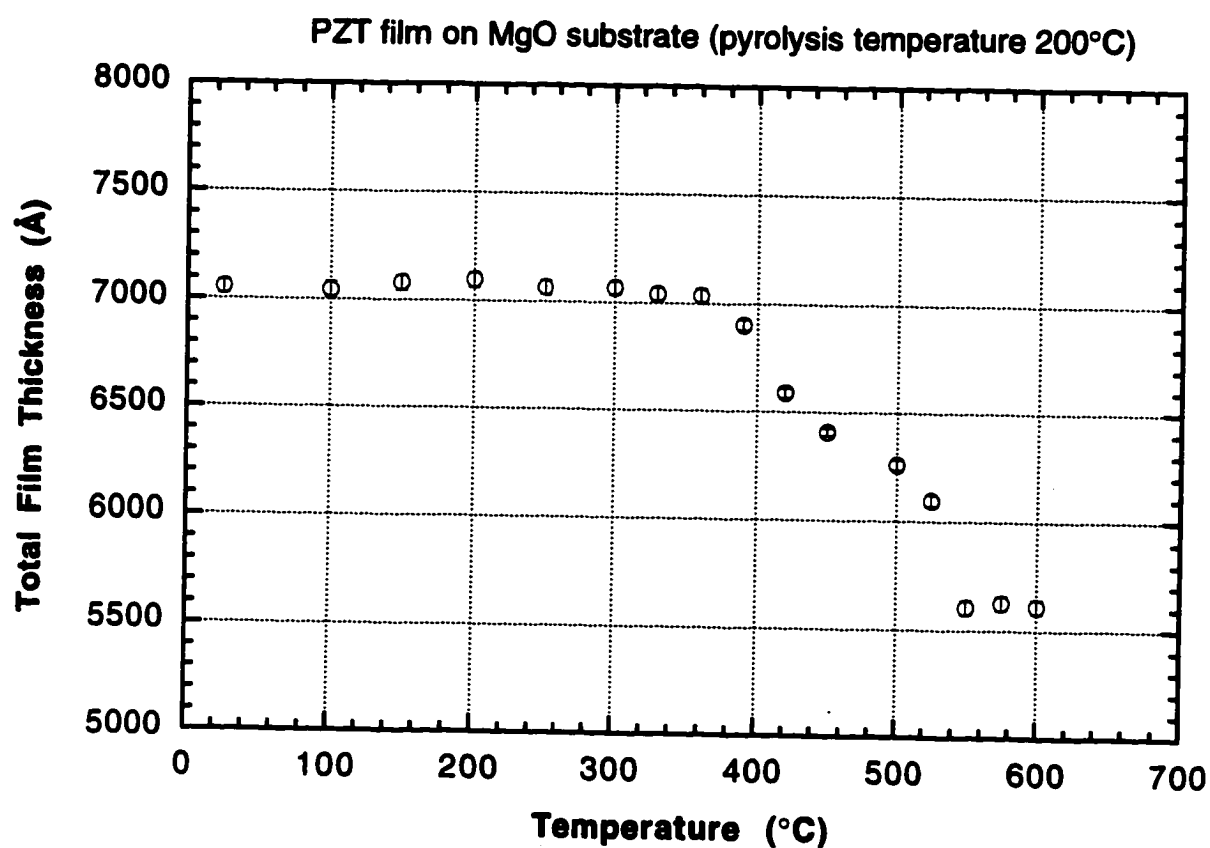
Figure 4.4. A plot of the total film thickness as a function of temperature for a film on an MgO substrate. The bars shown correspond to the 90% confidence limits for the thickness derived from the model.
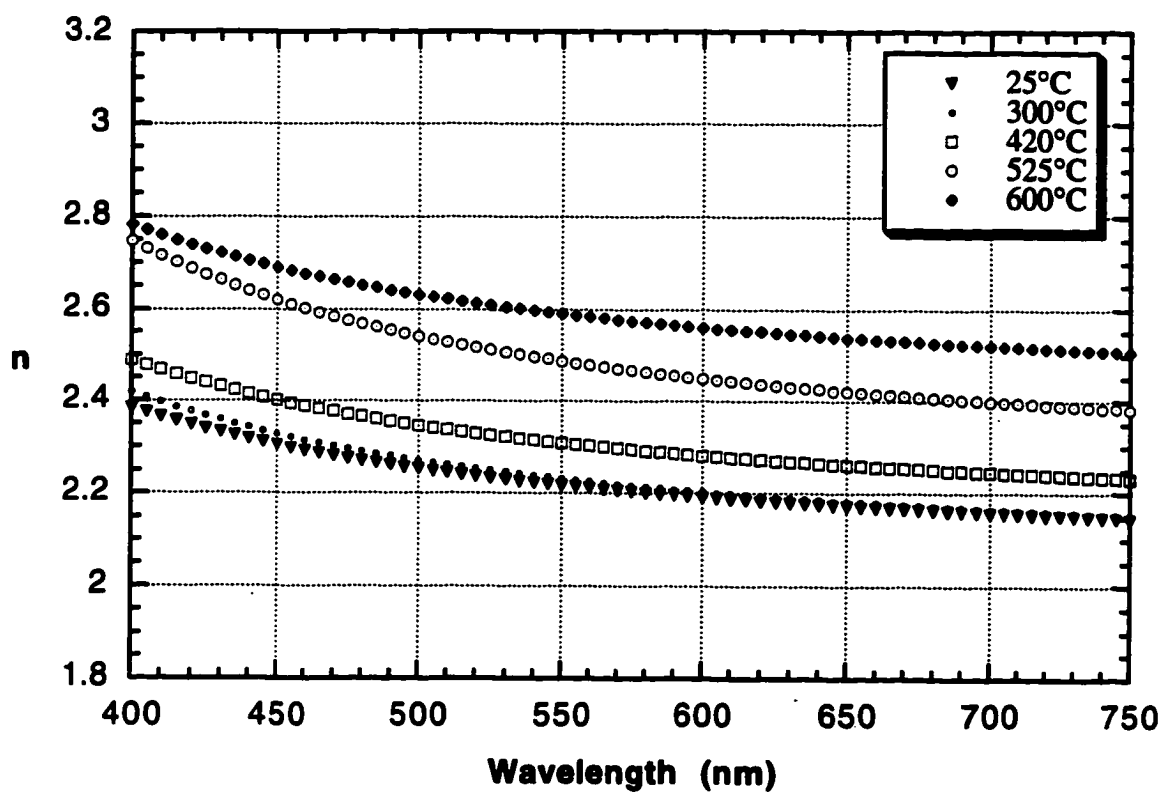
Figure 4.5. A plot of refractive index (n) over a range of wavelengths as a function of the annealing temperature for a PZT film on an MgO substrate.

crystalline phases such as intermediate fluorite-type or pyrochlore phase at around 500°C and the perovskite phase at the 600°C anneal. The high temperature X-ray diffraction results in section 4.2.2 are in agreement with this. In addition, the values of the calculated refractive indices of the film after a 600°C anneal are comparable to those of bulk lanthanum-doped PZT ceramics reported by Thacher (1977). At a wavelength of 550 nm, n for the PZT film on MgO after 600°C anneal was found to be 2.59, and those values for the PLZT reference data are 2.53 and 2.61 for PLZT (16/65/35) and PLZT (16/40/60), respectively. This result suggests the PZT film has a dense microstructure. The microstructural results section which is reported later in this chapter are also in agreement with this.

4.1.1.2. SE Data for PZT Films on Sapphire Substrates

For PZT films on sapphire substrates, spectroscopic ellipsometry data were also taken as a function of temperature. An incidence angle of 80° and the compensator were used, as for films on MgO. The sample was *in-situ* annealed in the ellipsometer from room temperature to 600°C with the same intervals and conditions as for the film on the MgO substrate.

The ellipsometric parameters, Δ and Ψ were also modeled with a single term oscillator to get the best fit. SE data were truncated to 450-750 nm for modeling to avoid the damping of the interference oscillation at low wavelengths. Figure 4.6 shows the best fit models for room temperature, 300°C, 500°C, and 600°C anneals for a PZT film on a sapphire substrate. In all cases, a surface roughness layer was required in order to obtain the best fits. As shown in a room temperature fit in Figure 4.7, the model with a thin surface

Room temperature
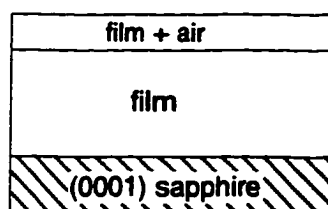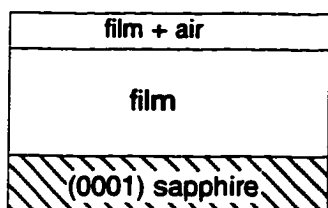
film + air	t = 33±9 Å Vol.% of air = 50%
film	t = 5398±28Å
(0001) sapphire	

σ = 0.010

300°C

film + air	t = 25±13 Å Vol% of air = 50%
film	t = 5438±36Å
(0001) sapphire	

σ = 0.012

500°C

film + air	t = 741±8 Å Vol.% of air = 32±0.2%
film	t = 4660±27Å
(0001) sapphire	

σ = 0.007

600°C

film + air	t = 933±13 Å Vol.% of air = 32±0.2%
film	t = 4302±28Å
(0001) sapphire	
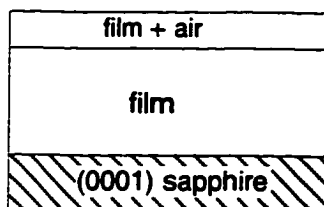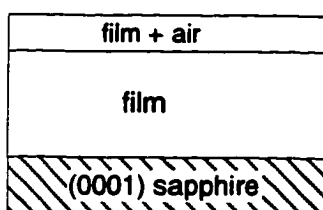
σ = 0.008

Figure 4.6. Best fit models for a sol-gel PZT film on a (0001) sapphire substrate at various annealing temperatures. The film was pyrolyzed at 350°C.
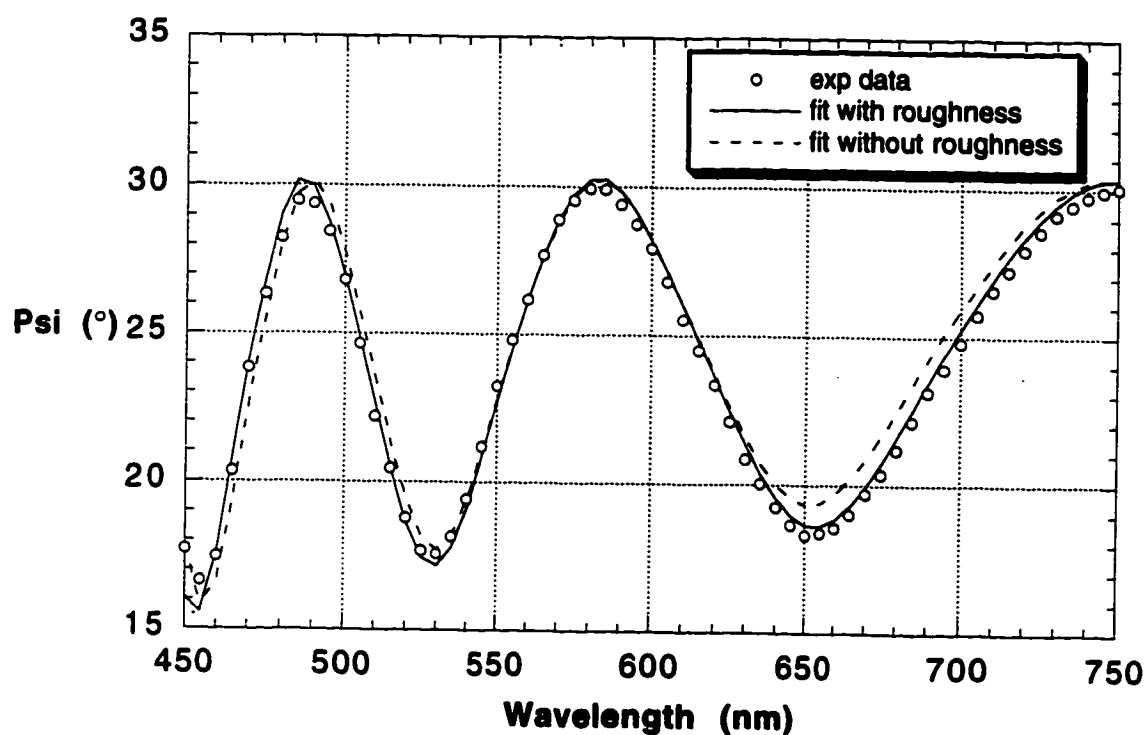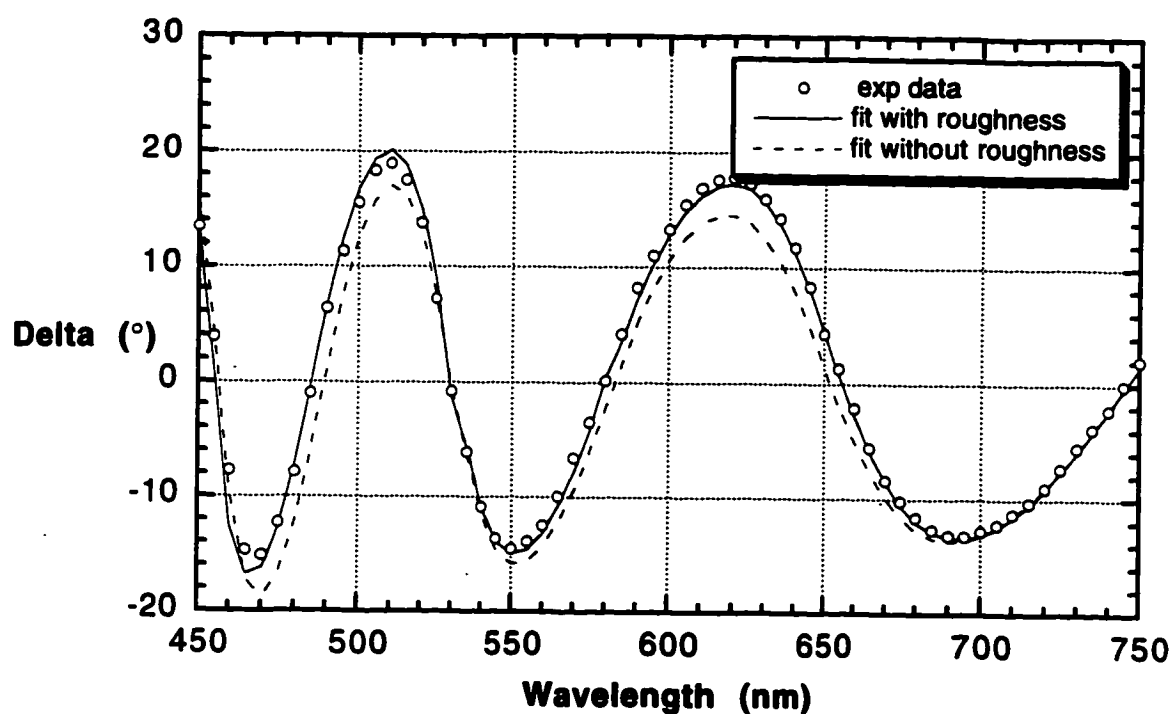
Figure 4.7. The fit of Δ and Ψ curves for a room temperature model for a PZT film on a sapphire substrate.

roughness layer improves the fits of Δ and Ψ when compared to the fit without the roughness layer. For a 600°C anneal, the fit of Δ and Ψ curves is also illustrated in Figure 4.8.

Table 4.2 summarizes the models of the microstructure evolution for the PZT film on a sapphire substrate during *in-situ* annealing in the ellipsometer from 25°C to 600°C. The film was pyrolyzed at 350°C prior to annealing. Structurally, the film is quite homogeneous with only a thin layer of surface roughness on the top of the dense layer of the film. A surface roughness layer appeared at all temperatures for PZT films on sapphire substrates. This roughness layer was found to be as thin as ~33 Å between room temperature and the 360°C anneal. At 390°C, the roughness layer started to show a slight increase in thickness and by 450°C, it has progressively increased to ~320 Å thick. As the film crystallized at 600°C the final thickness of the surface roughness layer was found to be ~900 Å. The total film thickness was also plotted over a range of annealing temperatures and shown in Figure 4.9. Since this film was pyrolyzed at 350°C, it shows only a slightly drop in the total thickness after a 600°C anneal.

Once again, the refractive index of the film over a range of annealing temperatures can be calculated by a single term oscillator equation (Eqn. 3.30), where the oscillator constants in Table 4.2 were obtained from modeling. Figure 4.10 shows the plot of refractive index (n) over a range of wavelengths as a function of annealing temperatures. As the film crystallized to either the intermediate phase or the perovskite phase, the refractive index of the film increased. These n values for films on sapphire, however, are low when compared to those for the film on the MgO substrate. This indicates that the film
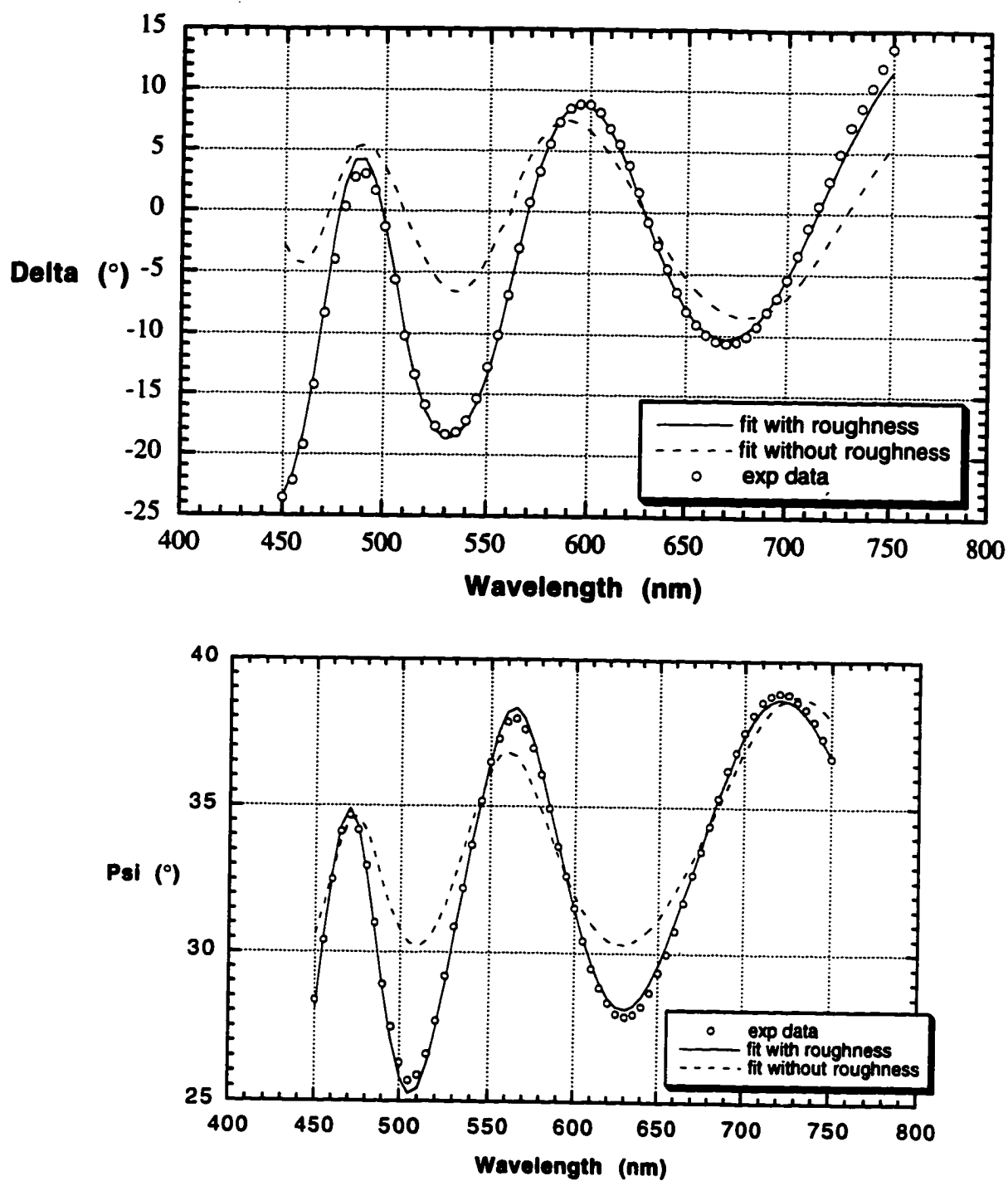
Figure 4.8. The fit of Δ and Ψ curves for a 600°C anneal for a PZT film on a sapphire substrate.

Table 4.2

Models of microstructure for a PZT film on a sapphire substrate.

Data were taken during *in-situ* annealing to 600°C on a spectroscopic ellipsometer from 25°C to 600°C

Temp (°C)	Dense Layer Thickness (Å)	Surface Roughness Thickness (Å)	% of air in Surface Roughness Layer	σ	A1	A2	A3 (nm)	A4
25	5398±28	33±9	50%	0.010	1	3.85±0.04	234.5±2.4	0
100	5379±35	26±12	50%	0.012	1	3.89±0.05	229.6±3.2	0
150	5418±38	24±13	50%	0.012	1	3.83±0.05	230.5±3.4	0
200	5414±39	21±13	50%	0.012	1	3.84±0.05	231.7±3.5	0
250	5429±36	22±13	50%	0.012	1	3.82±0.05	233.4±3.2	0
300	5438±36	25±13	50%	0.012	1	3.81±0.05	234.8±3.1	0
330	5397±28	33±10	50%	0.010	1	3.86±0.04	234.5±2.4	0
360	5432±28	39±9	50%	0.009	1	3.91±0.04	235.5±2.3	0
390	5407±31	70±11	50%	0.010	1	3.91±0.04	237.5±2.6	0
420	5327±26	148±7	50%	0.008	1	3.94±0.03	231.8±2.1	0
450	5143±23	317±4	50%	0.007	1	4.00±0.03	233.7±1.6	0
500	4660±27	741±8	32±0.2%	0.007	1	4.09±0.03	226.1±2.1	0
525	4482±20	918±10	29±0.2%	0.007	1	4.19±0.03	223.6±2.0	0
550	4396±19	932±9	29±0.2%	0.007	1	4.17±0.03	219.8±1.9	0
575	4345±11	920±25	29±0.2%	0.006	1	4.15±0.03	231±2.3	0
600	4302±28	933±13	32±0.2%	0.008	1	4.22±0.04	229.8±3.5	0

96
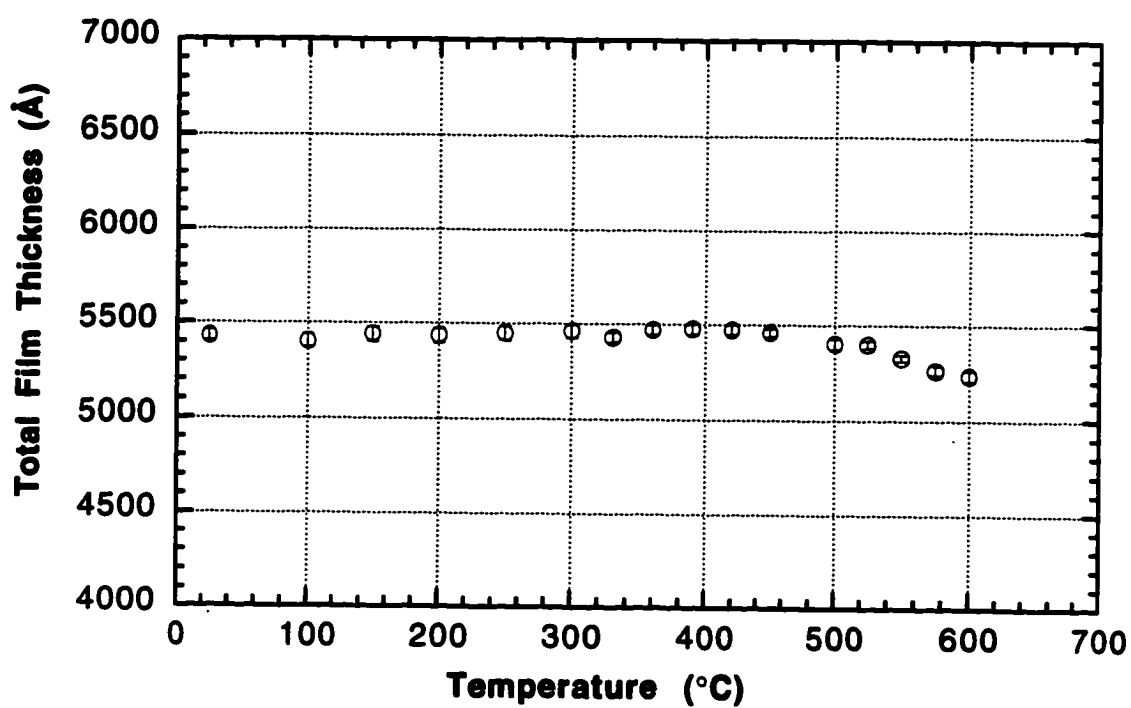
Figure 4.9. A plot of the total film thickness as a function of temperature for a film on a sapphire substrate, which had been pyrolyzed to 350°C.

PZT film on sapphire substrate
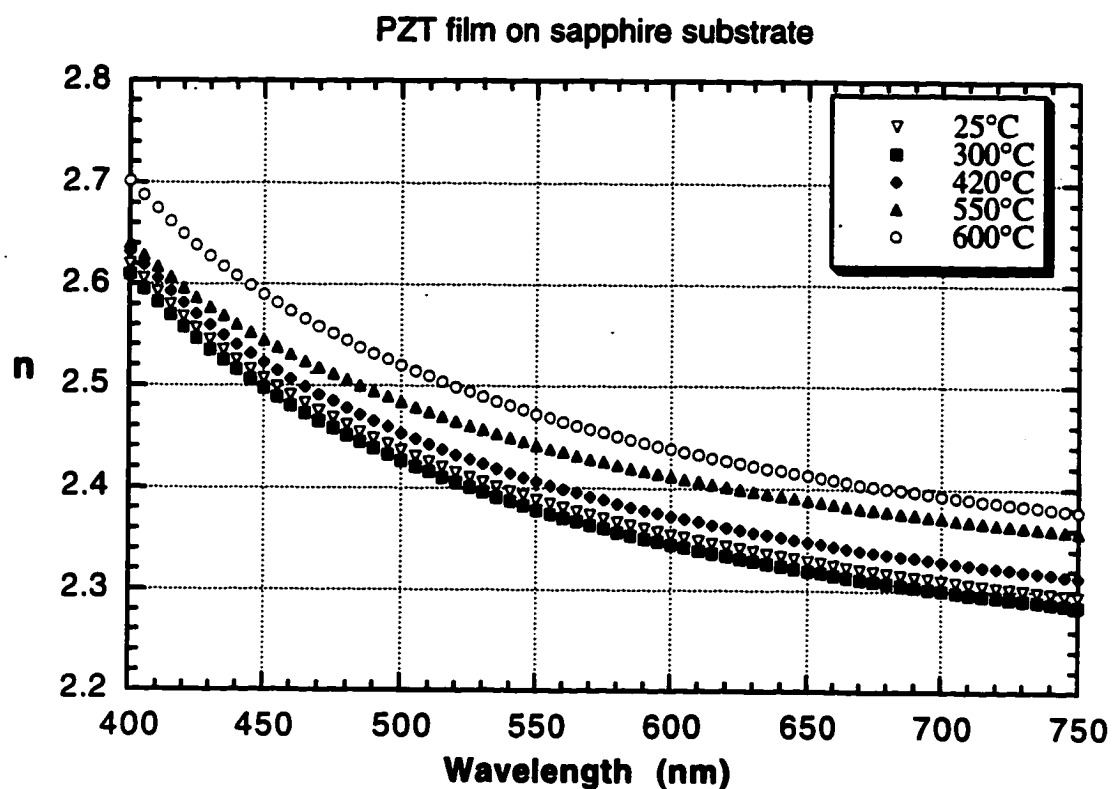
Figure 4.10. A plot of refractive index (n) change with wavelength as a function of annealing temperature for a PZT film on a sapphire substrate.

on sapphire after 600°C anneal may not be completely crystallized to a perovskite phase. As shown in Figure 4.11, the XRD pattern for this film after the 600°C *in-situ* anneal in the ellipsometer shows some intermediate phase peaks accompanying the perovskite peaks. Possible explanations for this observations are: 1) both sapphire and MgO substrates may absorb the radiated heat differently. More specifically, higher temperatures may be present on MgO; 2) error in the temperature measurement, associated with variations in the thermocouple position. Therefore, the readout temperature may be higher than the actual substrate temperature. Whatever the source, it is clear that the SE measurements are sensitive to the presence of the intermediate phase (possibly in conjunction with some porosity).

4.1.1.3. SE Data for PZT Films on Pt-coated Si Substrates

For films on Pt-coated Si substrates, spectroscopic ellipsometry data were taken as a function of temperature. An incidence angle of 70° was employed and no compensator was used since Pt-coated Si is not transparent. The sample was also *in-situ* annealed in the ellipsometer from room temperature to 600°C with the same intervals and conditions as for films on MgO and sapphire substrates.

The ellipsometric parameters, Δ and Ψ were modeled with a single term oscillator to get the best fit. Figure 4.12 shows the best fit models for room temperature, 300°C, 400°C, and 600°C anneals of PZT film on Pt-coated Si substrate. The geometry of other temperature models are shown in Table 4.3. The best fit of Δ and Ψ curves for a 600°C anneals are also shown in Figure
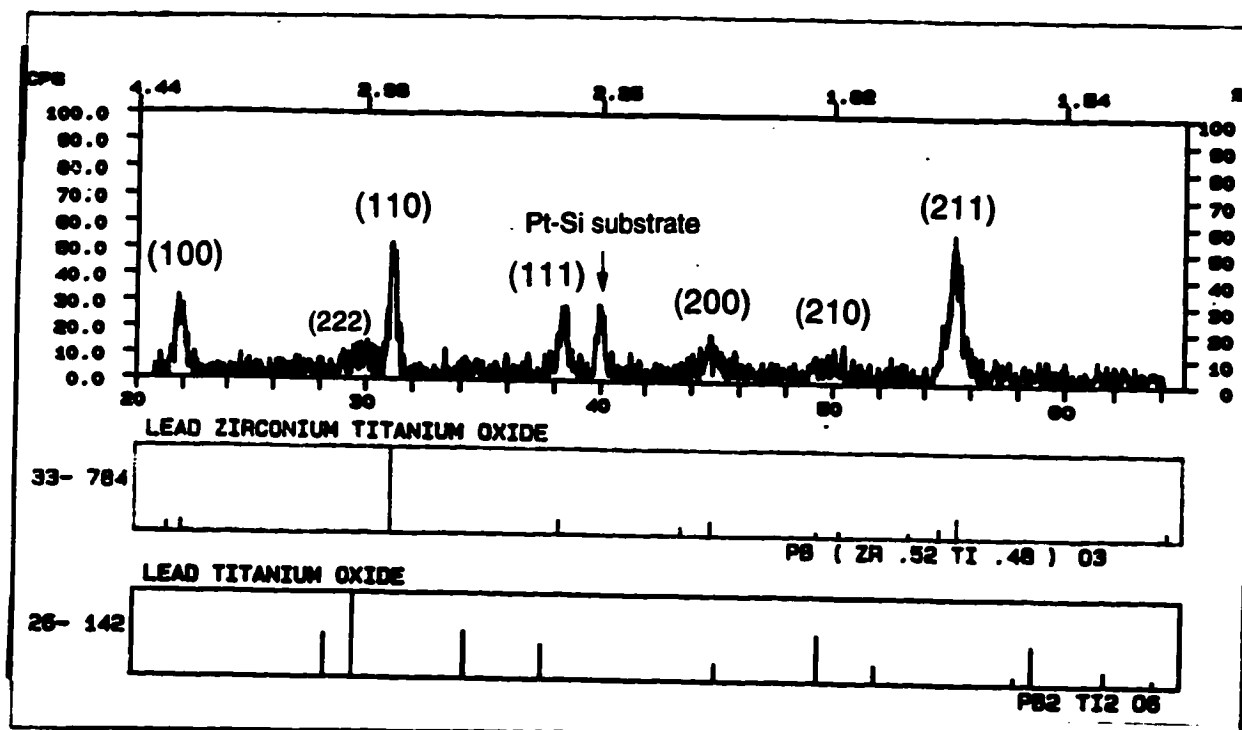
Figure 4.11. XRD pattern for a PZT film on a sapphire substrate after 600°C anneal in the ellipsometer.

air   Room temperature

film   t = 1664±19 Å

Pt-coated Si   σ = 0.08

air   300°C

film   t = 1373±10 Å

Pt-coated Si   σ = 0.12

                                       400°C
air

film   t = 1374±8 Å

Pt-coated Si   σ = 0.09

                                       600°C
air

film + air   t = 43±9Å   Vf = 50%

film   t = 1075±13 Å
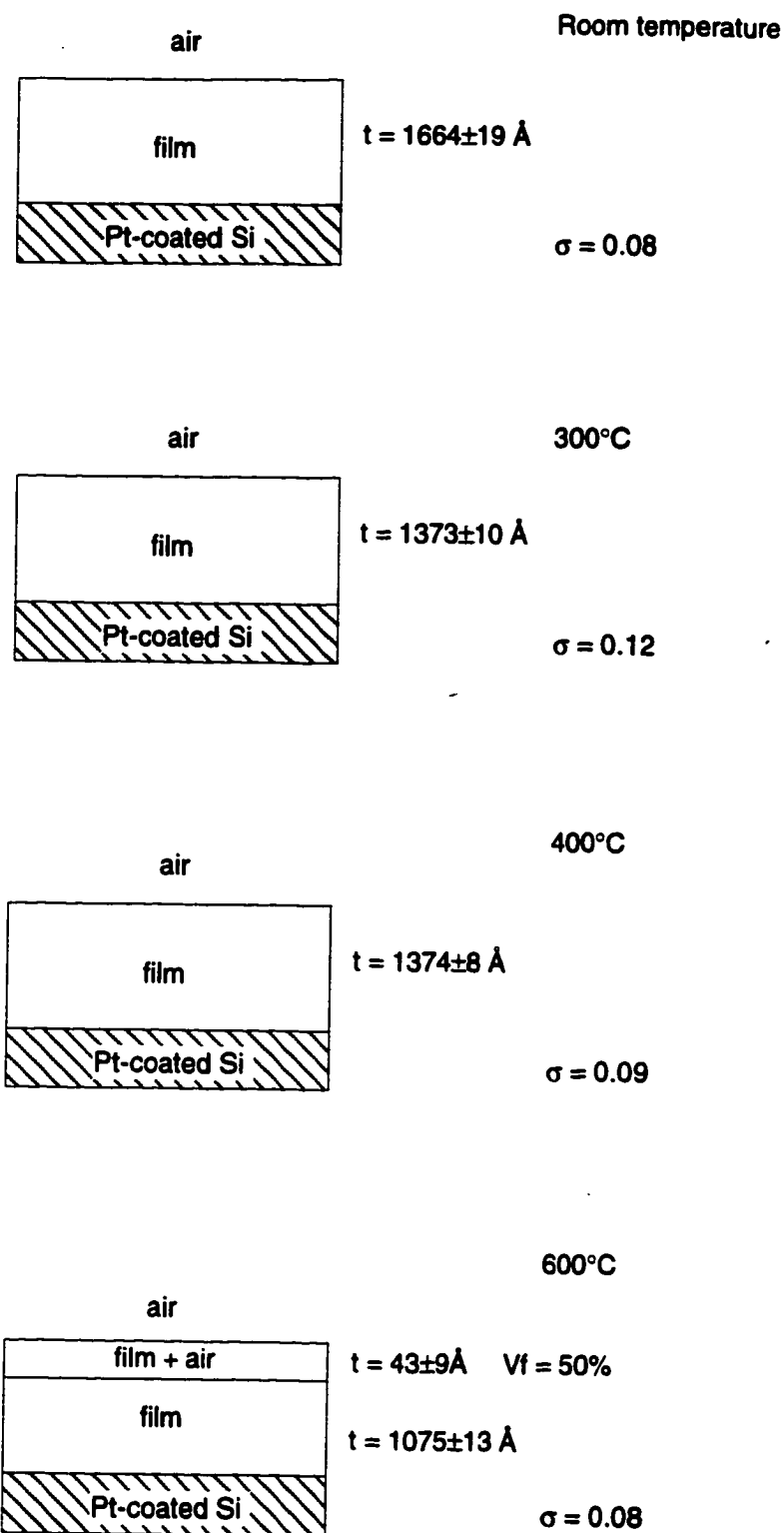
Pt-coated Si   σ = 0.08

Figure 4.12. Best fit models for a sol-gel PZT film on a Pt-coated Si substrate at various annealing temperatures. The film was pyrolyzed at 350°C.

Table 4.3

Models of microstructure for a PZT film on a Pt-coated Si substrate.
Data were taken during *in-situ* annealing to 600°C on a spectroscopic ellipsometer from 25°C to 600°C

Temp (°C)	Dense Layer Thickness (Å)	Surface Roughness Thickness (Å)	% of air in Surface Roughness Layer	σ	A1	A2	A3 (nm)	A4
25	1664±19	-	-	0.08	1	2.86±0.06	227.8±3.4	0
100	1643±25	-	-	0.09	1	2.78±0.09	235.2±4.2	0
200	1674±9	-	-	0.13	1	2.70±0.07	229.5±9.1	0
300	1373±10	-	-	0.12	1	4.03±0.16	221.7±12.2	0
350	1372±8	-	-	0.12	1	4.18±0.11	202.9±10.1	0
400	1374±8	-	-	0.09	1	4.00±0.13	225.9±9.1	0
450	1349±6	-	-	0.08	1	4.20±0.09	214.7±7.2	0
500	1262±7	-	-	0.06	1	4.65±0.08	220.3±5.2	0
550	1220±7	24±11	50%	0.05	1	4.68±0.07	229.1±4.2	0
600	1075±13	43±9	50%	0.06	1	5.26±0.17	222.0±7.1	0

4.13. It can be seen there that there is a good agreement between the experimental data and the fit. The σ value was as low as 0.08.

Table 4.3 shows the summary of models for the microstructure development of a PZT film on a Pt-coated Si substrate during *in-situ* annealing in the ellipsometer. The as-deposited film (which was pyrolyzed at 350°C) shows a layer approximately 1660 Å thick and no indication of changes for annealing temperatures below 300°C. Between 300°C and 450°C, the film thickness appears to show a slight drop to ~1350 Å which may be due to the removal of the residual organic materials. As the film crystallizes to one of the crystalline phases at 600°C the total film thickness continued to drop to 1100 Å. The changes of the total film thickness with the annealing temperature is shown in Figure 4.14.

As discussed by Kwok and Desu (1992a, 1992b), the pyrochlore-perovskite phase transformation involves a volume change of about 5.7%, due to the higher density of the perovskite phase. Thus, a decrease in the total thickness of the film at higher annealing temperatures is expected to accompany the pyrochlore-perovskite transformation. However, the total film thickness change for the film on Pt-coated Si substrate between the 500°C and 600°C anneals was found to be ~11.4% which might correspond to the densification of the amorphous material and the intermediate-perovskite phase transformation in the film.

It can be seen that at 550°C anneal, the film shows a very thin layer of surface roughness of about 24±11 Å thick at first, and the roughness layer increases to 43±9 Å thick at 600°C. The volume fraction of air in the surface roughness layer is fixed to 50% to avoid the correlation between the thickness
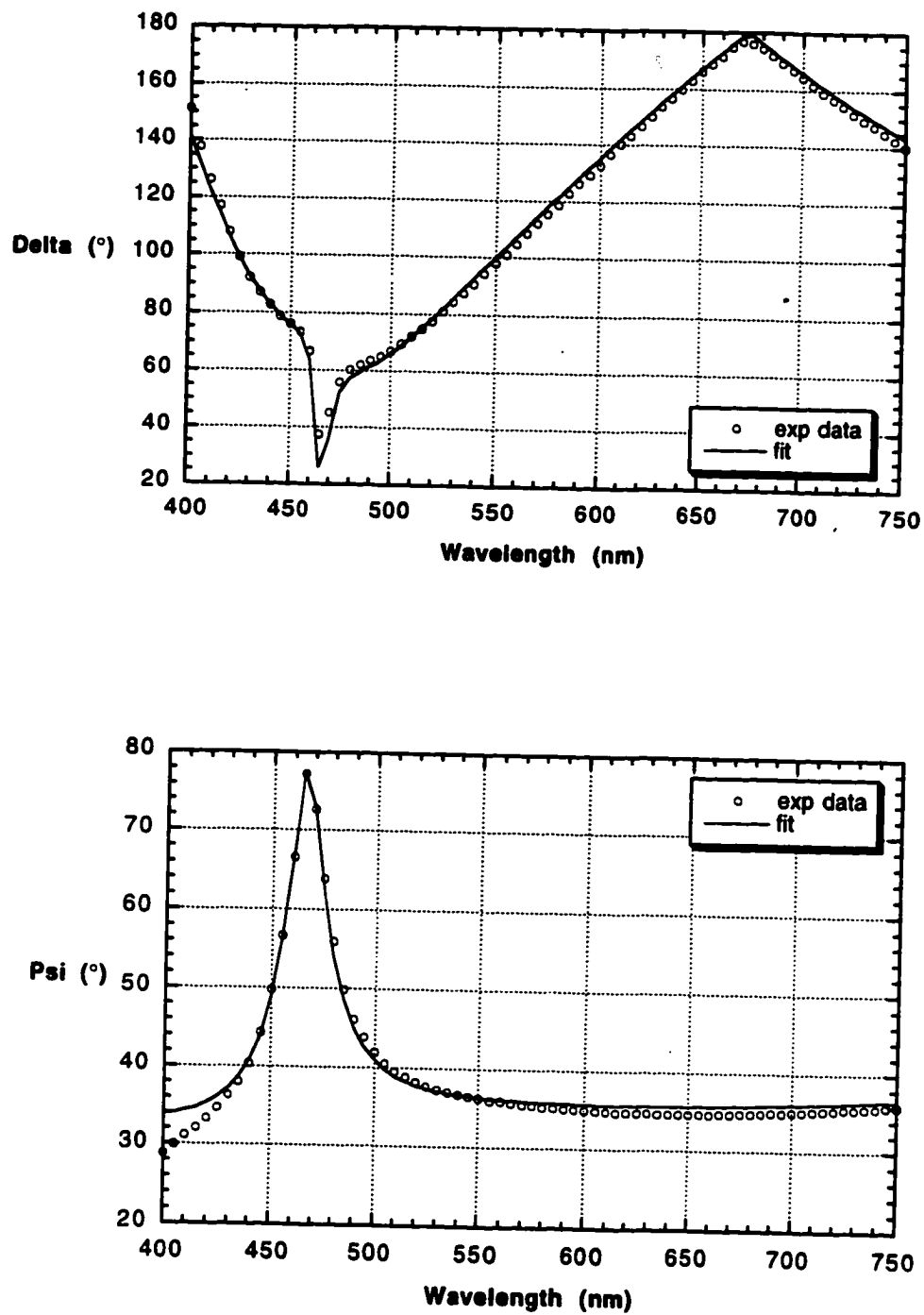
Figure 4.13. The fit of Δ and Ψ curves for a 600°C anneal for a PZT film on a Pt-coated Si substrate.
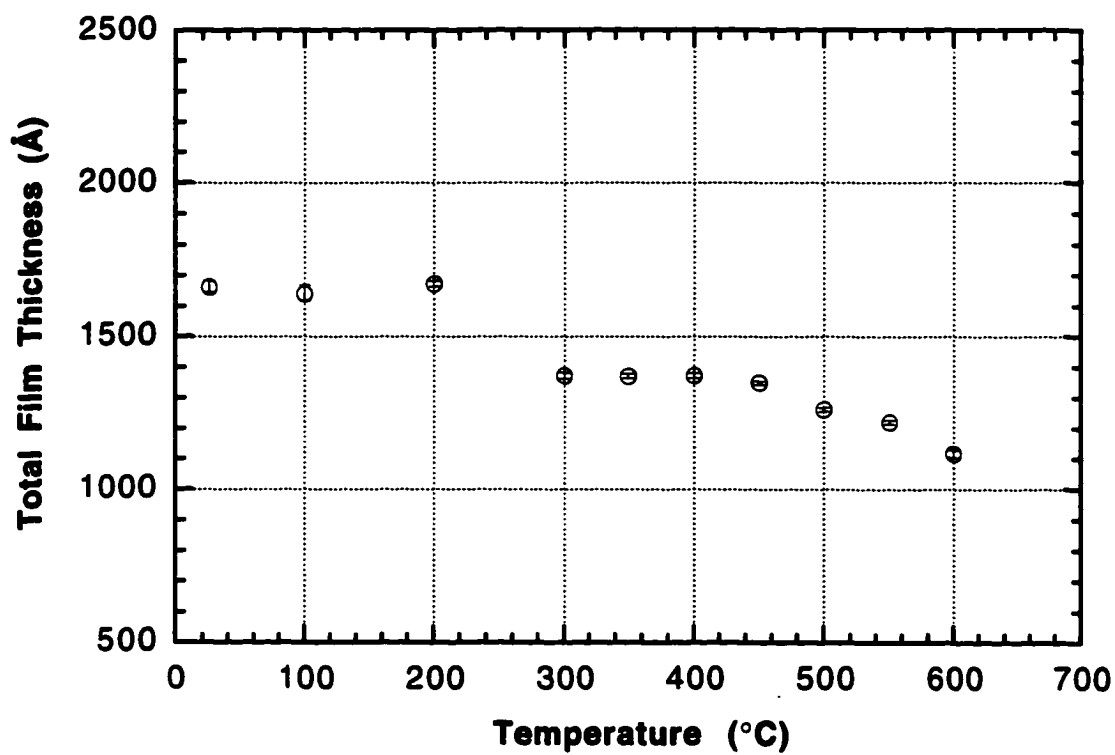
Figure 4.14. A plot of the total film thickness as a function of temperature for a PZT film on a Pt-coated Si substrate.

and the volume fraction of air in the roughness layer during modeling. This is a common occurrence when the roughness layer is extremely thin.

The refractive index of the film over a range of annealing temperatures was calculated, once again, by a single term oscillator equation (Eqn. 3.30), where the constants A_1, A_2, A_3, and A_4 in Table 4.3 were obtained from modeling. Figure 4.15 shows a plot of the refractive index of a PZT film on a Pt-coated Si substrate over a range of wavelengths as a function of temperature. At 600°C anneal, the film refractive index shows a marked increase which is believed to be due to the crystallization of perovskite phase.

In summary, the microstructure development of PZT films on various substrates can be tracked by SE measurements. The evolution of film crystallinity and the structural inhomogeneity during annealing of as-deposited films were also demonstrated. In all cases, the films show a homogeneous microstructure with a rather smooth surface at low annealing temperatures. Some thin layers of surface roughness, however, were found on PZT films on sapphire substrates and the films became progressively rougher with the annealing temperature. The total film thickness of sol-gel PZT films dropped with film crystallization, which was mainly due to the removal of the remaining organic materials after the pyrolysis step, in addition to the intermediate-perovskite phase transformation.

The refractive indices of the films show a significant increase as the films crystallized to the perovskite PZT phase. A comparison of the refractive index of these PZT films (after a 600° anneal) on various substrates and the values of lanthanum-doped PZT bulk ceramics (Thacher 1977) is shown in Figure 4.16. The plot shows that the n values of the film on MgO substrates are comparable
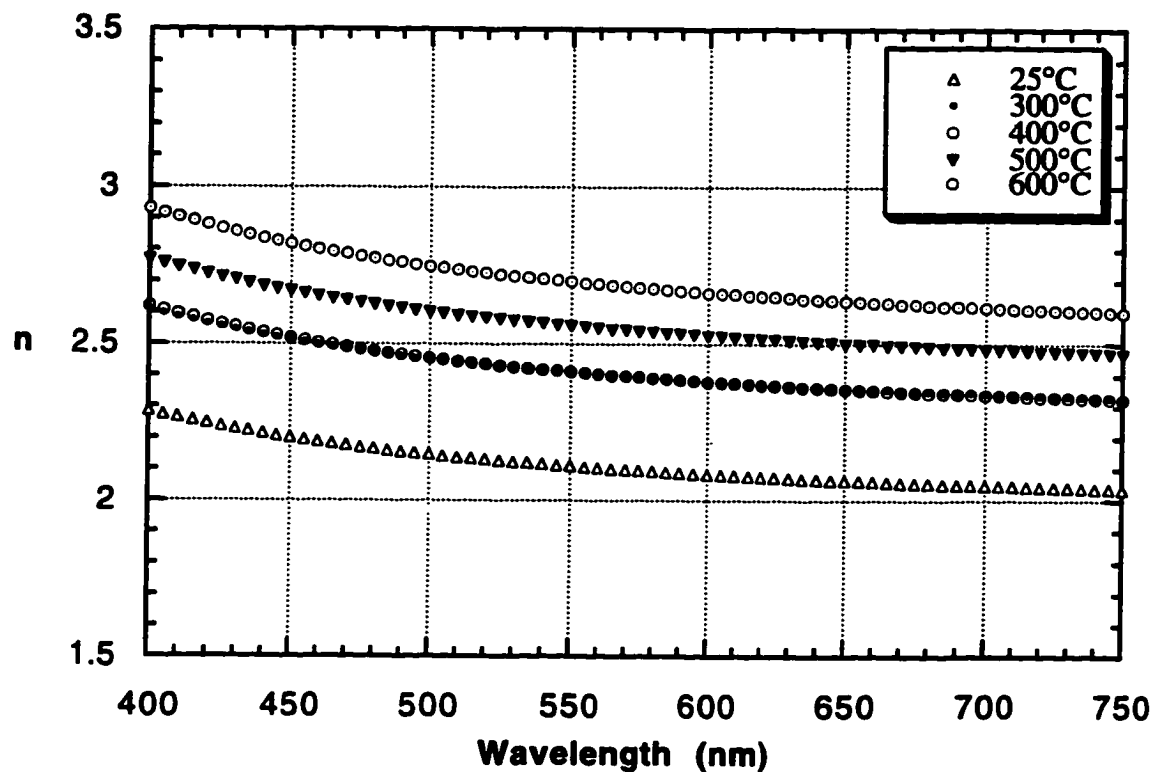
Figure 4.15. A plot of the refractive index (n) versus wavelength as a function of annealing temperature for a PZT films on a Pt-coated Si substrate.
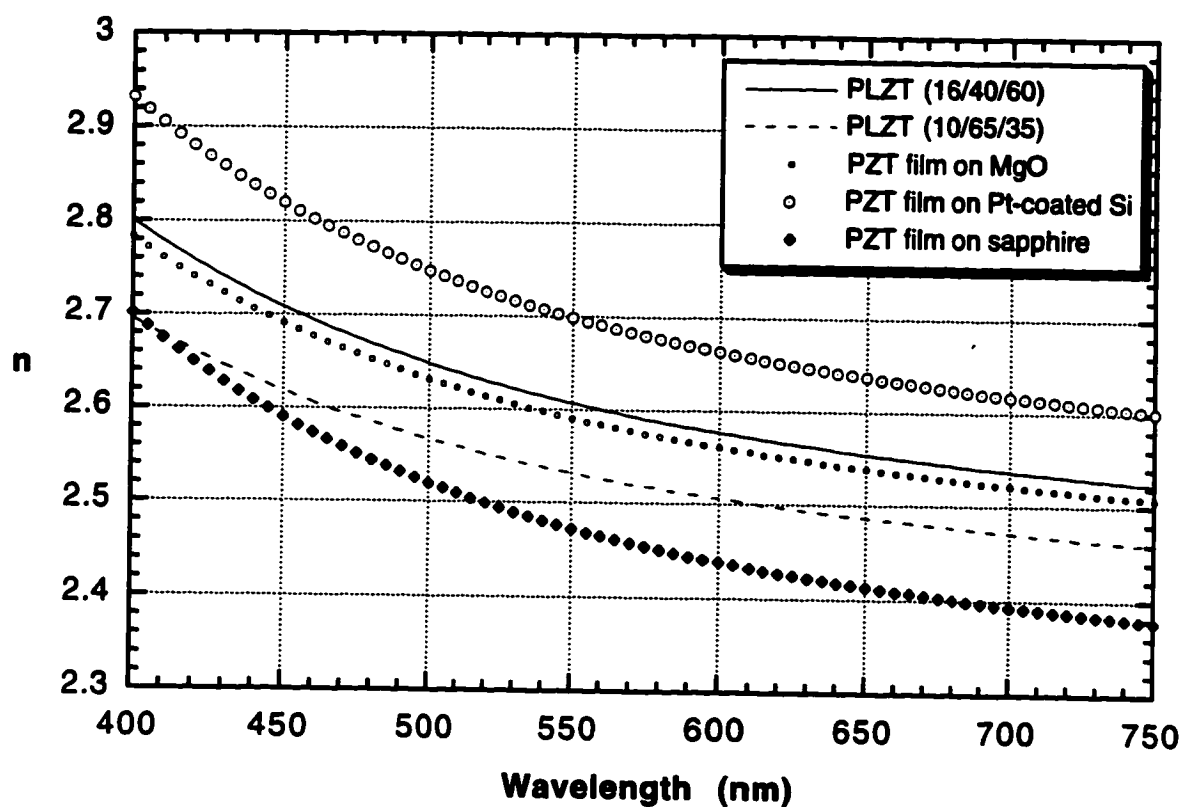
Figure 4.16. Comparison between the refractive index of PZT (52/48) films on different substrates (after a 600°C anneal) and lanthanum-doped PZT (10/65/35 and 16/40/60) bulk materials.

to those for dense bulk ceramics. In the case of the film on Pt-coated Si substrate, the n values shown are higher than those for the films on MgO. This might be due to the fact that the refractive index of the Pt-coated Si substrate itself changes over annealing temperatures, which possibly is associated with the Pt roughening and Ti migration at the substrate/film interface (Gibbons 1995). The refractive index for a PZT film on sapphire substrate (after a 600°C anneal) was found to be low compared to those of the reference data. Possible explanations for this finding were discussed previously.

It is demonstrated throughout this section that SE measurements permit the study of microstructure evolution in PZT thin films during annealing. SE is also sensitive to the surface roughness in thin films with a resolution of the Å level (McKinstry 1992). In addition, in terms of time resolution, for 50 mechanical cycles of the analyzer, it takes only 5 seconds for a single measurement of Δ and Ψ. Faster data can be taken if fewer cycles are averaged for each point, therefore, it should be possible to utilize SE as a probe to monitor the real-time crystallization kinetics and phase development of PZT films during annealing.

Recently, a few research groups have investigated the crystallization kinetics of PZT films during isothermal annealing via grazing-angle X-ray diffraction (Wilkinson et al. 1994 and Griswold et al. 1995), and TEM (Kwok and Desu 1992a). In those studies the volume fraction of the transformed perovskite phase was determined via the above methods. The Avrami's kinetic models were then applied to the phase transformation kinetics of the PZT films. In this study, attempts have been made to utilize SE to study the crystallization kinetics of both the intermediate and perovskite phases in PZT films using isothermal

RTA for various temperatures between 500°C and 700°C with a holding time of 0 to 75 seconds. The results on these films are discussed in the following section.

SE is sensitive to the phase changes in the material examined providing the optical properties of the two phases are different, Thus, given the optical reference data for both the intermediate and perovskite PZT phases, one could determine the volume fraction transformed of both phases in PZT films via SE measurements. Therefore, it is important to first determine the optical reference data for both the intermediate and the perovskite phases in order to be able to determine the volume fraction transformed of both phases via SE data modeling. Optical reference data for PZT films are reported in the next section.

4.1.2. Optical Reference Data for PZT Thin Films

In order to determine the volume fraction of both the intermediate fluorite-type or pyrochlore phase and the perovskite phase using SE, reference dielectric functions for these two phases are needed. First, SE data were obtained from 300 nm to 750 nm for PZT films which were rapid thermally annealed at 520°C and 700 °C. The processing condition of these films are detailed in Table 4.4.

After SE data were taken on the three samples in Table 4.4, the optical reference data from wavelengths between 400 and 750 nm were modeled using a Sellmeier oscillator (Eqn. 3.30), and the data between 300 and 400 nm were obtained from the direct inversion from the SE data. The best fit models for the three samples are shown in Figure 4.17. For the as-deposited film, there

Table 4.4

Annealing conditions for PZT films used to determine optical reference data

Substrate	Pyrolysis Temperature (°C)	RTA Temp. (°C)	RTA time (second)	XRD results
sapphire	300°C	-	-	amorphous pattern
sapphire	300°C	520	360 s	pure intermediate phase
sapphire	300°C	700	30 s	pure perovskite phase

air

film

sapphire

3451 ± 9

σ = 0.005

sap25

Pyrolysis temperature 300°C

A1 = 1
A2 = 3.03 ±0.02
A3 = 200.6 ±2.4 nm
A4 = 0

sap520

Pyrolysis temperature 300°C

air

film + air

film

film + air

sapphire

28 ± 6   Vol.% air 50%

1671 ± 40

499 ± 30   Vol% air 9 ± 0.4%

σ = 0.006

A1 = 1
A2 = 4.18 ±0.04
A3 = 209.7 ±3.6 nm
A4 = 0

sap700

Pyrolysis temperature 300°C

air

film + air

film

film + air

sapphire

27 ± 9   Vol.% air = 50%

1972 ± 29

478 ± 19   Vol% air = 9 ± 0.7%

σ = 0.010

A1 = 1
A2 = 4.88 ±0.04
A3 = 199.3 ±7.4 nm
A4 = 0

Figure 4.17. Best fit models for PZT films as deposited on sapphire substrate at room temperature, 520°C, and 700°C anneals.

appears to be only a bulk layer of film of a thickness about 3450 Å, whereas an interfacial layer and a surface roughness layer are required in modeling for films annealed at both 520°C and 700°C. Since the surface layer is so thin, the volume fraction of air in the roughness layer was fixed to 50% to avoid strong correlation between variables (Chindaudom 1991 and McKinstry 1992).

4.1.2.1. Optical Reference Data for Intermediate Phase

The calculated fit to SE data for the intermediate pyrochlore or fluorite-type PZT phase is illustrated in Figure 4.18. The σ value was found to be as low as 0.006 which implies a good fit between the calculated and experimental data. To date, reference dielectric function data of the intermediate pyrochlore or fluorite-type phase for PZT thin films has not yet been reported elsewhere. Figure 4.19 shows the reference dielectric function for the intermediate phase of a PZT thin film. This information is hoped to be useful in SE data modeling in order to identify the volume fraction transformed of the intermediate phase.

4.1.2.2. Optical Reference Data for Perovskite Phase

Thacher (1977) has reported the optical properties of bulk ceramic (Pb,La) $(Zr,Ti)O_3$ measured using the minimum deviation technique. The refractive index of PLZT for various compositions such as 10/65/35 (La/Zr/Ti ratio), 8/90/10, 16/40/60, etc. were determined. McKinstry et. al (1993) reported the refractive index of multi-ion-beam reactively sputtered PZT thin films with a Zr/Ti ratio of about 50/50 on (0001) sapphire substrates by SE measurements. As the refractive index of PLZT ceramics is largely controlled by

Figure 4.18. Δ and Ψ fits for the intermediate phase for a PZT film on a sapphire substrate following a 520°C anneal.
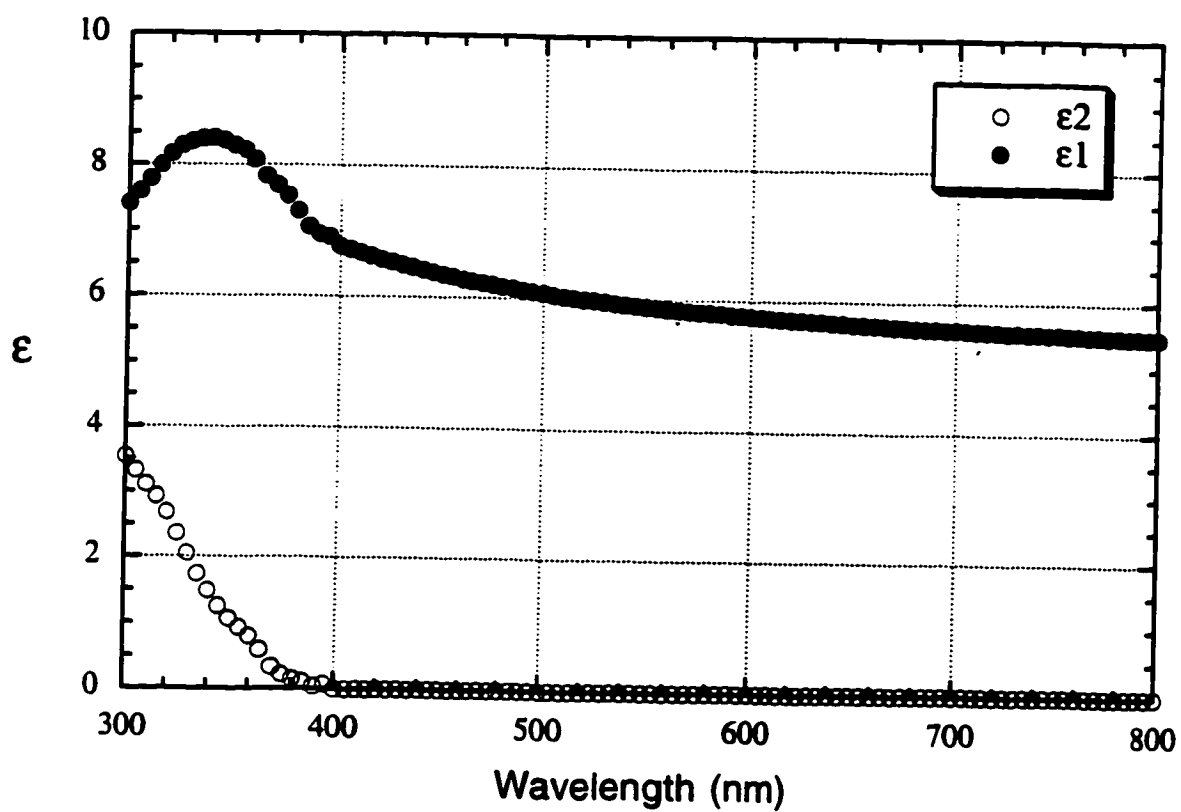
Figure 4.19. Optical reference dielectric functions, ε_1 and ε_2, for the intermediate phase ($\varepsilon = \varepsilon_1 + \varepsilon_2 i$).

the Zr/Ti ratio, they reported that films on (0001) sapphire in particular showed good agreement with the values which would be expected for a dense PZT 50/50 materials (McKinstry et. al 1993).

In this study, SE data were taken from a sol-gel PZT film (Zr/Ti ratio 52/48) on a (0001) sapphire substrate which was rapid thermal annealed at 700°C for 30 seconds to get the perovskite phase. The microstructure obtained for this film is shown in the sap700 model in Fig. 4.17. The Δ and Ψ fit to the SE data for the perovskite PZT phase is illustrated in Figure 4.20. Optical reference data for the dielectric functions for the perovskite PZT phase are plotted and shown in Figure 4.21. The refractive index for the perovskite PZT phase is also plotted and compared with the PLZT reference data (Thacher 1977) in Figure 4.22. It is worth noting that the refractive index of the perovskite PZT film prepared by sol-gel in this study shows an excellent agreement with the values which would be expected for a dense PZT 52/48 material.

In sum, SE measurements were used to determine optical reference data for thin film materials. SE has the advantage over other reflection techniques since it is possible to decouple the presence of surface roughness from the measured optical property data. The optical reference data for the intermediate pyrochlore or fluorite-type phase was investigated by SE in this study for the first time. For the optical reference dielectric functions for perovskite PZT thin films, the values found in this study show an excellent agreement with previous investigations by Thacher (1977) and McKinstry (1992). This optical reference data for PZT films are not only required for the SE data modeling in this study, but they will also be a valuable reference data set for PZT films for other potential applications, i.e. optical devices.

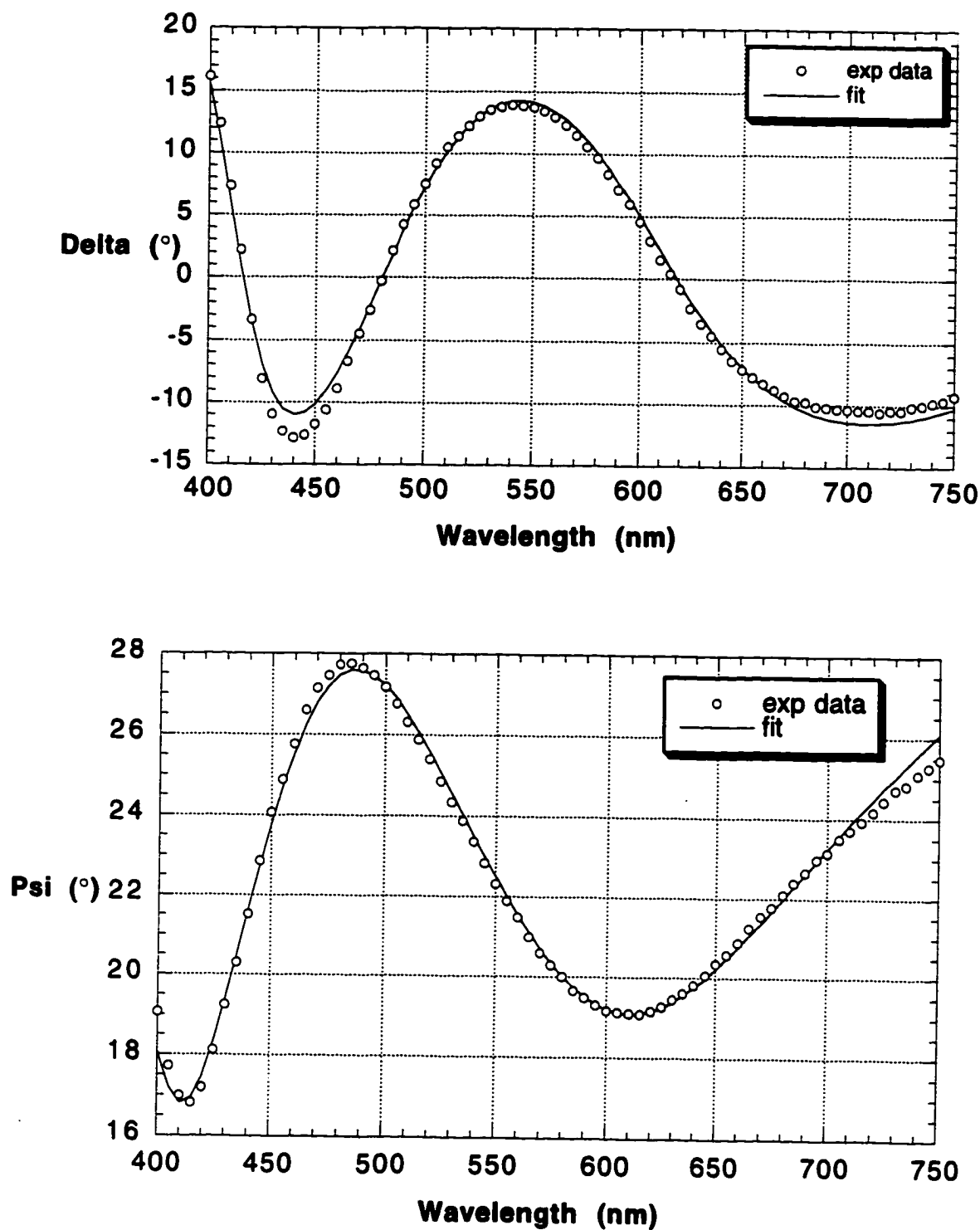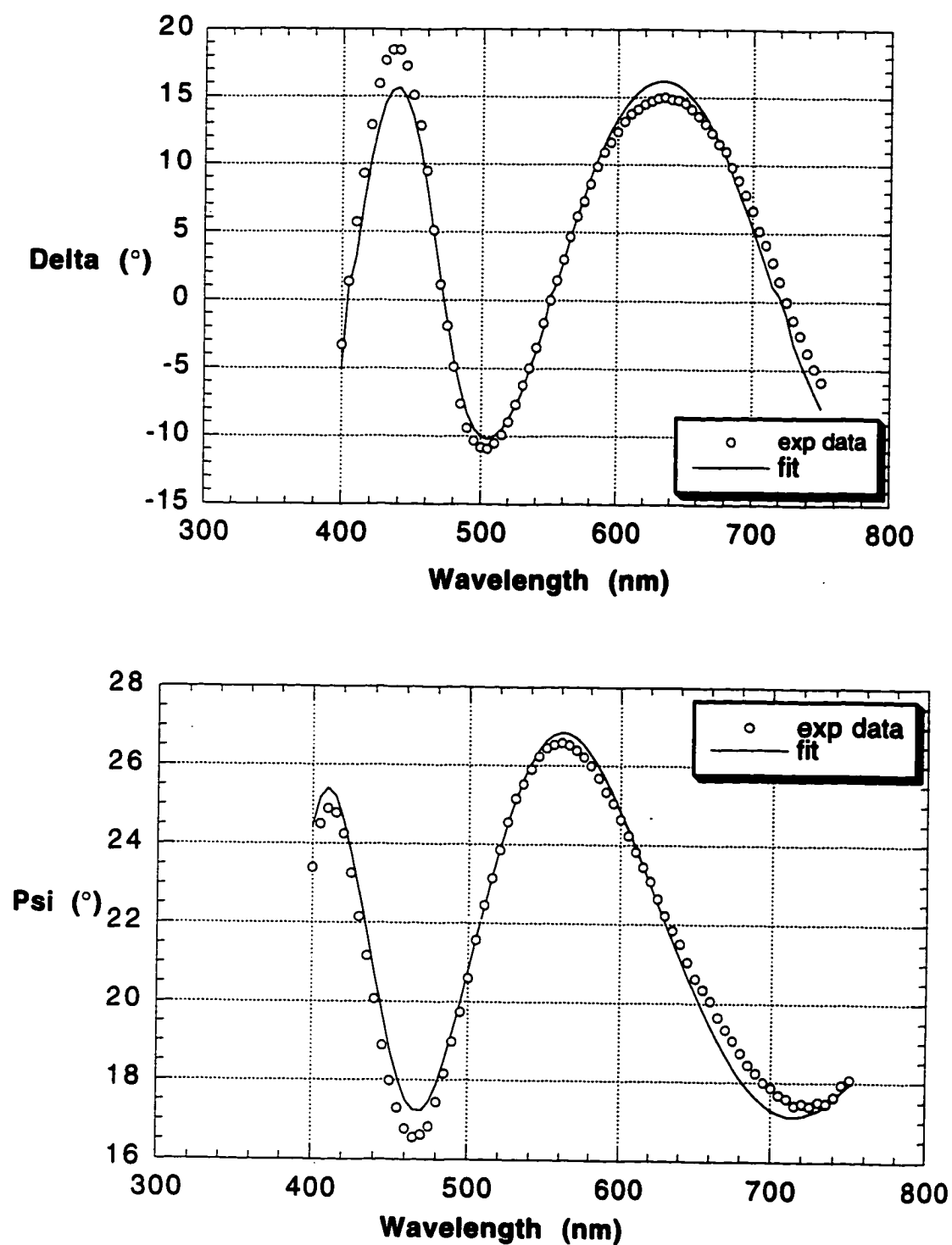Figure 4.20. Δ and Ψ fits for the perovskite phase for a PZT film on a sapphire substrate following a 700°C anneal.
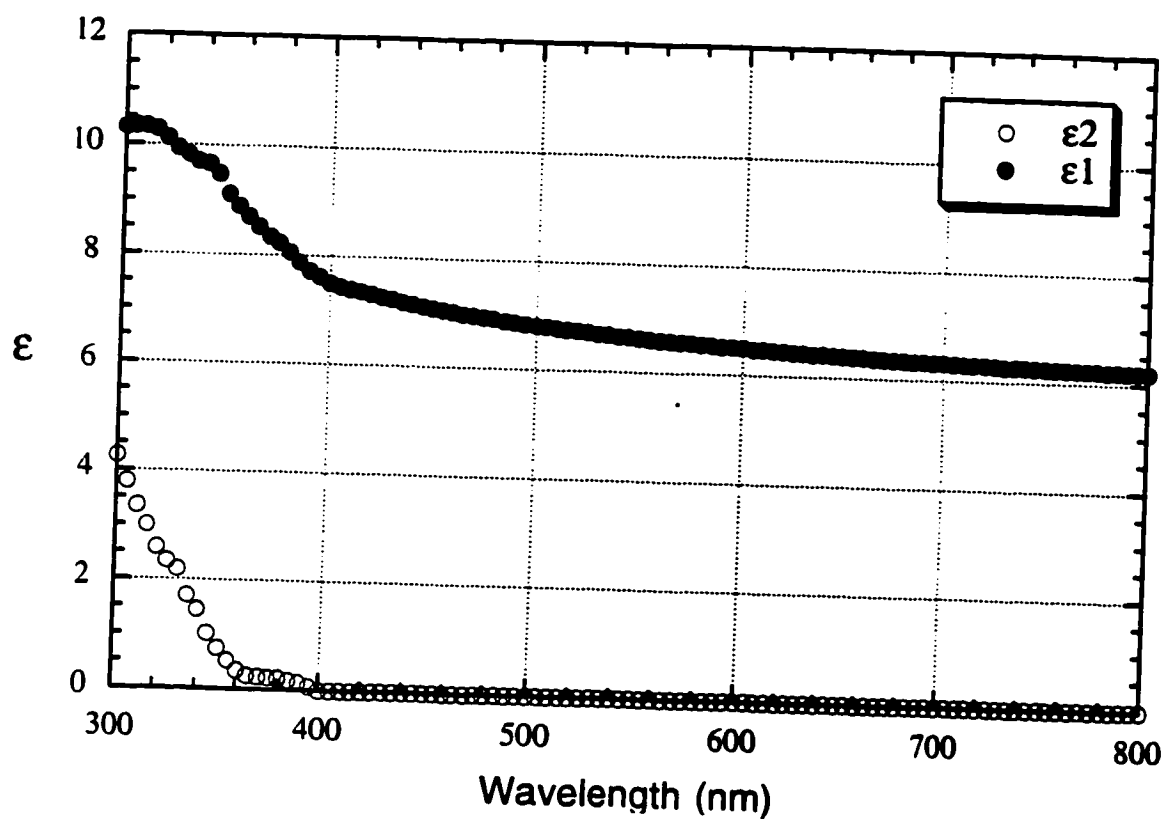
Figure 4.21. Optical reference dielectric functions, ε_1 and ε_2, for perovskite PZT $(\varepsilon = \varepsilon_1 + \varepsilon_2 i)$.
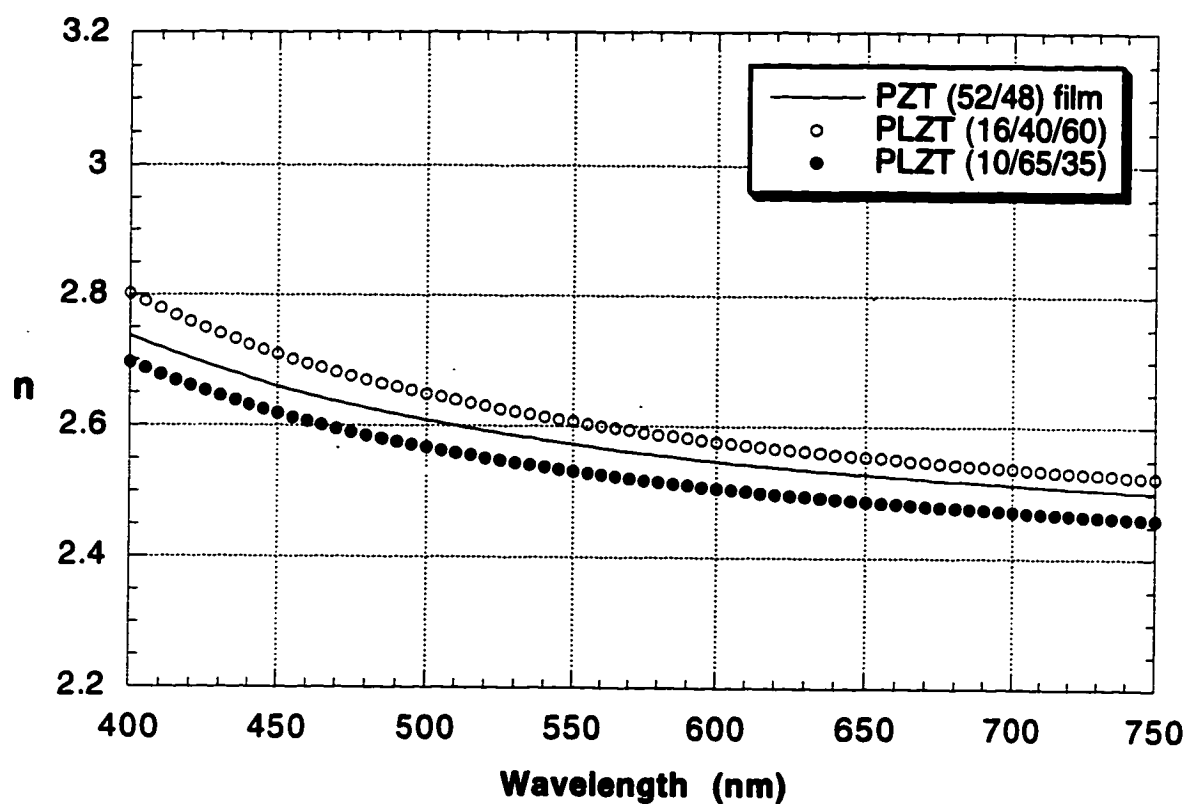
Figure 4.22. Comparison between the refractive index of a sol-gel PZT (52/48) film and PLZT (10/65/35 and 16/40/60) bulk materials.

As stated previously, the optical reference data for both the intermediate and perovskite phases for PZT thin films are needed for SE data modeling in order to determine the volume fraction transformed of both phases. Attempts were made to employ SE in the investigations of isothermally rapid thermal annealed films at various annealing temperatures and holding times. However, the results have shown that the time resolution is not good enough to apply Avrami's model for isothermal crystallization kinetics. This issue will be detailed in the next section.

4.1.3. Kinetic Studies via *In-situ* Annealing in SE

Attempts have been made to employ SE as a tool for studying the isothermal crystallization kinetics of both the intermediate and perovskite phases in PZT films which were rapid thermally annealed at various temperatures from 500 to 700°C for 0 to 75 seconds. However, ellipsometric data do not show significant discrepancies in the parameters, Δ and Ψ, for films which were isothermally RTAd at various times. An example of the Δ and Ψ changes for the film which was RTAd at 600°C for 0 to 45 seconds is shown in Figure 4.23. It is likely that the crystallization was sufficiently fast that the time intervals employed here did not sufficiently probe intermediate points in the crystallization process. Therefore, it is not possible to derive a model providing a good approximation on the phase development of the RTA films from this data.

Another approach to follow the crystallization kinetics of both the intermediate phase and perovskite phase in PZT films by SE has been made by *in-situ* annealing PZT films on the SE with a constant ramp rate of 5°C/minute.
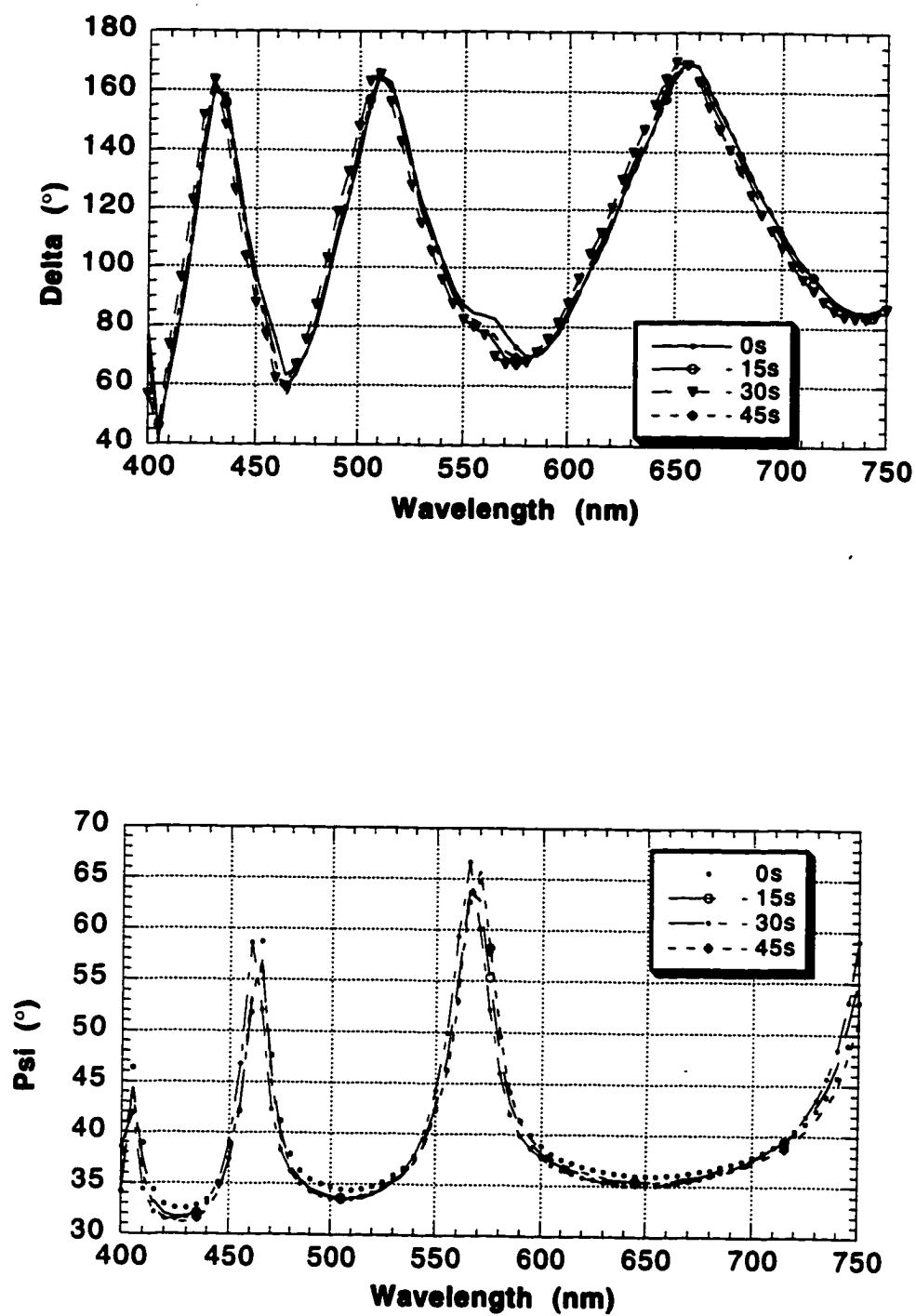
Figure 4.23. Δ and Ψ curves for a PZT film on a Pt-coated Si substrate after RTA processing at 600°C for 0, 15, 30, and 45 seconds. The spectra show no major changes in Δ and Ψ.

During the constant ramp up from room temperature to 500 or 700°C, ellipsometric measurements were taken at a fixed wavelength of 500 nm.

Figure 4.24 illustrates the plots of the ellipsometric parameters, Δ and Ψ, for a PZT film on an MgO over a range of annealing temperatures. This film was pyrolyzed at 300°C. Δ shows a continuous decrease as temperatures increased from room temperature to 430°C and between 430°C to 500°C, Δ shows a significant increase of 7° (Figure 4.24a). There was no major change in Ψ until temperatures reached 400°C, where Ψ started to drop around 0.3° (Fig. 4.24b). These changes in Δ and Ψ are possibly due to (1) crystallization of the amorphous phase; (2) changes in the total film thickness; and (3) development of surface roughness. To examine the relative importance of these factors, SE depth profiles before and after annealing were determined.

The refractive index of this film before heat-treatment (mg25) and after heat-treatment at 500°C (mg500) were determined and are presented in Figure 4.25. The refractive index which was calculated from the best fits models shows an increase with temperatures, i.e., from a value ~2.3 at room temperature to 2.5 (at 500 nm) after 500°C anneals, which suggested that film has crystallized, possibly to the intermediate fluorite-type or pyrochlore phase, since the annealing temperature fell into the range of the intermediate phase formation.

In addition, over this range of annealing temperatures, the total film thickness decreased slightly from ~6000 Å to ~ 5300Å as show in the best fit models in Figure 4.26. The refractive index calculated from these models shown in Fig. 4.25 has already taken the changes of film thickness and the surface roughness into account. The XRD pattern for this film on MgO shown in

(a)

(b)
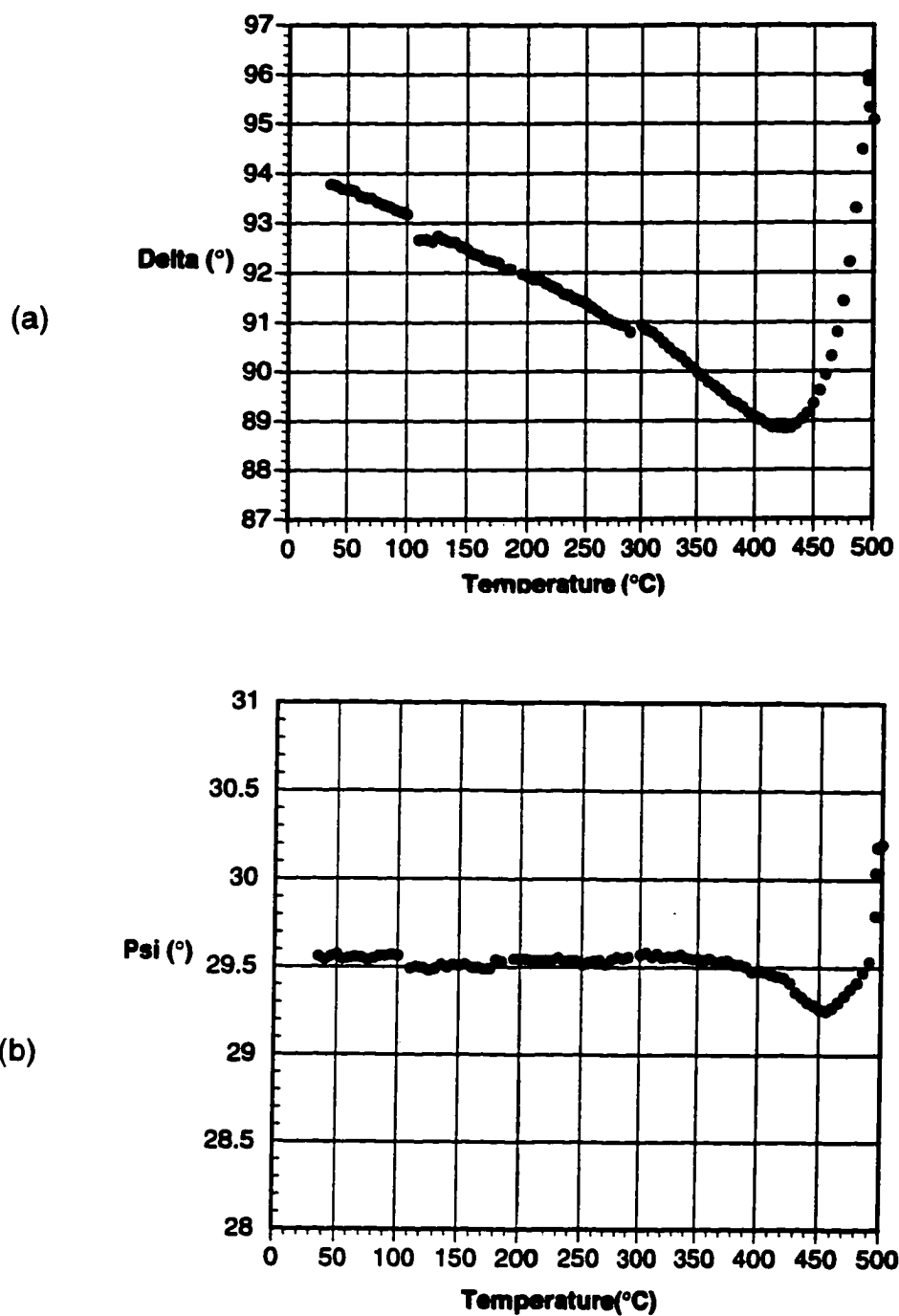
Figure 4.24. A plot of ellipsometric parameters changes over a range of annealing temperatures for a PZT film on an MgO substrate (a) Δ vs. temperature, and (b) Ψ vs. temperature.
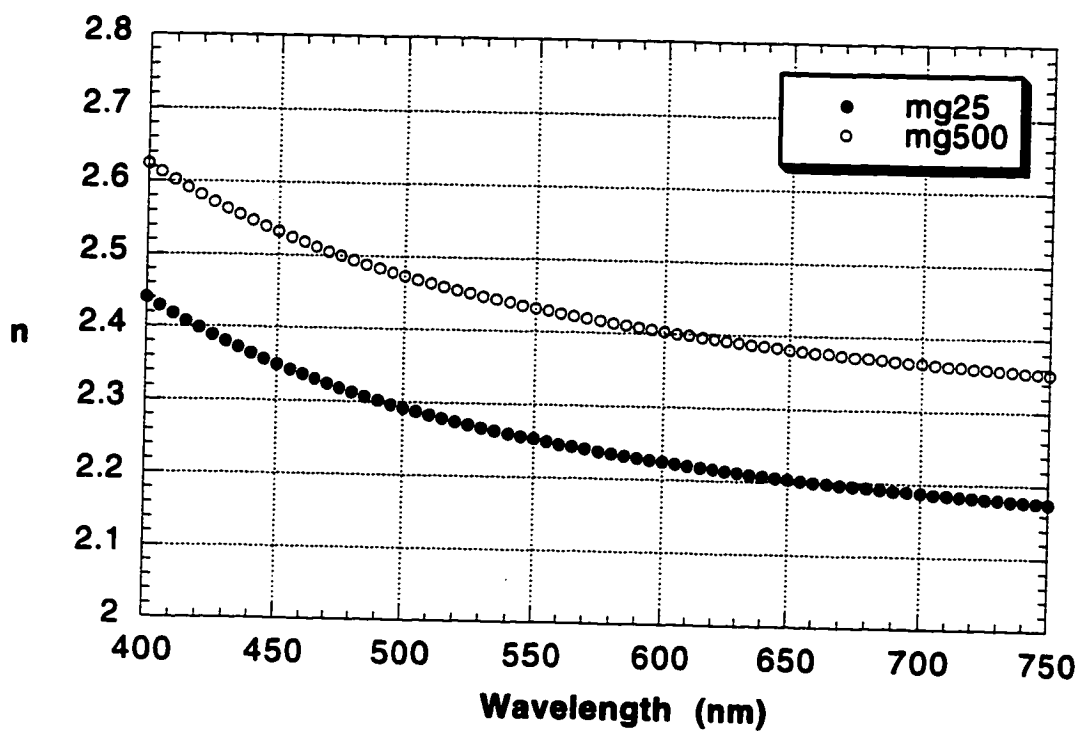
Figure 4.25. A plot of n over wavelength for a PZT film on an MgO substrate before heat treatment (mg25) and after 500°C anneal (mg500).

air

film

t = 6076±39 Å

(100) MgO

mg25

A1 = 1
A2 = 3.33±0.04
A3 = 224±2 nm
A4 = 0

σ = 0.009

mg500

film + air

film

MgO + film

(100) MgO

t = 273±19 Å   Vf = 5±1%

t = 4756±198 Å

t = 282±28 Å   Vf = 50%

A1 = 1
A2 = 4.33±0.15
A3 = 231±2 nm
A4 = 0

σ = 0.007

Figure 4.26. Best-fit models for a PZT film on MgO (a) at room temperature before heat treatment, and (b) after 500°C anneal with a 5°C/min heating rate.

Figure 4.27 also confirmed that the film has crystallized to the intermediate phase as expected.

To insure that the changes observed during the *in-situ* measurement were due to the film, a plain MgO substrate was heated on the SE at the same heating rate of 5°C/minute from room temperature to 500°C. The ellipsometric parameters, Δ and Ψ, as a function of temperature are shown in Figure 4.28. There was only small changes in Δ and Ψ for the MgO substrate over this temperature range. Therefore, it is clear that the observed changes in Δ and Ψ previously shown in Fig. 4.24 are associated with the PZT film itself, not the substrate.

In order to avoid the total thickness changes over the range of annealing temperatures, a PZT film on a sapphire substrate was rapid thermally annealed at 400°C for 10 minutes to allow more time for organic removal prior to the SE measurements. The film was once again annealed in the ellipsometer from room temperature to 500°C with a constant heating rate of 5°C/minute. The ellipsometric spectra are shown in Figure 4.29. From the plot, Δ stays constant from room temperature to around 320°C. From that temperature, Δ starts to increase and it reached its maximum of a 2° increase at 430°C. Between 430 and 470°C, Δ drops about 6.5°, it rises again above 480°C. Ψ shows a continuous decrease as annealing temperatures increase to 430°C, and it starts to increase between 430 and 470°C, and tends to decrease again as temperatures approach 500°C.

The best fit models for the film on sapphire before and after the heat treatment are illustrated in Figure 4.30. The total thickness of the film showed smaller change over the heat-treatment since the film was RTAd at 400°C for
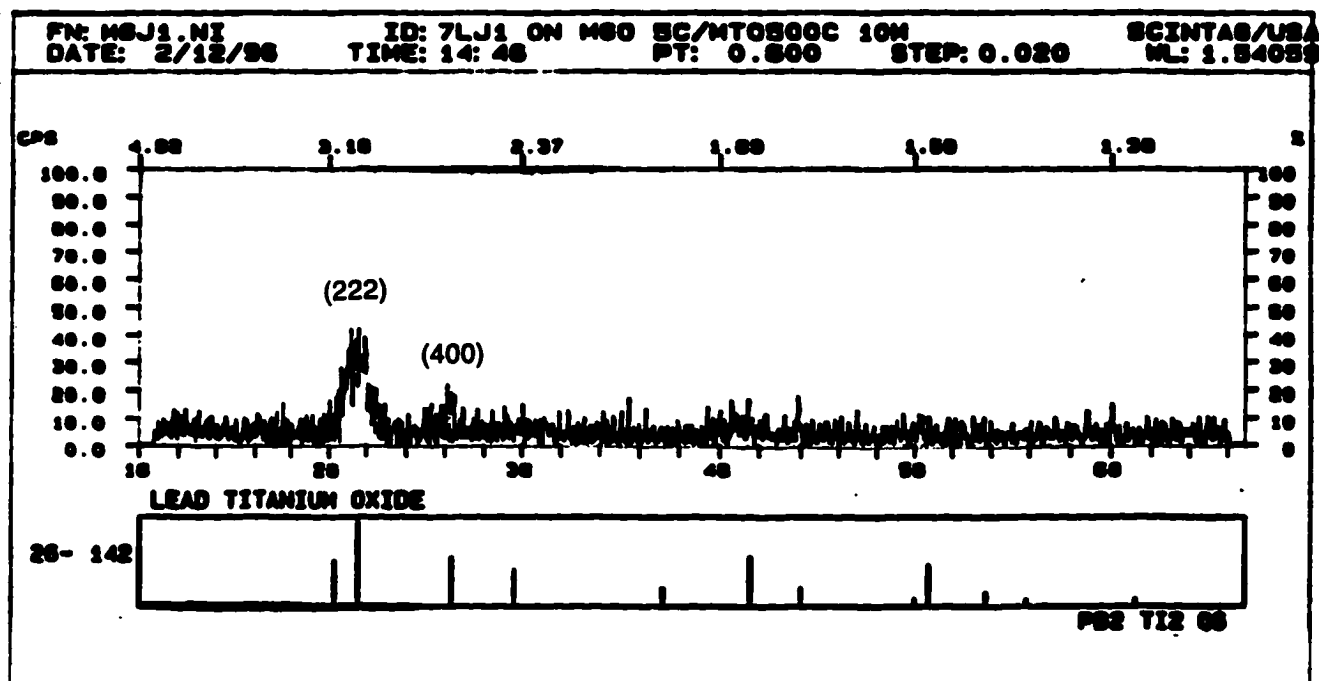
Figure 4.27. XRD pattern for a PZT film on an MgO substrate after 500°C anneal with a 5°C/min heating rate in the ellipsometer. The JCPDS pattern shown is for the pyrochlore phase.
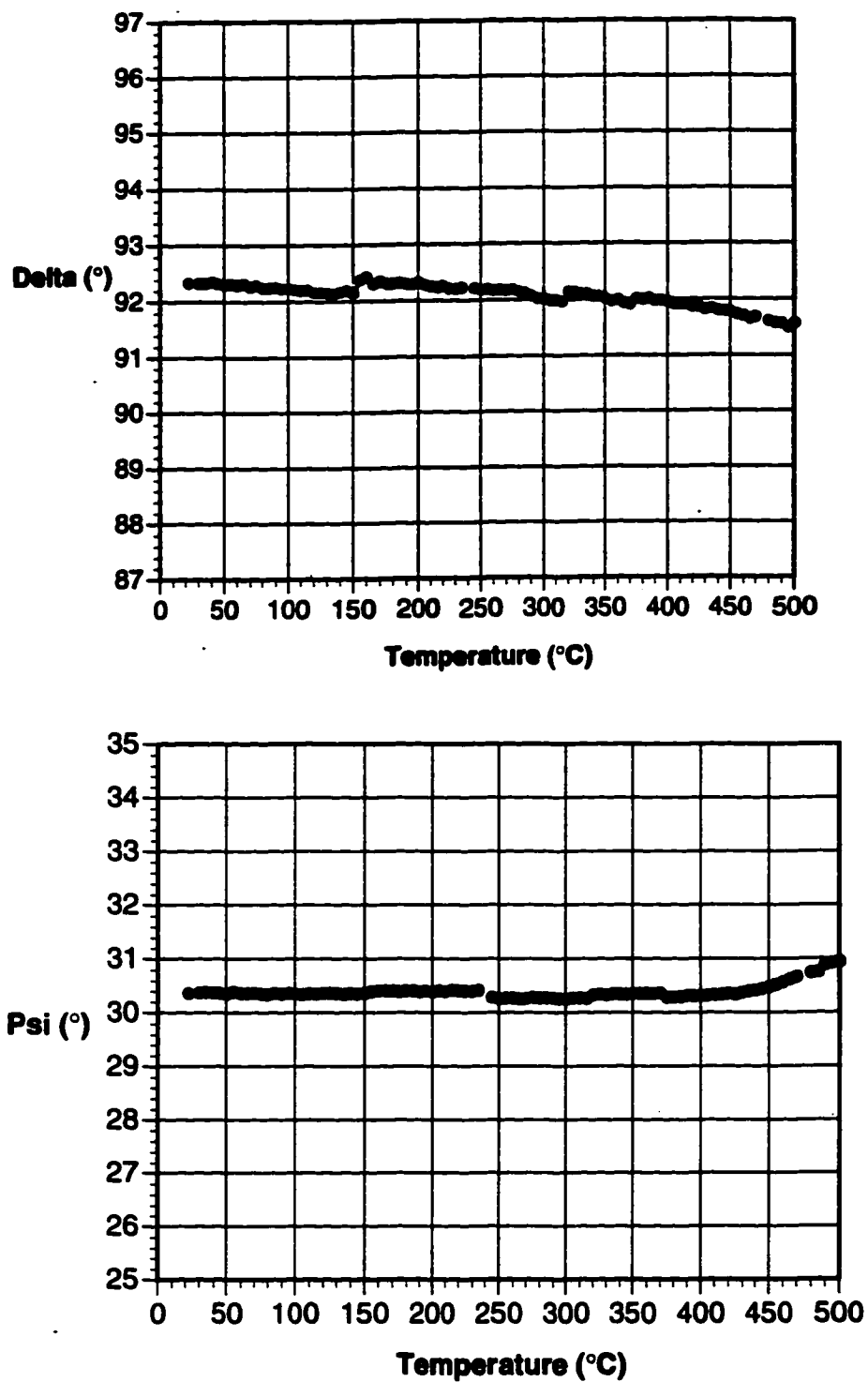
Figure 4.28. A plot of the ellipsometric parameters over a range of annealing temperatures for a plain MgO substrate (a) Δ vs. temperature, and (b) Ψ vs. temperature.
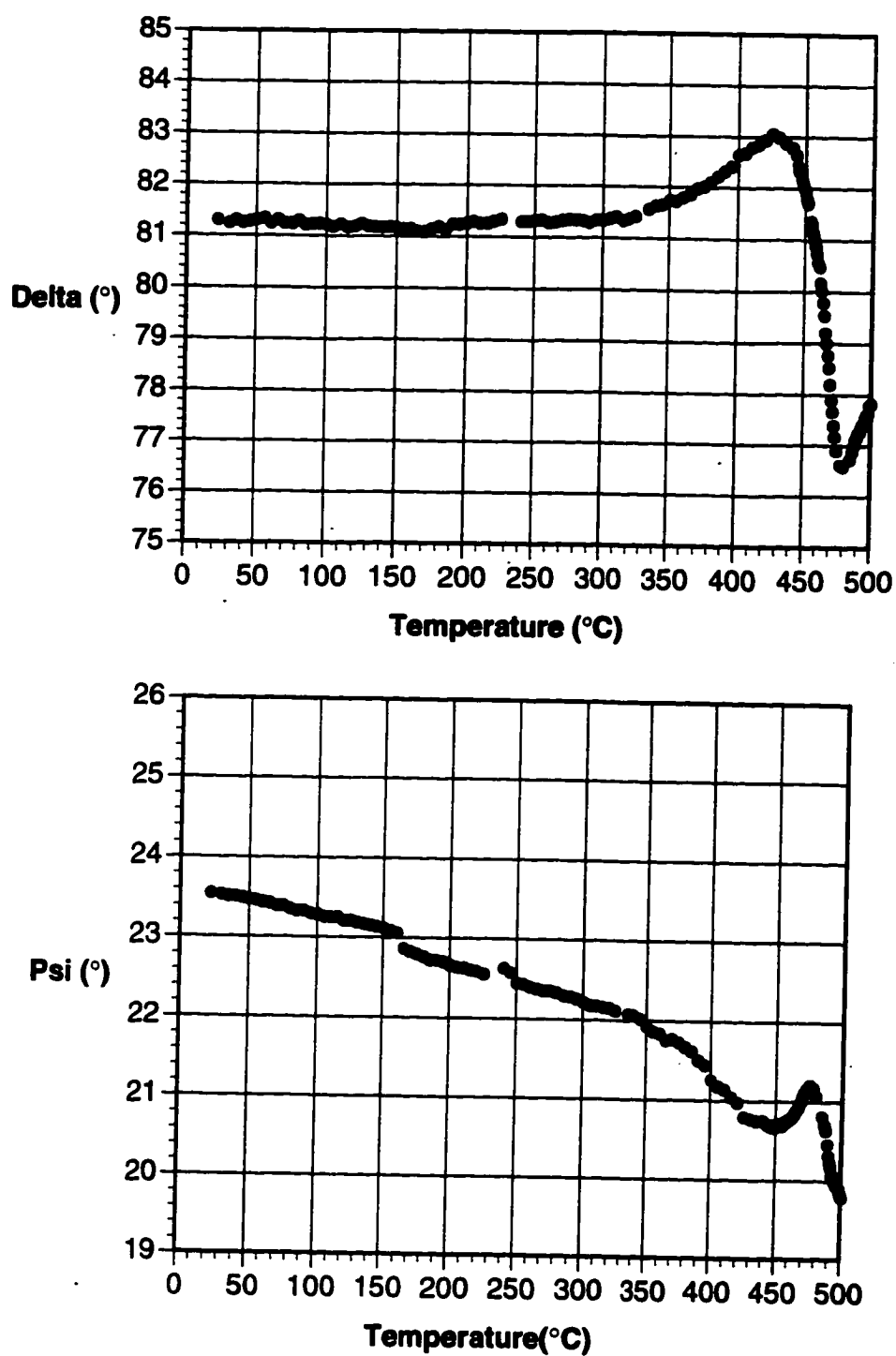
Figure 4.29. A plot of the ellipsometric parameters over a range of annealing temperatures for a PZT film on a sapphire substrate (a) Δ vs. temperature, and (b) Ψ vs. temperature.

sap25

air

film   t = 6362±20

(0001) sapphire

A1 = 1
A2 = 3.59±0.03
A3 = 202.4±3.7 nm
A4 = 4.22±0.40

σ = 0.005

(a)

sap500

air

film   t = 5900±19

(0001) sapphire

A1 = 1
A2 = 4.17±0.03
A3 = 214.1±2.1 nm
A4 = 1.35±0.27

σ = 0.006

Figure 4.30. Best-fit models for a PZT film on sapphire (a) after RTA 400°C for 10 mins prior to heat treatment, and (b) after 500°C anneal with a 5°C/min heating rate.

10 minutes. The film also shows no measurable surface roughness after the 500°C anneal. The refractive index (n) of this film which was calculated from the modeling parameters are plotted over wavelength as a function of temperatures in Figure 4.31. Similarly to the film on MgO, the refractive index of this film increased after heat treatment, e.g. from 2.3 (at room temperature) to 2.5 (after heat treatment at 500°C) at a wavelength 500 nm.

As previously discussed in this chapter, increase in the refractive index of PZT films with annealing temperature are most likely associated with the crystallization of the crystalline phases, i.e. an intermediate phase or perovskite PZT phase. Based on the XRD patterns for a film on MgO at a heating rate of 5°C/minute, an intermediate fluorite-type or pyrochlore-like peak appeared first in the temperature range 425-429°C. It is important to note that it is in this same temperature range that the ellipsometric parameters, Δ and Ψ, show some noticeable changes for films on both MgO and sapphire substrates. Therefore, it can be assumed from the SE study that an intermediate phase started to form at the point where Δ and Ψ show an abrupt change, which is at ~430°C for films on both MgO and sapphire substrates. To determine this type of information for the perovskite phase, further investigations for higher annealing temperatures such as 700°C are needed to fully crystallize perovskite PZT.

Therefore, another set of the *in-situ* annealing measurement in the ellipsometer was also obtained for a PZT film on a sapphire substrate. A constant ramp rate of 5°C/min was used to anneal a film from room temperature to 700°C in the conductive block heater *in-situ* in the ellipsometer. To minimize thickness changes during annealing, this film was also RTAd at 400°C for 10 mins prior to the SE measurement. Figure 4.32 shows the plots of Δ and Ψ as a

Figure 4.31. A plot of n over wavelengths for a PZT film on sapphire substrate before heat treatment (sap25) and after 500°C anneal (sap500).
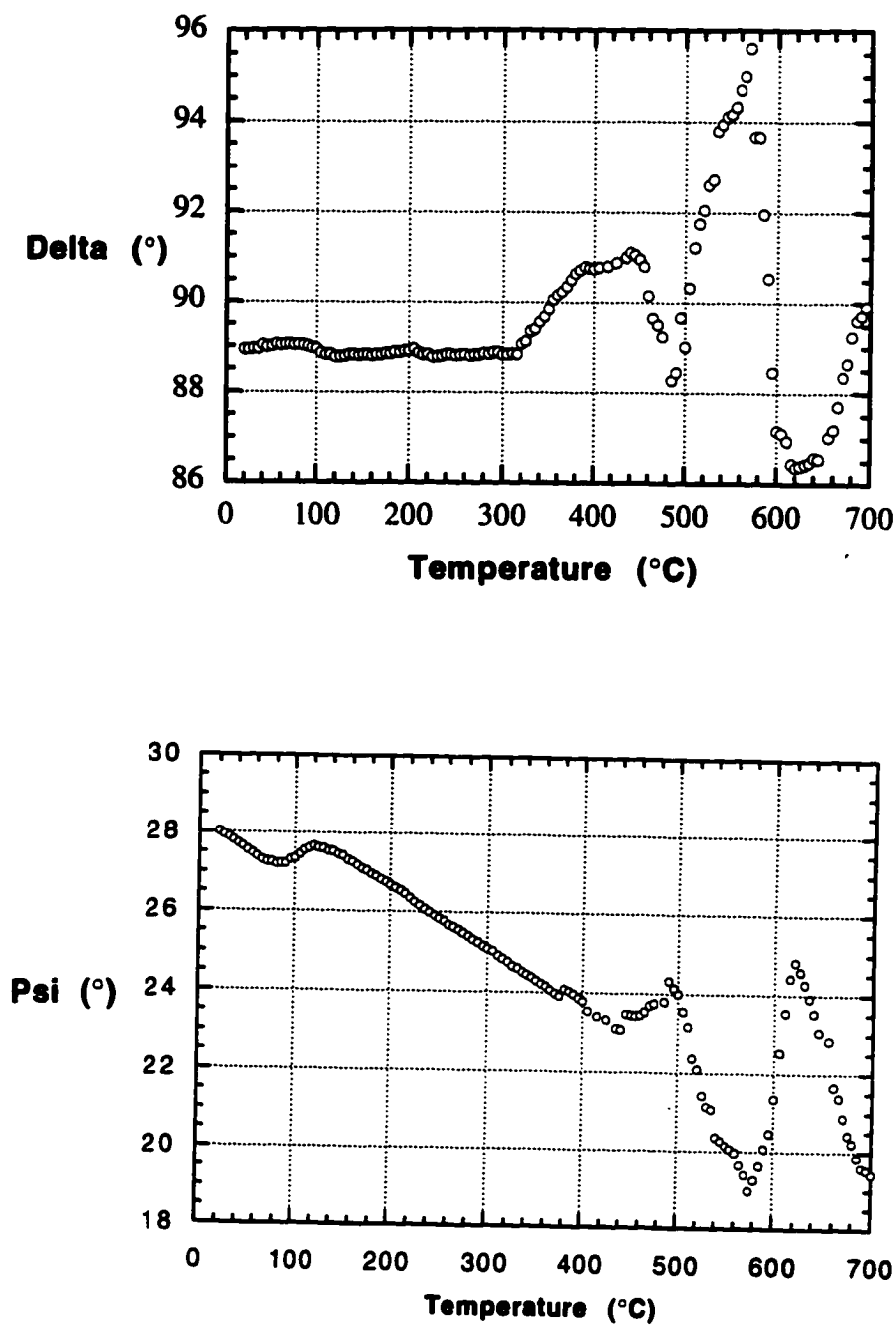
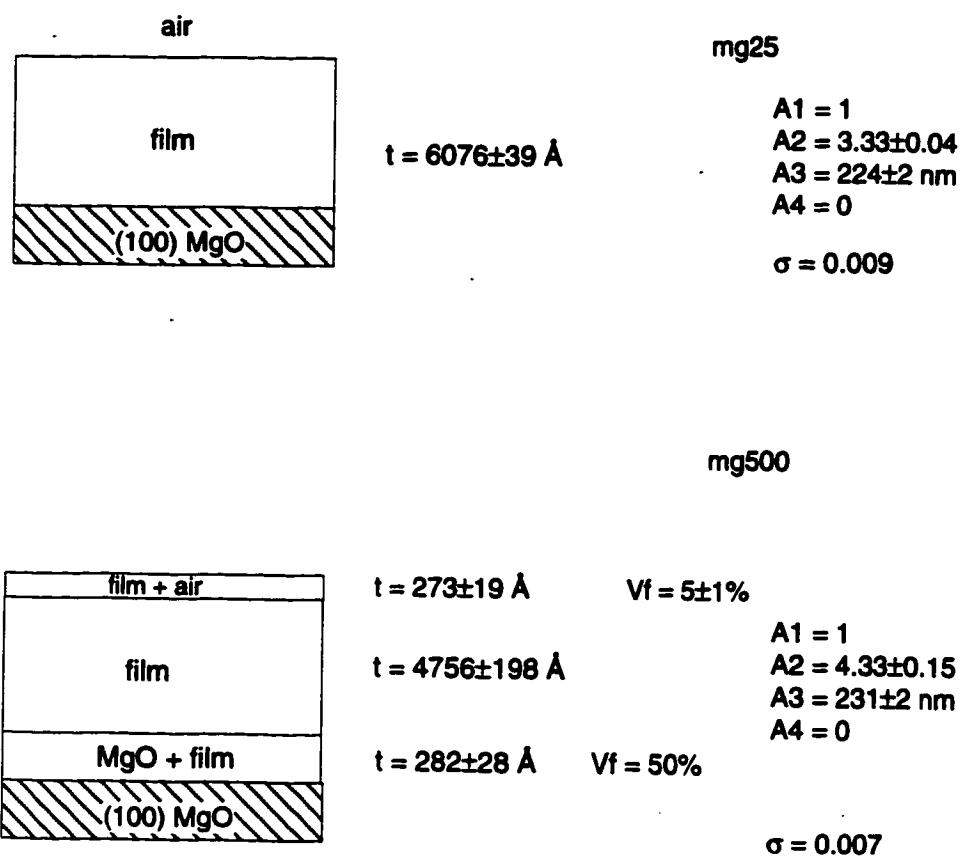Figure 4.32. A plot of the ellipsometric parameters over a range of annealing temperatures (25°C to 700°C) for a PZT film on sapphire substrate (a) Δ vs. temperature, and (b) Ψ vs. temperature.

function of temperature. It is believed that the sudden changes of Δ and Ψ from this plot correspond to crystallization from the amorp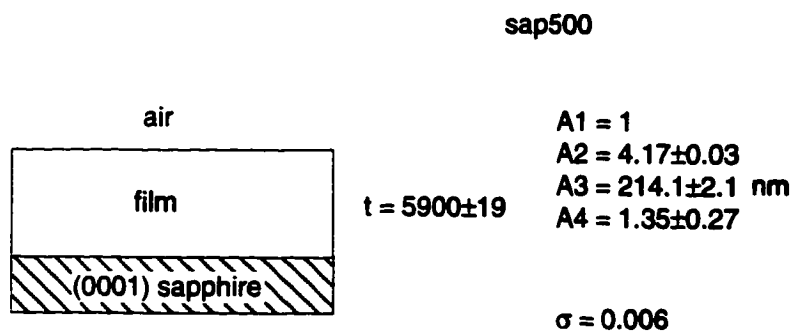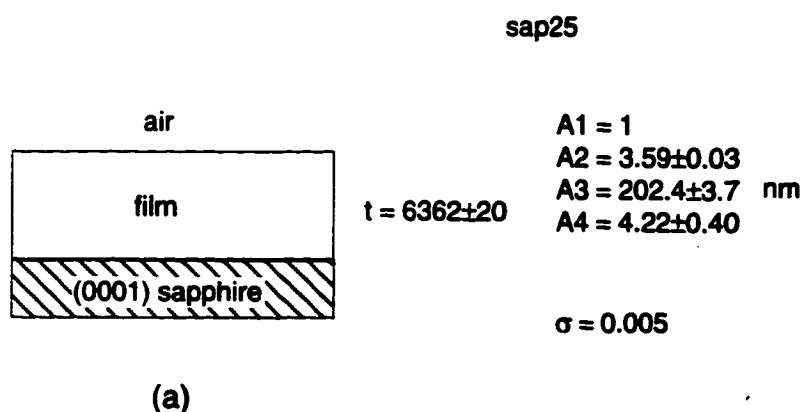hous to the intermediate phase, and from the intermediate to the perovskite phase. As shown in Δ curve, the intermediate phase may initially form at ~440°C, and the perovskite phase at 560°C where there was an abrupt change in Δ. This observation is in good agreement with the XRD results which are detailed later in this chapter.

The SE models for the film after RTA at 400°C for 10 mins and after 700°C anneal are shown in Figure 4.33. The film showed no major change in thickness and a thin layer of 200Å surface roughness was found after the 700°C heat treatment. The refractive index of this film while in the amorphous state and after crystallization were calculated from the modeling parameters and are plotted in Figure 4.34. After the 700°C anneal, the film shows a high value of n which is comparable to that of the reference data of lanthanum-doped PZT bulk ceramics (Thacher 1977). This implies that film has crystallized to the perovskite PZT phase.

In summary, attempts to employ the spectroscopic ellipsometry as a tool to follow the crystallization kinetics of PZT thin films during annealing demonstrated that the method has potential. During film crystallization, SE can also track the evolution of crystallinity, microstructural inhomogeneity, and the optical properties of such films. In addition, the time resolution for this SE measurement at a single wavelength is under 5 seconds for the 50 cycle averaging used here. Each Δ and Ψ measurement can be achieved within 4.2 second at a single wavelength. Therefore, it is possible to follow the crystallization kinetics of PZT films with a 4.2 second resolution.

sap25

air

| film | t = 2640±40Å |

(0001) sapphire

A1 = 1
A2 = 3.46±0.03
A3 = 201.4±2.1 nm
A4 =0

σ = 0.008

(a)

sap700

air

| film + air | t = 204±12 Å | Vf = 17±3% |
| film | t = 2410±36Å | |

(0001) sapphire

A1 = 1
A2 = 4.82±0.05
A3 = 200.3±6.4 nm
A4 =0

σ = 0.007
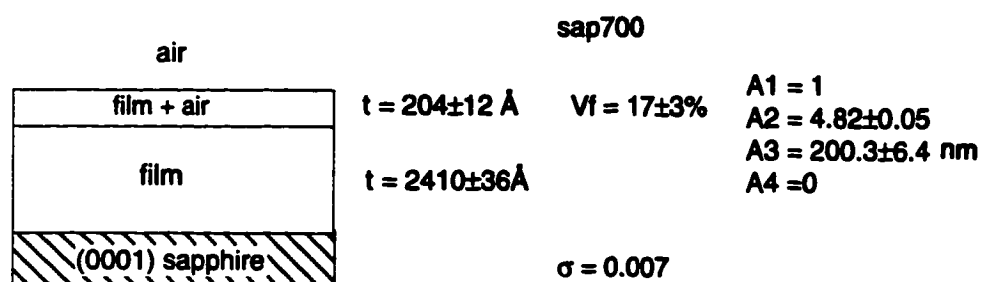
(b)

Figure 4.33. SE models for a sol-gel PZT film on a (0001) sapphire substrate (a) after RTA at 400°C for 10°C, and (b) after a 700°C anneal.
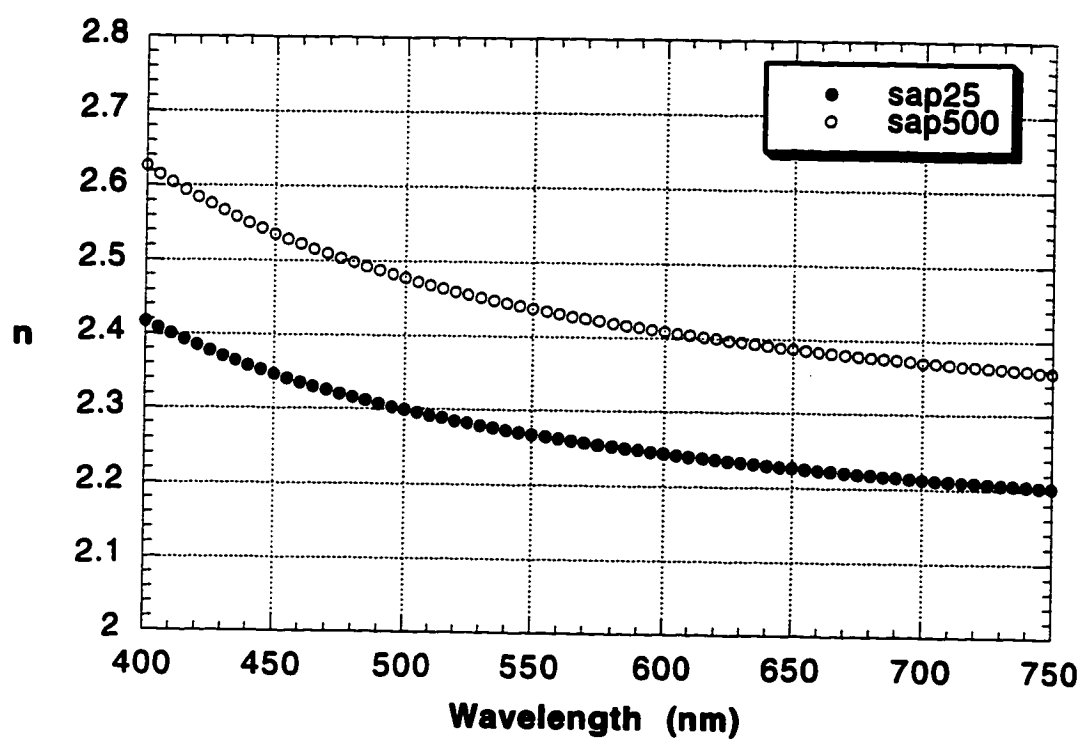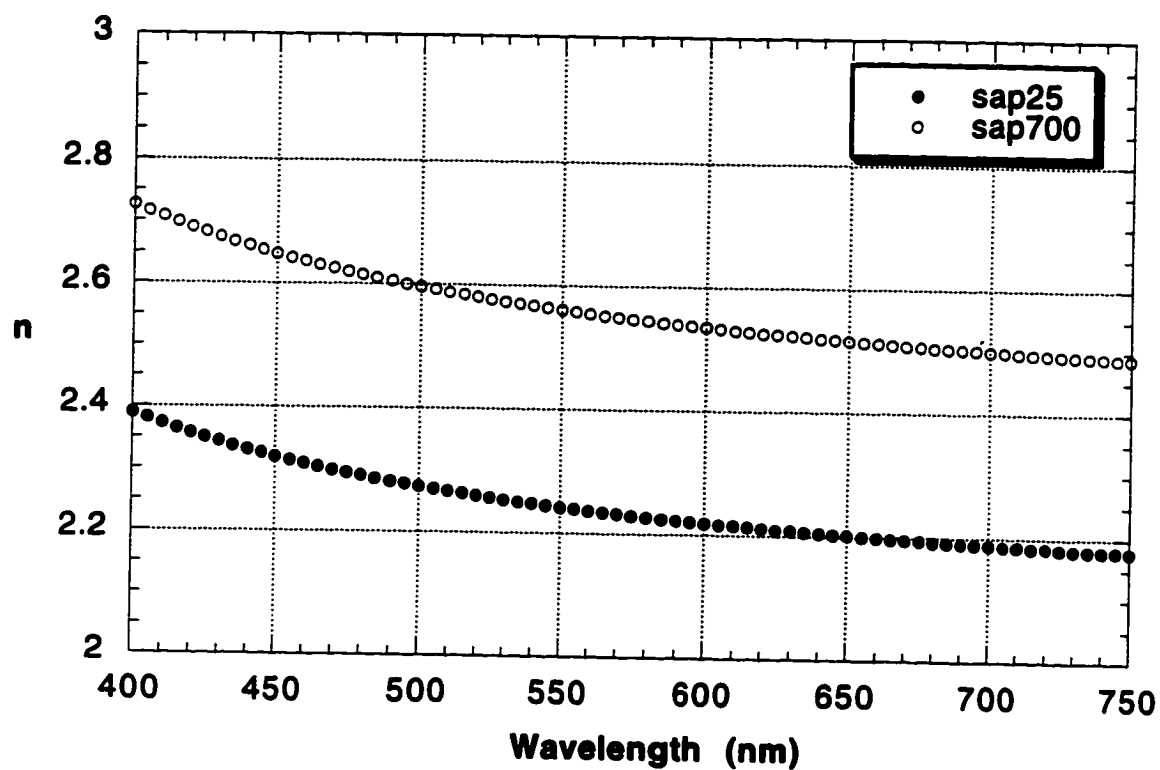
Figure 4.34. A plot of n over wavelength for a PZT film on a sapphire substrate before heat treatment (sap25) and after a 700°C anneal (sap700).
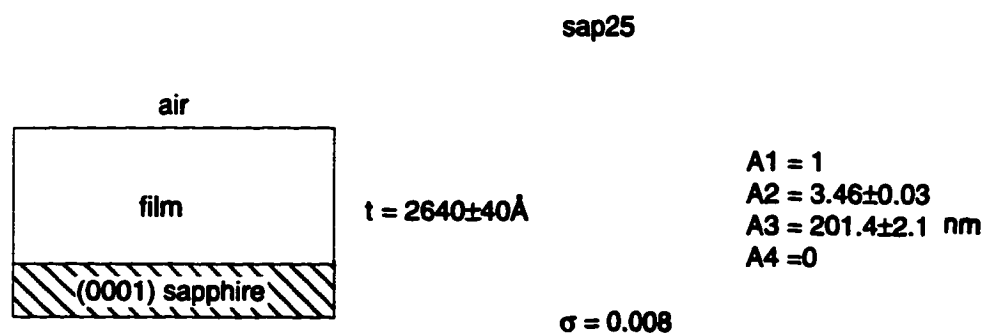
4.2. Structural Characterization

X-ray diffraction (XRD) methods were used throughout this study to identify the crystallized phases and to analyze the structural properties of PZT thin films during annealing. However, standard XRD systems which utilize Bragg-Brentano (Cullity 1978) diffractometer are designed to penetrate the thin film surface and enter the bulk of the substrate material. As a result, very little of the diffracting volume is from the film, and so intensities from the surface are very low. Thus, weak patterns from the PZT thin films on the substrate were overwhelmed by the strong peaks from the substrate.

In order to overcome this difficulty, grazing angle X-ray diffraction was used to analyze the films. In this method, a normal Bragg-Brentano diffractometer is used; the only difference is that the source-to-sample angle remains fixed at a small angle ($<10°$), controlling the penetration of x-rays into the sample surface. The grazing angle can be adjusted so that x-rays do not reach the substrate. Not only does this eliminate substrate interference, but it also increases the x-ray path lengths and therefore, diffraction intensities from the thin film. Thus, grazing angle XRD makes it possible to detect films thicker than 100-200 Å (Zevin 1988).

For room temperature X-ray diffraction studies, most of the XRD patterns for PZT thin films annealed by both RTA and conventional furnace annealing were collected by grazing angle XRD at the Materials Research Laboratory (MRL) of The Pennsylvania State University. The remainder were taken on a standard diffractometer. For the in-situ X-ray diffraction studies at elevated temperatures there were two XRD systems employed: the Ruud-Barrett position

sensitive scintillation detector (RB PSSD) X-ray diffractometer at the MRL, and the high-temperature X-ray diffractometer at the High Temperature Materials Laboratory (HTML) of the Oak Ridge National Lab, Oak Ridge, TN. Both X-ray systems were detailed in sections 3.3.1 and 3.3.2 in this thesis.

4.2.1. Room Temperature X-ray Diffraction

Once PZT films were prepared and crystallized by rapid thermal annealing, or *in-situ* annealed on either the ellipsometer or the RB-PSSD XRD system, routine x-ray diffraction patterns were collected to examine the phase development in the films. As shown in Figure 4.35 the x-ray diffraction patterns indicate that well-crystallized perovskite PZT was achieved for various substrates, including Pt-coated Si, (0001) sapphire, and (100) MgO after RTA at 700°C for 30 seconds. Most of the PZT films prepared in this study showed a nearly random orientation, with XRD patterns which match the JCPDS file no. 33-784, for $Pb(Zr_{0.52}Ti_{0.48})O_3$. However, some of the films on Pt-coated Si substrates showed strong (100) or (211) preferred orientations as seen in Figure 4.36.

Some films were rapid thermal annealed at lower temperature such as 520°C for 60 seconds, in order to crystallize the intermediate pyrochlore or fluorite-type phase on various substrates. The XRD patterns of these films on Pt-coated Si, sapphire, and MgO substrates are shown in Figure 4.37. It is believed that the broad X-ray peaks are due to the small grain size which is characteristic of the intermediate phase (Tuttle et al. 1993 and Kwok and Desu 1993). These sets of films were used in the spectroscopic ellipsometric
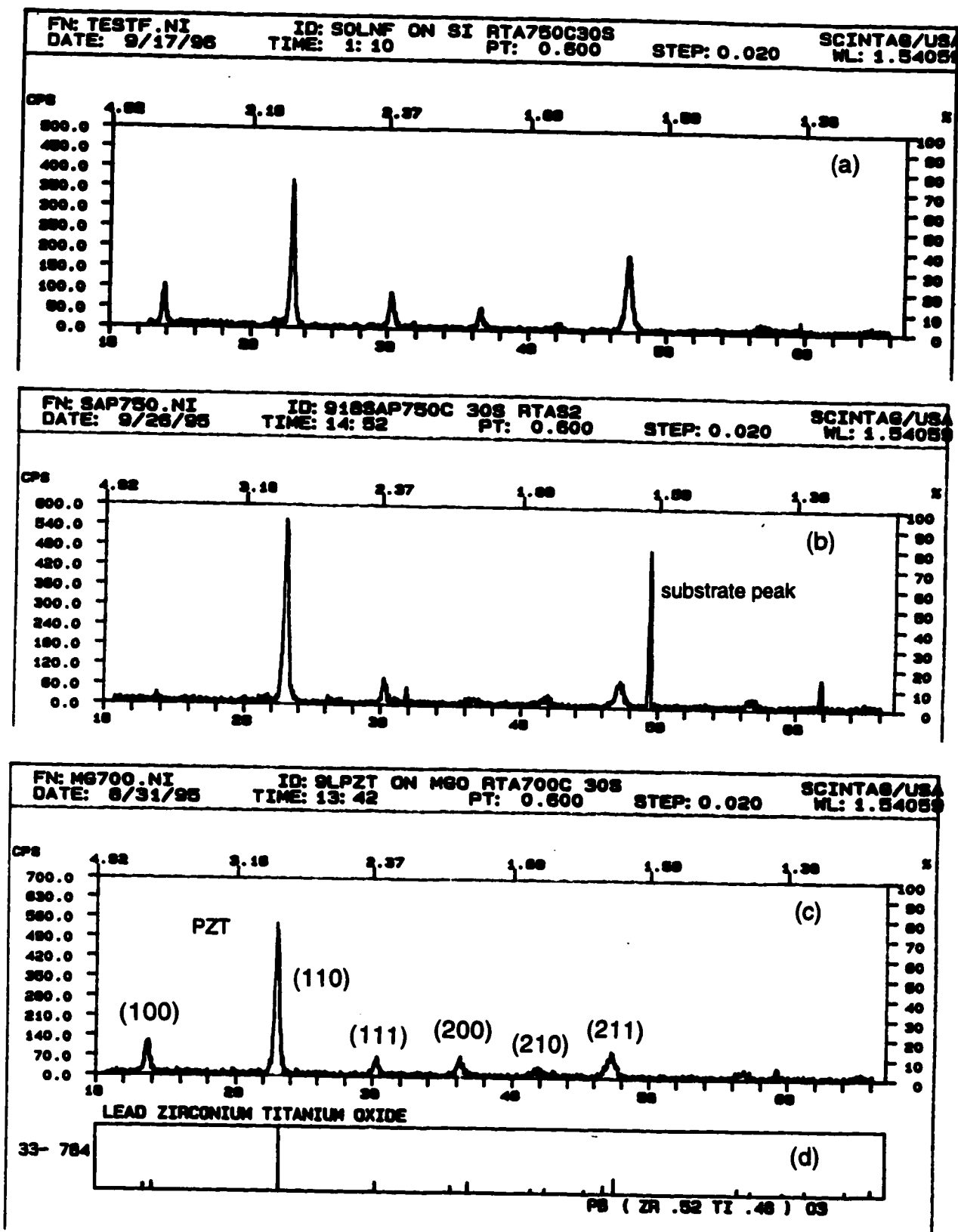
Figure 4.35. XRD patterns for PZT films on (a) Pt-coated Si, (b) sapphire, (c) MgO after RTA at 700°C for 30 seconds, and (d) the JCPDS pattern for PZT(52/48) reference data .

FN: SI50123.NI ID: 7LPZT ON SI 50C SC1
DATE: 1/23/95 TIME: 15:55 PT: 0.600 STEP: 0.020 SCINTAG/USA WL: 1.54059

CPS
1500.0
1350.0
1200.0
1050.0
900.0
750.0
600.0
450.0
300.0
150.0
0.0

(100)
PZT

Pt-Si substrate

(a)

LEAD ZIRCONIUM TITANIUM OXIDE

33- 784

PB (ZR .52 TI .48) O3

PLATINUM / PLATINUM, SYN

4- 802

PT

FN: SI700.NI ID: 9LPZT ON SI RTA700C 30S SCIN2
DATE: 8/31/95 TIME: 14:17 PT: 0.600 STEP: 0.020 SCINTAG/USA WL: 1.54059

CPS
750.0
675.0
600.0
525.0
450.0
375.0
300.0
225.0
150.0
75.0
0.0

PZT
(110)

PZT
(111)

Pt-substrate

PZT
(211)

Si substrate

(b)

LEAD ZIRCONIUM TITANIUM OXIDE

33- 784

PB (ZR .52 TI .48) O3

PLATINUM / PLATINUM, SYN

4- 802

PT

Figure 4.36. XRD patterns for PZT films on Pt-coated Si after RTA at700°C for 30 seconds. The films show preferred orientation in (a) 100, and (b) 211 perovskite PZT phase.
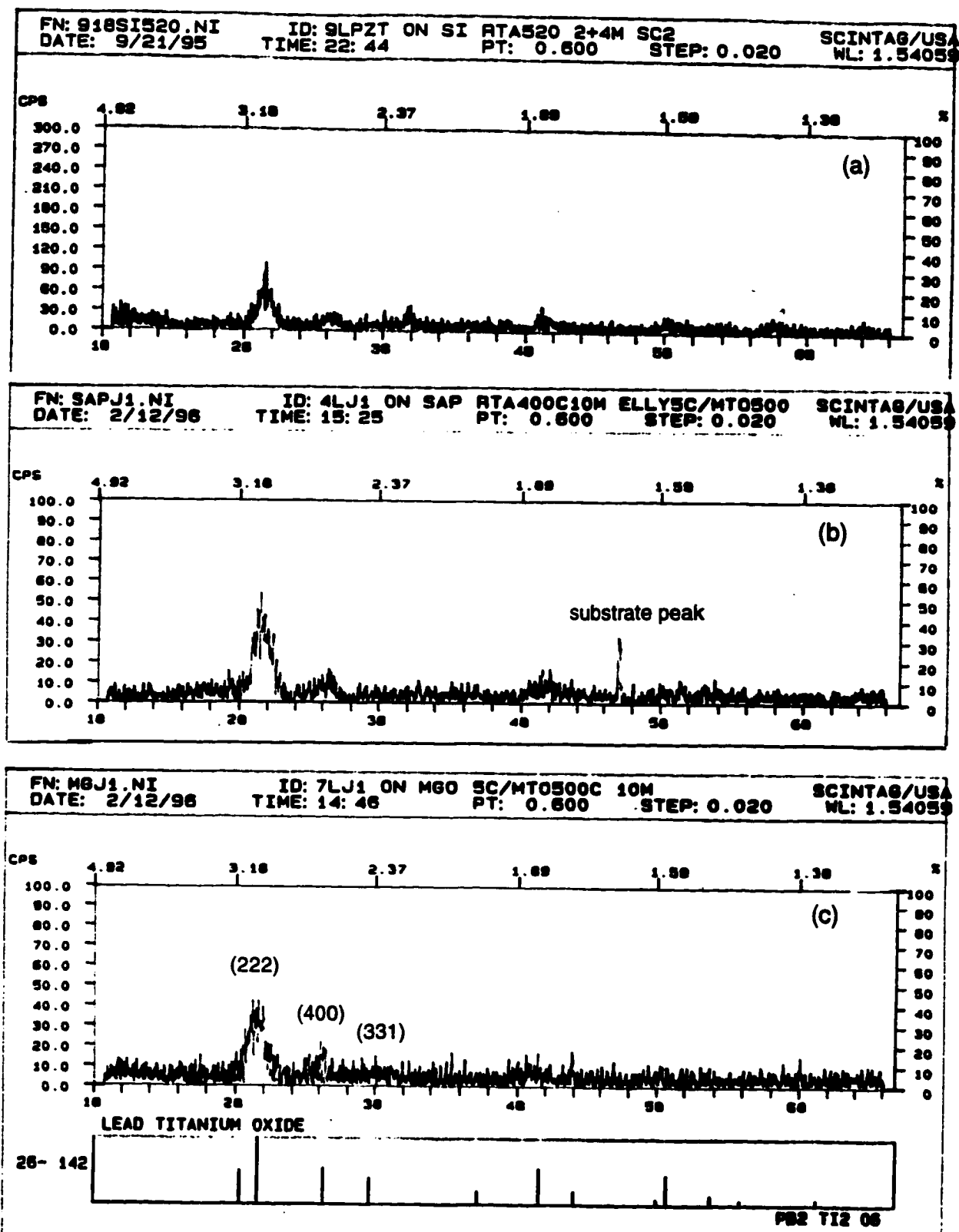
Figure 4.37. XRD patterns for PZT films on (a) Pt-coated Si, (b) sapphire, and (c) MgO after RTA at 520°C for 30 seconds. The films show only intermediate phase X-ray peaks.

measurements in order to determine optical reference data for the intermediate phase as discussed in the optical characterization section.

4.2.2. *In-Situ* Annealing Studies by X-Ray Diffraction

In order to examine the amorphous-intermediate phase and the intermediate phase-perovskite phase transformations using *in-situ* structure-sensitive techniques, two X-ray diffraction systems were employed in this study. A Ruud-Barrett position sensitive scintillation detector (R-B PSSD) X-ray diffractometer was used for the initial studies to identify temperature ranges for the transformations, as well as some information on the transformation kinetics. Since it was unavailable for the latter half of the study, quantitative measurements for the kinetics studies was obtained using the high-temperature X-ray diffractometer of the Oak Ridge National Lab. The operations of both systems are detailed in section 3.3, and the XRD results will be reported in the following sections.

4.2.2.1. R-B PSSD X-Ray Diffraction

In order to obtain the best signal out of this X-ray system, PZT thin films were spin-coated onto Pt-coated Si and MgO substrates as thick as possible, i.e., 5000-6000Å. The sample was placed inside an alumina tube furnace which was situated in the R-B PSSD X-ray diffractometer. The annealing rates using in this study were 50°C/ minute to 600°C and 650°C and 100°C/ minute to 600°C and 650°C. The thermocouple used to control the temperature was placed underneath the sample. The source-to-sample and the sample-to-

detector distance was 20 cm, this value being dictated by the size of the alumina heating furnace. The angle of incidence between the x-ray source and sample was 14°.

X-ray diffraction patterns of the thin film were collected every 30 seconds during the heating over a 2Θ range of approximately 6° under parafocusing conditions. The 2Θ ranged from 27° to 33° to permit observation of both the pyrochlore-like peak at 2Θ ~ 29° and the perovskite peak at 2Θ ~ 30.9°. Some run-to-run shift in the detector channel position for the two peaks was observed due to small difference in the flexible detector position. To normalize the position of the detector channel to the 2Θ angle, $CaSO_4$ powder was used as a standard for each run since it has the highest intensity peak around the same position of the perovskite peak.

At soak temperatures of 600°C and 650°C, x-ray patterns were collected once a minute. A 15 second exposure time was used for isothermal patterns during soaking at a given temperature. Some run-to-run shift in the detector channel position for the two peaks was observed due to small difference in the flexible detector position.

50°C/minute Annealing Rate

Figures 4.38 and 4.39 show the x-ray diffraction patterns of a PZT thin film on a platinized Si substrate during the annealing process. The sample was heated from room temperature to 600°C at 50°C/min. At 600°C, the sample was given an isothermal anneal for 60 minutes. From these figures, it is clear that an x-ray peak associated with the intermediate phase (either the pyrochlore or a fluorite- structured material) started to appear at the temperature range 490-

Figure 4.38. XRD patterns of a PZT film on a Pt-coated Si substrate collected from 393 to 613°C. An annealing rate of 50°C/min was used. The two theta angle covers from 28.5 to 34.5°.
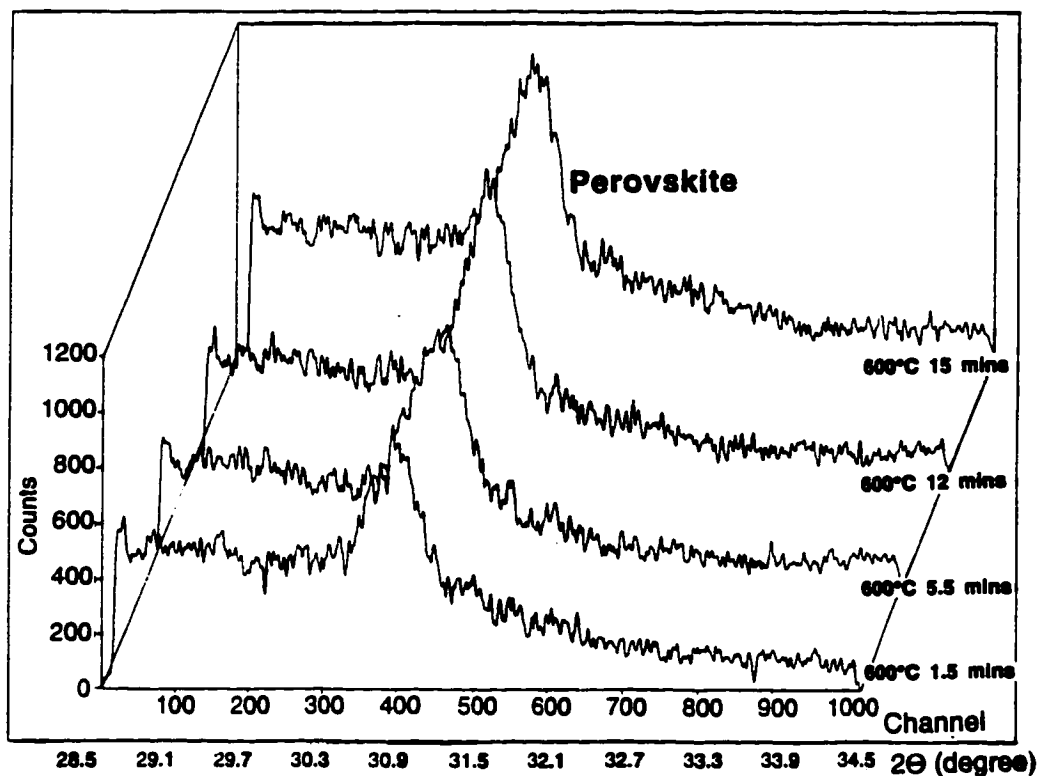
Figure 4.39. XRD patterns of a PZT film on a Pt-coated Si substrate collected at 600°C for 1.5 to 15 minutes. An annealing rate of 50°C/min was used. The two theta angle covers from 28.5 to 34.5°.

515°C and developed a maximum intensity at 540-566°C. Since only a single X-ray peak from this phase was observed, absolute phase identification was not possible. The perovskite phase first formed between 590-613°C and the peak grew from 0 to 93% of the final peak height as the temperature reached 600°C for 4.5 minutes. After 12 minutes soaking at 600°C, the remaining 7% of peak growth was seen and no significant phase development was observed after that point.

The integrated area under each peak was calculated using OMA Vision software (Oma Vision 1993). To do this, background subtraction on all scans was performed by selecting the highest temperature scan with no indication of crystallization to be the base line. This scan was then subtracted from each higher temperature scan. This helped minimize error due to the observed background drift at elevated temperatures. The area under each peak in the difference scans was determined using a consistent width of channel numbers for the peak (i.e. the area was integrated over the same range for each temperature). It was found in *ex-situ* measurements of these films after annealing on a standard diffractometer that the perovskite phase showed different degrees of preferred orientation. This, in combination with the relatively low signal-to-noise ratio in the *in-situ* experiments made it difficult to quantitatively determine the relative volume percent of the two phases during annealing from the peak area measurements.

Figure 4.40 shows a plot of the peak areas of the intermediate and perovskite phases over a range of temperatures and times. The largest amount of the intermediate phase was found in the temperature range 590-613°C. The perovskite phase progressively grew as the temperature reached 600°C. The

Figure 4.40. A plot of the peak areas of the intermediate and perovskite phase over a range of temperatures and times for a platinized Si substrate. An annealing rate of 50°C/min was used.

highest amount of perovskite phase was found at 600°C for a 13 minute soaking. It is worth noting that nucleation and growth of the intermediate phase occurred within 2 minutes at this heating rate. Conversion to the perovskite phase was largely completed within 5 minutes at 600°C. Additional growth in the perovskite peak area subsequent to this is probably due to an increase in either grain size or crystallinity.

A film on (100) MgO substrate was also prepared and annealed *in-situ* in the x-ray system. Again, an annealing rate of 50°C/ minute to 600°C and 650°C was used to study the influence of the substrate on the nucleation and growth of the perovskite phase. A series of x-ray diffraction patterns collected from 434°C to 650°C is shown in Figure 4.41. The x-ray pattern at 434-559°C shows the film in the amorphous state. By 483-507°C the intermediate peak first formed. This continued crystallizing with heat treatment in the temperature range 581-605°C (spectrum 4 in Fig. 4.41). As the temperature increased to 650°C this phase converted progressively to the perovskite phase. The fully developed perovskite peak was found at 650°C after a 17 minute anneal and the amount of intermediate phase was also suppressed at this point. No significant perovskite phase development was observed after 17 minutes at 650°C.

Figure 4.42 shows a plot of the peak areas of the intermediate and perovskite phases over a range of temperatures and times. The highest amount of intermediate phase was observed at 581-605°C. Within one minute, as the temperature increased to 600°C, growth of this phase was arrested, and perovskite nucleation was observed. The perovskite phase continued crystallizing to its highest amount at 650°C after a 17 minute soaking. In the
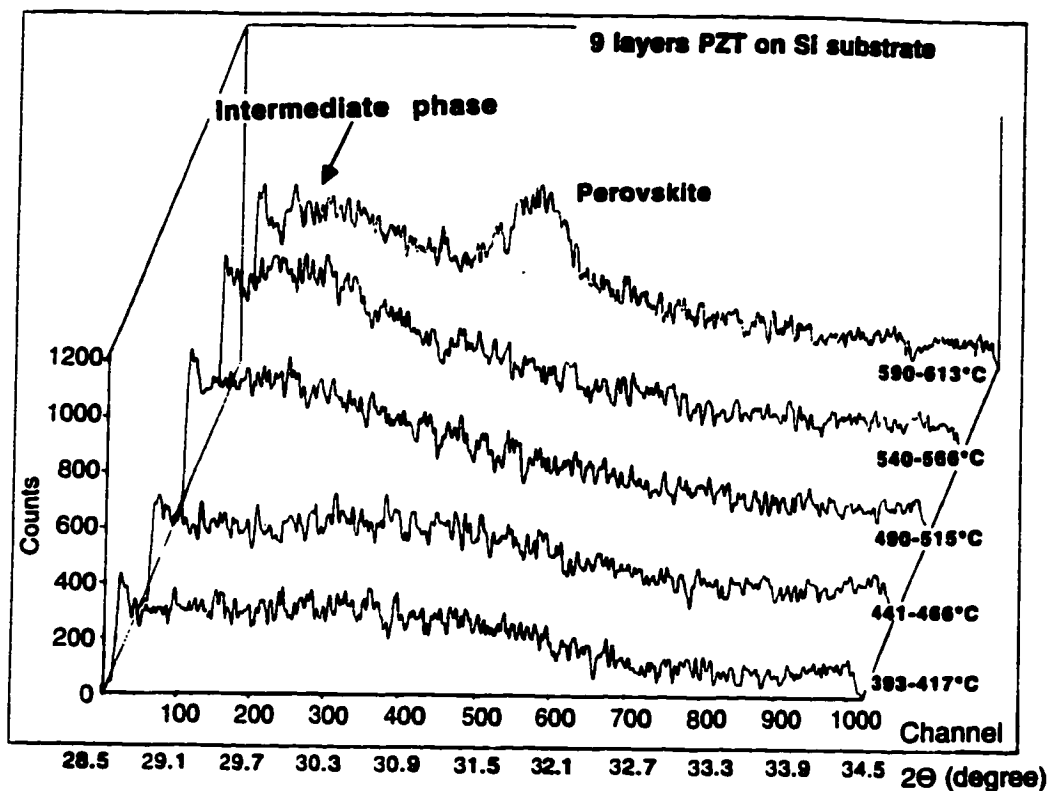
Figure 4.41. XRD patterns of a PZT film on an (100) MgO substrate collected from 434 to 650°C. An annealing rate of 50°C/min was used. The two theta angle covers from 29.1 to 32.1°.
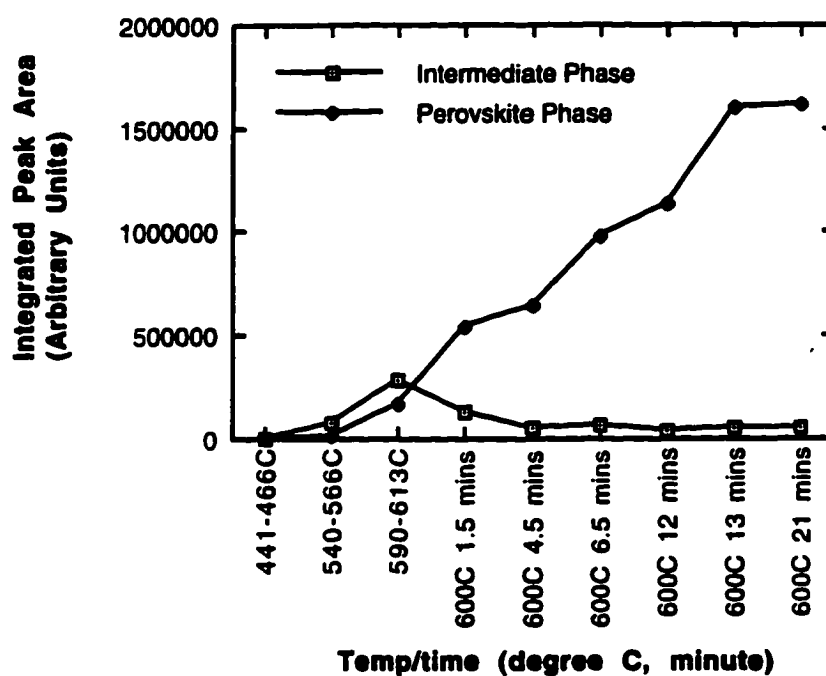
Figure 4.42. A plot of the peak areas of the intermediate and perovskite phase over a range of temperatures and times for an MgO substrate. An annealing rate of 50°C/min was used.

case of the film on the MgO substrate, considerable residual pyrochlore remained after the 600°C anneal. This was largely removed by annealing at 650°C.

For a 50°C/minute annealing rate, the nucleation temperatures of both the intermediate and perovskite phases appear to be slightly lower for the platinized Si than for the MgO substrate. Full conversion to the perovskite phase was completed at 600°C for a 12 minute soak on a platinized Si substrate and at 650°C for a 17 minute soak on an MgO substrate. The difference in temperatures may be due in part to the differing substrate emissivities for the two samples.

100°C/minute Annealing Rates

Films heat-treated at 100°C/minute to 650°C were also investigated to observe whether the intermediate phase formation could be bypassed at this heating rate. For a platinized Si substrate sample, a series of x-ray diffraction patterns collected from 480°C to 650°C is shown in Figures 4.43 and 4.44. It can be seen that the intermediate phase is still formed prior to the perovskite phase. Initial formation was apparent in the 480-498°C scan and it continued growing to the maximum amount at 584-595°C. The perovskite peak also appeared in this temperature range and grew quickly to its highest intensity as the temperature approached 650°C (Fig. 4.44). No significant perovskite peak development was observed after 27 minutes at 650°C.

A plot of the peak areas of the intermediate and perovskite phases over a range of temperatures and times is shown in Figure 4.45. The intermediate phase was first observed at 530-540°C and grew to the maximum amount

Figure 4.43. XRD patterns of a PZT film on a Pt-coated Si substrate collected from 480 to 595°C. An annealing rate of 100°C/min was used. The two theta angle covers from 27.6 to 33.6°.

Figure 4.44. XRD patterns of a PZT film on a Pt-coated Si substrate collected at 600°C for 5 mins and at 650°C for 0,5, 13, and 21 mins . An annealing rate of 100°C/min was used. The two theta angle covers from 27.6 to 33.6°.

Figure 4.45. A plot of the peak areas of the intermediate and perovskite phase over a range of temperatures and times for a PZT film on a platinized Si substrate. An annealing rate of 100°C/min was used.

within 1.5 minutes (the 597-598°C scan). With annealing at 600°C for 5 minutes, the intermediate phase converted progressively to the perovskite phase; this process continued until the temperature approached 650°C where a large amount of perovskite phase was found. At 650°C after a 27 minute hold the highest amount of perovskite phase was found with a small amount of residual intermediate phase.

A thin film on an MgO substrate was also subjected to the same annealing schedule. Figure 4.46 shows the x-ray diffraction patterns collected for various annealing temperatures. The intermediate phase peak was seen first in the temperature range 433-461°C (spectrum 2 in Fig. 4.46) and grew to the largest amount at 596°C. The perovskite peak also appeared first at 596°C (spectrum 3). As the temperature approached 600°C, the intermediate phase converted progressively to the perovskite phase. In addition, as the temperature increased to 650°C, a large perovskite peak without the intermediate phase peak was observed at 650°C after a 28 minute hold. The plot of the peak areas of intermediate and perovskite phases over a range of temperatures and times is shown in Figure 4.47.

For the 100°C/minute heat treatment, it was observed that the relative intensity of the intermediate phase peak was lower than that observed in the case of 50°C/minute heating rate for films on platinized Si substrates. Similarly, for the films on MgO substrates, the 100°C/minute annealing rate showed less pronounced intermediate phase peaks than in the 50°C/minute case.
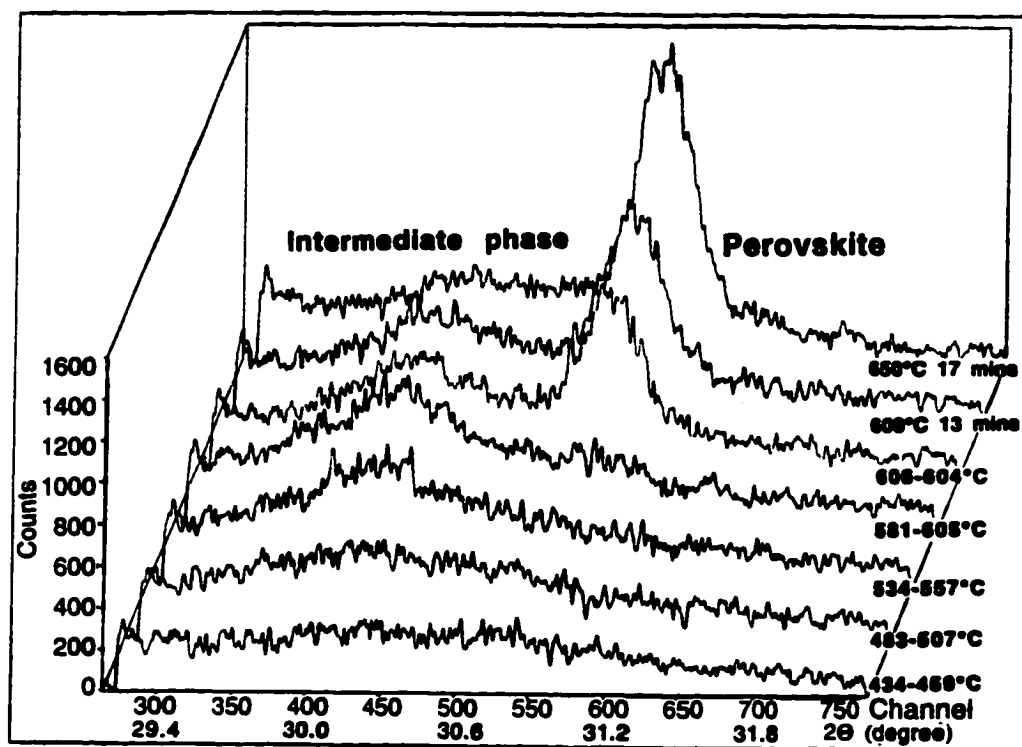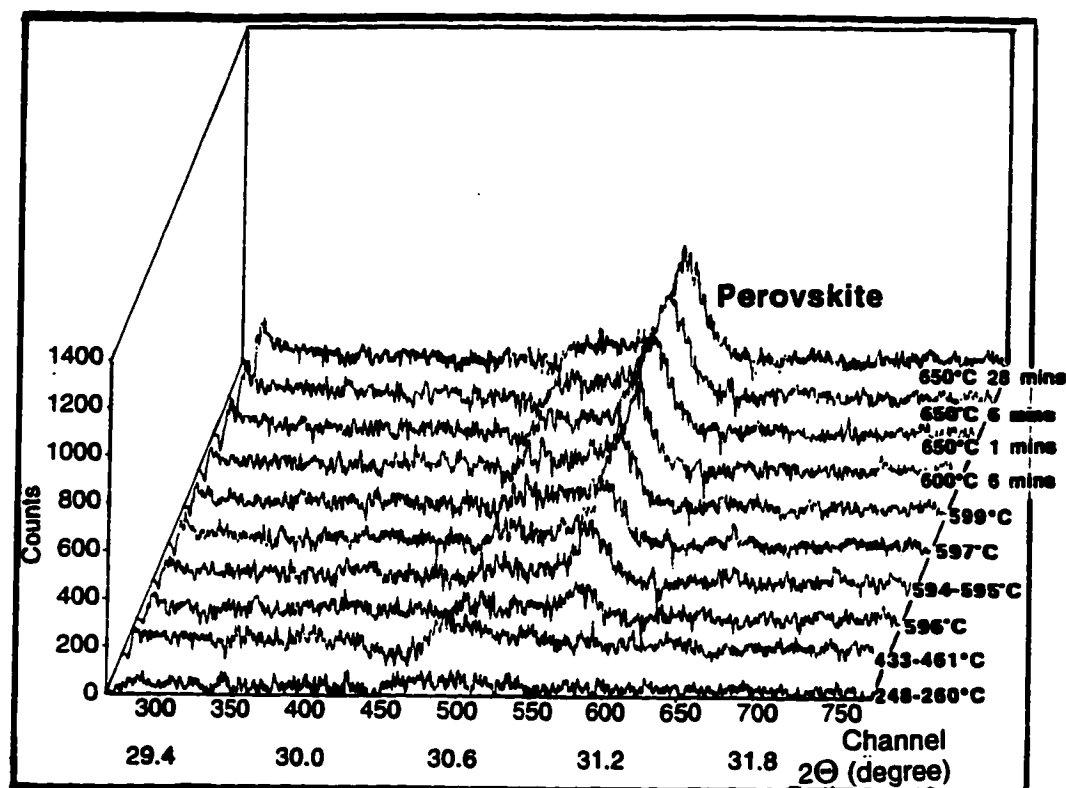
Figure 4.46. XRD patterns of a PZT film on an (100) MgO substrate collected from 248 to 650°C. An annealing rate of 100°C/min was used. The two theta angle covers from 29.1 to 32.1°.
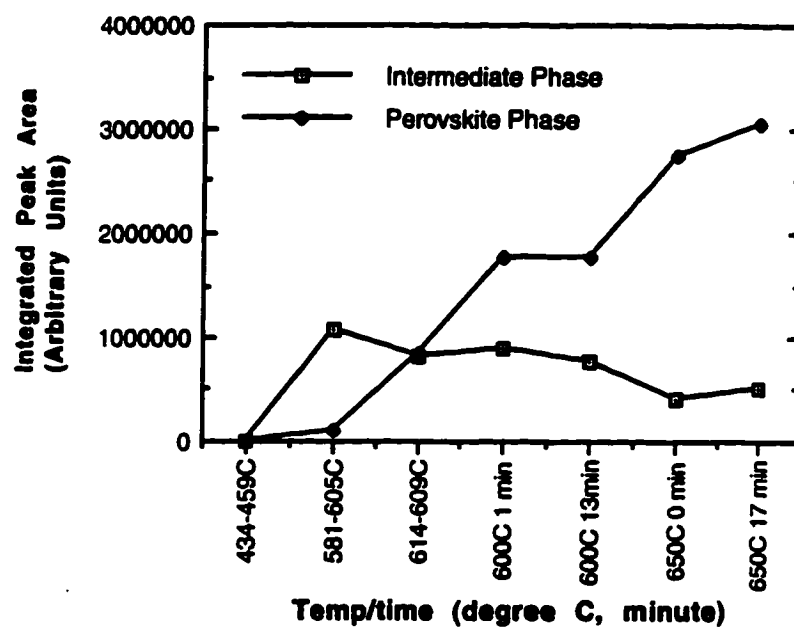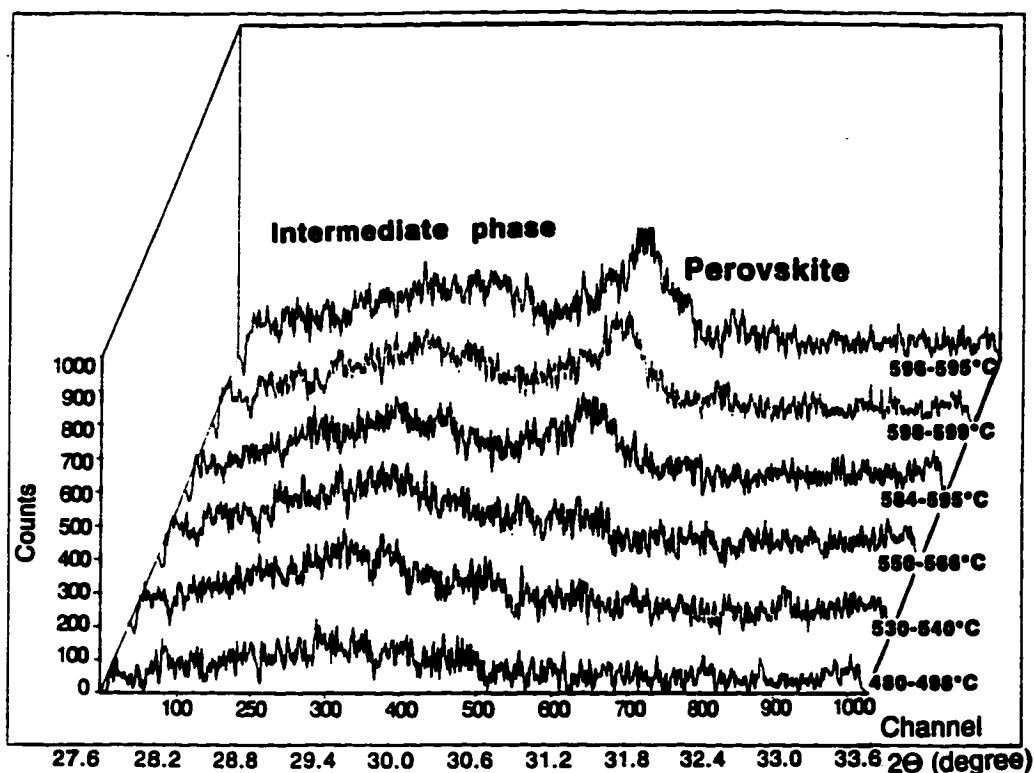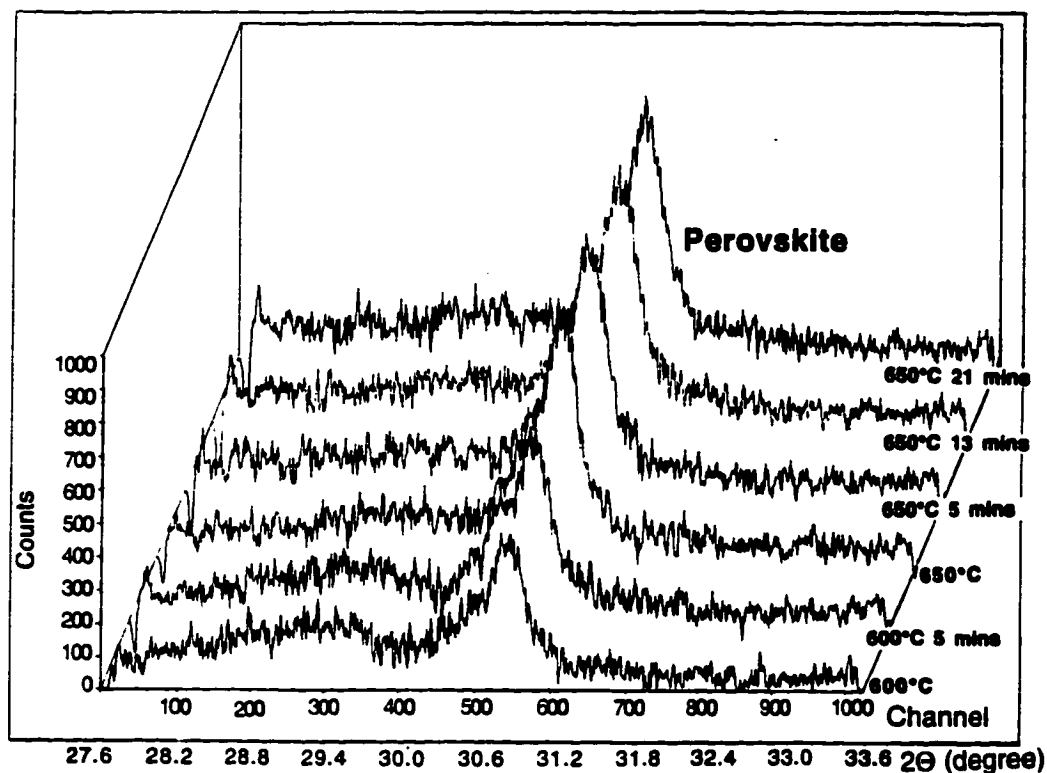

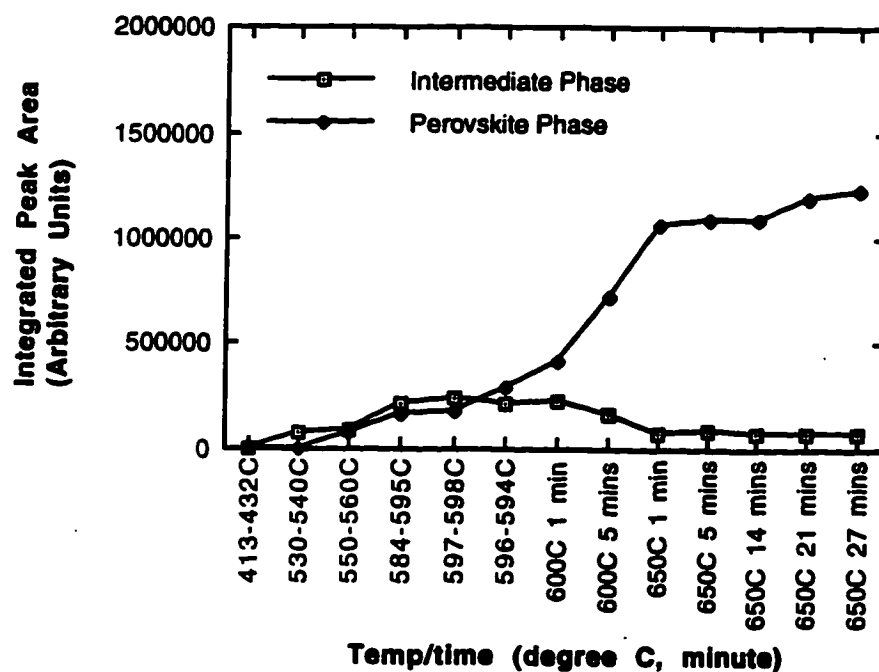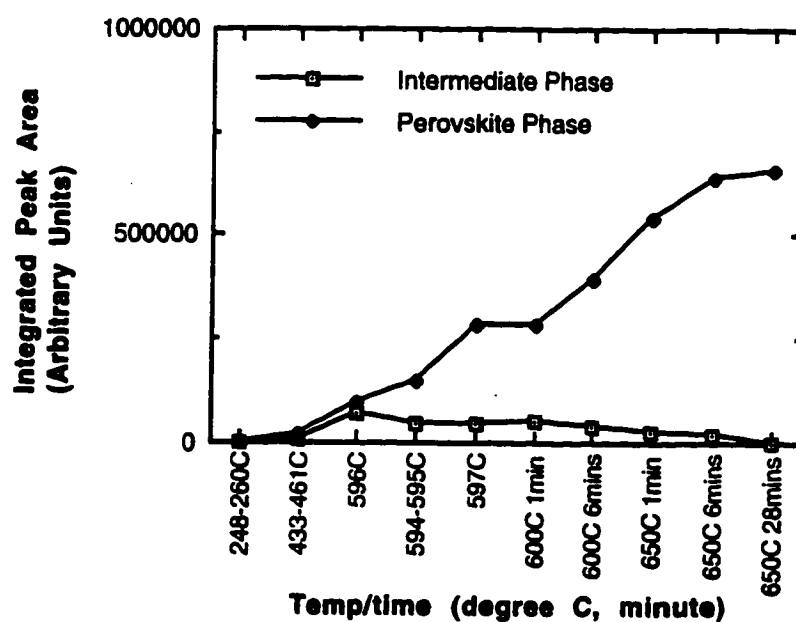**Figure 4.47.** A plot of the peak areas of the intermediate and perovskite phase over a range of temperatures and times for a MgO substrate. An annealing rate of 100°C/min was used.

In sum, the phase development of PZT thin films on platinized Si and (100) MgO substrates was studied using an *in situ* annealing x-ray diffraction system at elevated temperatures. It was found that R-B PSSD x-ray system is capable of following transformation kinetics in thin films with a time resolution on the order of 30 seconds. It is expected that by optimizing the system and the sample further, this time resolution will be improved.

For both 50°C/minute and 100°C/minute heat treatments, the nucleation temperatures of the intermediate and perovskite phases were found to be lower for platinized Si than for MgO substrates. Again, this may be due, in part, to the different thermal emissivities of the 2 samples and the radiative furnace used. The intermediate phase started to form in the temperature range 530-566°C for films on platinized Si substrates and in the range 581-605°C for films on MgO substrates. Similarly, the perovskite phase formed in the temperature range 550-590°C for films on platinized Si and in the range 596-604°C for films on MgO substrates. With increasing annealing temperature to 650°C, the intermediate phase converted to the perovskite phase. As expected, x-ray diffraction patterns showed the minimum amount of intermediate phase where the maximum perovskite phase was found.

The annealing rates used in this study (50°C/minute and 100°C/minute), did not permit bypass of the intermediate phase formation. However, it was observed from the plots of the peak area over a range of temperatures and times that at the 100°C/minute rate, the amount of intermediate phase appeared to be smaller than for the 50°C/minute ramp rates for films on both platinized Si and MgO substrates.

4.2.2.2. High Temperature X-ray Diffraction

For more quantitative measurements suitable for crystallization kinetics determination, as-deposited PZT thin films on Pt-coated Si and (100) MgO substrates were also *in-situ* annealed in the high temperature X-ray diffractometer (HTXRD) with heating rates from 5 to 100°C/min from room temperature to 700°C. These sets of X-ray measurements were done at the high temperature materials lab (HTML) of the Oak Ridge National Laboratory, Oak Ridge, TN. The schematic and the operation of the HTXRD were detailed in chapter 3, section 3.3.3. This system can operate in oxidizing, reducing, or inert gas environments at temperatures up to 1600°C. In this study, PZT films were annealed in air with constant ramp rates of 5°, 10°, 20°, 50°, and 100°C/minute from room temperature to 700°C without any soaking times. The annealing conditions, including the scan rates and scan times of all PZT thin films are summarized in Table 4.5. X-ray diffraction patterns were collected during heat treatment of PZT thin films over a 2Θ range of 7° (from 27° to 33°) to cover the peaks of interest at $2\Theta \sim 29°$ for a pyrochlore-like peak, and at 30.9° for a perovskite peak. This HTXRD system also employed the scanning position-sensitive detector (PSD) in order to perform the high speed measurements.

Since this set of HTXRD diffraction data will be used to apply Avrami non-isothermal kinetics, it is important to insure that all films prepared on both Pt-coated Si and MgO show a random orientation in order to evaluate the fraction transformed (f) between the intermediate and the perovskite phase. To achieve this, PZT films were spin-coated onto both substrates and RTAd at 700°C for 30 seconds. Standard XRD patterns at room temperature were then taken. The

Table 4.5

Annealing conditions and scan rates and times for PZT films used in HTXRD.

Materials	Starting Temperature (°C)	Ending Temperature (°C)	Heating Rate (°C/minute)	Scan Rate (°/min)/ Scan time (min)
PZT film on Pt-coated Si	25	700	5	20/0.928
PZT film on MgO	25	700	5	20/0.928
PZT film on Pt-coated Si	25	700	10	20/0.928
PZT film on MgO	25	700	10	20/0.928
PZT film on Pt-coated Si	25	700	20	20/0.928
PZT film on MgO	25	700	20	20/0.928
PZT film on Pt-coated Si	25	700	50	50/0.748
PZT film on MgO	25	700	50	50/0.748
PZT film on Pt-coated Si	25	700	100	50/0.748
PZT film on Pt-coated Si	25	700	100	50/0.748

XRD patterns of these films on both Pt-coated Si and MgO shown in Figure 4.48 indicate a random orientation. The JCPDS shown is a reference pattern for the PZT (52/48) with a random orientation. This set of films were then be heat-treated in the HTXRD system at the Oak Ridge National Lab. The heating rates used were varied from 5°C to 100°C/min. The XRD patterns were collected continuously from room temperature to 700°C anneal.

5°C/minute Heating Rate

XRD patterns for a PZT film on a platinized Si substrate were collected at a constant heating rate of 5°C/minute from room temperature to 700°C. A series of XRD patterns are shown in Figure 4.49. The PZT film appeared to be amorphous at temperatures lower than 374°C. An intermediate pyrochlore or fluorite-type phase was first seen in the temperature range 374-378°C and developed to a maximum intensity at 438-442°C (3rd scan from the bottom of Fig. 4.49b). The perovskite phase first formed between 447-451°C and it continued growing to its maximum at 556-560°C (Fig. 4.49d). After that, there was no significant phase development as temperatures approached 700°C.

The integrated area under each peak was calculated using Kaleidagraph software. User-defined 2Θ minima and maxima were used as limits for the definite integral. For all cases, the 2Θ minimum and maximum used to calculate the area under the intermediate phase peak were 28.5° and 30.4°, respectively. In the case of perovskite phase, the 2Θ minimum and maximum were 30.6° and 31.6 °, respectively. Figure 4.50 shows a plot of the peak area of the intermediate and perovskite phases over a range of
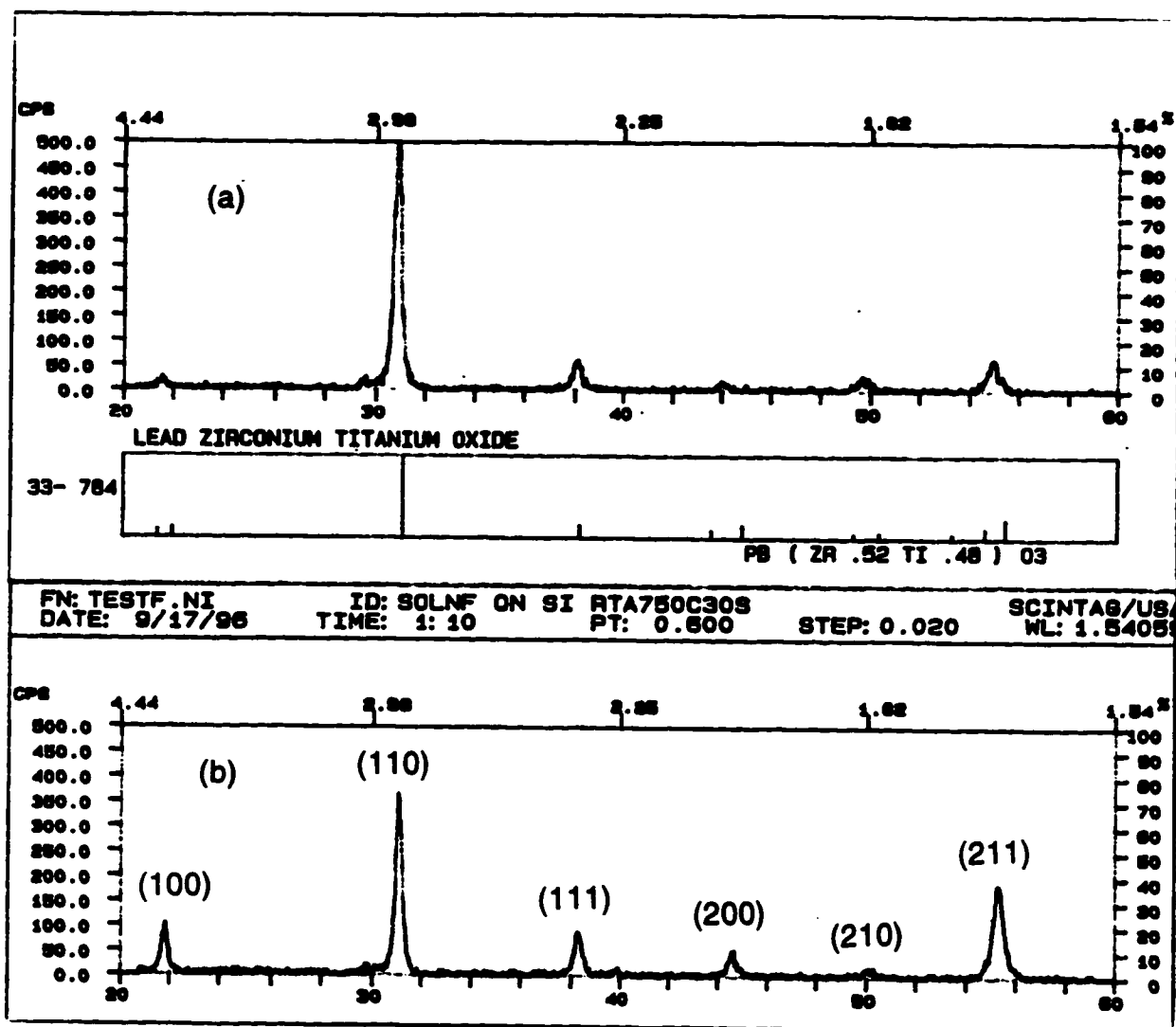
Figure 4.48. XRD patterns for PZT films on (a) Pt-coated Si and (b) MgO after RTA at 700°C for 30 seconds. Patterns showed approximately random orientations comparable to the JCPDS reference data for PZT (52/48) shown in the figure.
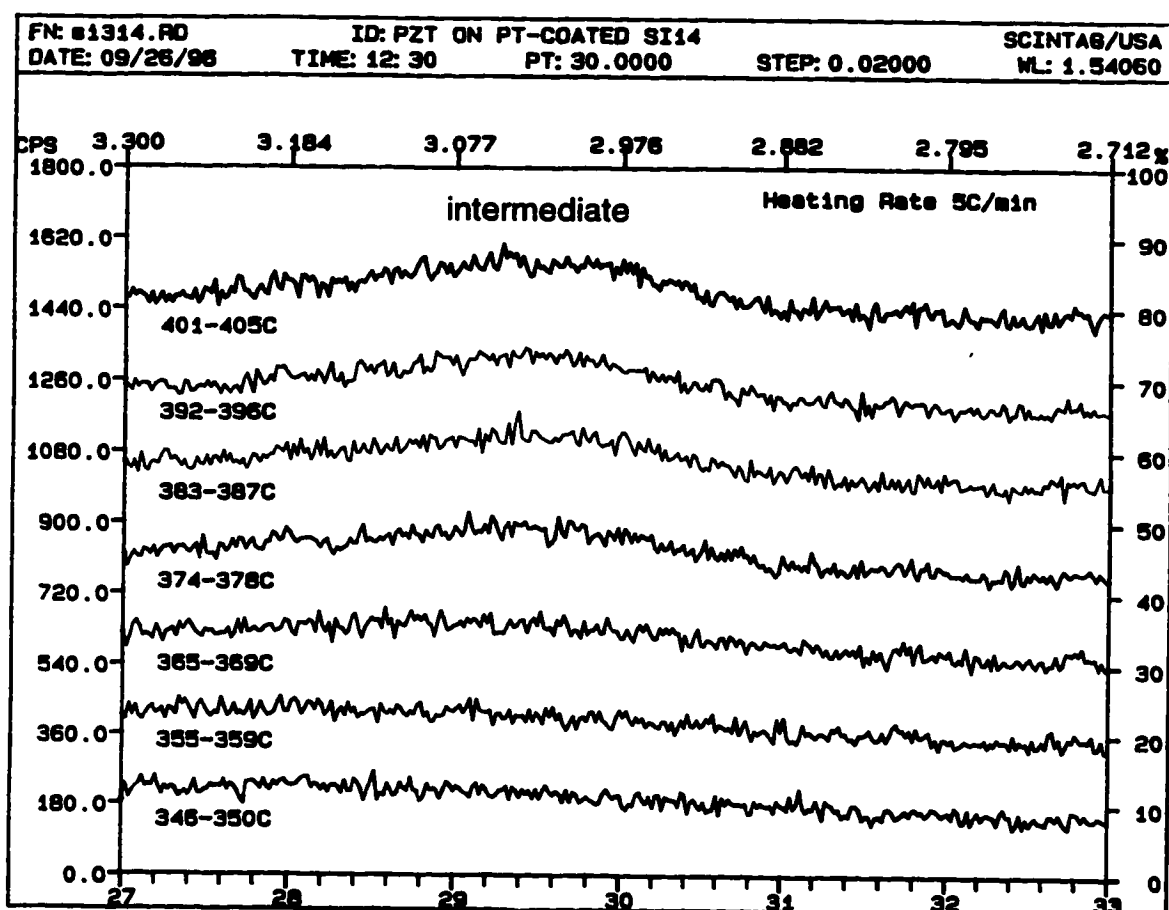
(a)

Figure 4.49. A series of XRD patterns of a PZT film on a Pt-coated Si substrate collected from room temperature to 700°C with a 5°C/min heating rate. The 2Θ range covers 27-33°.
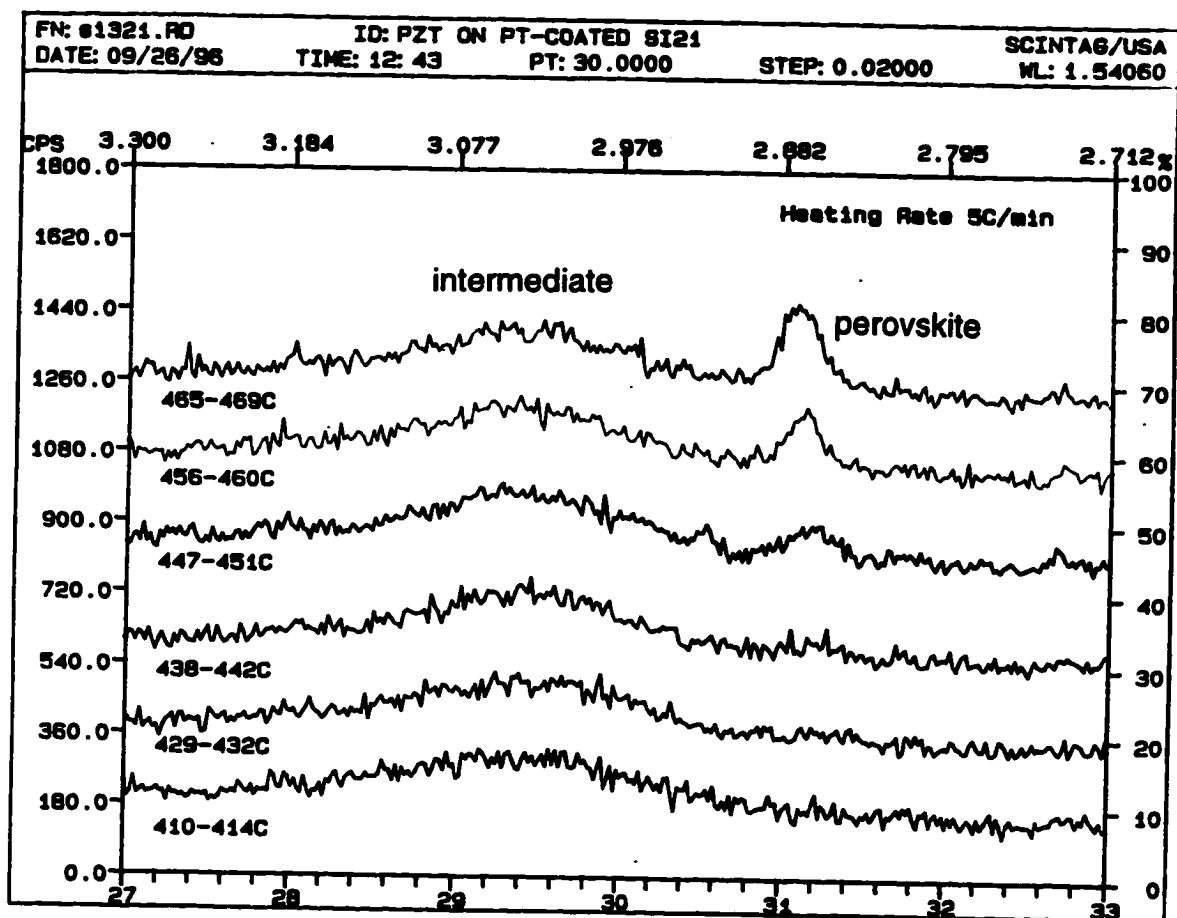
(b)

Figure 4.49 (cont.)
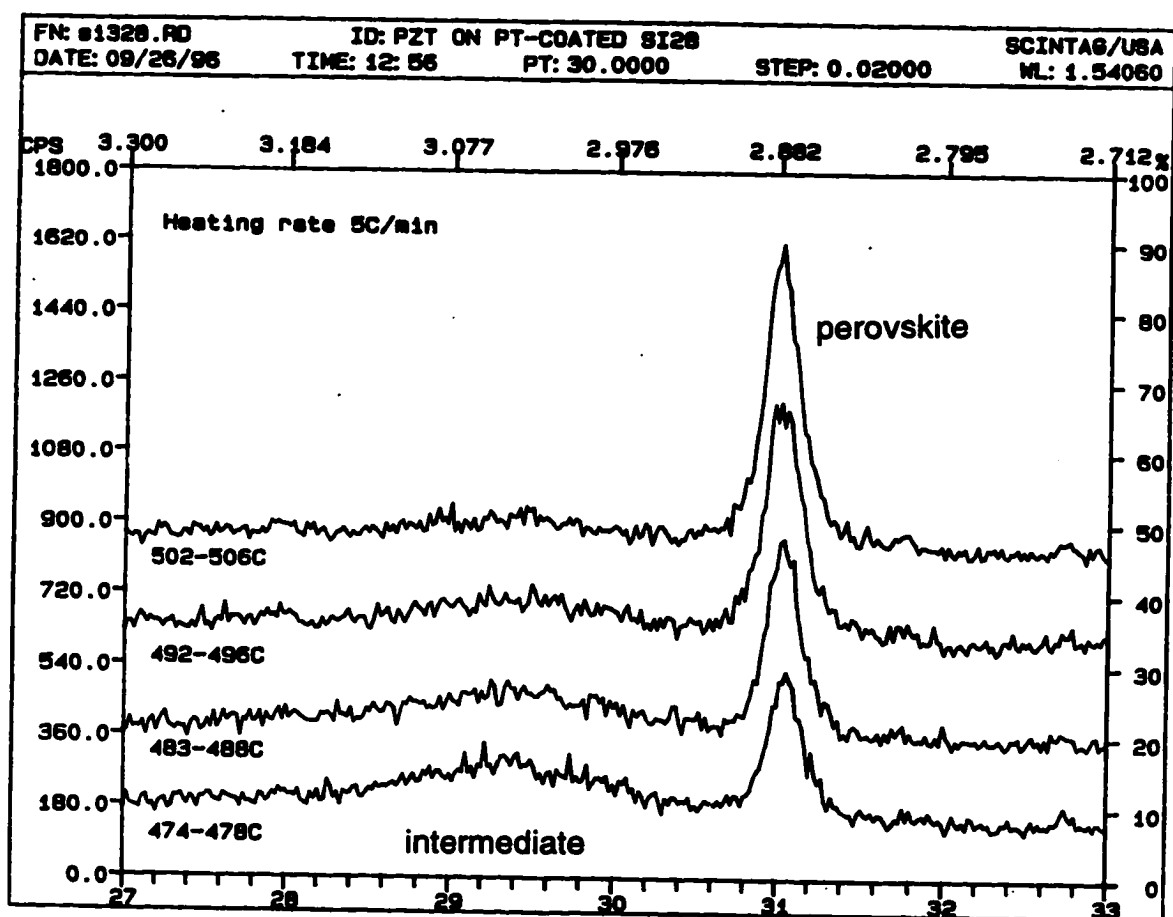
(c)

Figure 4.49 (cont.)

(d)

Figure 4.49 (cont.)

FN: s1346.RD   ID: PZT ON PT-COATED SI46   SCINTAG/USA
DATE: 09/26/96   TIME: 13:29   PT: 30.0000   STEP: 0.02000   WL: 1.54060

Heating Rate 5C/min

perovskite

700C

685-689C

646-652C

639-643C

(e)

Figure 4.49 (cont.)

Figure 4.50. A plot of the integrated peak areas of the intermediate and perovskite phases over a range of temperatures for a PZT film on a Pt-coated Si substrate. A ramp rate of 5°C/min was used.

temperatures. Conversion to perovskite phase was largely completed around 556-560°C.

XRD patterns were also collected for a PZT film on an MgO substrate at the same heating rate, 5°C/minute. A series of XRD patterns collected from room temperature to 700°C are shown in Figure 4.51. An intermediate pyrochlore or fluorite-type phase started to form at 388-391°C (3rd scan from bottom of Fig. 4.51a) and continued to grow to its maximum intensity at 498-502°C, where the perovskite phase started to nucleate. A distinct perovskite peak appeared at 508-512°C and it showed a progressive growth as temperatures increased to 627-631°C, while the amount of intermediate phase peak was suppressed in these temperature ranges. Once again, there was no major change of the intensity of the perovskite peak above 631°C. Figure 4.52 shows a plot of the peak areas of the intermediate and perovskite phases over a range of temperatures. A very small amount of residual intermediate phase remained after 600°C anneals and at the final crystallization temperature (700°C), the intermediate phase was negligible.

10°C/minute Heating Rate

For a 10°C/minute ramp rate from room temperature to 700°C, a series of XRD patterns for a PZT film on a platinized Si substrate were collected continuously. Below 357°C, the PZT film was X-ray amorphous. An intermediate pyrochlore or fluorite-type phase initially formed at 369-377°C, and it grew remarkably as temperatures rose to 424-433, where the intermediate phase reached its maximum intensity. A perovskite peak started to appear noticeably at 433-451°C. The intermediate phase converted largely to

(a)

Figure 4.51. A series of XRD patterns of a PZT film on an MgO substrate collected from room temperature to 700°C with a 5°C/min heating rate. The 2Θ range covers 27-33°.
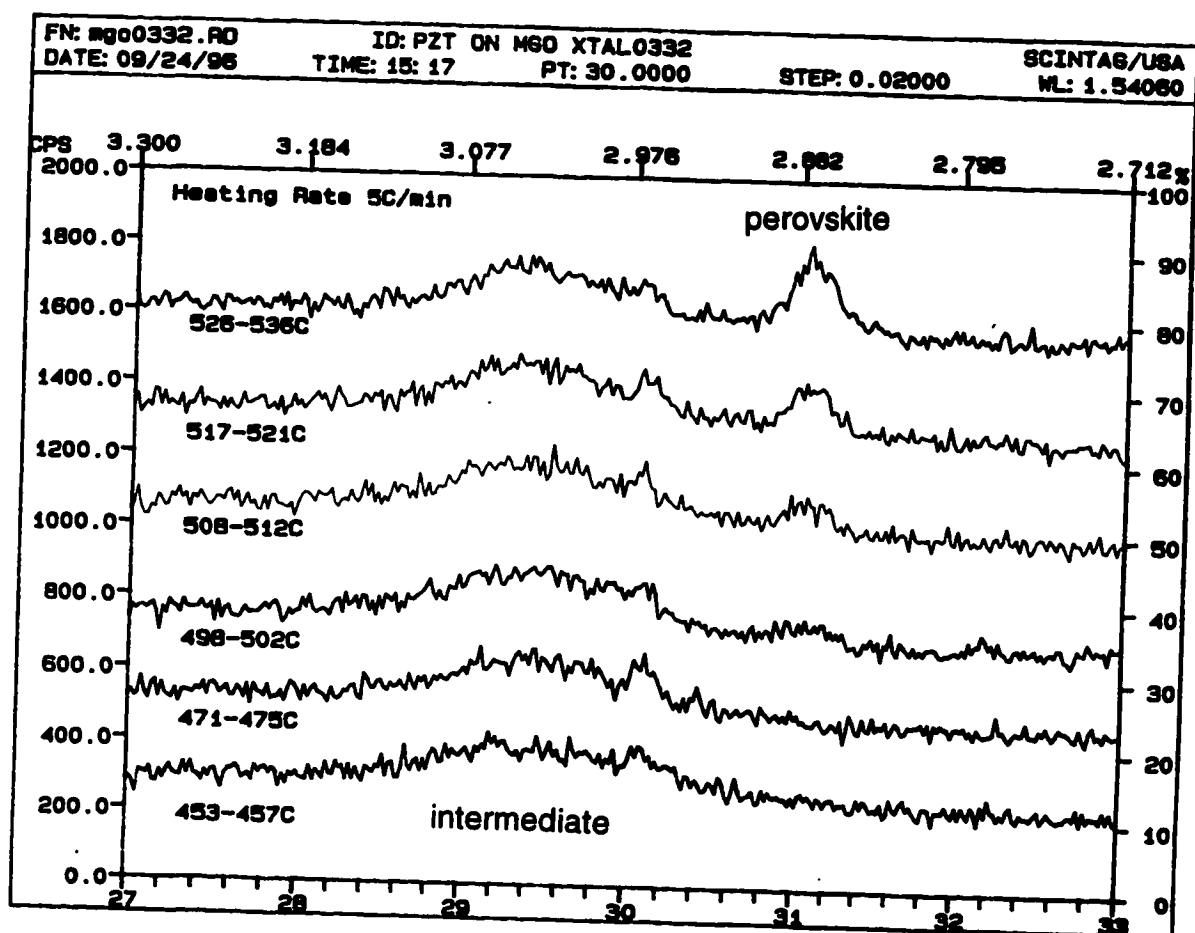
(b)

Figure 4.51 (cont.)
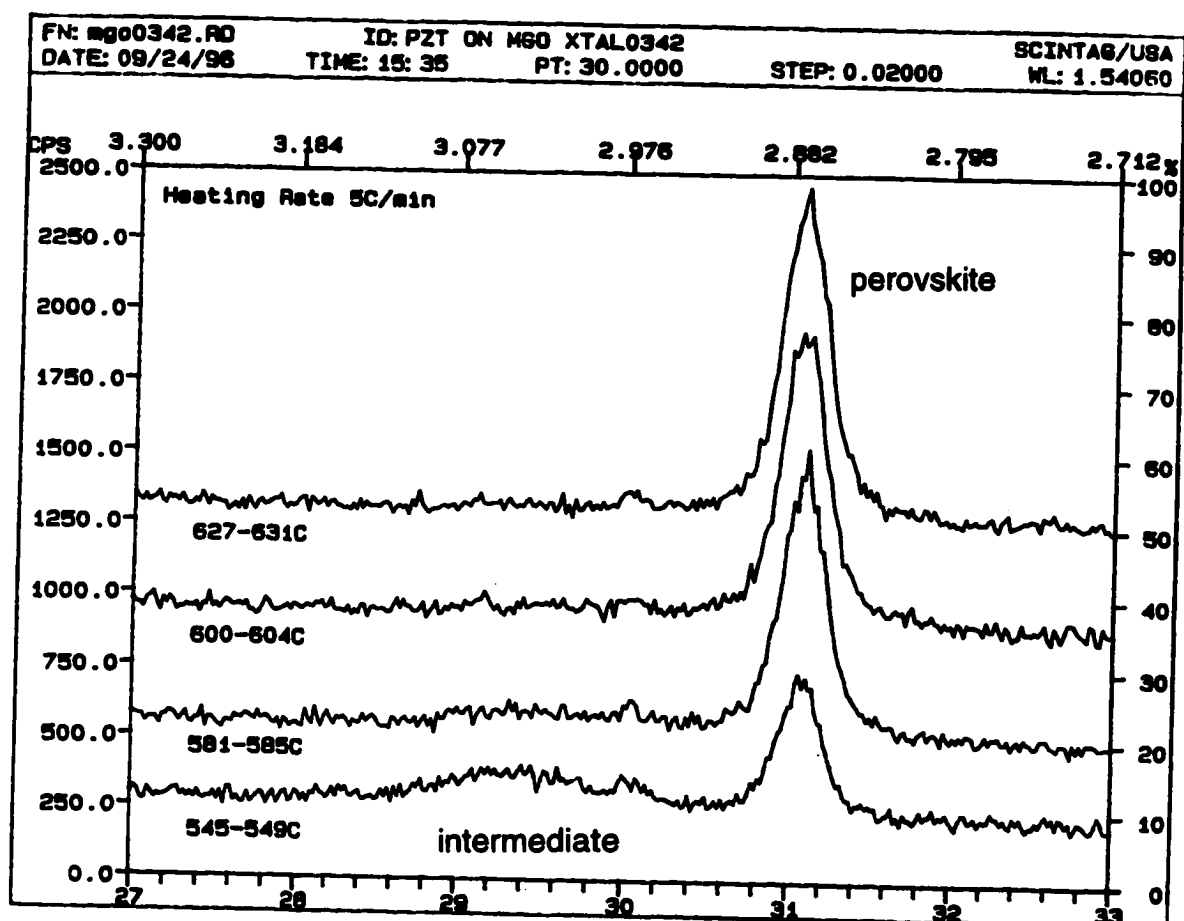
(c)

Figure 4.51 (cont.)
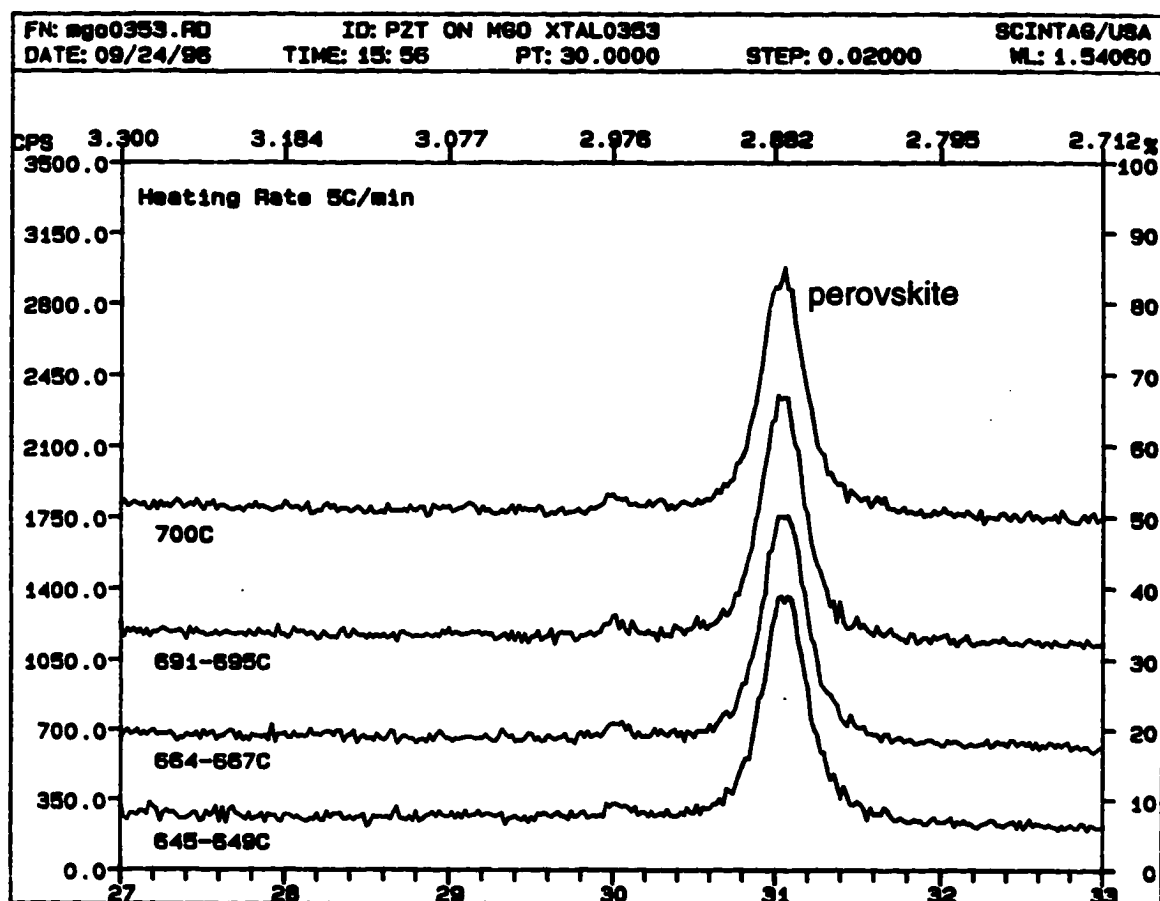
(d)

Figure 4.51 (cont.)
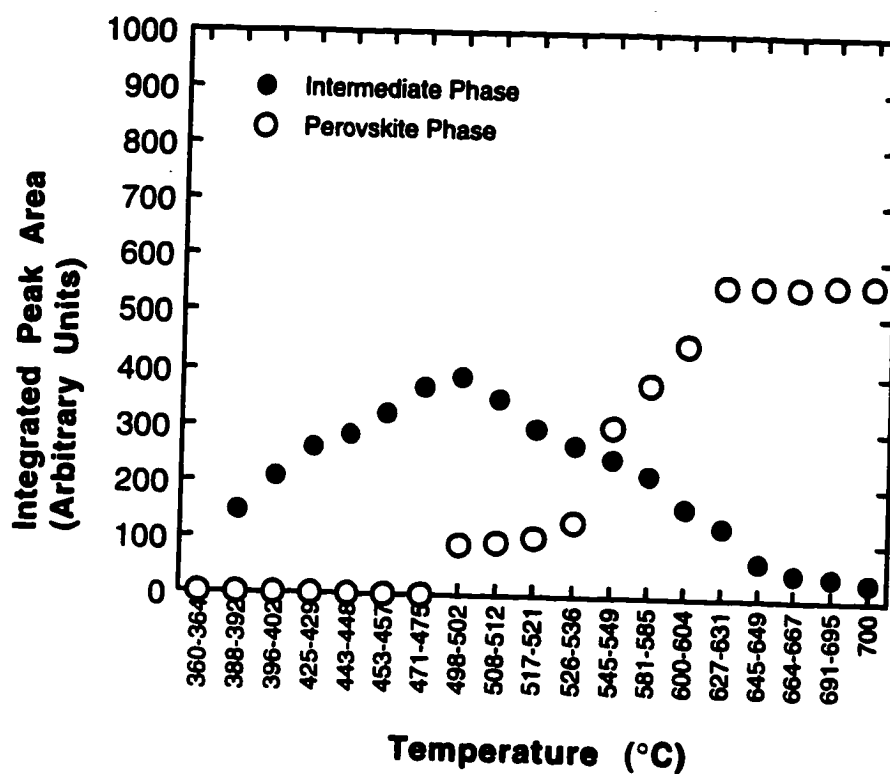
Figure 4.52. A plot of the integrated peak areas of an intermediate and perovskite phase over a range of temperature for a PZT film on an MgO substrate. A 5°C/minute heating rate was used.
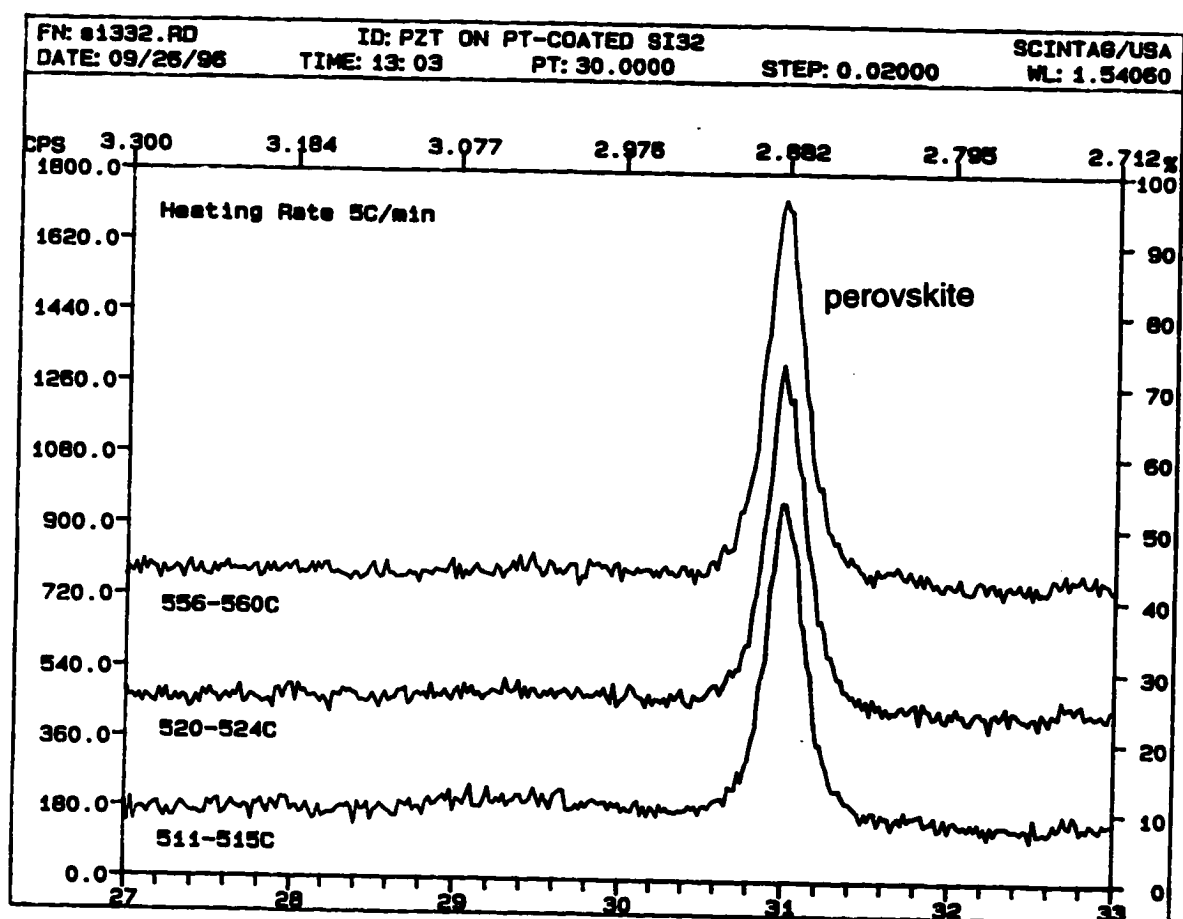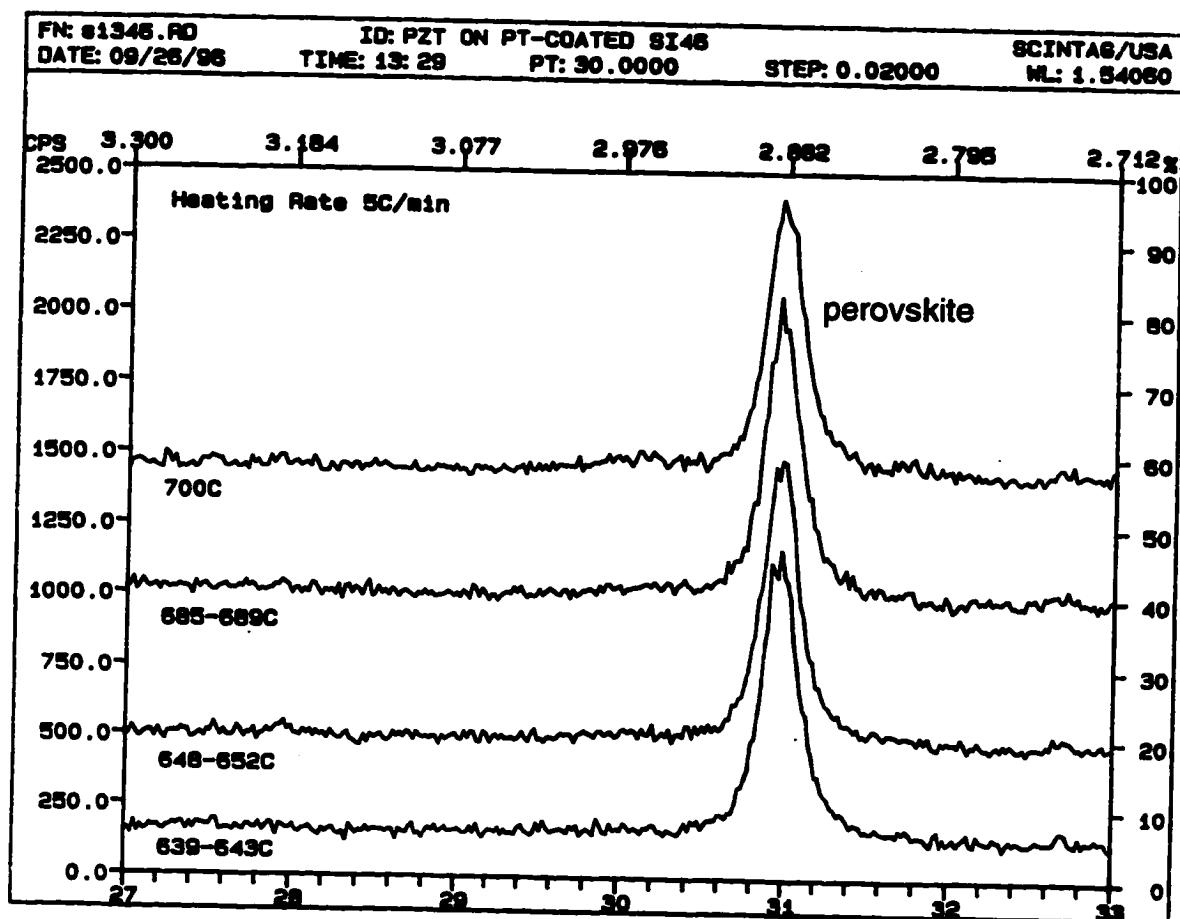
perovskite at higher temperatures. As temperatures approached 700°C, there was no indication of an intermediate phase and no significant perovskite phase development. A plot of the integrated areas under both intermediate and perovskite peaks over a range of annealing temperatures for PZT film on Pt-coated Si substrate are illustrated in Figure 4.53.

For a film on an MgO substrate, a series of XRD patterns were also collected from room temperature to 700°C at a constant ramp rate of 10°C/min. The XRD pattern at 365-373°C shows the film in the amorphous state. A small and broad hump of an intermediate phase started to form in the temperature range 420-428°C and it continued growing to its maximum intensity as temperatures increased to 548-557°C°. The perovskite phase was first observed at 529-538°C where it coexisted with the intermediate phase. At 585-593°C, a large amount of the intermediate phase had converted to the perovskite phase. The perovskite phase peak grew progressively from that point and reached its maximum intensity as temperatures rose to 641-649°C. There was no indication of an intermediate phase between 650°C and 700°C and also, there was no critical change of the perovskite phase development in this temperature range. The integrated areas under both intermediate and perovskite peaks over a range of annealing temperatures are plotted in Figure 4.54. Full perovskite phase development can be seen at 641-649°C.

20°C/minute Heating Rate

A ramp rate of 20°C/minute from room temperature to 700°C was used to *in-situ* anneal PZT films on both Pt-coated Si and MgO substrates in the HTXRD. For the film on a platinized Si substrate, a sequence of XRD patterns
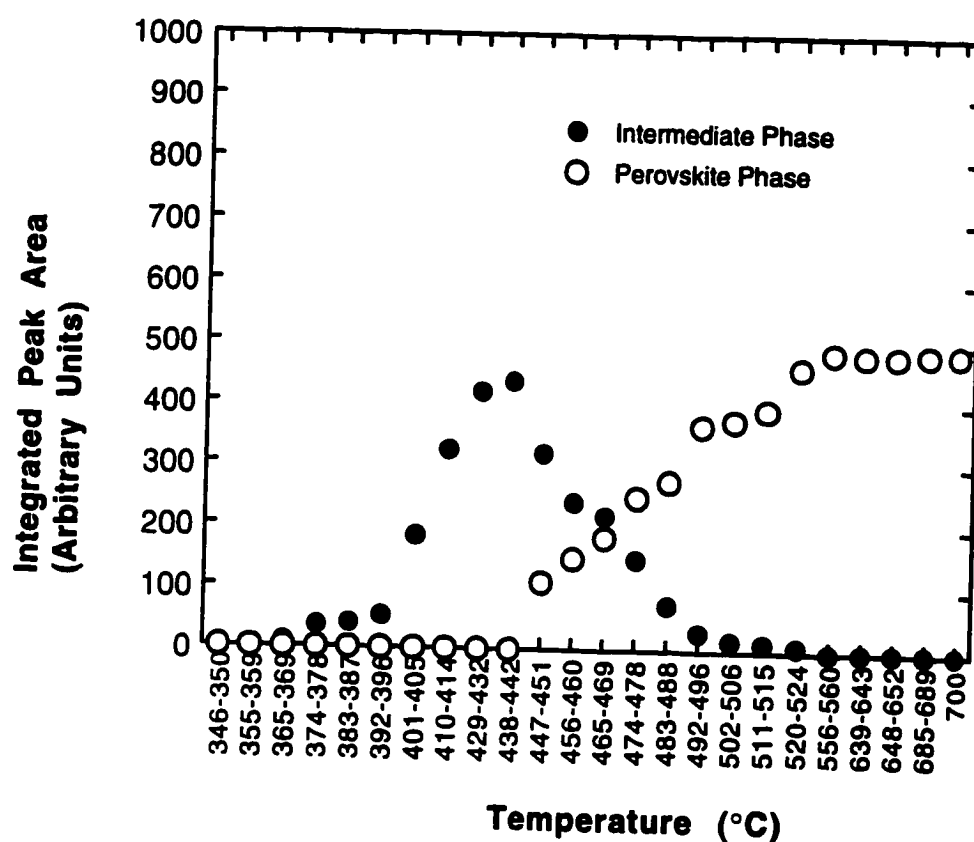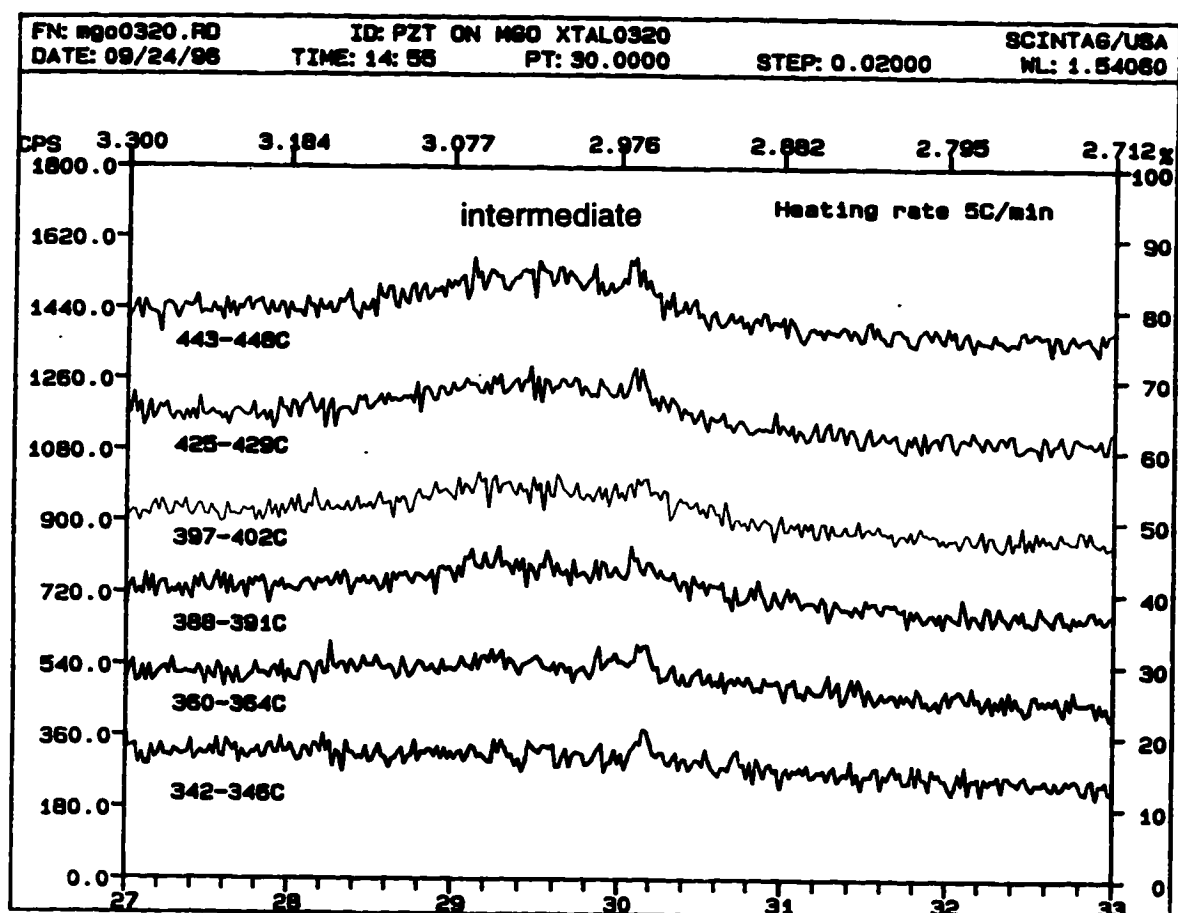
Figure 4.53. A plot of the integrated peak areas of an intermediate and perovskite phase over a range of temperature for a PZT film on a Pt-coated Si substrate. A 10°C/minute heating rate was used.

Figure 4.54. A plot of the integrated peak areas of the intermediate and perovskite phases over a range of temperature for a PZT film on an MgO substrate. A 10°C/minute heating rate was used.

were collected during heat treatment in the same manner as at low heating rates. The PZT film was found to be in an amorphous state at and below 340-355°. A broad hump of the intermediate phase peak was first observed at 392-410°C and it continued to grow until reaching its maximum amount at 450-466°C, where the perovskite peak started to develop. As temperatures increased, a considerable amount of the intermediate phase converted to the perovskite phase (i.e., at 524-540°C). The perovskite peak grew quickly to its highest intensity as temperatures approached 561-578°C, where no trace of any residual intermediate phase peak was found at that point. Between the temperatures 598-614°C and 700°C, there was no major change in perovskite phase development. Figure 4.55, once again, shows a plot of the integrated peak areas of these 2 phases over a range of temperatures for a 20°C/min ramp rate.

For this ramp rate of 20°C/min, a sequence of XRD patterns were also collected during annealing to 700°C for a PZT film on an MgO substrate. At temperatures lower than 376-392°C, XRD scans indicate that the film is in an amorphous state. An intermediate pyrochlore or fluorite-type material was initially nucleated between 412-430°C and it continued to grow appreciably with heat treatment. By 558-575°C, the intermediate phase peak extended to its maximum intensity. At this same temperature range, a small, but noticeable, perovskite peak was first formed. The higher the annealing temperatures, the more the intermediate phase converted to perovskite. As temperatures increased to 668-684°C, there was no evidence of the intermediate phase left in the film. The perovskite peak continued crystallizing until the 700°C anneal was approached. The integrated areas under both intermediate and perovskite

Figure 4.55. A plot of the integrated peak areas of the intermediate and perovskite phases over a range of temperature for a PZT film on a Pt-coated Si substrate. A 20°C/minute heating rate was used.

peaks were plotted over a range of annealing temperatures as shown in Figure 4.56.

50°C/minute Heating Rate

A faster ramp rate of 50°C/minute was also used to *in-situ* anneal PZT films in the HTXRD. To keep up with this fast heating rate, a faster scan rate of 50°/minute was employed for the same 2Θ range of interest. For a film on a platinized Si substrate, a series of XRD patterns were collected continuously during the heat treatment. At 324-342°C, the film appeared to be in an amorphous state. A very small and broad hump of an intermediate pyrochlore or fluorite-type material was initially found at 398-408°C and it grew to its maximum amount at 459-476°C. At this same temperature range, a tiny perovskite peak was observed to coexist with the intermediate phase. The perovskite peak then quickly grew to its highest intensity as temperatures reached 594-610°C, whereas there was no sign of any intermediate phase left in this temperature range. Between 610° and 700°C, there was no additional growth of the perovskite phase peak. The integrated areas under both intermediate and perovskite peaks plotted over a range of annealing temperatures are reported in Figure 4.57.

For a film on MgO with a 50°C/min ramp rate, a sequence of XRD patterns were also collected continuously during heat treatment. The PZT film appeared to be in an amorphous state at temperatures below 404-412°C. A small and broad hump of an intermediate phase was initially found at 471-488°C and it grew to its highest amount as temperatures reached 537-555°C.

Figure 4.56. A plot of the integrated peak areas of the intermediate and perovskite phases over a range of temperatures for a PZT film on an MgO substrate. A 20°C/minute heating rate was used.
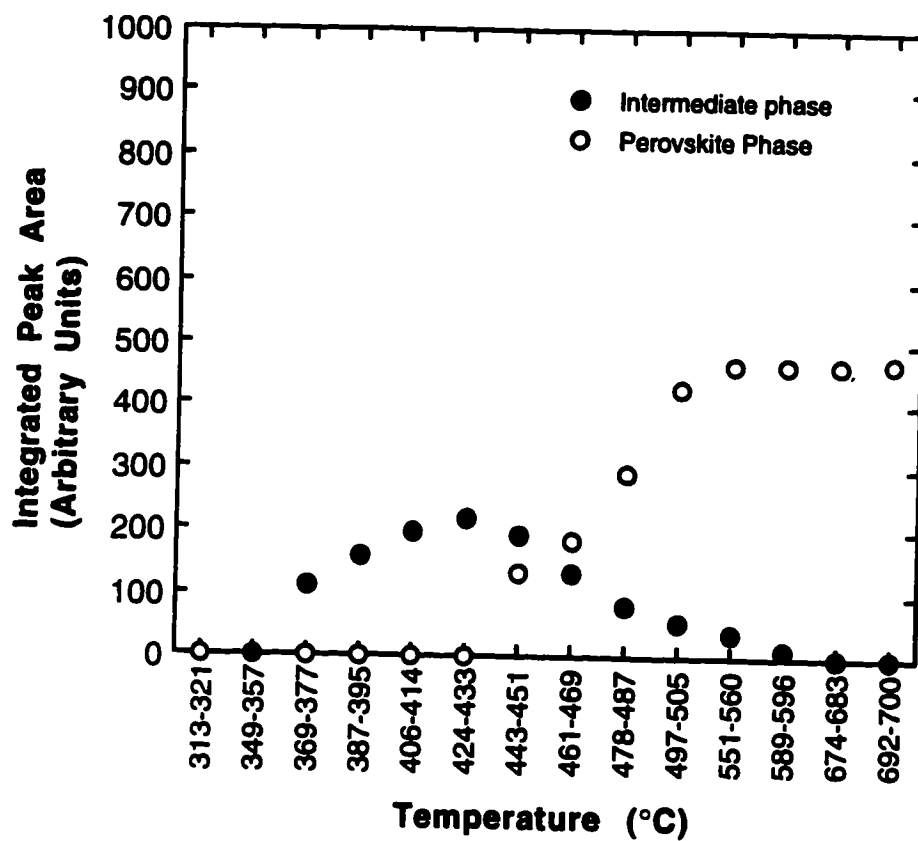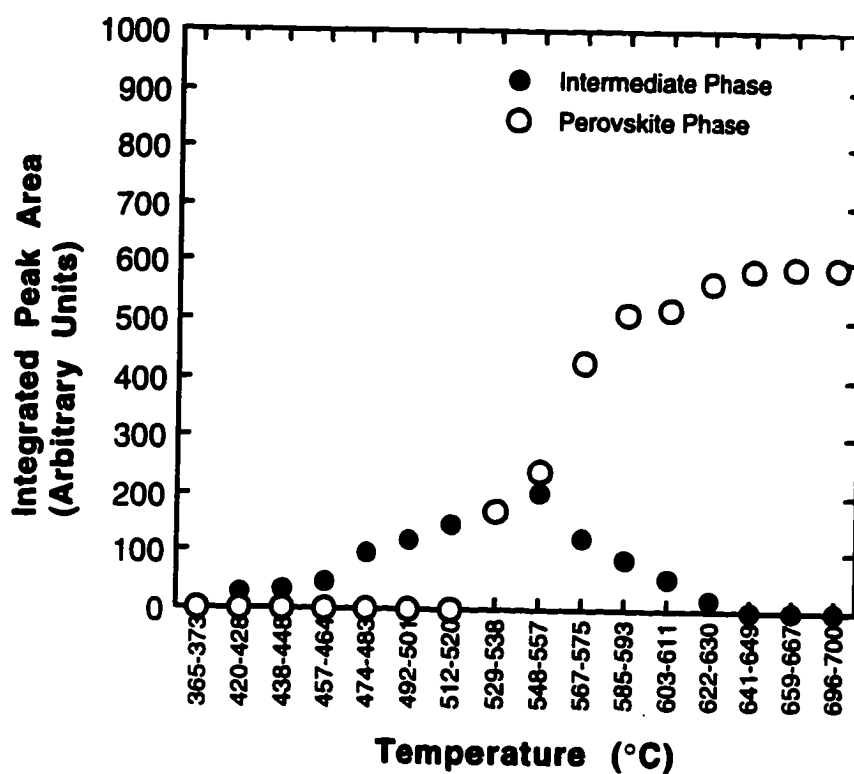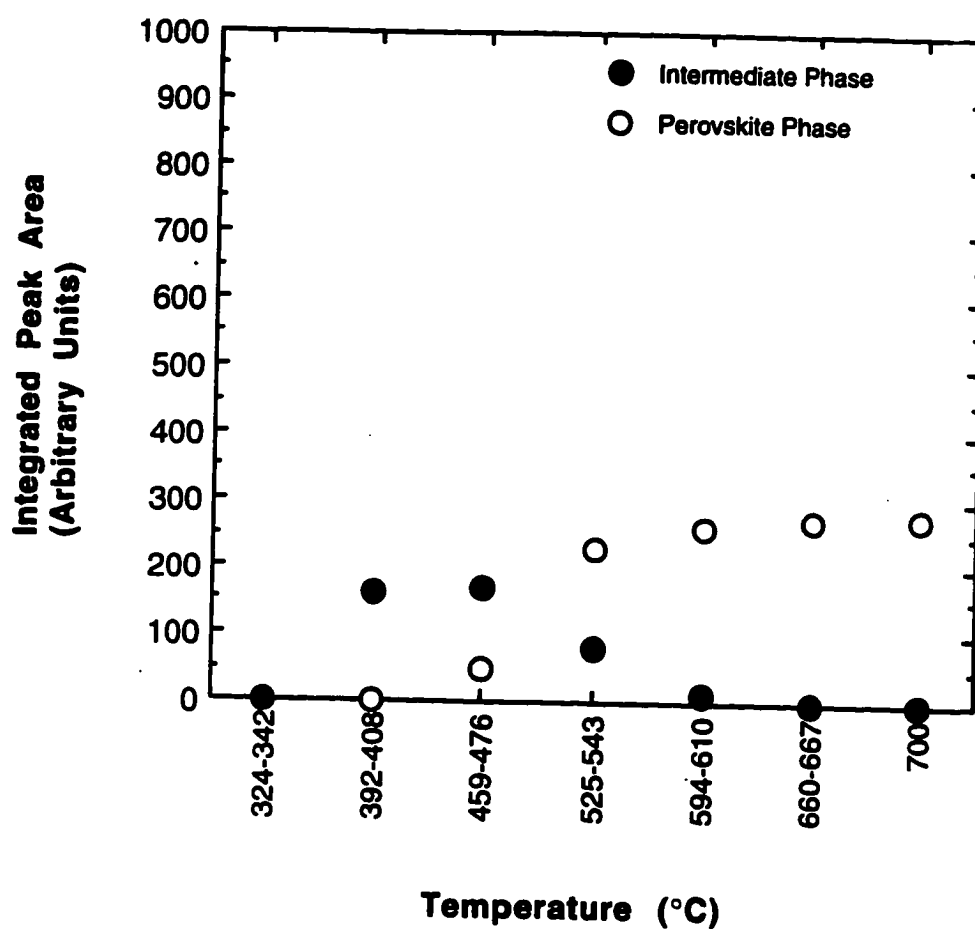
Figure 4.57. A plot of the integrated peak areas of the intermediate and perovskite phases over a range of temperature for a PZT film on a Pt-coated Si substrate. A 50°C/minute heating rate was used.

The first appearance of a high intensity perovskite peak was seen at 606-623°C. Unfortunately, at this fast ramp rate of 50°C/minute, the dead time of the HTXRD (approximately 1.5 minutes) made it impossible to scan between 555°C and 606°C. Thus, the initial temperatures of the perovskite phase growth can not be determined. As temperatures increased to 700°C, a large amount of the intermediate phase was converted to the perovskite phase. A plot of the integrated peak areas of both the intermediate and perovskite phase over a range of annealing temperatures is shown in Figure 4.58. Full perovskite phase development can be seen at 700°C.

100°C/minute Heating Rate

A 100°C/minute ramp rate was the fastest annealing rate employed in these *in-situ* XRD studies in order to determine whether the intermediate pyrochlore or fluorite-type material could be bypassed. A sequence of XRD patterns which were collected for a film on a Pt-coated Si substrate during annealing to 700°C are shown in Figure 4.59. The X-ray pattern at 440-456°C indicates that a small amount of an intermediate phase formed. As temperatures increased to 557-576°C, the perovskite peak was first seen, whereas the intermediate phase was suppressed. Full conversion to the perovskite phase was completed as the temperature reached 700°C. Figure 4.60 shows a plot of the integrated areas under these two phases over a range of annealing temperatures.

For a film on MgO, a series of XRD patterns collected from room temperature to 700°C with a 100°C/min heating rate is shown in Figure 4.61. The X-ray pattern at 330-347°C shows the film to be in the amorphous state. By
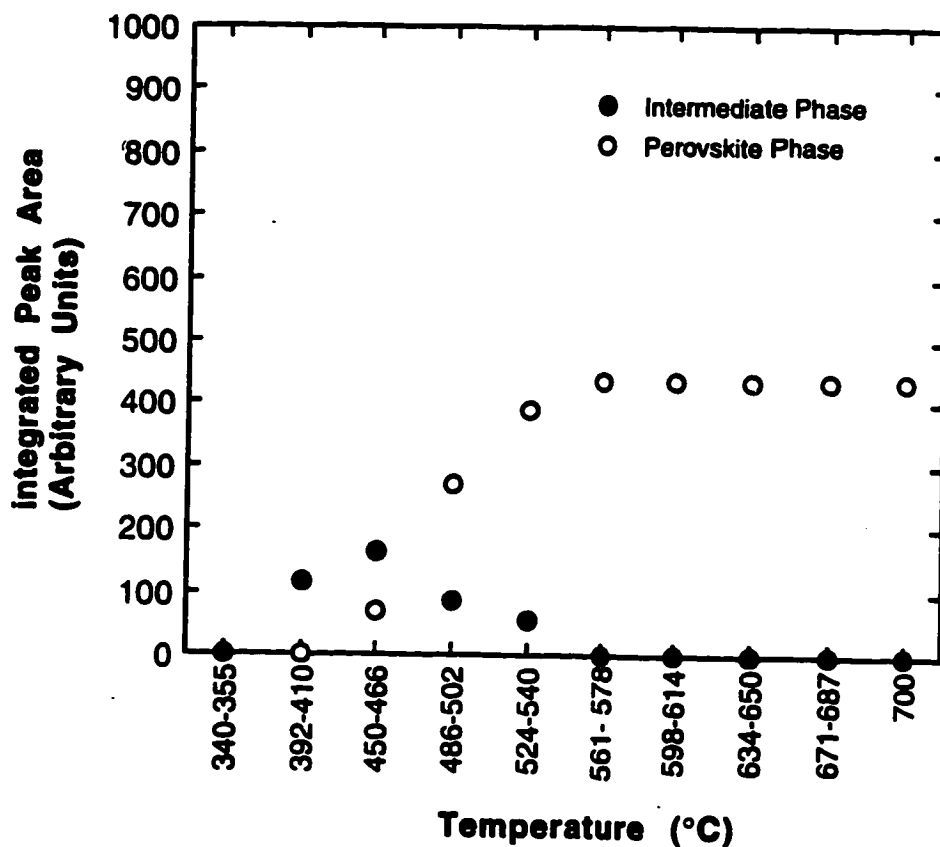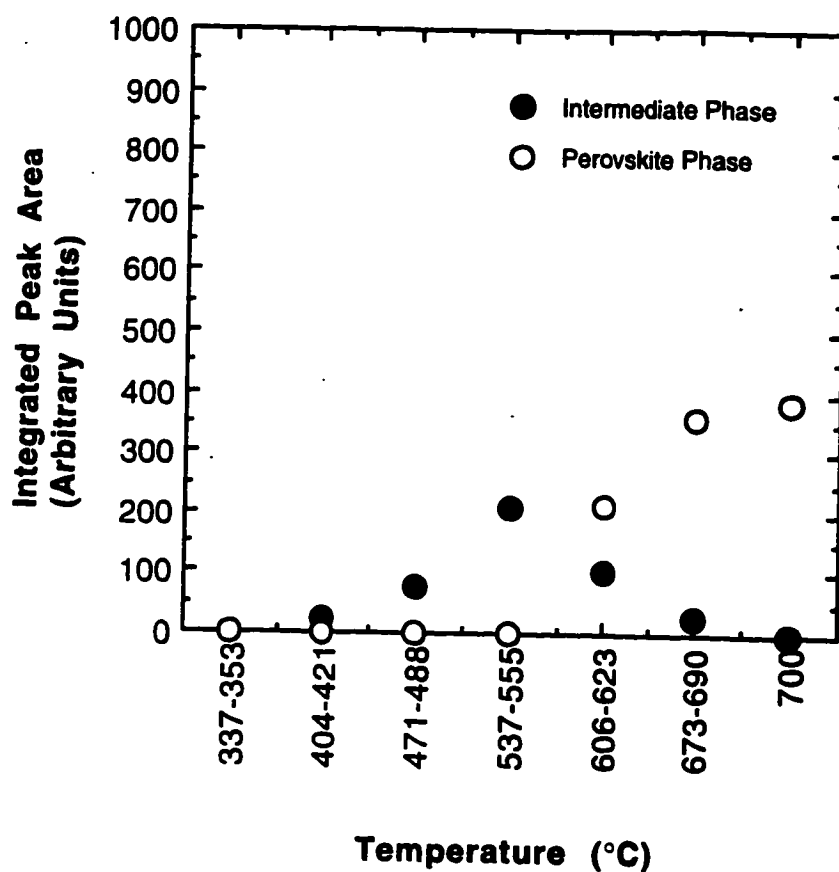
Figure 4.58. A plot of the integrated peak areas of the intermediate and perovskite phases over a range of temperatures for a PZT film on an MgO substrate. A 50°C/minute heating rate was used.
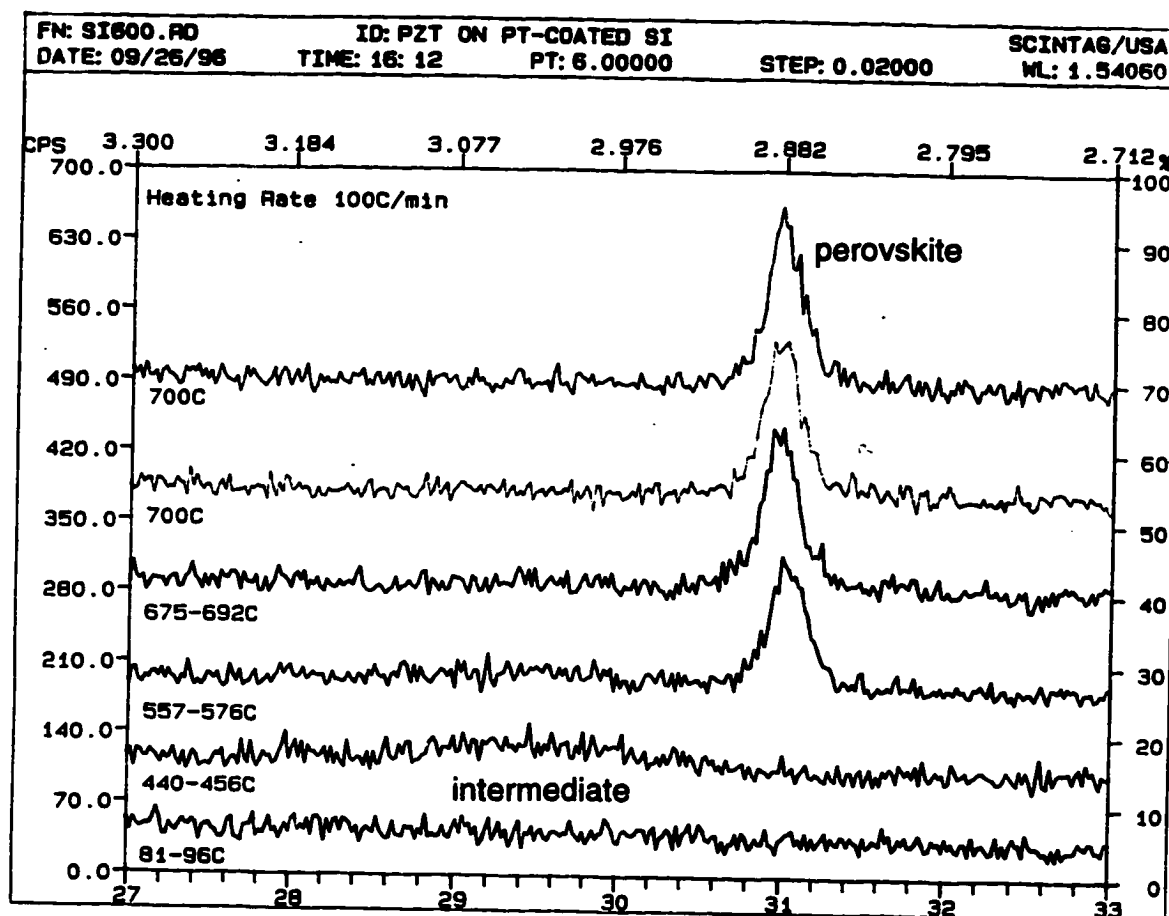
Figure 4.59. A series of XRD patterns of a PZT film on Pt-coated Si substrate collected from room temperature to 700°C with a 100°C/min heating rate. The 2Θ range covers 27-33°.
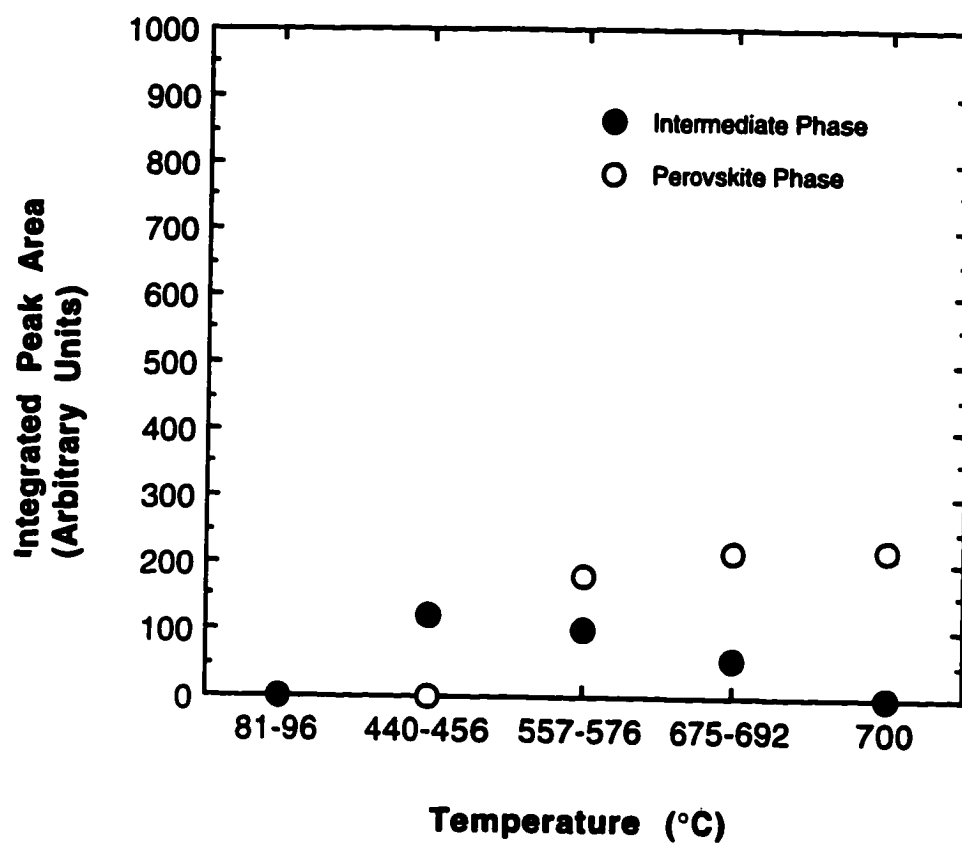
Figure 4.60. A plot of the integrated peak areas of the intermediate and perovskite phases over a range of temperatures for a PZT film on a Pt-coated substrate. A 100°C/minute heating rate was used.

FN: mgo0702.RD   ID: PZT ON MGO XTAL0702   SCINTAG/USA
DATE: 09/25/96   TIME: 11: 09   PT: 6.00000   STEP: 0.02000   WL: 1.54060
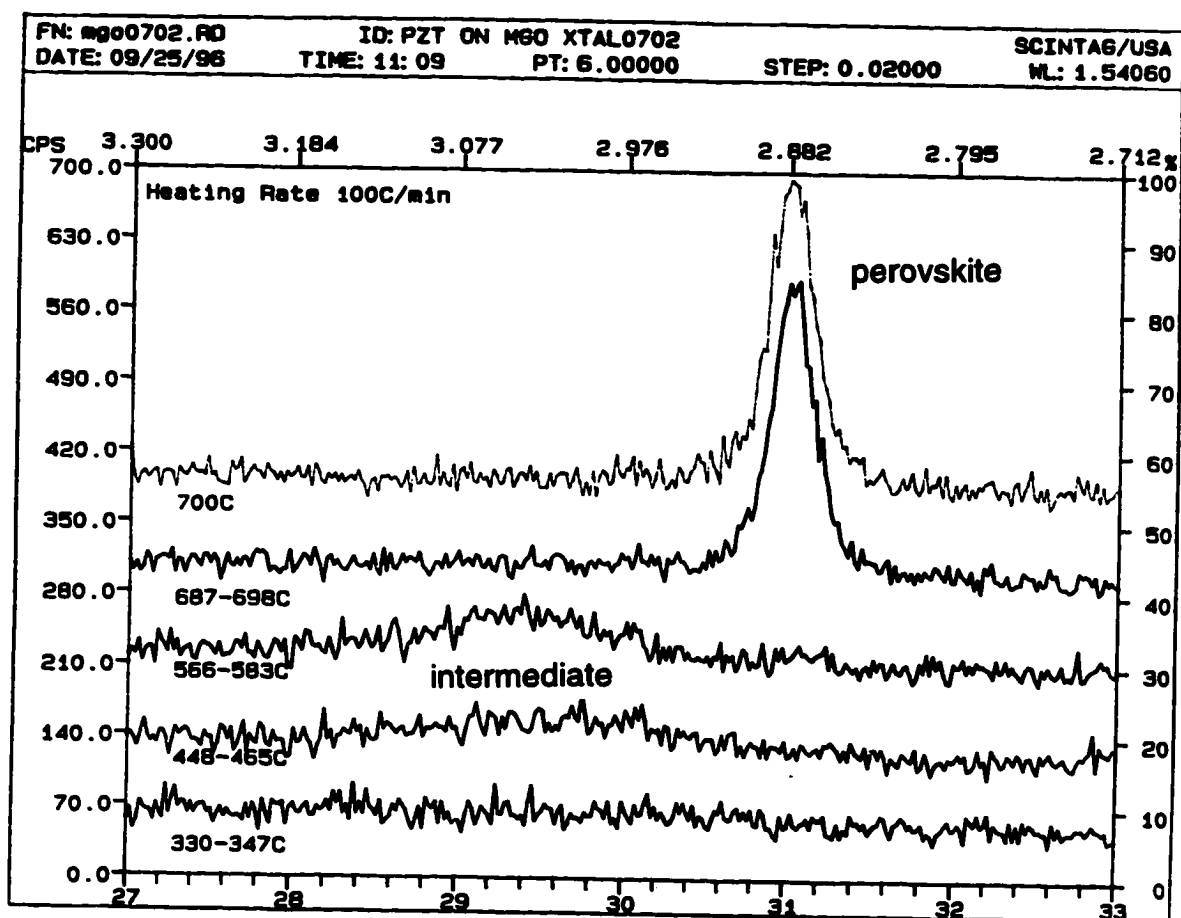
Figure 4.61. A series of XRD patterns of a PZT film on an MgO substrate collected from room temperature to 700°C with a 100°C/min heating rate. The 2Θ range covers 27-33°.

448-465°C the intermediate peak initially formed and it continued crystallizing to its maximum amount at 566-583°C. At this temperature range, a small amount of perovskite phase started to nucleate (the 566-583°C scan). As the crystallization temperature approached 700°C, the perovskite peak progressively grew to its highest intensity. Figure 4.62 depicts the integrated peak areas of both the intermediate and perovskite phase over a range of temperatures.

For several of the heating rates, it was observed that the very first perovskite peak which appeared was centered at a slightly higher 2Θ values than subsequent peaks. One possible explanation for this would be there may be some composition heterogeneity in these sol-gel films. In particular, the observed peak shift would imply that the initial perovskite nuclei is slightly Ti-rich, which is consistent with previous reports that the intermediate phase is Zr-rich (Lakeman et al 1994). If this occurs, then the composition rapidly homogenizes after crystallization. A second possible explanation for the peak shift would be stresses on the crystallites.

In summary, none of the ramp rates used in these studies, from 5 to 100°C/minute permitted the bypass of the intermediate phase formation prior to perovskite phase formation. This finding is in good agreement with the previous X-ray studies using the R-B PSSD system. The temperatures where both intermediate and perovskite phases initially formed and where they reached their maximum intensity are summarized in Table 4.6. It is important to note that some of the variability in temperatures is due in part to the finite dead time of the detector.

It was found in all heating rates that the nucleation temperatures of the intermediate and perovskite phases were lower for Pt-coated Si than for MgO. For all heating rates, the nucleation temperature of the intermediate phase for a film on Pt-coated Si was found lower than that for MgO. A similar observation was also found for the case of the perovskite phase. The explanation for these nucleation temperature differences
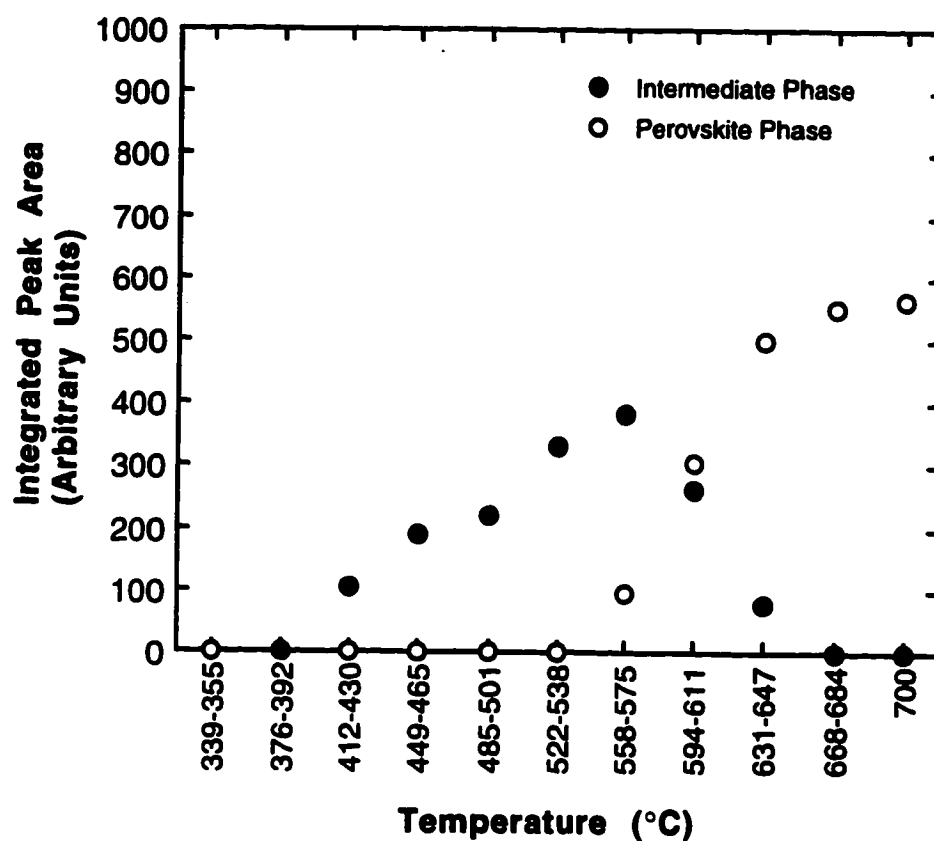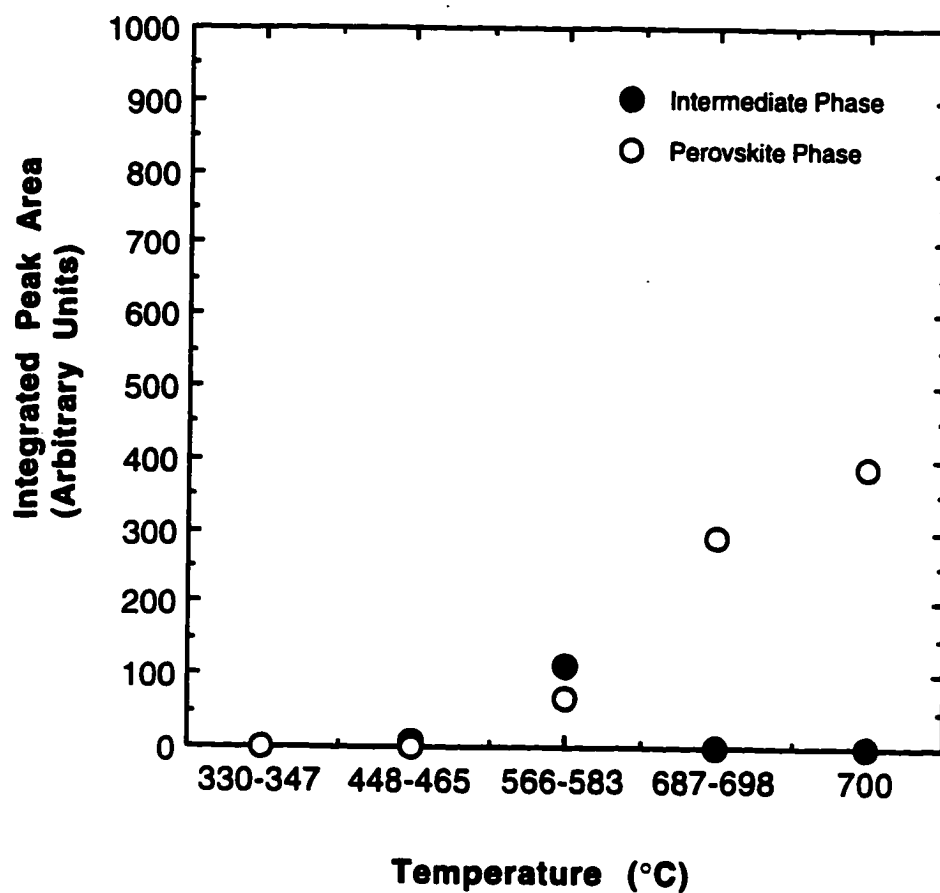
Figure 4.62. A plot of the integrated peak areas of the intermediate and perovskite phases over a range of temperatures for a PZT film on an MgO substrate. A 100°C/minute heating rate was used.

Table 4.6

A summary of phase formation temperatures for PZT thin films by HTXRD
studies at various heating rates

Heating Rate (°C/minute)	Substrate	Intermediate Phase		Perovskite Phase	
		Observed T Starting (°C)	T max (°C)	Observed T Starting (°C)	T max (°C)
5	Pt-coated Si	374-378	438-442	447-451	556-560
5	MgO	388-392	498-502	498-502	627-631
10	Pt-coated Si	369-377	424-433	443-451	551-560
10	MgO	420-428	548-557	529-538	641-649
20	Pt-coated Si	392-410	450-466	450-466	561-578
20	MgO	412-430	558-575	558-575	700
50	Pt-coated Si	392-408	459-476	459-476	594-610
50	MgO	404-421	537-555	606-623	700
100	Pt-coated Si	440-456	440-456	557-576	675-692
100	MgO	448-465	566-583	566-583	700

may be due to the difference of the thermal emissivities between both the Pt-coated Si and the transparent MgO substrates. Thus, films on Pt-coated Si may have experienced a higher temperatures than films on MgO for a particular ramp rate.

4.2.2.3. Non-Isothermal Kinetics via High-Temperature XRD

As previously discussed in section 3.3.3, the *in-situ* high temperature X-ray diffractometer has been used to monitor the crystallization kinetics of both the intermediate and perovskite phases in PZT films in these studies. According to the series of XRD data at various heating rates in the HTXRD studies, the relative amounts of the fraction transformed between the intermediate and the perovskite phase can be estimated by considering the integrated peak areas, A (arbitrary units) of both phases. The following equation was used;

$$\text{Perovskite Volume Fraction Transformed} = \frac{A_{110}}{A_{110} + A_{222}} \qquad (4.1)$$

where A_{110} and A_{222} are the integrated peak areas of the diffraction peaks for (110) perovskite and (222) intermediate phase (indexed for the pyrochlore cell) at each XRD scan, respectively. Since all of these PZT films on both Pt-coated Si and MgO used in the HTXRD studies at constant ramp rates of 5°C to 100°C/min showed nearly random orientation, attempts to apply non-isothermal kinetics to high temperature XRD results were made in order to determine the Avrami coefficient (n). In order to determine whether the JMA rate equation was appropriate, the rapid check suggested by Henderson (1979) was performed. As described in that work, the JMA equation is appropriate for crystallization

data which shows the maximum transformation rate at the point where 60 to 63% of the transformation is completed.

In this study, the volume fraction transformed of the perovskite phase for each heating run was approximated with a polynomial expression as a function of temperature over the transformation range. The derivative of this expression was then taken. Since the heating rate was constant, the maximum rate of crystallization will correspond to the point where dx/dT goes through a maximum. This point was determined and the volume fraction transformed at this maximum point was then calculated. It was found that the peak transformation rate did not occur at the point where 60 to 63% of the transformation completed. Values ranged from ~0.3 to 0.7. Consequently, the data analyzed here does not satisfy the JMA equation to non-isothermal conditions.

Several reasons for this can be envisioned, which fall into two categories; failure to satisfy the assumptions which permit the JMA equation rate to be applied under non-isothermal conditions and uncertainties in calculations of the volume percent transformed at a given temperature. As previously discussed, to apply the JMA equation to a non-isothermal case, the sample should have; 1) spatially random nucleation, 2) a transformation rate which is independence of the thermal history, and 3) a constant activation energy. Since, in general, the nucleation rate and the growth rate have different activation energies, the last point in particular may not describe the kinetics of the intermediate to perovskite phase transformation over the heating range studied here.

Additional problems could be due to the calculation of the volume fraction transformed from the X-ray data. In particular, since the intermediate phase peak was low intensity, small changes in the 2Θ integration limits did affect the measured peak area somewhat. Such variations reflect directly into the calculated % transformed. The error source was much less important for the perovskite peak area calculations. In addition, small sample-to-sample variations in the film preferred orientation complicate the calculation of the volume fraction transformed. Several normalizations of the relative peak areas were tried to minimize these errors, but it was not possible to find a consistent normalization factor for all the data sets which permitted the JMA equation to be applied unambiguously.

In sum, the crystallization of PZT films has been assessed as a function of annealing temperature and heating rates. The transformation proceeds from the amorphous to the intermediate phase, and from the intermediate to the perovskite phase. The heating rates from 5 to 100°C/minute used in this studies do not allow the intermediate pyrochlore phase to be bypassed.

4.2.3. Microstructural Study

4.2.3.1. Field Emission Scanning Electron Microscopy

To examine the microstructure of PZT films in this study, a field-emission scanning electron microscope (FESEM) was employed. Sol-gel PZT films with a composition 52/48 (Zr/Ti ratio) were spin-coated onto Pt-coated Si and sapphire substrates and then rapid thermally annealed at 700°C or 750°C for 30 seconds. Thin film surfaces were then gold-coated for 10 seconds before

taking micrographs using the *JEOL JSM-6300F* microscope with a 30 KeV accelerating voltage. The magnifications were varied from 2300X to 200,000X.

The micrographs of the surface morphology of PZT films on Pt-coated Si substrates after RTA at 700°C for 30 seconds are shown in Figures 4.63 and 4.64. Based on these figures, the sol-gel PZT films prepared in this study have a uniform, fine-grained, and dense microstructure at its surface. The primary grain size at the 100,000X magnification in Fig. 4.63 is approximately 10 to 15 nm. Figure 4.64 shows a high magnification image at 200,000X of the surface of a PZT film on Pt-coated Si which was, again, RTAd at 700°C for 30 seconds. The micrograph shows a cluster structure consisting of approximately 150 to 230 nm cluster size.

The clusters are bounded by dark regions which were defined as cluster boundaries (Fox 1992). It is interesting to note that sol-gel derived PZT thin films also formed cluster structures after being rapid thermally annealed. Previous studies by Fox (1992) and Fox et al. (1992) also reported cluster structures for annealed lead lanthanum titanate (PLT) thin film grown by multi-ion-beam-reactive sputtering.

A sol-gel PZT film which was spin-coated on a sapphire substrate was also examined by FESEM. The film was RTAd at 700°C for 30 seconds as was done for the films on Pt-coated Si substrates. Figure 4.65 shows the image of the surface of a film at a magnification of 2300X. The image shows a dense cluster structure with various cluster sizes ranging from 300 nm to 10 μm in diameter. The cluster boundaries are clearly observed in this figure.

```
                                    100nm
PSUMCL      30KU  X200,000   12mm
```
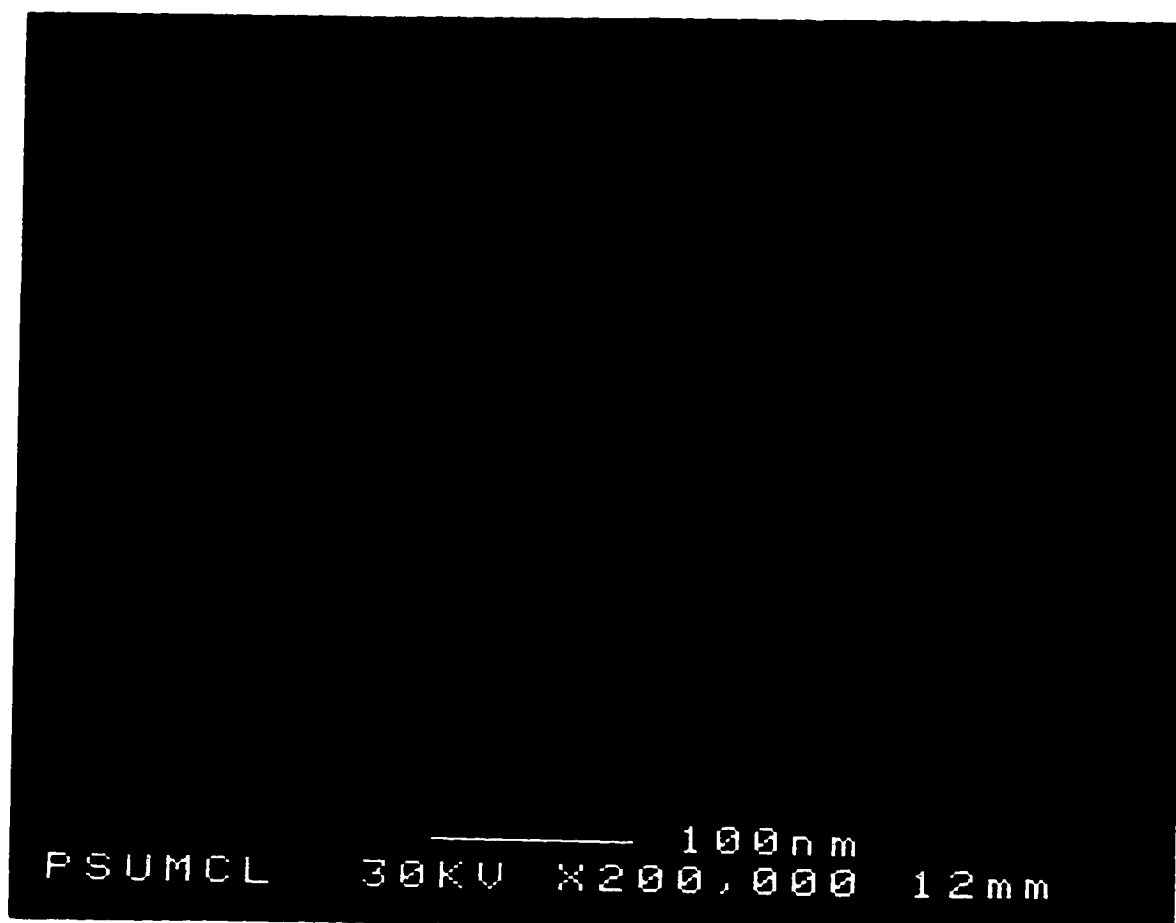
Figure 4.63. A FESEM micrograph of the surface of a PZT film on a Pt-coated Si substrate at 100,000X magnification. Film was RTAd at 700°C for 30 seconds.

PSUMCL   30KV   X100,000   11mm   ——— 100nm
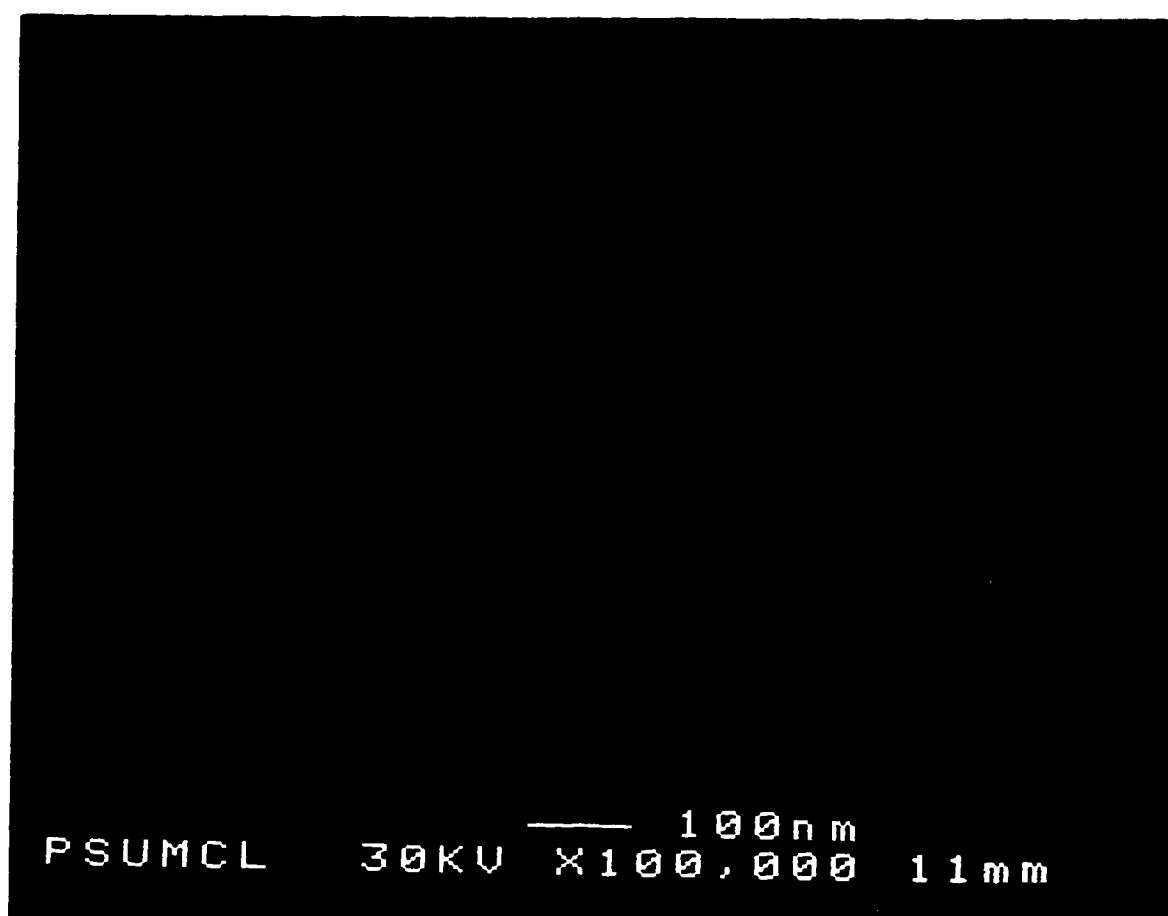
Figure 4.64. A FESEM micrograph of the surface of a PZT film on a Pt-coated Si substrate at 200,000X magnification. Film was RTAd at 700°C for 30 seconds.

PSUMCL　30KU　　10μm　X2,300　12mm
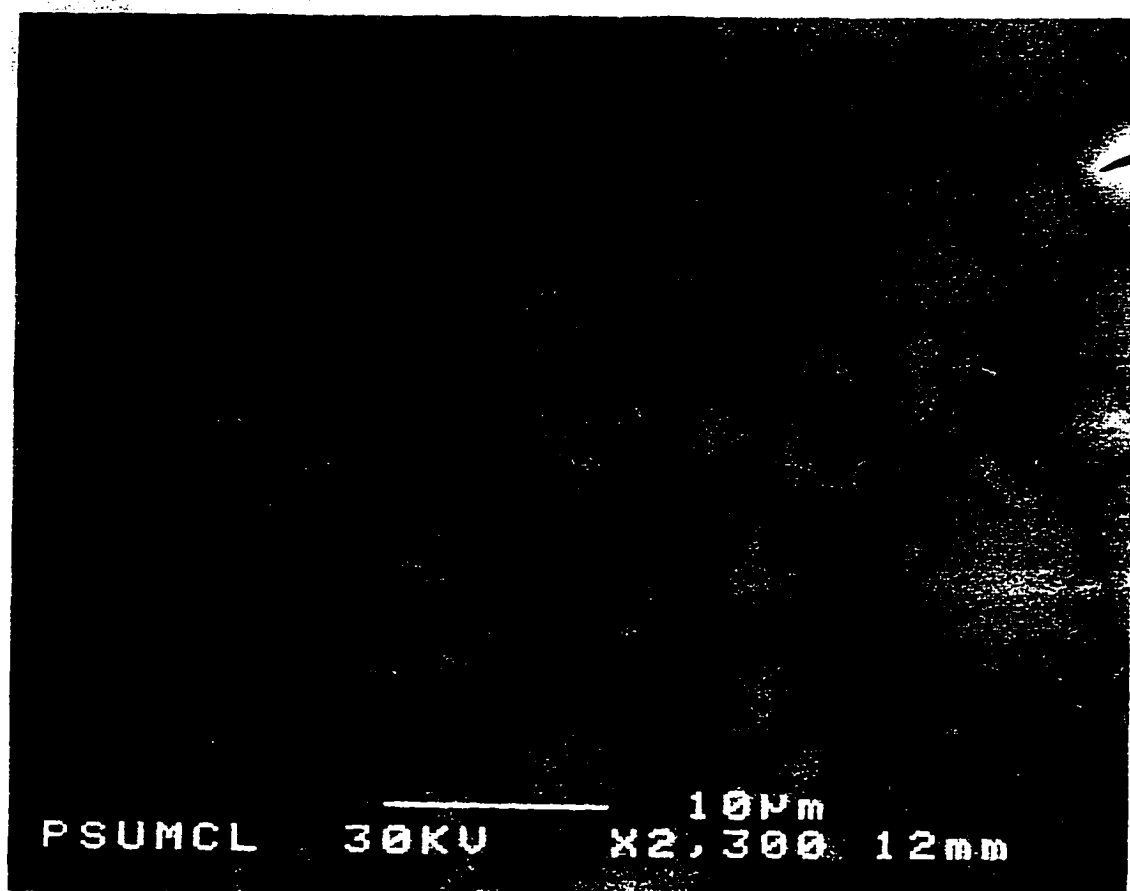
Figure 4.65. An FESEM micrograph of the surface of a PZT film on a (0001) sapphire substrate at 2300X. The film was RTAd at 700°C for 30 seconds.

The micrographs at higher magnifications for the PZT film on the sapphire substrate are shown in Figures 4.66 and 4.67. A 65,000X magnification image shown in Fig. 4.66 indicates long and narrow cluster structures with the size of approximately 300 to 700 nm in length. The reason for this elongated cluster structure on the surface of the film is unknown. An image at 150,000X is shown in Figure 4.67. The cluster size of the film shown is approximately 500 nm in diameter and the primary grain size of PZT films on sapphire substrate appeared to be around 10 to 15 nm in diameter. Compared to previous studies (Fox et al. 1992 and Gibbons 1995), the RTA sol-gel PZT thin films prepared in this study appeared to have much finer grained microstructure. This may be due to the fact that films were rapid thermally annealed at a ramp rate of 100°C/ second which is fast enough to suppress most grain growth.

In sum, it is evident that RTA sol-gel PZT film shows a nicely uniform, and dense microstructure which is needed for the synthesis of high quality ferroelectric materials. Moreover, the films also show quite a smooth surface structure, which will be discussed more in the next section.

4.2.3.2. Atomic Force Microscopy

The surface morphology of the sol-gel PZT films prepared in this study was also investigated using atomic force microscopy (AFM). This measurement was done at the Department of Chemistry of Syracuse University, Syracuse, NY by G. Zavala and J. H. Fendler.
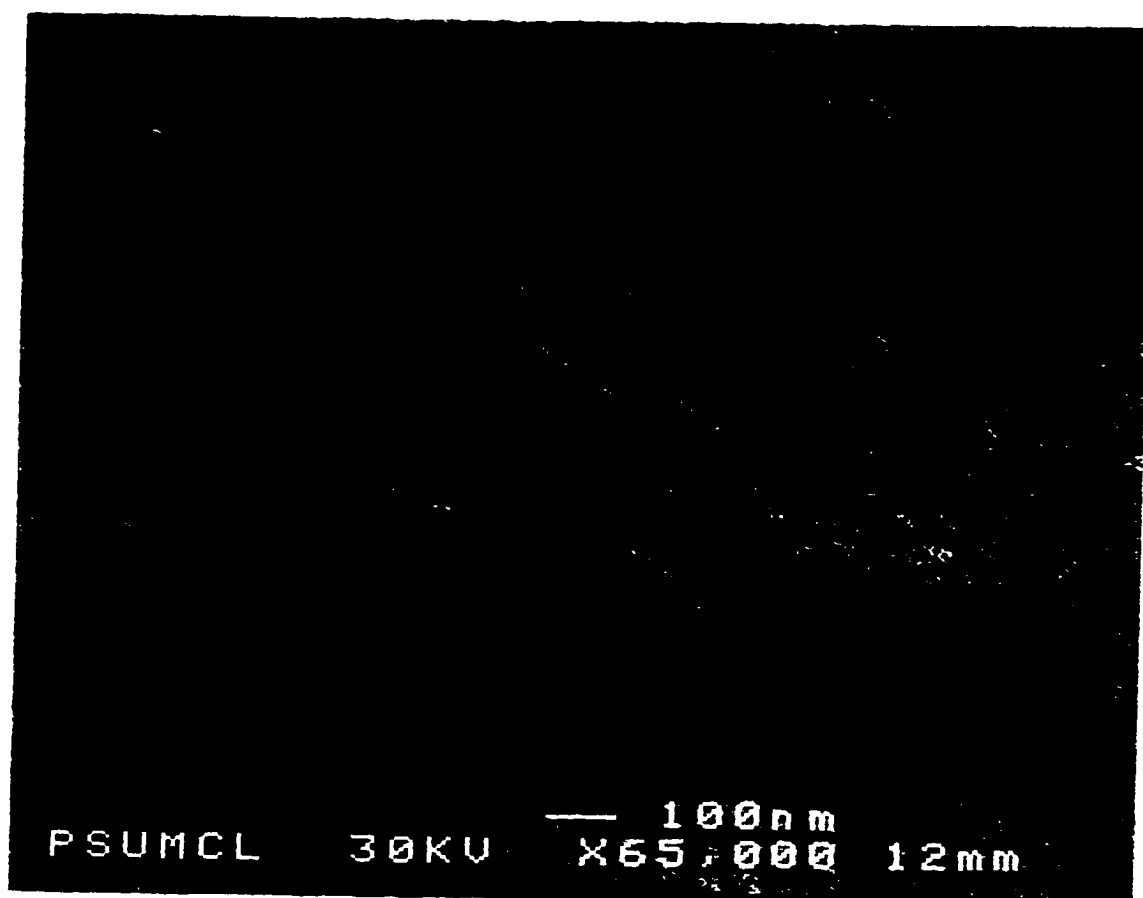
Figure 4.66. An FESEM micrograph of a PZT film on a (0001) sapphire substrate at 65,000X. The film was RTAd at 700°C for 30 seconds.
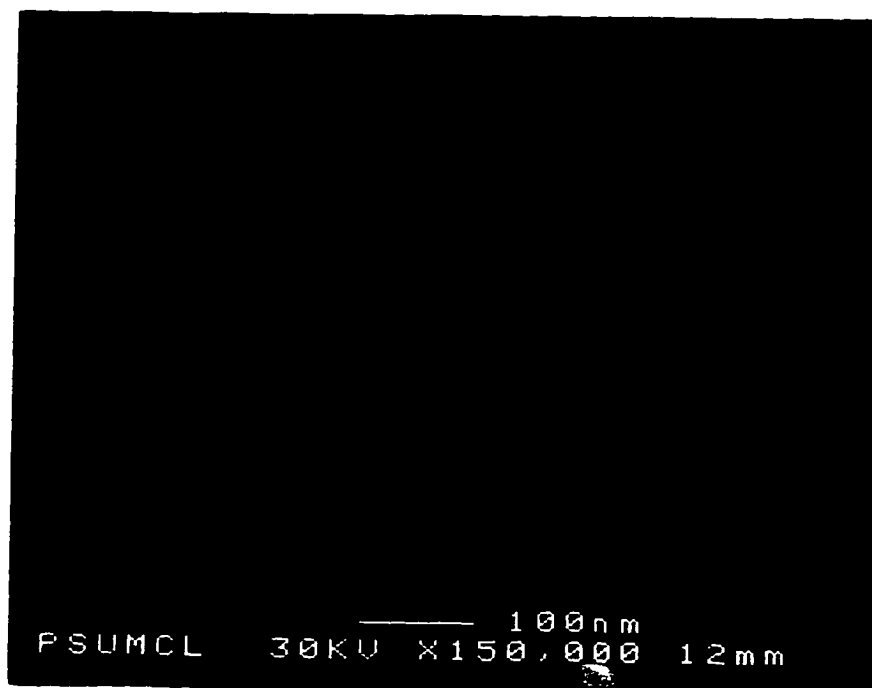
Figure 4.67. An FESEM micrograph of a PZT film on a (0001) sapphire substrate at 150,000X . The film was RTAd at 700°C for 30 second.

An AFM topography image of a PZT film on a Pt-coated Si substrate (RTA 700°C for 30 seconds) which was obtained in a contact mode using a silicon nitride tip is shown in Figure 4.68. The force per unit length employed by the silicon nitride tip was 0.064 N/m (Zavala et al. to be published). The image in Fig. 4.68 indicates that the surface roughness of the PZT film, which was determined by the root mean square method, is approximately 7 nm in thickness. This image also clearly shows that the sol-gel PZT films prepared in this study have a uniform microstructure with a very low surface roughness. It should be noted that this technique provides a direct measurement of the surface roughness. The results show excellent agreement with the modeled depth profiles acquired from the spectroscopic ellipsometry (SE). Figure 4.69 shows a SE model for a comparable PZT film which was RTAd at 700°C for 30 seconds.

4.3. Electrical Characterization

Although through the course of this study, the microstructure evolution and the phase transformation between the intermediate pyrochlore or fluorite-type phase and the desirable perovskite phase in PZT thin films has been the main focus, the electrical properties of these films are also an important measure of quality. Thus, hysteresis measurements and the dielectric constant of the sol-gel PZT films prepared in this study have also been examined. Testing of the ferroelectric and dielectric properties of these films is necessary to determine how these PZT materials will perform under device operating conditions.

500 nm

7.37 nm

0 nm

0 nm   250 nm   500 nm
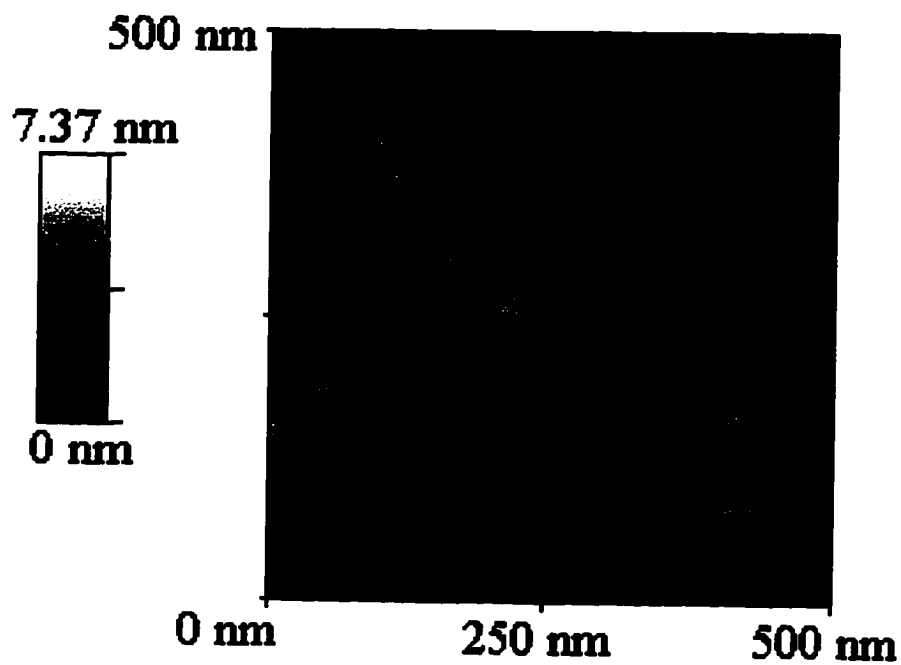
Figure 4.68. An AFM topography image of a PZT film on a Pt-coated Si substrate. The film was RTAd at 700°C for 30 seconds (Measurements made by G. Zavala and J. Fendler at Syracuse University).

air

film + air

t = 87 ± 9 Å   Vf of air = 50%

film

t = 2370±12 Å

Pt-coated Si

σ = 0.07

A1 = 1
A2 = 5.16 ±0.15
A3 = 222.7 ± 5.8 nm
A4 = 0
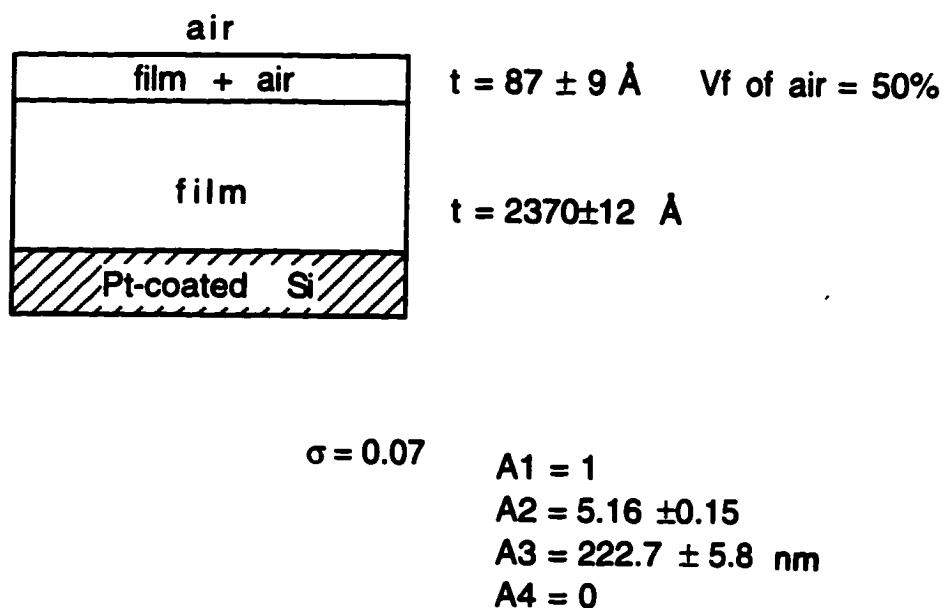
Figure 4.69. The best-fit model for a PZT film on a Pt-coated Si substrate which was RTAd at 700°C for 30 seconds.

Several studies (Udayakumar 1992, Chen et al. 1992b, Krupanidhi et al. 1992, McKinstry et al. 1993, and Gibbons 1995) have been done on PZT thin films of this composition of 52/48 (Zr/Ti) and the dielectric constants have been reported between 800 and 1300 depending on deposition methods, orientations (Brooks et al. 1994), and annealing conditions (Tuttle et al. 1993, Hu et al. 1993, and Griswold et al. 1995). For example, films with an inhomogeneous structure or with second phases show a great degradation in the dielectric constant (Kwok and Desu 1992 and Chen and Chen 1994).

To measure the capacitance and loss of the films in this study, a Hewlett Packard multi-frequency LCR meter (model 4275A) was used at 1 kHz. The dielectric constant (K) can then be determined from the following equation:

$$K = \frac{C_0 t}{\varepsilon_0 A}$$

(4.2)

where K represents the dielectric constant, C_0 is the capacitance, t is the film thickness, ε_0 is the permittivity of free space (8.85×10^{-12} F/m), and A is the area of electrode which 7.065×10^{-4} cm^2 is used in this study. The dielectric constant and the dielectric loss of sol-gel PZT films prepared in this study are reported in Table 4.7. Films show a reasonable value of dielectric constant and low dielectric loss.

Table 4.7

A summary of dielectric constants found on sol-gel PZT films after RTA at 700°C for 30 seconds.

Film Thickness (Å)	Capacitance (nF)	Dielectric Constant	Dielectric Loss
2500	2.054	820	0.032
3000	1.985	950	0.032
3000	2.088	1000	0.033
3500	2.044	1140	0.047

The hysteresis data for a PZT film on a Pt-coated Si substrate after rapid thermally annealing at 700°C for 30 seconds were measured. Voltages from 7 to 19 volts were applied to the films and the loops at various applied voltages are shown in Figure 4.70 The remanent polarizations was 32 $\mu C/cm^2$ for an applied voltage of 19 volts. The coercive field was typically ~ 70 kV/cm for films with thickness of 3500 Å.

In summary, the RTA conditions of 700°C, 30 seconds anneals seem to be the best for the sol-gel PZT films prepared in this study. The good hysteresis behavior and a relatively high dielectric constants of these films should be due to the fact that they are fully crystallized to the desirable perovskite phase and also have the uniform and dense microstructure with very low surface roughness as previously discussed.
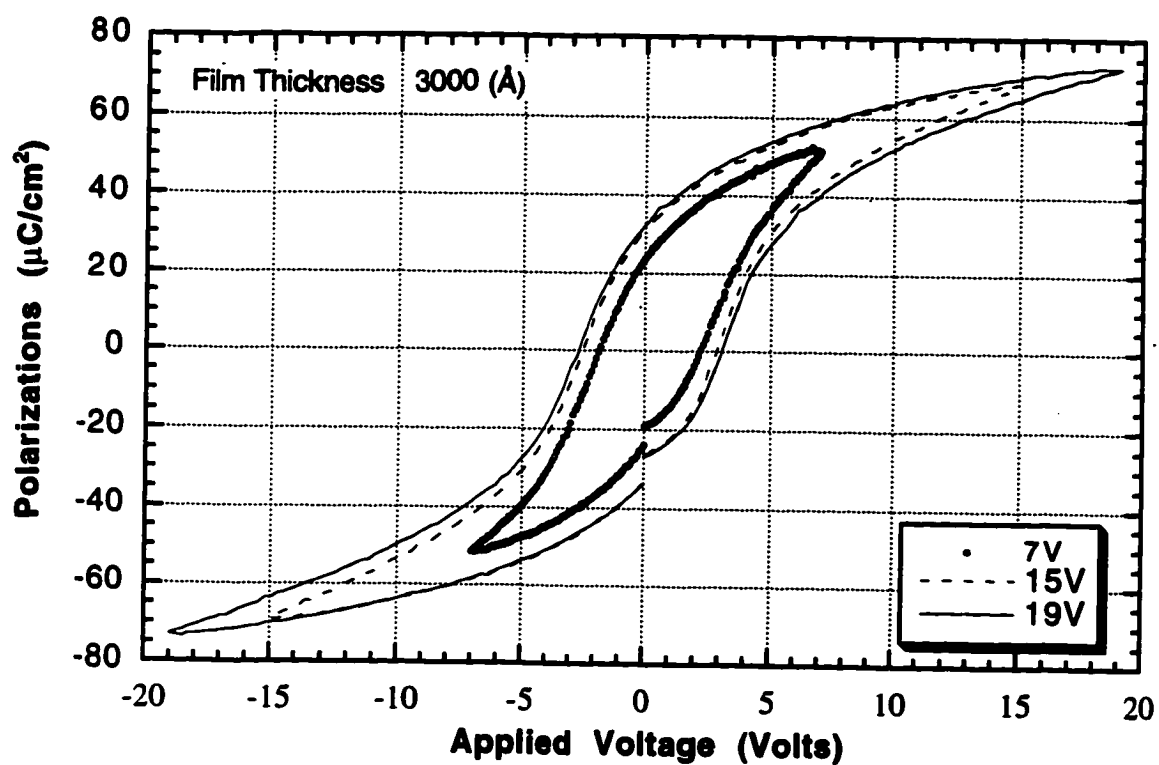
Figure 4.70. A plot of hysteresis measurements for a PZT film on a Pt-coated Si substrate after RTA at 700°C for 30s.

Chapter 5

CONCLUSIONS AND FUTURE WORK

Controlling the microstructure evolution and the phase development in PZT ferroelectric thin films are essential for the fabrication of devices with optimized electrical and optical properties. In this thesis, *in-situ* SE measurements and high-temperature X-ray diffraction were used not only to study the real-time crystallization and growth kinetics of PZT thin films, but also to follow the microstructure development and the optical properties of thin films during annealing. This type of information will be useful for the synthesis of high quality PZT thin films in applications including microelectronics and optical devices, non-volatile Random Access Memories (RAMs), pyroelectric detectors and sensors, and microelectromechanical systems (MEMS).

The key results along with the characteristics and properties of PZT thin films are summarized as follows:

1) Sol-gel PZT thin films with compositions at the morphotropic phase boundary (52/48) were prepared using metal alkoxides and 2-methoxyethanol as a solvent. Films were spin-coated onto various substrates including Pt-coated Si, (0001) sapphire, and (100) MgO. Following an RTA (700°C for 30 seconds) crystallization step, the films showed good electrical properties. The remanent polarizations for PZT films with varying thickness from 2500 to 3500Å ranged between 23.7 to 35 $\mu C/cm^2$. The dielectric constant was between 820 and 1140, and the dielectric loss ~ 0.03-0.05.

2) The optical properties (i.e. the refractive index and optical reference data) and the microstructure evolution of PZT films were determined by spectroscopic ellipsometry measurements between 400 and 750 nm during annealing. From the SE modeling, the PZT films showed quite a homogeneous microstructure with a thin layer of the roughness at the surface after 600°C anneals. As PZT films crystallized to the perovskite phase, the film refractive indices were high and comparable with bulk lanthanum-doped PZT ceramics (Thacher 1977). This result indicates that the PZT films are near full density.

3) The intermediate-perovskite phase transformation in PZT films on both Pt-coated Si and MgO substrates during annealing was investigated using an *in-situ* X-ray diffractometer. Constant heating rates from 5° to 100°C/minute were utilized in order to examine the crystallization kinetics of both phases. The nucleation temperatures and the temperatures which show the maximum growth of both the intermediate and the perovskite PZT phases were examined. The fastest ramp rate (100°C/minute) used in this study did not permit the bypass of the intermediate phase formation.

4) The microstructures of PZT films (RTA at 700°C for 30s) were also examined by the field emission scanning electron microscope (FESEM). The surface image of the films showed dense, fine-grained cluster structures of sizes ranging between 150 nm and 10 μm with a primary grain size of 10-15 nm. Results from AFM also confirmed that sol-gel PZT films prepared in this study had a dense and uniform microstructure with a low surface roughness of ~ 7 nm thick.

5) The crystallization kinetics of PZT thin films were investigated by high-temperature X-ray measurements using constant heating rates of 5° to

100°C/minute during annealing to 700°C. Based on the XRD results during annealing, attempts to apply the Johnson-Mehl-Avrami (JMA) transformation rate equation were made to determine the Avrami's exponent (n) values for the transformation of the intermediate to perovskite phase in sol-gel PZT films on both Pt-coated Si and MgO substrates. However, it was found that it was not appropriate to apply the JMA equation to the kinetics of the intermediate-perovskite phase transformation in PZT thin films in this study. Possible explanations include failure to satisfy the assumptions which permit the JMA equation to a non-isothermal case. In particular, the assumption of a constant activation energy in the kinetics of the intermediate to perovskite phase transformation over the heating range studied here may not be true. Certainly, if it is true that the intermediate phase can be bypassed at high heating rates (faster than those used in this study), then the nucleation activation energy must change with heating rate. In addition, error due to the calculation of the volume fraction transformed from the X-ray data could also contribute to the apparent failure to fit JMA non-isothermal kinetics.

The crystallization kinetics of PZT films were also investigated by *in-situ* SE measurements during annealing to 500°C or 700°C at 5°C/min heating rate. Results showed that during film crystallization, the ellipsometric parameters Δ and Ψ, which were measured at a single wavelength at 500 nm, show noticeable changes. Based on the XRD results, it could be qualitatively assumed from the SE study that an intermediate phase started to form at the point where Δ and Ψ show an abrupt change, which is at ~430°C for conductively heated films on both MgO and sapphire substrates. In addition, SE measurements have a high time resolution. Thus it can be used to follow

crystallization of thin films with better than 5 second resolution for one Δ and Ψ measurement at a single wavelength.

FUTURE WORK

Investigations of the microstructure development in sol-gel PZT thin films during annealing by spectroscopic ellipsometry and high-temperature X-ray diffraction have presented some opportunities for further research. Some suggestions are listed below:

1) Alternative PZT compositions: The role of excess lead or variations in the Zr/Ti ratio in controlling the crystallization kinetics should be studies. Many studies report (Tuttle et al. 1990 and Schwartz et al. 1992) that additions of excess PbO content compensate for lead-loss during heat treatment and lead to the crystallization of phase-pure perovskite PZT films at lower annealing temperatures. In addition, the intermediate phase was analyzed to be richer in Zr and more deficient in Pb than the perovskite structure (Wilkinson et al. 1994). Therefore, the role of different Zr/Ti ratios and changes in the PbO stoichiometry in controlling the kinetics should be studied.

2) Crystallization studies: SE has shown a great potential in studying crystallization kinetics for PZT films at a single wavelength during annealing from room temperatures to 500°C and 700°C in this study. The crystallization temperatures of the intermediate and perovskite phases could be determined. It would be interesting to further investigate the ellipsometric parameters changes with temperature at different wavelengths. This would facilitate development of

models for the Δ, Ψ trajectories which could be used to follow crystallization more rapidly than is possible with current X-ray equipment.

3) Development of an *in-situ* SE and XRD measurement system during annealing; since both spectroscopic ellipsometry and X-ray diffraction studies have shown quite a good performance in monitoring the real-time microstructure evolution and the phase transformations in PZT thin films during annealing, it would be intriguing if these two instruments could be used simultaneously. The optical characterization, and the structural characterization including the microstructure evolution and phase development of a material could then be examined at once.

REFERENCES

Adachi, H., T. Mitsuyu, O. Yamazaki, and K. Wasa, *Jpn. J. Appl. Phys. Suppl.* **24**, 3 (1985).

Afify, N., *J. Non-Cryst. Solids.*, **128**, 279 (1991).

Afify, N., M. A. Abdel-Rahim, A. S. Abd El-Halim, and M. M. Hafiz, *J. Non-Cryst. Solids.*, **128**, 269 (1991).

Ameen, M. S., T. M. Graettinger, S. H. Rou, H. N. Al-Shareef, K. D. Gifford, O. Auciello, and A. I. Kingon, in Ferroelectric Thin Films, ed. E. R. Myers and A. I. Kingon, *Mater. Res. Symp. Proc.*, **200**, 65 (1990).

Araujo, C. A., L. D. McMillan, B. M. Melnick, J. D. Cuchiaro, and J. F. Scott, *Ferroelectrics* **104**, 241 (1990).

Aspnes, D. E. *Optics Commun.* **8**, 222 (1973).

Aspnes, D. E., *J. Opt. Soc. Amer.* **64** [6] 812 (1974).

Aspnes, D. E., *Appl. Opt.* **14**, 1131 (1975).

Aspnes, D. E., and A. A. Studna, *Appl. Opt.* **14**, 220 (1975).

Aspnes, D. E, *Amer. J. Phys.*, **50**, 704 (1982).

Atkin, R. B., *Ferroelectrics* **3**, 213 (1972).

Augis, J. A., and J. E. Bennett, *J. Thermal. Anal.*, **13**, 283 (1978).

Avrami, M., *J. Chem. Phys.*, **7**, 1103 (1939).

Avrami, M., *J. Chem. Phys.*, **8**, 212 (1940).

Avrami, M., *J. Chem. Phys.*, **9**, 177 (1941).

Azzam, R. M. A., N. M. Bashara, in *Ellipsometry and Polarized Light*, North-Holland, Amsterdam (1977).

Bennett, K. W., P. S. Brody, B. J. Rod, L. P. Cook, and P. K. Schenok, *Proc. ISIF*, 541 (1992).

Blocher, J. M., in *Deposition Technologies for Films and Coatings*, ed. R. F. Bunshah, Noyes (1982).

Bondurant, D., and F. Gnadinger, *IEEE Spectrum*, **30**, 30 (1989).

Bondurant, D., *Ferroelectrics* **112**, 273 (1990).

Brooks, K., I. M. Reaney, R. Klissurska, Y. Kuang, L. Bursill, and N. Setter, *J. Mater. Res.*, **9** [10] 2540 (1994).

Bruggeman, D. A. G., *Ann. Phys. (leipz)*, **24**, 636 (1935).

Budd, K. D., S. K. Dey, and D. A. Payne, *Br. Ceram. Soc. Proc.*, **36**, 107 (1985).

Burfoot, J. C., and G. W. Taylor, *Polar Dielectrics and Their Applications*, University of California Press, Los Angeles (1979).

Cahan, B. D., and R. F. Spanier, *Surf. Sci.*, **16**, 166 (1969).

Castellano, R. N., and L. G. Feinstein, *J. Appl. Phys.*, **50**, 4406 (1979).

Cavin, O. B., and J. S. Wolf, in *Advances in X-Ray Analysis*, ed. J. V. Gilfrich, **36**, Plenum Press, New York (1993).

Chapin, L. N., and S. A. Myers, *Mat. Res. Soc. Symp. Proc.*, **200**, 153 (1990).

Chen, C. J., E. T. Wu, Y. H. Xu, K. C. Chen and J. D. Mackenzie, *Ferroelectrics* **112**, 321 (1990).

Chen, J., K. G. Brooks, k. R. Udayakumar, and L. E. Cross, *Mat. Res. Soc. Symp. Proc.*, **243**, 33 (1992a)

Chen, X., A. I. Kingon, L. Mantiese, O. Auciello, and K. Y. Hsieh, in *Proc. ISIF-92* (4th International Symposium on Integrated Ferroelectrics, March 9-11, Monterey, CA (1992b).

Chen, K. C., A. Janah, and J. D. Mackenzie, *Mater. Res. Soc. Proc.*,73, 731 (1986).

Chen, S. Y., and I. W. Chen, *J. Am. Ceram. Soc.*, 77 [9] 2337 (1994).

Chiang, C. K., W. Wong-ng, P. K. Schenck, L. P. Cook, M. D. Vaudin, P. S. Brody, B. J. Rod, and K. W. Bennett, *Mat. Res. Soc. Symp. Proc.*, 230, 321 (1992).

Chindaudom, P., *Ph.D Thesis*, The Pennsylvania State University, (1991).

Christian, J. W., in *The Theory of Transformations in Metals and Alloys*, 2nd ed., Pergamon, Oxford (1975).

Chung, D. D. L., *X-Ray Diffraction at Elevated Temperatures, a Method for In-Situ Process Analysis*, New York (1993).

Clarke, R., A. M. Glazer, F. M. Ainger, D. Appleby, N. J. Poole, and S. G. Porter, *Ferroelectrics* 11, 359 (1976).

Collins, R. W., *Rev. Sci. Instrum.* 61 [8] 2029 (1990).

Conde, C. F., H. Miranda, A. Conde, *J. Mat. Sci.*, 24, 1862 (1989).

Cullity, B. D., Elements of X-Ray Diffraction, 2nd, Addison-Wesley Publishing Company, Inc., London (1978).

Dana, S. S., K. F. Etzold, and J. Clabes, J. *Appl. Phys.*, 69 [8] 4398 (1991)

Dang, E. K. F., and R. J. Gooding, *Phys. Rev. Lett.*, 74, 3848 (1995).

Dey, S. K., and R. Zuleeg, *Ferroelectrics*, 112B, 309 (1990).

Dey, S. K., D. A. Payne, and K. D. Budd, *IEEE UFFC*, 35, 80 (1988).

Dimos, D., S. J. Lockwood, R. W. Schwartz, and M. S. Rodgers, *IEEE Trans. Components, Packaging, and Manufacturing Tech. A*, **18** [1] 174 (1995).

Drude, P., *Ann. Phys.* (Leipzig), **39**, 481 (1890).

Fan, L. S., Y. C. Tai, and R. S. Muller, *Sensors and Actuators*, **20**, 41 (1989).

Fox, G. R., *Ph. D Thesis*, The Pennsylvania State University, (1992).

Fox, G. R., S. B. Krupanidhi, K. L. More, and L. F. Allard, *J. Mater. Res.*, **7** [11] 3039 (1992).

Frost, H. J. and C. V. Thompson, *Proc. of SPIE- The International Society for Optical Engineering*, **82** (1987).

Fukishima, J., K. Kodaira, and T. Matsushita, *J. Mater. Sci.*, **19**, 595 (1984).

Gibbons, B. J., *M.S. Thesis*, The Pennsylvania State University, (1995).

Graydon, J. W., S. J. Thorpe, and D. W. Kirk, *J. Non-Cryst. Solids*, **175**, 31 (1994).

Greer, A. L., *Acta Metallurgica*, **30**, 171 (1982).

Griswold, E. M., *Ph.D Thesis*, Queen University, Ontario, CA (1995).

Griswold, E. M., L. Weaver, M. Sayer, and I. D. Calder, *J. Mater. Res.*, **10** [12] 3149 (1995)

Hankey, D. L., and J. V. Biggers, *J. Am. Ceram. Soc.*, **64**, c172 (1981).

Hauge, P. S., and F. H. Dill, *IBM J. Res. Dev.*, **17**, 472 (1973).

Henderson, D. W., *J. Non-cryst. Solids*, **30**, 301 (1979).

Hiremath, B. V., A. I. Kingon, and J. V. Biggers, *J. Am. Ceram. Soc.*, **66**, 790 (1983).

Howe, R. T., Micromachining and Packaging of Transducers, Elsevier, p. 169 (1985).

Hsu, S. T., and I. H. Kalish, *Integrated Ferroelectrics*, **2**, 179 (1992).

Huang, Y., I. M. Reaney, and A. J. Bell, *Ferroelectrics*, **134**, 225 (1992).

Hu, H., V. Kumar, and S. B. Krupanidhi, *J. Appl. Phys.*,**71**, 376 (1992).

Hu, H., C. J. Peng and S. B. Krupanidhi, *Thin Solid Films*, **223**, 327 (1993).

Iijima, K., Y. Tomita, R. Takayama, and I. Ueda, *J. Appl. Phys.*, **60**, 361 (1986).

Jaffe, B., R. S. Roth, and S. Marzullo, *J. Res. Nat. Bur. Stand.*, **55**, 239 (1955).

Jaffe, B., W. R. Cook, H. Jaffe, in *Piezoelectric Ceramics*, Academic Press, London (1971).

Jeppesen, M. A., *J. Opt. Soc. Am.*, **48**, 629 (1958).

Jerrard, H. G., *Surf. Sci.*, **16**, 137 (1969).

Johnson, W. A., and R. F. Mehl, *Trans AIME*, **135**, 416 (1939).

Jona, F. and G. Shirane, *Ferroelectric Crystals*, New York (1962).

Jones, R. C., *J. Opt. Soc. Amer.*, **31**, 488 (1941).

Jones, R., *Fundamental Principles of Sol-gel Technology*, Institute of Metal, London (1989).

Kingery, W. D., H. K. Bowen, and D. R. Uhlmann, *Introduction to Ceramics*, John Wiley & Sons, New York, (1960).

Klug, H. P., and L. E. Aexander, in *X-Ray Diffraction Procedures for Polycrystalline and Amorphous Materials*, 2nd ed., Wiley, New York (1974)

Kohli, M., Y. Huang, T. Meader, C. Wuethrich, A. Bell, P. Muralt, N. Setter, P. Ryser, M. Foster, *Microelectronic Engineering*, (1996) in press.

Kojima, M., M. Okuyama, T. Nakagawa, and Y. Hamakawa, *Jpn. J. Appl. Phys.*, **22**, Suppl.2, 14 (1983).

Kolmogorov, A. N., Izv. Acad. Nauk USSR, Ser. Math., 3, 355 (1937).

Komatsu, T., R. Sato, Y. Kuken, and K. Matsusita, *J. Am. Ceram. Soc.*, 76 [11] 2795 (1993).

Kozazeck, D. J., D. Kurtz, J. D. Fittings, and C. O. Ruud, *Proc. 6th Int. Symp. on Nondestructive Characterization of Materials, Oahu, Hawaii,* Plenum, New York, p. 285 (1993)

Krupanidhi, S. B., N. Maffei, M. Sayer, and K. El-Assal, *J. Appl. Phys.*, 54, 6601 (1983).

Krupanidhi, S. B, *Integrated Ferroelectrics*, 1, 161 (1992).

Krupanidhi, S. B., H. Hu, and V. Kumar, *J. Appl. Phys.*, 71 [1], 376 (1992).

Kwok, C. K., S. B. Desu, and L. Kammerliner, *Mater. Res. Symp. Proc.*, 200, 83 (1990).

Kwok, C. K., and S. B. Desu, *Appls. Phys. Lett.*, 60 [12] 1430 (1992).

Kwok, C. K., and S. B. Desu, and L. Kammerliner, Ferroelectric Thin Films, in *Ceramic Transactions,* ed. A. S. Balla and K. M. Nair, 25, 85 (1992).

Kwok, C. K. and S. B. Desu, *J. Mat. Res.*, 8 [2] 339 (1993).

Kwok, C. K. and S. B. Desu, *J. Mat. Res.*, 9 [7] (1994).

Lakeman, C. D. E., and D. Payne, *Ferroelectrics*, 152, 145 (1994).

Larsen, P. K., R. Cuppens, and G. A. C. M. Spierings, *Ferroelectrics*, 128, 265 (1992).

Lee, J., L. Johnson, A. Safari, R. Ramesh, T. Sands, H. Gilchrist, and V. G. Keramidas, *Appl. Phys. Lett.*, 63 [1] (1993).

Lines, G., and A. Glass, *Priciples and Applications of Ferroelectrics and Related Devices,* Clarendon Press, Oxford (1977).

MacFarlane, D. R., M. Matecki, and M. Poulain, *J. Non-Cryst. Solids*, **64**, 351 (1984).

Mahadevan, S., A. Giridhar, and A. K. Singh, *J. Non-Cryst. Solids*, **88**, 11 (1986).

Mahin, K. W., K. Hanson, and J. W. Morris, Jr., *Acta. Metall.*, **35**, 529 (1987).

Mariner, J., *Ph.D. Thesis*, The Pennsylvania State University, (1985).

Malitson, I. H., *J. Opt. Soc. Am.*, **52**, 1377 (1962).

Matusita, K., and S. Sakka, *J. Non-Cryst. Solids*, **38&39**, 741 (1980).

Matusita, K., T. Komatsu, and R. Yokota, *J. Mater. Sci.*, **19**, 291 (1984).

McClune, W. F., ed., *Powder Diffraction File - Inorganic Phases* (Int. Centre for Diffraction Data, Swarthmore), Files No. 21-949, 21-949A, and 27-1201 (1986).

McKinstry, S. E., *Ph.D. Thesis*, The Pennsylvania State University, (1992).

McKinstry, S. T., H. Hu, S. B. Krupanidhi, P. Chindaudom, K. Vedam, and R. E. Newnham, *Thin Solid Films*, **230**, 15 (1993).

McKinstry, S. T., J. Chen, K. Vedam, and R. E. Newnham, *J. Am. Ceram. Soc.*, **78** [7] 1907 (1995).

McMarr, P., *Ph.D Thesis*, The Pennsylvania State University, (1985).

Melnick, B. M., C. A. Paz de Araujo, L. D. McMillan, D. A. Carver, and J. F. Scott, *Ferroelectrics*, **116**, 79 (1991).

Muralt, P., A. Kholkin, M. Kohli, T. Maeder, K. G. Brooks, R. Luthier, *Integrated Ferroelectrics*, **11**, 213 (1995a).

Muralt, P., M. Kohli, T. Maeder, A. Kholkin, K. G. Brooks, N. Setter, and R. Luthier, *Sensors and Actuators* A, **48**, 157 (1995b).

Muralt, P., A. Kholkin, M. Kohli, and T. Maeder, *Sensors and Actuators A*, **53**, 397 (1996).

Naik, I. K., L. E. Sanchez, S. Y. Wu, and B. P. Maderic, *Integrated Ferroelectrics*, **2**, 133 (1992).

Nakagawa, T., J. Yamaguchi, M. Okuyama, and Y. Hamakawa, *Jpn. J. Appl. Phys.*, **21** [10] L655 (1982).

O' Brien, S., J. R. Shealt, D. P. Bour, L. Elbaum, and I. Y. Chi, *Appl. Phys. Lett.* **56**, 1365 (1990).

Ogawa, T., H. Kidoh, H. Yashima, A. Morimoto, and T. Shimizu, *Ferroelectrics*, **157**, 381 (1994).

Ohring, M., *The Materials Science of Thin Films*, Academic press, Inc., London (1992).

Oikawa, M., and K. Toda, *Appl. Phys. Lett.*, **29**, 491 (1976).

Okada, A., *J. Appl. Phys.*, **49**, 4494 (1978).

Okada, M., S. Takai, M. Amemiya, and K. Tominaga, *Jpn. J. Appl. Phys.*, **28**, 1030 (1989a).

Okada, M., K. Tominaga, T. Araki, S. Katayama, and Y. Sakashita, *Jpn. J. Appl. Phys.*, **29**, 718 (1989b).

OMA VISION-PDA, Data Aquistion/Analysis Software Instruction manual, EG&G Instruments Corporation, p. 80 (1993).

Ord, J. L., and B. L. Willis, *Appl. Opt.*, **6**, 1673 (1967).

Othmer, K., in *Encyclopedia of Chemical Technology*, **10**, 3rd ed., John Wiley & Sons Inc. (1980).

Ozawa, T., *Polymer*, **12**, 150 (1970).

Pascual, R., M. Sayer, C.V.R. Vasant Kumar, and L. Zou, *J. Appl. Phys.*, **70**, 2348 (1991).

Peng, C. H., J. F. Chang, and S. B. Desu, *Mat. Res. Soc. Symp. Proc.*, **243**, 335 (1992).

Peng, C. H., and S. B. Desu, *J. Am. Ceram. Soc.*, **77** [4] 929 (1994).

Polla, D. L, *Microelectronic Engineering*, **29**, 51 (1995).

Polla, D. L., and P. J. Schiller, *Integrated Ferroelectrics*, **7**, 359 (1995).

Polli, A. D., and F. F. Lange, *J. Am. Ceram. Soc.*, **78** [12] 3401 (1995).

Porter, D. A. and K. E. Eastering, *Phase Transformations in Metals and Alloys*, Chapman and Hall, New York (1992).

Ramkumar, K., J. Lee, A. Safari, and S. Danforth, *Mat. Res. Soc. Symp. Proc.*, **200**, 121 (1991).

Ranganathan, S., and M. Von heimendahl, *J. Mater. Sci.*, **16**, 2401 (1981).

Reaney, I. M., K. Brooks, R. Klissurska, C. Pawlaczyk, N. Setter, J. Am. Ceram. Soc., 77 [5] 1209 (1994).

Robbins, W., *Integrated Ferroelectrics*, **11**, 179 (1995).

Roy, R. A., K. F. Etzold, and J. J. Cuomo, *Mat. Res. Soc. Symp. Proc.*, **200**, 141 (1990).

Saetre, T. O., O. Hunder, and E. Nes, *Acta. Metall.*, **34**, 981 (1986).

Sakashita, Y., T. Ono, and H. Segawa, *J. Appl. Phys.*, **69**, 8852 (1991).

Sayer, M., C. V. R. Vasant Kumar, D. Barrow, L. Zou, and D. T. Amm, in Ferroelectric Thin Films II, ed. A. I. Kingon, E. R. Myers, and B. Tuttle, *Mat. Res. Soc. Symp. Proc.*, **243**, 39 (1992a).

Sayer, M., Z. Wu, C. V. R. Vasant Kumar, D. T. Amm, and E. M. Griswold, *Can. J. Phys.*, **70**, 1159 (1992b).

Schuegraf, K. K., *Hanbook of Thin-Film Deposition Process and Techniques*, Noyes, Park Ridge, NJ (1988).

Schwartz, R. W., R. A. Assink, and T. J. Headley, in Ferroelectric Thin Films II, ed. A. I. Kingon, E. R. Myers, and B. Tuttle, *Mat. Res. Soc. Symp. Proc.*, **243**, 245 (1992).

Scott, J. F., and C. A. Araujo, *Science*, **246**, 1400 (1989).

Scott, J. F., and C. A. Araujo, H. B. Meadows, L. D. McMillan, and A. Schawabkeh, *J. Appl. Phys.*, **66**, 1444 (1989).

Scott, J. F., and C. A. Araujo, H. B. Meadows, L. D. McMillan, *Ferroelectrics*, **116**, 107 (1991).

Shorrocks, A. Patel, M. J. Walker, and A. D. Parsons, *Microelectronic Engineerings*, **29**, 59 (1995).

Shur, V. Ya, S. A. Negashev, E. L. Rumyantsev, A. L. Subbotin, and S. D. Makarov, *Ferroelectrics*, 1995 (in press).

Singh, R., *J. Appl. Phys.*, **63** [8] R59 (1988).

Sinharoy, S., H. Buhay, D. R. Lampe, and M. H. Francombe, *J. Vac. Sci. Tech. A*, **10** [4] (1992).

Sreenivas, K. and M. Sayer, *J. Appl. Phys.*, **64**, 1484 (1988).

Stobie, R. W., B. Rao, and M. J. Dignam, *Appl. Opt.*, **14**, 999 (1975).

Subbanna, G. N., and C. N. R. Rao, *Eur. J. Solid State Inorg. Chem.*, **26**, 7 (1989).

Takasaki, H., *J. Opt. Soc. Am.*, **51**, 463 (1961).

Takayama, R., Y. Tomita, K. Iijima, and I. Ueda, *J. Appl. Phys.*, **61** [1] 411, (1987).

Tani, T., C. D. E. Lakeman, J. F. li, Z. Xu, and D. A. Payne, in Ferroic Materials: Design, Preparation and Characteristics, ed. A. S. Bhalla, K. M. Nair, I. K. Lloyd, H. Yanagida and D. A. Payne, *Ceramic Transactions*, **43**, 89 (1994).

Thacher, P. D., *Appl. Opt.*, **16**, 3210 (1977).

Tohge, N., S. Takahashi, and T. Minami, *J. Am. Ceram. Soc.*, **74** [1] 67 (1991).

Tuttle, B. A., *Mater. Res. Soc. Bull.*, **12**, 40 (1987).

Tuttle, B. A., R. W. Schwartz, D. H. Doughty, and J. A. Voight, in Ferroelectric Thin Films, ed. E. R. Myers and A. I. kingon, *Mat. Res. Soc. Symp. Proc.*, **200**, 159 (1990).

Tuttle, B. A., J. A. Voight, D. C. Goodnow, T. J. Headley, M. O. Eatough, G. Zender, R. D. Nasby, S. M. Rogers, *J. Am. Ceram. Soc.*, **76** [6] 1537 (1993).

Tuttle, B. A., J. A. Voight, T. J. Headley, B. G. Potter, D. Dimos, R. W. Schwarts, M. T. Dugger, J. Michael, R. D. Nasby, T. J. Garino, and D. C. Goodnow, *Ferroelectrics*, **151**, 11 (1994).

Udayakumar, K. R.,J. Chen, S. B. Krupanidhi, and L. E. Cross, in *Proceedings of 7th International Symposium on Applications of Ferroelectrics*, Bethlehem, PA (1990).

Udayakumar, K. R., S. F. Bart, A. M. Flynn, J. Chen, L. S. Tavrow, L. E. Cross, K. A. Brooks, and D. J. Ehrlich, in *Proc. 4th IEEE Workshop on Micro Electro Mechanical Systems*, ed. H. Fujita and M. Esashi, 109, (1991).

Udayakumar, K. R, *Ph.D Thesis*, The Pennsylvania State University, (1992).

Valasek, J., *Phys. Rev.*, 2nd Ser., **17**, 475 (1921).

Vasant Kumar, C. V. R., M. Sayer, R. Pascual, and D.T. Amm, Z. Wu, and D. M. Swanston, *Appl. Phys. Lett.*, **58**, 1162 (1991).

Vasant Kumar, C. V. R., R. Pascual, and M. Sayer, *J. Appl. Phys.*, **71** [2] 864, (1992).

Vest, R. W., *Ferroelectrics*, **102**, 53 (1990).

Voigt, J. A., B. A. Tuttle, T. J. Headley, M. O. Eatough, D. L. Lamppa, and D. Goodnow, *Mater. Res. Soc. Symp. Proc.*, **310**, 15 (1993).

Walck, J. C. and C. G. Pantano, *J. Non-Cryst. Solids*, **124**, 145 (1990).

Wei, W. C., and J. W. Hallaran, *J. Am. Ceram. Soc.*, **71**, 581 (1988).

Whatmore, R. W., *Ferroelectrics*, **118**, 241 (1991).

Wilkinson, A. P., J. S. Speck, A. K. Cheetham, S. Natarajan, and J. M. Thomas, *Chem. Mater.*, **6**, 750 (1994).

Wu, S. Y., *IEEE Trans. on Electron Devices*, **21**, 499 (1974).

Wu, E., K. C. Chen, J. D. Mackenzie, *Mater. Res. Soc. Symp. Proc.*, **32**, 162 (1984).

Xiao, D. Q., J. G. Zhu, and Z. H. Qian, *Ferroelectrics*, **151**, 27 (1994).

Xu, Y., and J. D. Mackenzie, *Mat. Res. Soc. Symp. Pcoc.*, **32**, 162 (1984).

Xu, Y., and J. D. Mackenzie, *Integrated Ferroelectrics*, **1** [1] 17 (1992).

Yang, B., *Ph.D Thesis*, The Pennsylvania State University, (1988).

Yi, G., Z. Wu, and M. Sayer, *J. Appl. Phys.*, **64**, 2717 (1988).

Yi, G., and M. Sayer, *Am. Ceram. Soc. Bull.*, **70** [7] 1173 (1991).

Yinnon, H., and D. R. Uhlmann, *J. Non-Cryst. Solids*, **54**, 253 (1983).

Zavala, G., J. Fendler, S. Trolier-McKinstry, to be published.

Zevin, L. S., Powder Diffraction, **3**[1], 25 (1988).

Zheludev, I. S., *Physics of Crystalline Dielectrics*, Plenum Press, New York (1971).

Zuleeg, R., and H. H. Weider, *Solid State Electronics*, **9**, 657 (1966).

VITA

Pavadee Aungkavattana was born in Udornthani, Thailand. She received a Bachelor of Science degree in Materials Science in 1988, from Chulalongkorn University, Bangkok, Thailand. After serving as a ceramist at the Thai-German Ceramic Industry, Bangkok, Thailand for 1 year, she was granted a scholarship from the Royal Thai Government to further her education through study in the U.S.A. She attended The Pennsylvania State University where she obtained her Master of Science degree in Ceramic Science in December 1992, with a specialty in mixed-conducting oxide electrode materials for solid oxide fuel cell. Pavadee is a member of the American Ceramic Society and the Materials Research Society.